The Development of a Prediction Tool for Utility Boiler Performance

By

Thomas Michael Rees-Gralton

Submitted for the degree of PhD

Division of Mechanical Engineering and Energy Studies

Cardiff School of Engineering

2007

Abstract

Coal combustion looks set to continue in the near future, however, with the pressure being put on power generators, by the UK government, to reduce carbon emissions, ways of reducing CO_2 emissions are constantly being sought. Co-firing of biomass in pulverised coal-fired boilers is one possible solution. An investigation into this technology has been carried out with particular attention being paid to combustion modelling techniques. Following a comprehensive review of related literature two tasks were carried out; the simulation of a 500kW downfired furnace using the FLUENT CFD code, and the development of a universal boiler performance prediction tool.

During the CFD task, blends of $5\%_{th}$ and $10\%_{th}$ sewage sludge and pure coal were simulated. Particle impaction rates were predicted on two deposition probes; however, the task highlighted the need to produce a high quality computational grid as part of the modelling process. In the second task empirical correlations, later to be replaced by artificial neural networks, were derived, which could predict the temperature profile, deposition performance and corrosion performance of a full-scale boiler. These models were tested using predictions for the $618MW_{th}$ Langerlo boiler and the $1316MW_{th}$ Cottham boiler, producing consistent results. These results were found to satisfy what was expected from the literature.

Acknowledgements

I would like to take this opportunity to express my thanks to all of the people who have contributed their time and support throughout the course of my research at Cardiff University.

Firstly, I would like to extend my deepest gratitude to my supervisors Professor Nicholas Syred and Anthony J Griffiths for their continued support, guidance and inspiration through out the course of my work.

Special thanks go to PowerFlam colleagues Dr. C. K. Tan, Dr. Adlansyah Abd Rahmann and Steve Morris for their contributions to this research.

To fellow researchers Dr. Katon Kurniawan and Dr. Darrell Egar for their continued help and advice.

To the masters, Euroflam and project researchers, Gianfranco Scribano, Romolo Carrieri, Tristan Lermitte, Dr. Ruby Ray and especially Jorn Bruchmüller for their help and advice.

Finally, thanks to my family for their encouragement and to my wife Rachel for her endless support and understanding throughout my research.

Publications

Papers:

Syred. N, Griffiths. A. J, Gralton. T. M. R and Wilcox. S. J. *Evaluation of a spreadsheet-based model to aid diagnostics of slagging and fouling problems in utility boilers*. Session 5A, Fouling and Slagging and Ash, 6th European Conference on Coal Research and Its Applications, University of Kent, September 2006.

Presentations:

Gralton. T. M. R, Syred. N and Griffiths. A. J. *Approaches to Modelling Slagging in Utility Boilers*, IFRF 14th Members Conference: A sustainable Energy Supply For Industry – A Challenge for the IFRF. Noordwijkerhout (NL), 12 – 14 May 2004.

Gralton, T. M R. *Development of a Performance Indicator for Industrial Boilers*. Energy Institute South Western and South Wales Branch Young Persons' Paper Presentation Evening, Cardiff University,

Contents

List of Figures

List of Tables

Acronyms and Abbreviations

AISI - American Iron and Steel Institute
AZCM - Advanced Zonal Computational Method
CCSEM - Computer Controlled Scanning Electron-microscopy
CFB - Circulating Fluidised Bed
CFD - Computational Fluid Dynamics
CHP - Combined Heat and Power
COP - Conference of Parties
FC - Fixed Carbon
FEGT - Furnace Exit Gas Temperature
FT - Fluid Temperature
HFC - Hydrofluorocarbon
HGI - Hardgrove Grindability Index
HT - Hemispherical Temperature
HV - Heating Value
IPCC - Intergovernmental Panel on Climate Change
IT/ID/IDT - Initial Deformation Temperature
MSW - Municipal Solid Waste
MtC - Million Tonnes of Carbon
PF - Pulverised Fuel
PFC - Perfluorocarbon
Ppm - Parts per million
RDF - Refuse Derived Fuel
ROW - Right of Way Trimmings
SRWC - Short Rotation Woody Crop
ST - Softening Temperature
UBC - Unburned Carbon
UNFCCC - United Nations Framework Convention on Climate Change
VM - Volatile Matter
1D - One dimensional
2D - Two dimensional
3D - Three dimensional

$\%_{mol}$ - Percentage by mole (mole fraction)

$\%_{th}$ - Percentage by thermal contribution

$\%_{vol}$ - Percentage by volume

$\%_{wt}$ - Percentage by weight

Chapter 1 – Introduction

1.1 Background

Since the 17th century average temperatures in central England have risen by 0.7°C; 0.5°C of this rise was seen in the 20th century [1]. It has been predicted that within the next 100 years global temperatures could rise by between 1.4 and 5.8°C [1]. The potential influence on the global climate caused by this change will have many far reaching effects and are a concern for politicians and scientists the world over. A temperature rise of this magnitude could cause an increase in hot days and heat waves over nearly all land areas, resulting in higher mortality from heat related illnesses in the elderly, increased stress on livestock and wildlife and an increase in electric cooling demand [2]. Coupled with this will be an increase in the intensity of precipitation events worldwide and specifically increased wind speeds and rainfall in tropical cyclones [2]. This increases the threat of landslides, avalanches as well as structural damage to buildings and infrastructure [2]. Summer droughts will become more likely in mid-latitude continental interiors, resulting in crop damage or failure, threat to water resource quantity and quality and an increased risk of forest and scrub fires [2]. These changes will increase the threat to human life and could prove damaging to many ecosystems world wide [2].

1.2 International Efforts to Combat Climate Change – The Kyoto Protocol

Many Governments are seeking to take action to ensure that these changes do not take place; signing international agreements to reduce global greenhouse gas emissions. Work began some 25 years ago when the first World Climate Conference was held in 1979. In 1988 the Intergovernmental Panel on Climate Change (IPCC) was created to gather and assess scientific data on the subject and by 1990 had issued their first assessment report identifying the threat of climate change as real [2]. In 1992, at the earth summit in Rio de Janeiro, the United Nations Framework Convention on Climate Change (UNFCCC) was opened for signature. Since coming into force in 1994, the convention has been joined by 188 states who meet annually for the Conference of Parties (COP). At the 3rd COP, held in Kyoto, Japan, an extension to the convention was adopted, outlining legally binding commitments for emissions reduction by member states; this became known as the Kyoto Protocol. Since its inception, further meetings in Buenos Aires (Argentina), The Hague (The Netherlands), Bonn (Germany), Marrakech (Morocco) and New Delhi (India) have been held to clarify the details of the protocol. A separate process of signing and ratification by governments has been required before it could be enforced [2].

Under the terms of the agreement, European countries have taken on a commitment to reduce their greenhouse gas emissions to a level 8% lower than 1990s levels by the period 2008 - 2012 [1]. The UK is committed by the agreement to reducing its emissions to a level 12.5% below 1990 levels, however, the UK government has made a domestic pledge to reduce levels to 20% below 1990 levels by the year 2010 [1]. The six greenhouse gases identified by the protocol are: [1, 2]

- Carbon Dioxide (CO_2)
- Methane (CH_4)
- Nitrogen Oxides (NO_x)
- Hydrofluorocarbon (HFC)
- Perfluorocarbon (PFC)
- Sulphur hexafluoride (SF_6)

1.3 The Effects of Kyoto to Date

In 1990 the UK produced the equivalent of 208.4 million tonnes of carbon (MtC) of greenhouse gases, with CO_2 providing 79% of the direct global warming potential, methane 10%, NO_x 9% and the others 2%. By 1999, the UK had succeeded in reducing its total greenhouse gas emissions to 14.5% below 1990 levels [1]. This saw a 9% drop in CO_2, a 28% drop in methane, a 36% drop in NO_x and PFC and a 60% drop in HFC [1]. SF_6 rose by 18% [1].

A large proportion of the carbon dioxide reduction is due to the switch from burning coal in old power stations for power generation to new more efficient gas fired boilers [1]. The reduction is also attributed to the fact that "coal has the highest CO_2 emission factor (ratio of CO_2 emission to plant efficiency) of all fossil fuels, caused by its intensive carbon property and low conversion efficiency" [3]. However, this sort of reduction is a 'one-off' and will not be repeated. Therefore the current trend of CO_2 reduction is not sustainable. It has been forecast that without additional policies to tackle emissions, greenhouse gas levels will have risen from 15% below 1990 levels in 2005 to only 11.7% below 1990 levels by 2020 [1]. This problem is set to worsen as the UK's dependence on fossil fuels looks set to continue due to the de-commissioning of the fleet of nuclear power stations as they reach the end of their licensed lifetimes; removing 25% of the country's electricity supply [1]. Coupled with a predicted rise in the population of 5% by 2021 [1] and a steady increase in household energy consumption, power generators will face enormous difficulty in maintaining a trend of CO_2 reduction.

The UK energy policy, adopted by the British government to attempt to combat this potential downturn in greenhouse gas reduction is to "ensure secure, diverse and sustainable supplies of energy at competitive prices, best achieved by the operation of competitive markets in energy production and supply in which commercial pressures ensure that companies strive at all times to improve their efficiency" [1]. One of the measures by which the government hopes to achieve this is the renewables obligation, which states that by 2010 "10% of sales from licensed electricity suppliers will be generated from eligible renewable sources" and that the use of "biomass energy sources" is to be encouraged [1]. This presents an opportunity for power generators to substitute a percentage of their standard fuel with biomass fuel sources at a considerable cost saving.

1.4 Biomass as a Fuel Source

There is a continuous radiant power of 10^{17}W incident on the top of the earth's atmosphere, 0.02% of this is used or collected by plants, giving a total annual energy storage of 10^{21}J [4]. This means there is enormous global potential for biomass utilisation as an energy source. Generally, the word biomass is a term used to describe a large variety of fuels, some of which one might not consider to be 'true biomass fuels' i.e. wastes and refuse derived fuels. They can generally be split into four classes:

(1) Wood and woody materials
(2) Herbaceous and other annual growth materials
(3) Agricultural Residues and by-products
(4) Refuse derived fuels and wastes

Table 1.1 shows the types of fuel that fall into each of these categories following a comprehensive search of related literature.

Table 1.1 - Classification of Biomass Fuels

Wood and Woody Materials	Herbaceous and Annual growth Plants	Agricultural Wastes and Residues	Refuse Derived Fuels and Wastes
Wood Crops (trees) including specifically:	**Grass:**	**Crop Residue:**	Waste Paper
Hybrid Poplar	Switchgrass	Bagasse (sugarcane residue)	Cardboard
Willow	Giant Reeds (*Arundo Donax*)	Corn Stover	Waste Plastics
Eucalyptus	C4 Energy crop (*Miscanthus Sinenesis*)	Mustard Stalk	Tyres
Beech	**Cereals:**	Cotton Gin	Clinical Waste
Spruce	Barley (straw)	Orchard / Plantation Residue	Domestic Waste
Black Locust	Wheat (straw)	Straws (Barley, Wheat & Rice)	Industrial Waste
Wood Wastes :	Rice (straw)	**Food Preparation Residues:**	Sewage Sludge
Wood Chips	Oats	**Groundnut shell**	
Sawdust (mill residue)	**Others:**	Walnut Shell	
Logging Residue	Alfalfa Stems	Almond Shell	
Bark	Rape	Coconut Shell	
Construction Wood Wastes:	Soy Beans	Hazelnut Shell	
Telephone poles	Sunflowers	Pistachio Shell	
Railway Sleepers	Kelp	Olive Husk / Pits	
Pallets	Cardoon (*Cynara Carduncu lus*)	Peach Pits	
Construction / Building Waste		Corn Husk	
		Rice Husk	
		Manures:	
		Chicken Litter	
		Cattle Manure	

This broad spectrum of fuels qualifying as biomass has led to some difficulty in estimating the total biomass usage world wide and its potential exploitation in the future. In many countries biomass is the primary energy source, providing 35% of energy in the developing world [5, 6], however, this mostly through "primitive, low efficiency, high polluting cooking and heating fires" [4]. Globally, biomass ranks 4th as an energy provider, supplying some 14% of the world's energy [5, 6]. It is estimated that by 2050 biomass could provide nearly 38% of the world's direct fuel use and 17% of the world's electricity [5].

1.5 Driving Forces behind Biomass Fuel Use

There are several favourable factors associated with the use of biomass as a fuel for energy supply. These factors can be split into three main driving forces, these are: environmental benefits, financial drivers and political forces.

1.5.1 Environmental Benefits

The Primary driving force behind the use of biomass as a fuel for power generation is that it holds many environmental advantages over the continued use of coal and other fossil fuels. These advantages can be divided into two categories; (1) those arising from the combustion of plant matter and related material and (2) those arising from the combustion of wastes and residues.

1.5.1.1 Environmental Benefits of Plant Based Biomass Fuels

One of the main advantages of using biomass fuels derived from plant matter are that they can result in a reduction of greenhouse gas emissions into the atmosphere. The benefit that is cited most often is that these types of fuel can be considered 'CO_2 neutral' [3, 5, 6, 7]. This is because the combustion of plant matter follows the reverse of the photosynthesis reaction for plant/tree growth [3], meaning that these types of fuel emit as much CO_2 into the atmosphere during combustion as they scavenge from it during growth [5]. Therefore, there is no "net increase" in atmospheric CO_2 as a result of burning plant derived fuels. Currently, coal is responsible for approximately 27% of the world primary commercial energy use and around 34 - 38% of all of the electricity generated in the world [8, 9]. Given the very high carbon property of coal, blending biomass fuels with coal provides enormous potential to reduce fossil fuel-based CO_2 emissions [6]. It has also been reported in the literature that these fuels can reduce NO_x and SO_x emissions as a result of co-firing with coal [5, 6, 7, 10, 11]. It is believed that this is primarily due reduced nitrogen and sulphur contents in the fuel [6, 10, 11]. However, it has also been suggested that thermal effects, such as lower combustion temperatures or staging effects, caused by low volatile burnout, can contribute to the reduction in NO_x by reducing thermal NO_x produced [7, 10].

Aside from global warming, a reduction in these atmospheric pollutants can mitigate other undesirable atmospheric effects. For example, carbon monoxide (CO), NO_x, SO_x, and unburned hydrocarbons can lead to the formation of atmospheric smog in the troposphere over urban environments along with atmospheric reactions and destructive processes within the stratospheric ozone layer [8]. Finally, given the lower ash content of plant-based biomass fuels it is generally accepted that solid waste production will be lower than when firing pure coal [6], reducing the amount of solid residue sent to landfill.

1.5.1.2 Environmental Benefits of Waste and Refuse Derived Biomass Fuels

Utilising wastes and refuse derived fuels as a source of energy for electrical generation can also result in a reduction of greenhouse gases. However, this is not as a direct result of their combustion; rather, if these fuels are used in combustion, then they will not be sent to landfill where they decompose producing methane (CH_4), which is "21 times more potent than CO_2 in terms of global warming impact" [7]. Here the benefits are seen as a reduction of landfill gas due to the lower volumes of waste being sent to landfill. Co-combustion of wastes and refuse derived fuels also offers a solution to their long term disposal problems [12]. The UK generates around 30 million tonnes of municipal solid waste (MSW) per year, 90% of which is landfilled [5]. The main problem with this is that the scale of waste production causes great difficulty in finding sufficient room at landfill sites to take it all. Combustion of these wastes could provide a viable alternative to landfill. This is already happening in some European countries with Sweden only sending 34% of its MSW to landfill sites [5].

Disposal problems are particularly acute with sewage/sewage sludge. Due to the threat of long term reactions in dumps, disposal of sewage sludge in landfill sites is being reduced [12], and has already been banned in some countries [13]. Coupled with the ban on disposal at sea [14], incineration is becoming an increasingly viable alternative. Co-combustion of sewage sludge in coal-fired power stations can reduce the volume of waste to less than 10% of the mechanically de-watered sludge, leaving a stable non-reactive ash [13, 14]. Another advantage of disposing of sewage sludge in this manner is that any toxic organic constituents within the sewage are thermally destroyed [14], Not only does this reduce the need for treatment before disposal, but it reduces the threat posed to the environment by otherwise toxic waste.

1.5.2 Financial Drivers

Alongside the reduced greenhouse gas emissions and other environmental benefits, there are political and financial driving forces behind the move towards using biomass over traditional fossil fuels. Financially, the primary incentive is lower fuel costs [8, 14, 15]. At present co-firing is the most practical and cost effective way of utilising biomass fuels [10]. The estimated fuel cost at source for biomass (approximately $40 (£23) per short ton dry, for wood and straw) is much higher than that of coal ($10 - $30 (£6 - £17) per short ton dry), which makes the energy cost of biomass considerably higher ($2 to $3 /MMBtu (£1.10 - £1.60 /GJ) compared to $0.74 to $1.30/ MMBtu for coal (£0.40 - £0.70 /GJ)) [10]. However, cost savings can still be made by co-firing biomass; for example the lower fuel bound sulphur of plant-based biomass fuels opens up the opportunity to use a wider array of coals, i.e. a coal with an otherwise prohibitively high sulphur content could be counteracted by the lower sulphur in the biomass share [15]. These undesirable fuels are usually cheaper than the 'higher quality' coals that are traditionally used. If the saving in the cost of coal outweighs the added cost of the biomass fuel then the incentive is provided. The delivered cost of some wastes however, can be lower than coal; it is estimated that the energy supply from a ton of burnt sewage sludge can be translated into a cost saving of $25 (£14) in coal consumption [14].

These financial incentives could be increased further with the introduction of carbon taxes [8, 10, 15]. It is thought that in order to reduce emissions to 1990 levels a carbon tax of $50 (£29) per ton of carbon would be required. This carbon tax could add from between $14 (£8) to $20 (£12) per MWh to the cost of coal based electricity [10], compared with only $5 (£3) for natural gas [10]. This would equate to a 30 – 40% increase in fuel costs in coal fired plants, increasing the energy cost of coal to around $2 /MMBtu (£1.05 /GJ); comparable to that of some biomass fuels [10].

1.5.3 Political Forces

Perhaps the most compelling incentive for the widespread use of biomass fuels is that the global supplies of economically recoverable fossil fuels are fast running out [16]. Proven oil reserves stood at 1147.7 thousand million barrels in 2003, however, with consumption set to continue climbing, especially with the emergence of the far eastern economies, it is thought that these oil supplies will only last for the next 41 years [16]. Natural is predicted to last longer, with the 175.78 trillion cubic metres of proven reserves in 2003 estimated to last 67 years [16]. Finally the reserves of 98.445 billion tonnes of coal are expected to last 192 years [16]. The need to find alternatives for these fuels will grow stronger with every passing year and biomass fuel provides one alternative [11]. Aside from reducing the dependence on fuel imports, biomass fuel offers one other main political advantage [11]. This is that the farming of fast growing crops for use as biomass fuels could generate many jobs and see the re-utilisation of otherwise unused agricultural land [11]. Biomass use could also have a positive effect on the forestry and secondary wood products industries by providing a new market for wastes and residues as well as providing a secure income from the provision of dedicated feedstocks [6]. This would promote economic stability in these industries and the opportunity to develop a feedstock infrastructure and jobs for future biomass development and use [6].

1.6 Co-firing Biomass With Coal

Whilst pure firing of biomass fuels has its merits, co-firing demonstrates the most economically viable use for biomass fuels at present [11, 17, 18]. This is primarily due to the cost of producing facilities capable of exclusive biomass firing [11]. Due to the widely dispersed nature of biomass fuel sources, a single large scale plant is not feasible; instead several smaller de-centralised plants would be required, which is a far more expensive option [17]. It is estimated that the cost of building new biomass specific plants could be up to ten times higher per kW of thermal capacity by biomass than retrofitting an existing coal-fired boiler for co-firing [8, 17]. A similar problem is seen when considering the combustion of wastes and sewage sludges [12, 19]. It is thought that for the construction of a new sewage sludge fired facility to be economically viable, an assured supply of at least 50,000kg per day of sludge would be required [19]. With the average person producing approximately 0.18kg of sewage sludge per day [19], a plant of this scale would require a population of almost 300,000 to support it. This means that in order to keep fuel supply costs low, this type of plant could only be supported in the most densely populated areas; therefore widespread use of sewage sludge as a fuel is only viable in large cities, rural regions could not sustain a plant of this scale, so the more expensive option of smaller de-centralised plants would be needed [12, 19].

Fuel supply problems are not limited to their dispersed nature; the seasonality of biomass fuel sources means that a plant firing biomass exclusively would require large storage areas for stockpiling of fuel for times of the year when the fuel is not readily available [11]. This can push up the capital costs of land acquisition for new plants. The other reason that co-firing of biomass fuels is preferred over sole source technologies is that the high moisture and ash content of some biomass fuels can cause ignition and combustion problems [7]. In addition to the flame stability problems caused by this, burnout can be affected which can cause the unburned carbon in ash to increase which in turn affects its saleability [3].

Co-firing biomass fuels with coal can eliminate or mitigate most of these problems, firstly retrofitting existing coal fired plants to fire biomass will eliminate much of the capital cost incurred in the construction of new pure-fired powerstations. Also due to the fact that the dependence of the facility on the biomass share is lower, problems with fuel supply and seasonality are reduced. Finally because the combustion characteristics of coal are well understood, fuel blends can be tailored to provide suitable combustion conditions such that ignition and flame stability problems are eliminated.

1.7 Problems Associated With Biomass Co-firing

When considering co-firing, there are several important factors for a powerstation manager to weigh up before deciding on the thermal load that can be met by the biomass fuels. The most important of these is the effect that the substitute fuel will have on the combustion regime inside the boiler.

1.7.1 Ash Deposition Problems

The use of biomass fuels can affect the combustion process in several ways, the most important of which is the behaviour of the fuel ash inside the boiler. It is well established with in the literature that biomass fuels have ash that is more alkaline in nature than coal ash which may aggravate fouling problems [5, 7, 20, 21]. One source states "the comparison of ash melting data of coals and biomass reveals that sticky particles and slags in a much wider temperature range are expected when firing biomass in existing pulverised fuel boilers that are designed for coal only" [20]. The reasons behind this will be discussed in detail in subsequent chapters but principally, the alkali metals potassium and sodium and also phosphorous within the biomass ash can reduce the melting temperature of the ash, which increases the likelihood of it sticking to heat transfer surfaces within the boiler [7, 8, 20]. Potassium is the primary source of alkali in biomass fuel with concentrations of K_2O in their ash as high as 10 – 33% [10]. Phosphorous can also feature highly with concentrations of 4 – 16% [10].

The effects of the alkali metals in biomass fuel ash are not just limited to deposition problems. The presence of high quantities of potassium and chlorine in fuels such as straw can also lead to corrosion problems [10, 21, 22, 23]. The alkali metals react with other ash species to form low melting point alkali salts which can attack the steel heat transfer surfaces within the boiler [21], it is stated in the literature that deposits formed on tubes can "accelerate the rate of fireside corrosion in biomass fuel fired boilers" [24]. This phenomenon will also be discussed in more detail in subsequent chapters.

1.7.2 Combustion Related Problems

In addition to ash related combustion problems, consideration needs to be given to the combustion properties of the biomass fuels themselves. The literature shows that the combustion properties of biomass fuels differ considerably from those of coal [5, 7]. One of the main differences is that for most plant based biomass fuels the fractional heat contribution by volatiles is much higher than for coal [7]. As much as 70% of the thermal output of biomass fuels can come from volatile matter compared to only 36% for coal, which means that pyrolysis can begin earlier in biomass fuels affecting the temperature profile and atmospheric composition in the burner region [7]. Also the high moisture content of biomass fuels can mean that the heating value of the fuel is significantly reduced when compared to that of coal [4]. "Typically a 90:10 coal:sawdust blend will have a heating value approximately 3% less than that of pure coal" [7] whilst "the calorific value of a coal – sewage sludge blend will decrease by 0.6% for every 1% of heat input supplied by sewage sludge" [8]. A lower calorific value can lead to peak temperature, ignition and flame stability problems [7].

Aside from combustion problems, the quantity and variation of ash within biomass fuels can also affect the heating value of the fuel. For example some wood derivative biomass fuels can have as little as 0.2%$_{wt}$ ash [11] whilst sewage sludge can contain up to 50 – 60%$_{wt}$ ash [3, 5, 11]. This difference in ash quantity can cause significant variations in heating values between biomass fuels; wood and sawdust can have heating values as high as 20MJ/kg [4, 7] whilst sewage sludge can have a heating value as low as 6MJ/kg [13]. As with high moisture content, the lower heating values can result in lower temperatures which, in turn can cause flame stability problems unless the mass flowrate of composite fuel is increased to maintain the thermal output [7]. The lower heating value of sewage sludge means that large quantities are required to make a significant reduction on the total thermal energy received from coal. In addition to the lower heating value, the higher ash content of sewage sludge means that the ash flow into the boiler will be greatly increased. One source states that "whilst producing the same thermal output, 25% sewage sludge co-combustion leads to an ash mass five times higher than in pure coal combustion" [20]. These large quantities of ash can lead to a cloudy atmosphere within the boiler which can affect radiant heat transfer rates leading to higher gas temperatures along the centreline of the boiler [12, 13]. These combustion problems typically serve to reduce the efficiency of the combustion process [25]. Figures within the literature state a reduction in efficiency of between 0.5% and 1% for every 10% of thermal energy supplied by biomass [7, 10].

1.7.3 Fuel Handling and Storage Problems

Aside from combustion problems, the other main consideration for a plant manager is the fuel handling and storage problems which can be associated with biomass fuels, these can range from limitations imposed by the capacity of mills and pulverisers, particularly if the fuel mass flowrate is increased [10, 15], to increased fire and explosion risks [8, 15].

The grindability of some fibrous or woody biomass fuels or those with high moisture contents can be a concern regarding fuel preparation [25]. This can affect the coarseness of the coal grind which can have knock-on effects on the unburned carbon quantity in ash, affecting its saleability [15]. The lower heating value of biomass fuels often means higher fuel feed rates. Sometimes these feed rates can exceed the mill capacity and hinder the ability to maintain full load [10, 15]. The higher volatile content of biomass fuels can increase the risk of mill fires and fuel smoking within the mills [8, 15], whilst the lower flash point of pulverised sewage sludge can increase the likelihood of dust explosions [8]. Storage of biomass fuels can also present a problem to plant managers; the lower density (100 to 800 kg/m^3) [7, 26] of biomass fuels compared to coal (circa 1100 – 2330 kg/m^3) [7] means that larger storage areas/silos are required. In addition, wastes and residues can pose potential odour control issues and health risks particularly to workers who may be exposed to them for any length of time [8].

1.7.4 Capital Cost

There are also several financial issues which can affect the decision of a plant manager when considering biomass fuels. Primarily, these issues arise from the need to modify the plant to cope with the biomass fuel supply system. As was mentioned above the ability of the mills to cope with the biomass fuel can limit the biomass fuel share. It has been suggested that in order to fire quantities of biomass greater than 5 to 10% by weight, a separate dedicated biomass fuel handling and supply system is needed [26]. In wall fired boilers, the added complication of creating new penetrations into the furnace wall to accommodate specialised biomass burners is present, this is coupled with the cost of modifying the windbox to ensure adequate air supply to the biomass burners [26]. When considering co-firing of waste or sewage sludge, additional costs can be incurred through ash disposal problems. When firing pure coal the ash residue from the boiler is classified as an inert material, however when sewage sludge is added, the classification of the ash is upgraded to an active material which incurs higher taxation for disposal [8].

1.8 Suitability of Combustion Prediction Techniques

Given that biomass co-firing is one of the key ways in which power generators can combat greenhouse gas emissions, it is important to gain maximum benefit from the process in terms of combustion performance and process efficiency whilst minimising both financial and environmental impact. In order to do this a powerstation manager must consider all of the issues raised above and consider how they will affect his situation. When dealing with new or unused fuel types, a plant manager's specific knowledge and experience may not be sufficient to make a judgement on these issues. In these situations he will often turn to modelling and prediction techniques to aid in the decision making process. However it is often the case that these techniques are limited in their application, being specific to a particular boiler or fuel type. Specific models tailored to predict results for the intricacies of particular boiler geometries and fuel types can often take years to develop with high research and development costs. Computational Fluid Dynamics (CFD) modelling, whilst producing results over a shorter time scale can still take weeks or months to create and refine. They also require specialist software knowledge which means a powerstation manager may have to outsource to a consultancy which could prove costly. Empirical indices are often too general in their application, only considering simple ratios or quantities and producing global predictions. What is required is a tool that occupies the middle ground; able to make fast informative predictions covering a range of boiler configurations and fuel types which is easily operated by a plant manager with little or no training. Given a tool such as this, a plant manager could investigate the effects of a wide range of fuel types and substitution ratios on the combustion process, deposition and corrosion problems as well as other factors such as ash saleability and emissions before committing to the required changes or financial outlay.

1.9 Aims of the Work

This thesis aims to investigate how co-firing biomass and waste derived fuels in pulverised coal fired boilers will affect the combustion regime and associated combustion equipment, before outlining the development of a predictive tool that attempts to account for these effects. In order to do this, it is essential that the fundamentals of pulverised fuel combustion are understood and as such, a description of the operation of a pulverised fuel fired boiler is given along with an outline of coal and biomass combustion processes. One of the principal concerns a powerstation manager will have is the effect of the fuel ash on the combustion system. Problems caused by fuel ash will manifest themselves in two ways; ash deposition and corrosion. It is therefore important to understand how these processes occur in order to be able to predict them. Hence, a review of related literature is presented which outlines the causes of ash deposition and corrosion processes for both coal and biomass fuels.

A spreadsheet based predictive tool has been developed utilising artificial neural networks trained using thermodynamic and thermochemical data sets for a range of coals and biomass fuels. The spreadsheet aims to be capable of predicting the combustion performance of a range of co-firing systems using a simple and easily obtainable input data set. A review of existing predictive techniques and models is given followed by an account of experience of using CFD techniques to predict combustion systems. Finally a detailed description of the development process behind the predictive spreadsheet is given, followed by a discussion over how well the results compare to experiments and experience detailed in related literature.

1.10 Structure of the Thesis

Following a review of the related literature, an account of the ash deposition problems associated with pulverised coal combustion is given. The problems identified, and discussed in detail include slagging, fouling and high temperature corrosion. Following this, a discussion of biomass fuel combustion is given focussing on the differences between biomass fuels and coal and the problems that can arise from these differences. A review of modelling techniques employed to simulate combustion regimes follows, before a description of the development process for the boiler performance prediction tool is given. In addition to this, the CFD modelling of a 500kW$_{th}$ downfired boiler is presented. Finally a discussion of the findings is given, followed by the conclusions drawn from the research and the recommendations for continuation of the work.

Chapter 2 - Slagging and Fouling

2.1 Introduction

In order to fully understand slagging and fouling phenomena it is necessary to have a good knowledge of what a pulverised fuel-fired boiler is and what processes occur inside during its operation.

2.2 Pulverised Fuel-fired Boilers.

Figure 2.1 shows a typical 500MW coal fired boiler which, put simply is a means of converting the stored chemical energy within the coal into electrical energy which is supplied to the national grid. Figure 2.2 shows a schematic of the entire boiler system and illustrates the type of ancillary plant required. The coal is burned to raise steam which is expanded through turbines to turn generators, producing electricity. A boiler can be split into two main systems; the gas side and the steam side.

2.2.1 The Gas Side.

The gas side begins at the fuel mills; here large pieces of coal are ground to a very fine powder, typically 70% below 75μm and less than 2% greater than 300μm [28]. The pulverised coal is transported to the furnace at a temperature of around 60 – 90°C [28] suspended in the primary air stream which is supplied by the primary air fans. The remaining combustion air (secondary and tertiary air supplied by the secondary air fans) is preheated in air heaters by the hot combustion gases to around 300°C [28]. Secondary air is supplied to windboxes which surround the burners; from here it passes into the furnace through the outer quarls of each burner. Tertiary air, if it is required can be supplied as over-fire air which enters the furnace through ducts above the burner bank. For a typical bituminous coal the stoichiometric air requirement is approximately 11kg of air for every 1kg of fuel [28] and is typically split 20% primary air and 80% secondary air [27]. In practice it is necessary to supply more air than the stoichiometric requirement [27]; this is due to inefficiencies of the mixing of fuel and oxygen at the point of injection, meaning extra air is required to achieve complete combustion. Typical excess air values are around 20% giving approximately 3.5% oxygen in the flue gas [27]. The burners eject the coal into the combustion zone at velocities of around 36 - 38m/s [27]. Here, the coal mixes with the secondary and tertiary air and combustion proceeds with temperatures climbing as high as 1750°C. The combustion of the majority of particles should be complete by the time they reach the boiler nose, shown in figure 2.2. The temperature of the combustion gases at this point, known as the furnace exit gas temperature (FEGT), is kept to between 1100 and 1400°C [28].

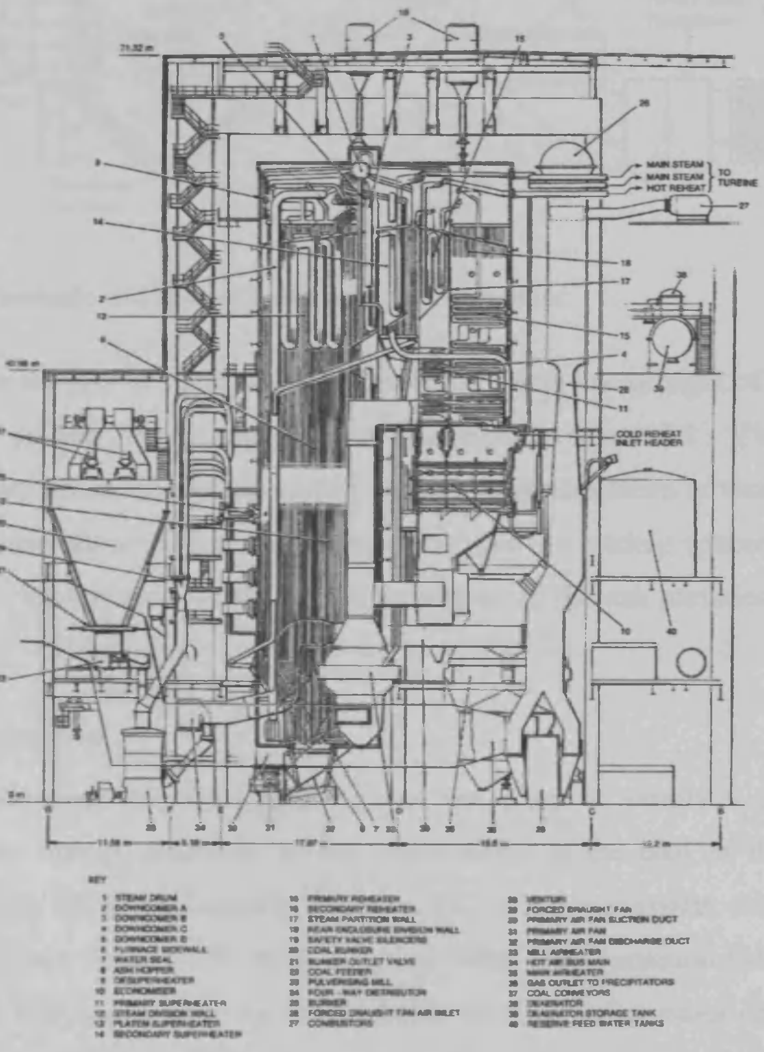

Figure 2.1: A typical front fired pulverised bituminous coal fired boiler [27]

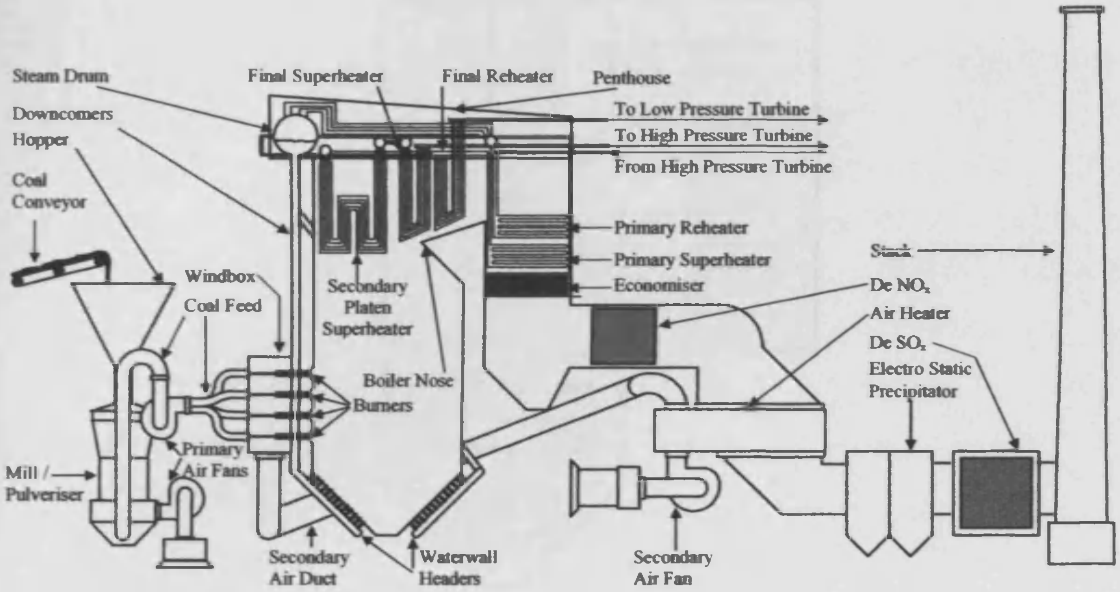

Figure 2.2: Schematic of a typical boiler and ancillary plant

The area where the heat transfer surfaces are within direct line of sight of the flame is known as the radiant section, this area is identified in figure 2.3. The only heat transfer surfaces within the radiant section are the evaporator tubes or water walls and the platen superheaters. These superheater pendants are widely spaced to prevent deposition problems caused by the high temperature of the ash particles within this zone.

2.2.2 The Steam Side

The water and steam on the steam side of the plant is simply a medium for transmitting the energy produced by the combustion of the coal to the electrical generators. Data from the Langerlo boiler, a 230 MW$_e$ (megawatts electrical) coal fired boiler has been used to illustrate a typical steam side operation [31]. Water is supplied to the condenser either by re-circulation of the existing water or fresh water is drawn in from a feedwater source, usually a lake. The water is first used to cool parts of the generating plant such as the alternators before being heated to ca. 100°C by bleeds taken from the low pressure turbine. From here it passes through the pumps which pressurises the water to ca. 150 bar. Bleeds from the medium pressure turbines heat the water to 230°C before it passes into the economiser at 135 bar.

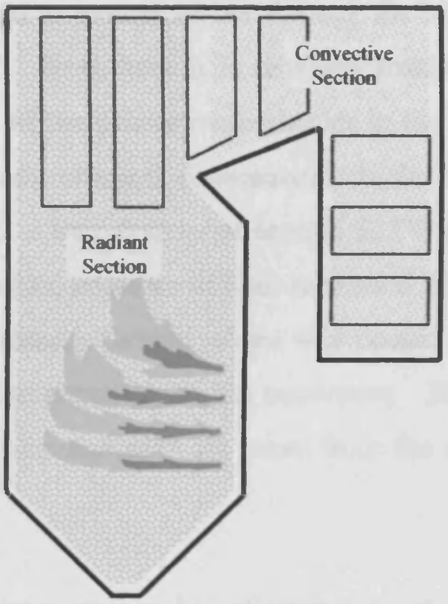

Figure 2.3: Modes of heat transfer in different boiler sections

On leaving the economisers, the water, having been heated to around 300°C, passes into the steam drum which is situated in the penthouse above the boiler. Here the water passes from the bottom of the steam drum into downcomers and into the bottom of the waterwalls surrounding the combustion zone of the boiler. As the water travels up through these waterwalls, it is evaporated to form saturated steam at around 330°C and 130 bar. Approximately 195kg of steam is produced every second for a 230 MWe boiler. Headers at the top of the waterwalls feed the steam back to the steam drum; here any remaining water is fed back to the downcomers whist the saturated steam passes from the top of the steam drum into the primary superheater.

The primary superheater is located in the convective section, usually near the top of the downward pass. Here the steam is heated to ca. 390°C at around 130 bar. Following this the steam passes into the platen superheaters, located in the top of the boiler in the radiant section where it is heated to around 415°C. The final superheater stage is usually located above the boiler nose with superheated steam leaving at a temperature of 535°C at approximately 125 bar. Attemperators are used to control the temperature of the steam in each superheater stage; this is achieved by bleeding off water from cooler parts of the process and injecting it in the superheater headers, this is important to protect the steel heat transfer tubes from damage.

The steam is then expanded to around 25 bar through the high pressure turbine where it cools to around 340°C. From here it is reheated firstly in the primary reheater, usually situated upstream of the primary superheater in the downward pass, and then in the final reheater usually situated downstream of the final superheater. Steam leaves the final reheater at a temperature of around 525°C and 25 bar. The steam is expanded through the medium pressure turbine to around 280°C and 3 – 4 bar, it then passes through the low pressure turbine where it is cooled to room temperature at a pressure of 40 mbar before returning to the condenser. Bleeds used to preheat the water prior to entering the economisers are taken from the medium and low pressure turbine stages.

Larger modern powerstations are capable of producing almost 600 kg of steam per second at temperatures approaching 570°C and 180 bar. This represents the limit of temperature and pressure for recirculating steam/water systems. These boilers can attain conversion efficiencies of between 35 and 40%; in order to better this, higher temperatures and pressures need to be reached [32, 33, 34]. This is possible if the boiler is operated with supercritical steam conditions, where the steam pressure is above 221 bar, leading to no phase distinction between liquid and vapour [33]. The use of a once through water/steam system lends itself to this kind of operation, however, increased operational and treatment costs would require a substantial increase in operating pressure to make it financially viable [27]. Despite this, several supercritical boilers have been commissioned in Japan and across Europe seeing steam temperatures of 600 – 620°C and design pressures of up to 332 bar in the Avedorevaerket 2 boiler [33, 34]. Many of these plants feature a sliding pressure operation which allows them to operate efficiently at low loads, this is particularly useful in Japan where the coal fired boilers are used to support the predominantly nuclear base supply during times of peak load [34]. It is believed that the jump to 700°C steam temperatures could be seen within the next decade but only with serious advances in materials technology [33].

A Typical 500MWe boiler will require some 7,000m^2 of heat transfer surface in the boiler water walls and a further 30,000m^2 in the superheater and reheater tubes [27], this can be higher for supercritical boilers due to the smaller temperature difference between the steam and the gas [33]. It can be seen from figure 2.4 that the maximum heat flux is in the combustion zone near the burner banks, here a typical maximum of 350 – 440 kW/m^2 heat flux is seen [27, 30].

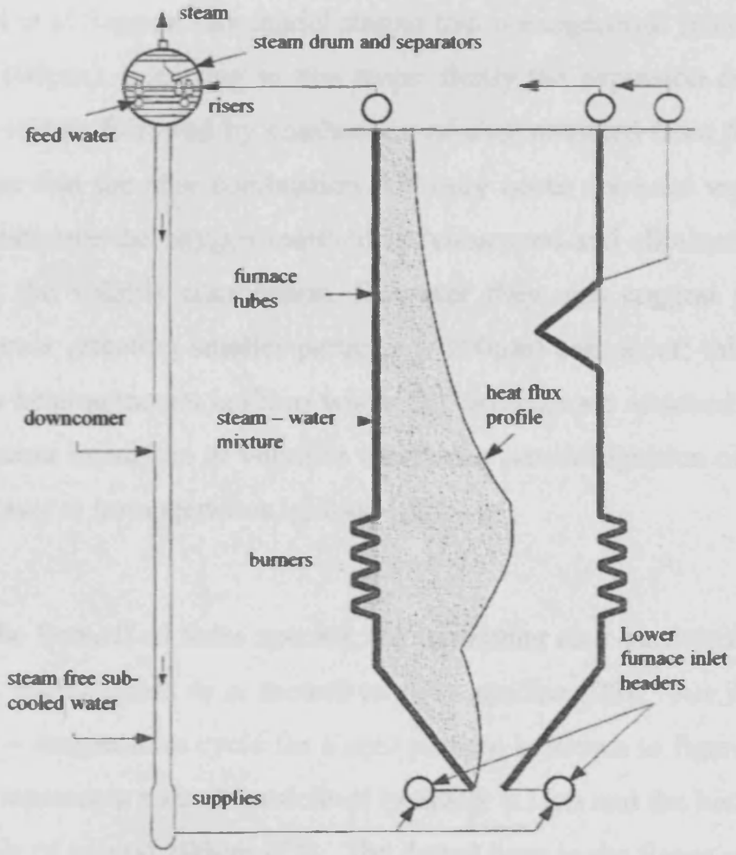

Figure 2.4: Typical heat flux profile in the combustion zone [30].

2.3 The Combustion Process

Skorupska suggests that the combustion phenomenon can be split into four processes; particle heating, release of volatile matter, combustion of volatile matter and combustion of char [36]. Once inside the boiler, the particles are heated very rapidly, with particle heating rates reaching 10^4 to 10^6 °C per second [28]. Therefore, particles of 60μm can reach furnace temperature within 0.05 – 0.1 seconds [36]. During the first stage, particle heating, the particle undergoes a drying process; surface moisture evaporates at 100°C, followed by the evolution of pyrolitically formed water between 300 and 400°C [37]. The expulsion of the volatile matter begins at around 300°C [37]. The volatile species are known to include tars, oils, and gaseous hydrocarbons along with CO, CO_2 and H_2O [28]. The devolatilisation process occurs as the coal particle softens and hydrogen and tars are released within the 400 – 900°C temperature range, above 900°C CO and H_2 are evolved [37]. The traditional model for particle ignition, known as homogeneous ignition, is that these volatile species ignite and burn, followed by the ignition of the remaining char particle and its subsequent combustion [37]. Davini et al Support this model stating that homogeneous ignition, affects larger particles (>100μm), occurring in two steps: firstly the expulsion and combustion of the volatile matter followed by combustion of char obtained from the initial process. They suggest that the char combustion will only occur once the volatile combustion has ceased because the oxygen required is "consumed and eliminated from the solid surface" by the volatile combustion. However they also suggest a second type of ignition process affecting smaller particles (<100μm) can occur; this type of ignition is known as heterogeneous ignition where the particles are attacked by reagent gases with consequent expulsion of volatiles which can prevent ignition of the coal particle in a similar way to homogeneous ignition [38].

Following the burnoff of these species, the remaining char particle can take anything from a few milliseconds to a second to fully oxidise [28]. An illustration of the typical time – temperature cycle for a coal particle is shown in figure 2.5 [28]. Here, the top line represents a small particle of typically 0.1μm and the bottom line that of a larger particle of around 100μm [28]. The dotted lines in the figure represent particles deposited on a surface.

A stable flame is achieved by balancing the heat loss in the near burner region with the heat released at the ignition temperature [39]. This is done by matching the fuel feed velocity with the flame velocity (rate of burning). Failure to achieve this condition will result in the point of ignition travelling in the direction of the lower velocity, causing blowoff if the fuel feed velocity is too high and flash back, which can lead to mill fires, if the fuel feed velocity is too low [39].

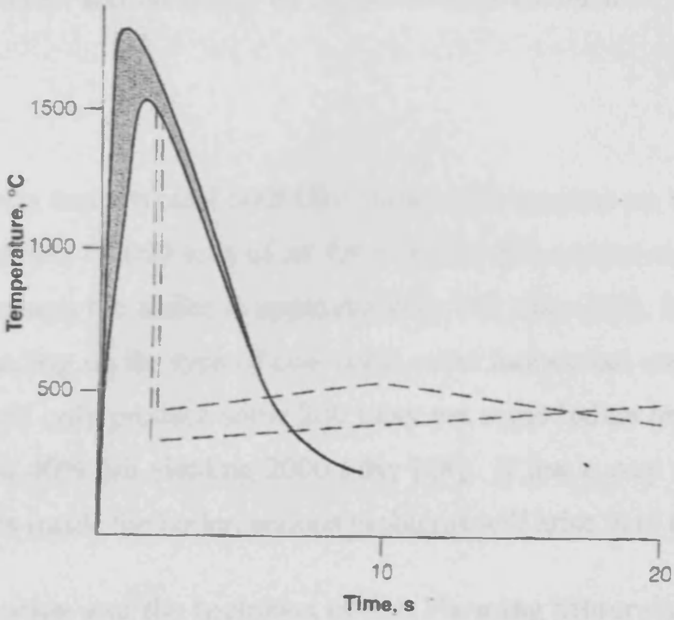

Figure 2.5: Generalised time-temperature cycle for a coal particle [39]

2.3.1 Particle Fragmentation.

It is believed that as the char particles burn they undergo a process of fragmentation [40, 41, 42]. Dacombe et al believe that this is caused by the rapid heating of the particle which establishes a temperature gradient within it leading to thermal stresses. They believe that these thermal stresses cause the particle to crack during the char combustion stage [40]. Liu et al suggest that approximately 40% of char particles form cenospheres with a large central void and 0.7 – 0.9 porosity. The remainder of the particles exist in varying states of density ranging from 0.4 – 0.7 porosity. They suggest that it is the highly porous particles that are responsible for the majority of the fragmentation seen. They suggest that these particles fragment by the percolation of oxygen into pores left by the devolatilisation process. The char is consumed at the surface of these pores which grow creating large macro-pores. These macro-pores combine and weaken the structure of the char shell allowing fragments to form and break off. [41]. Gajewski and kosowska suggest a three step fragmentation mechanism [42]; firstly, small fragments break off upon entry into the boiler as the stresses created by thermal shock cause the particle to burst. Secondly, pressure inside the particle increases as devolatilisation begins, causing the particle to break into several large fragments. Finally, as the volatiles burn off, the particle takes on a cenospherical structure and breaks up by the percolation mechanism suggested by Liu et al.

2.4 Fuel Ash

Couch [28] suggests that a typical 500MWe boiler will consume up to 5,000 tons per day of coal and almost 60,000 tons of air for a typical bituminous coal. The amount of ash passing through the boiler is approximately 750 t/day [28], however this can vary greatly depending on the type of coal used; some Indonesian coals containing as little as 4% ash will only produce some 200 t/day yet some Indian or Bulgarian coals can contain almost 40% ash yielding 2000 t/day [28]. If just a very small proportion of this ash deposits inside the boiler, serious problems will arise very quickly.

2.4.1 Coal Formation and the Inclusion of Ash Forming Minerals

Strictly speaking "coal does not contain 'ash' but both organically-bound inorganic elements and mineral matter which result in ash formation during combustion" [28]. It is believed that this inorganic mineral matter becomes "intimately mixed" with the combustible organic material as the coal is formed by the "compression of plant material over millions of years" [28]. This inorganic matter can be split into three distinct forms [43]. These forms are; minerals included within the coal matrix (inherent minerals), organically bonded elements and excluded minerals [43].

The process of coal formation (coalification) can influence the types of minerals contained within the coal [44]. It is believed that the coal seams harvested today started out as large peat swamps located on coastal plains and river deltas [44]. These peat swamps are formed as plant material containing high quantities of cellulose ($C_6H_{10}O_5$), die and decay [7]. Over time the swamps subside and are covered with layer upon layer of fallen vegetation [44]. Increasing pressure and heat over time coupled with anaerobic micro-organisms turn the rotting vegetation into peat [7]. As sediment builds up on top of the swamp, chemical decomposition occurs, forcing out moisture and methane and carbon dioxide is formed within pores in the coal [7, 44]. These chemical processes, known as petrification, humidification, gelification and vitrification, followed by partial oxidation transform the decaying vegetation into char. As this process progresses the oxygen and hydrogen concentrations within the coal decreases, so with increased coalification, the coal becomes carbon enriched forming first lignite, then sub-bituminous coal and finally anthracite [7, 44].

It is thought that the first group of inorganic constituents, the inherent minerals found within the coal matrix, are those minerals which were drawn into the plant tissue during its lifetime [44]. Bryers [44] states that "these minerals are also composed from silt deposited from discharging rivers and dust from wind storms and volcanic eruptions". These are knows as detrital minerals and consist mainly of silicates including clay and quartz [28]. He also suggests that as swamps were engulfed by sea water, they were "injected with sulphates" [44]. The second group of minerals known as syngenetic minerals [28, 44] are formed later in the coalification process by the crystallisation of aqueous sulphates by bacterial reduction [44]. These consist mainly of carbonates, sulphides, oxides and phosphates. Included in this group are minerals known as epigenetic minerals which are formed by the "filling of fissures, cracks or cavities in the coal matrix as it is weathered or eroded" [44]. Again, consisting mainly of carbonates, sulphides and oxides, these minerals, due to the way in which they were formed are most likely to be intimately bonded with the organic coal material [28]. The final group, excluded minerals, are those minerals which are loosely attached to the coal substance or those which have become mixed with the coal during the mining process [30]

Couch [28] has split the ash forming minerals in the coal into seven groups, three major groups; silicates, carbonates and disulphides and four minor groups; sulphates, feldspars, sulphides and oxides. These can include alumino-silicate (clay), and quartz which represent 60-90% of the total mineral matter [30]. Alumino-silicates of potassium, sodium and calcium are common [30] whilst carbonates, chlorides and sulphates of iron, magnesium, potassium, calcium and also copper and zinc are also found [30]. Sodium and chlorine ions are usually associated with the inherent minerals whereas the alumino-silicates usually make up the excluded mineral matter.

2.4.2 Ash Formation During Coal Combustion.

As the coal particles are burned the mineral matter within them is exposed to extremely high temperatures. The inherent matter with in the coal can often reach temperatures above the peak flame temperature due to exothermic reactions within the char [28]. This heating causes most of the mineral matter to decompose, soften and eventually fuse together [28]. Due to their close proximity, the inherent minerals can react easily with one another [28]. The inherent minerals initially appear as "molten particles on a receding char surface" [28], before coalescing to form a single molten particle [28, 45]. The transformations within the extraneous material are quite different to those of the inherent mineral matter. This is due to the fact that they are exposed to lower temperatures and are not necessarily "affected by the locally reducing environment of the coal particle" [28]. The integrity of the char particle can have a great effect on the size of the ash particles produced; "if the char particle retains its integrity, burning as a single shrinking particle, then the ash will form a single coalesced particle" [28], meanwhile if the char particle disintegrates at high heating rates (fragmentation), then much finer ash particles will be produced. Generally, extraneous material fragments to form fine ash particles whilst inherent material agglomerates/coalesces to form larger ash particles [45].

Species such as sodium, calcium, magnesium, iron and aluminium along with organically bound elements such as sulphur and chlorine are volatilised during the early stages of burnout [28]. Thermodynamic equilibrium calculation suggests that the tendency for volatilisation is greatest in K, Na, P and Mg followed by Ca, Fe and Ti and lastly Al and Si [46]. This volatilisation is thought to be responsible for the formation of the finest particles. As they begin to cool, the volatilised species begin to condense forming an "aerosol of sub micron droplets" [28] which will eventually form particles of 0.1 – 0.2μm.

2.4.3 The Fate of Fuel Ash Particles

All of the ash entering the boiler will suffer one of two fates. Either it will be removed from the boiler either as bottom ash through the ash hoppers at the bottom of the combustion chamber and the convective pass, or as fly ash via filters and cyclone separators in the bag house. Or the ash is deposited on heat transfer surfaces inside the boiler. Given the vast quantities of ash [28] passing through the boiler daily, only a fraction of a percent needs to be deposited to create serious operational problems with associated decreases in thermal efficiency and power [47]. Ash deposits manifest themselves in two ways; slagging and fouling.

2.4.3.1 Slagging

Slagging is defined as the formation of sintered and molten deposits on heat transfer surfaces or refractory lining in the main furnace cavity. Slagging will only occur in regions directly exposed to flame radiation, mainly the furnace water walls and pendant superheaters [28, 36, 44, 48, 49]. The nature, composition and degree of slags can vary greatly depending on coal type or rank and combustion conditions [36, 44]. These factors include "heat transfer surface temperature, flame temperature, direction of gas flow, mineral composition, absorption rates, mineral and coal size distribution, concentration of mineral matter and oxygen levels" [44]. The nature of slags can vary from highly porous and friable deposits with very low mechanical strength and tenacity to dense, glassy fused deposits with very high strength and tenacity [36]. Slagging is not strictly confined to the radiant section of the furnace; depending on residence time and particle size distribution, slagging can be seen in the lower regions of the superheater bundles at the inlet to the convective pass.

2.4.3.2 Fouling

Fouling is defined as the formation of sintered deposits on those heat transfer surfaces in the convective pass of the boiler which are not directly exposed to flame radiation and where the flue gas temperature is below the melting temperature of the bulk coal ash [36, 44, 50]. Fouling deposits do not contain the molten phases found in slagging deposits and contain "a combination of silicates and sulphates which sinter the ash particles together" [50].

2.5 The Effects of Fuel Ash Deposition

The principal effects of fuel ash deposition (slagging and fouling) are five fold. Firstly, heat transfer can be reduced in the furnace (radiant) section "due to the thermal resistance of the deposits" [36]. Secondly, the gas flow through the furnace can be impeded by large deposits bridging across tube banks. The tube banks themselves can become deformed or damaged by the sheer mass of deposits captured; in some cases large clinkers weighing several tonnes can form [28]. These can pose a serious threat to the water walls and ash hopper should they become detached and fall to the bottom of the furnace. The tube banks can also be attacked chemically by the constituents of the ash, causing severe tube wastage. Finally, the heat transfer tubes can be eroded by the abrasive action of impacts by fly ash particles [36].

These problems are often interrelated [36]. Typically, slagging in the furnace section of the boiler can lead to a reduced heat transfer rate to the water walls. This will lead to an increase in the FEGT, which means that more particles will enter the superheater tube banks in a sticky or molten state, increasing their chances of adhering to the tubes. The higher gas temperature in the superheater banks means that the tube surface temperature is increased allowing "the formation of liquid phase components which enhance tube corrosion" [36]. Also, if the deposits in the tube banks grow large enough it can partially block the ducting which means that firstly, local gas and fly ash particle velocities are increased as the gas flow accelerates around the blockage, increasing tube erosion and secondly, extra load is put on the fans as draught is lost [36]. Couch cites an example of this where a large boiler experienced a "light slagging" after 5000h operation time which caused the FEGT to climb from 1230°C to 1400°C [28].

The degree to which slagging and fouling affects the efficiency of a boiler can be highly significant. A 10–20% reduction in power and 10% reduction in thermal efficiency have been reported by Lee et al [47] for a boiler suffering severe deposition. Mulcahy et al [51] report a 20–40% reduction in heat flux due to ash fouling of heat transfer surfaces which severely alters the operating conditions within the boiler. Couch [28] cites figures calculated by the Pennsylvania Power and Light Co, with 12 coal fired plants at a combined capacity of 8GWe, who estimated their annual losses due to deposition problems caused by poor quality coal at $5 million/year. He also mentions earlier work by Honea et al [52] who estimated the financial losses of a single 500MW_e boiler firing a high fouling lignite at $8million/year. These financial losses are generated through forced shutdowns for repair/maintenance as a result of the altered boiler operating conditions or for removal of stubborn deposits.

2.5.1 Forms of Deposit

Deposits can manifest themselves in different forms. Beginning in the bottom of the furnace, molten slag can solidify in the ash hopper as it runs down the furnace walls from the hotter combustion zone above. This slag, if left unchecked can bridge across the ash hopper. This problem can be exacerbated by large clinkers falling down from the superheater pendants in the roof of the furnace [28]. This forms a very dense and glassy slag which in very severe casees may need to be removed using explosives during shutdown [28]. Moving up to the burner zone, deposits known as eyebrows can form above and below the burner. These deposits form due to the fact that in the combustion zone, flame temperatures are hot enough to allow the slag to run freely. When this molten slag comes into contact with the burner quarl which is cooled by the secondary/tertiary air it solidifies [27]. At their worst eyebrows can cause flame distortion, burner blockage or even flame extinction [28]. These problems are difficult to correct once they have occurred [28].

Above the combustion zone, in the platen superheater pendants, deposition begins on the leading and lower edges of the tube bundles. As the deposits grow they can spread backward towards subsequent rows of tubes. If the deposits are severe enough they can bridge across from one superheater pendant to the next, this is known as birdnesting. These types of deposits can lead to flow distortion, erosion and increased pressure drop through the furnace [28]. These deposits can harden with age making on-load cleaning difficult [28]. Bonded deposits are seen right through the convective pass of the boiler to the inlets of the air pre-heaters. Initial deposits can be difficult to remove however, as the deposits grow, differential expansion during load variation can dislodge them.

2.6 Deposit Formation Mechanisms.

There are two main mechanisms by which deposits are formed; particulate deposition, where the deposits reach the surface as particles which adhere and condensation where the deposits are formed by the condensation of volatilised minerals from the hot flue gases onto the cold tube surface.

2.6.1 Particulate Deposition.

There are five processes which allow particles to impact heat exchanger tube surfaces. Particulate deposits will form in irregular patterns on the tube surface dictated by the fluid dynamics and fly ash distribution with in the gas stream [43].

- **Inertial impaction** – This process only affects larger particles of >10 μm [28], resulting in a coarse granular deposit. As the gas flows around the tubes, larger particles have sufficient momentum to overcome the drag forces and deviate from the gas streamlines penetrating the boundary layer [30]. The number of impacts is highest at the leading edge of the tube since lower gas velocities in and around the stagnation point allow particles to escape the streamlines more readily [28]. If particles are sticky or molten, particle to particle impacts can cause agglomeration [30] resulting in even larger particles which are more likely to penetrate the boundary layer and impact the tube surface.

- **Convective Diffusion** – This is controlled by particulate concentration gradients and turbulence. Particles are trapped in convection currents and transported to tube surfaces. In regions of the boiler where turbulence is high smooth streamlines are unable to form, which makes particle transit to the tube surface easier. The turbulence is governed by local gas velocities whilst the concentration of particles is a direct consequence of fuel quality and combustion conditions [30].
- **Thermophoresis** – This is diffusion of particles caused by temperature gradients [30] and is particularly relevant where tube surface temperatures are significantly lower than the gas temperatures. In regions where the hot combustion gases come into contact with the cold tube surfaces, the temperature driving force for heat transfer can be as high as 1000°C [28]. Particles are pushed towards the cooler region by "thermal pressure" [30] caused by the molecules on the hotter side of the particle being agitated to a higher degree than those on the cold side [30] resulting in a driving force towards the cooler region. This type of transport mechanism will only affect particles smaller than 1μm [43, 53] and in areas where the velocity is sufficiently low to negate the effects of gas flow streamlines.
- **Electrophoresis** - This is the Attraction to and trapping of particles on the tube surface by electrostatic forces [28]. Particles with the opposite electrical charge to the tube are attracted towards it and trapped.
- **Gravitational Effects** – This occurs where the gas velocities are no longer sufficiently high to support the particles in suspension [30].

2.6.2 Condensation and Vapour Diffusion.

Condensation deposition occurs as vapours of inorganic species volatilised in the hotter combustion zone are suddenly cooled as they diffuse towards tube surfaces

[30]. This type of deposition usually manifests as a thin uniform layer around the tube surface [28, 43]. Vapours can deposit either directly onto tube surface or onto entrained or deposited particles. If the condensate remains molten or semi-molten then the surface of the tube or particle may become sticky, making it more open to adhesion [28]. Particles covered in sticky condensate are able to agglomerate, forming larger particles. The process of condensation occurs by the formation of small airborne droplets as the vapours pass close to the cooler surface [30]. Depending on local gas velocity these particles can go on to form solid particles before impact or impact whilst still in a molten or semi molten state [30], droplets can also coalesce as they approach the surface.

2.6.3 Deposit Initiation / Adhesion.

One of the most important processes to understand is how the deposits adhere to a clean tube. In the radiant section of a boiler where temperatures are high enough for particles to exist in a molten state, the main form of deposit initiation is inertial impaction of molten or semi-molten particles [53, 54].

2.6.3.1 Deposit Initiation in the Radiant Section

In the radiant section of the boiler, high temperatures (circa 1750°C), make it possible for some of the particles to exist in a molten or sticky state [53, 54] in particular iron sulphides and sulphide oxide mixtures derived from extraneous iron particles [54] and "low melting point particles containing mixtures of iron oxides with alumina and silica in the presence of calcium, magnesium potassium and sodium" [54]. Pyrrhotite ($Fe_{0.9}S$) and Troilite (FeS), which form as a result of the decomposition of iron sulphide, will begin to melt at 1175°C [54], whilst mixtures containing potassium may begin to melt at temperatures as low as 725°C [54]. In the combustion zone these particles can still be quite large, enabling them to reach the tube surfaces by inertial impaction. Particles greater than 20μm will experience negligible cooling within the thermal boundary layer of the tube [54] and will reach its surface in a molten state. When these molten or sticky particles hit the tube surface they experience plastic deformation, dissipating their kinetic energy and making them less likely to rebound. Once in contact with the surface, the particles freeze due to quenching by the much colder surface, allowing them to form a solid deposit layer [54].

2.6.3.2 Deposit Initiation in the Convective Section

Whilst the leading edge of platen superheaters can experience deposit initiation by the mechanism described above, the main method by which deposition can begin within the convective section is through deposition of solid particles. Generally the heat transfer surfaces within a boiler are designed such that the flue gases entering the convective section are below the initial deformation temperature of the fuel ash [44]. The boiler nose, a screen of cooled water is also used to protect the convective superheater pendants from flame radiation and also cools the furnace exit gas by an additional 30°C [44]. These precautions ensure that, on the whole, the ash particles are in a solid state when they enter the convective section.

2.6.3.2a The Role of Alkali Salts in Deposit Formation

In general the literature points to the volatilization and condensation of alkali salts as the main method of deposits initiation [43, 44, 47, 55]. The condensation of alkali salts onto tube and particle surfaces is thought to form a sticky 'glue' which captures solid particles or allows coated particles to adhere to clean tubes. The belief is that in the combustion zone of the boiler, under high temperatures, the alkali metals within the coal particles are volatilized. Bryers [44] states that sodium and potassium are volatilized by the decomposition of sodium and potassium chloride and feldspars to form the volatile species Na, K, NaOH, KOH, Na_2O and K_2O among others. Once released into the combustion gases, they are free to react with SO_2 and SO_3 in the gas stream, forming the alkali salts Na_2SO_4 and K_2SO_4 [44]. Sugawara et al [46] showed that in bituminous coals as much as 35% of sodium and 22% of potassium content can be released from the coal, with volatilization beginning at around 350 – 400°C for both. Michel and Wilcoxon [56] suggest that this type of problem becomes significant when the alkali content of the coal exceeds 0.8% by weight.

There are several ways in which these vapour phase salts can affect or initiate deposition; Bailey et al [53] believe that deposition in the convective section is initiated by adhesion of very fine sub-micron particles which have been transported to the surface by thermophoresis and are captured by Van der Waals and electrostatic forces. They believe that these particles are predominantly alumino-silicates which are much less than one micron in diameter supplemented by larger, iron rich particles of 1 – 5 microns [53]. However, others believe that they are comprised mainly of alkali salts [44, 47] which have been "homogenously condensed to form sub-micron aerosol mists" as they enter the vicinity of the tube [47] and are transported to the surface via thermophoresis and freeze on contact. They too are held on the tube surface by Van der Waals and electrostatic forces. As the thickness of the deposit increases the surface temperature of the deposit rises which can increase the time taken for the condensate to freeze [44]. This can increase the likelihood of the surface capturing incident fly ash particles as the energy of their impact is dissipated by the molten or semi-molten condensates. Eventually the surface temperature may exceed the melting temperature of the alkali salts which causes them to remain molten after reaching the surface. The resulting sticky layer on the tube surface greatly increases the collection efficiency of the tube as solid particles are trapped by the sticky 'glue' [43, 44]. Another school of thought is that the condensed alkali salts react with iron in the protective oxide layer surrounding the tube to form highly corrosive alkali iron trisulphates which remain molten at normal superheater operating temperatures [29, 57, 58, 59]. This molten layer increases the collection efficiency in much the same way as mentioned above. The formation of these species is discussed in greater detail in Chapter 3.

Alternatively, the volatilized salts can condense heterogeneously onto the surface of larger fly ash particles [44, 47]. Since the particles are generally hotter than the superheater tube surface, the condensate remains molten after depositing on the particle. This results in a particle with a sticky layer of alkali salts known as a surface coated particle [47]. When one such particle hits a clean superheater tube through inertial impaction, the molten layer will deform plastically and dissipate the kinetic energy of impact, increasing the probability that the particle will stick.

2.6.3.3 Impact Dynamics of a Surface Coated Particle

There are several factors that will influence whether a particle will stick to a surface on impact (sticking probability) including: impact velocity, particle viscosity, impact angle and surface roughness. Lee et al [47] have proposed a relationship to calculate the sticking probability (ξ) of an impacting particle coated with a layer of sodium sulphate of thickness δ_p. The relationship is discussed in more detail in Chapter 5. The relationship is very complex and is dependant upon many factors, however, it does show that sticking probability is proportional to the impact angle, inversely proportional to the square of impact velocity and inversely proportional to the particle size [47]. Walsh et al also state that sticking probability increases as viscosity decreases [54]. So the smaller and less viscous a particle is, the more likely it is to stick. Likewise a lower velocity and a trajectory closer to normal to the tube surface will increase its likelihood of sticking.

When a solid particle impacts a clean tube surface, it will experience a slight elastic deformation [47]. The kinetic energy dissipated by this type of impact is very small compared to the initial kinetic energy of the particle, so the particle has sufficient energy following the impact to overcome the surface – particle interactions and reflect [47]. The degree of deformation is controlled by the particle viscosity, so when a surface coated particle with a low viscosity outer layer impacts a clean tube, "the velocity of the particle is decreased by the viscous effect of the coated layer" [47]. When the core of the particle impacts the surface, considerably more of its kinetic energy has been dissipated so it has less energy to overcome the particle-surface interaction energy, which itself is higher, due to the larger contact area and surface tension of the molten layer [47, 54]. As a result the particle sticks to the surface. Essentially, the particle sticking probability is a balance of energies as stated by Lee et al "if the surface-particle interfacial energy is greater than the kinetic energy of the reflected particle then the particle will stick" [47].

2.6.4 Deposit Life Cycle

After deposit initiation, deposits go through a growth – shedding cycle. The mechanism of deposit buildup is shown schematically in figure 2.6. Frandsen et al suggest that deposit growth begins as large particles of iron impact the sticky sulphate layer and adhere (a) [21]. Couch describes how, following the initiation of deposition by condensed alkali salts, forming a sticky film on the tube surface, solid particles which otherwise would have rebounded are retained [28]. This is supported by Skorupska who states capture of large fly ash particles gives rise to an increasingly irregular deposit surface, forming the secondary deposit layer (b) [36]. These particles are large enough to penetrate the thermal boundary layer of the heat transfer tube and protrude into the hot gas stream, because of this, these particles remain sticky or molten and do not freeze on the tube surface, allowing them to collect other solid iron and alumino-silicate particles which impact them [21]. These particles slowly build up to form a strong fused mass through the processes of sintering and sulphation. The insulating effect of this deposit layer leads to an increase in the surface temperature of the deposit. Depending on heat flux to and thermal conductivity of the deposit, as it thickens, surface temperatures can increase at the rate of 30-100°C per mm [36], which can cause the viscosity of any liquid phases to decrease, facilitating the capture of further large fly ash particles. This can result in the formation of a sticky or molten surface which will capture almost any impacting particle leading to a rapid increase in the rate of deposit growth in the direction of the gas flow [28]. This produces large fins of deposit which can be up to 300mm in length [28] which protrude into the gas stream in front of the heat transfer tubes as shown in figure 2.6(c).

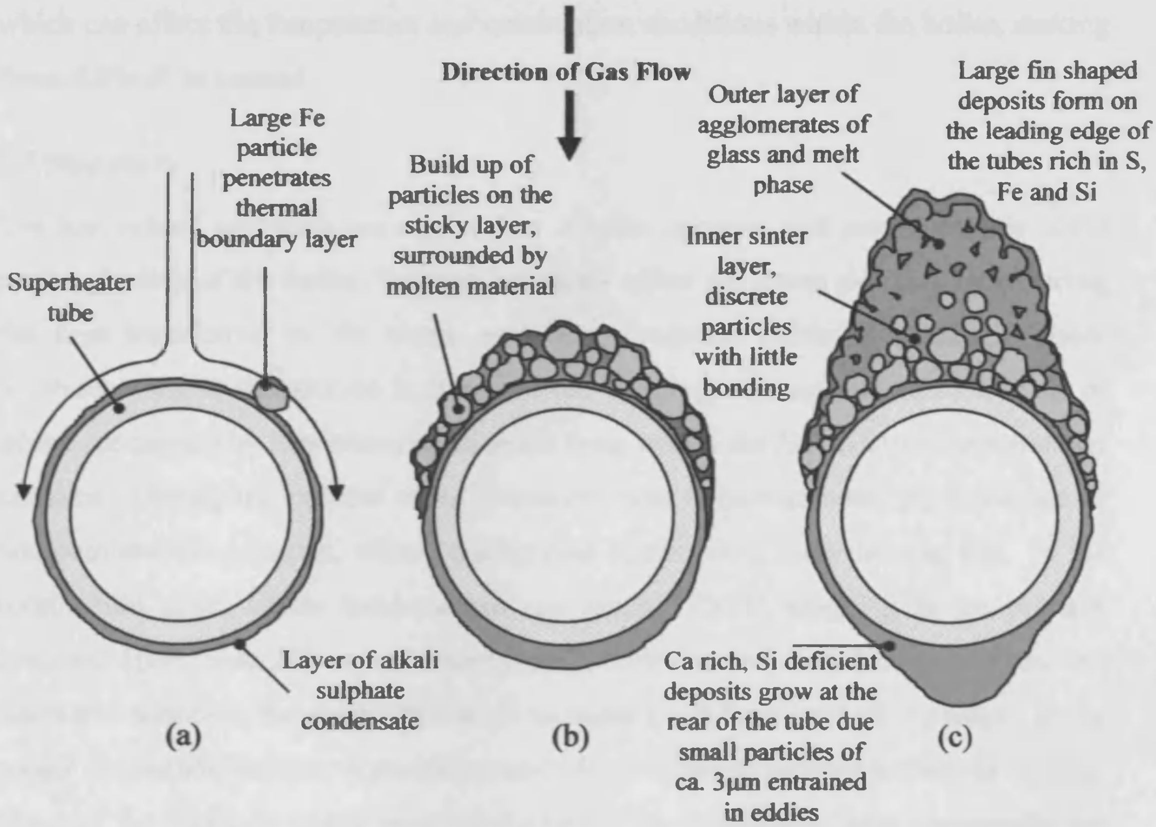

Figure 2.6: Method of deposit growth in the convective section adapted from Walsh et al [54] and Couch [28].

Due to the reduction in heat transfer caused by the increased deposit thickness, downstream gas temperatures rise, causing thermal and chemical changes at the deposit surface which result in the migration downstream of the region of worst deposition [55]. If soot blowing is not carried out regularly, these deposits can grow sufficiently large that they can span between tubes and even tube banks in a process known as 'birdnesting' [28]. These deposits can become very large and harden with age making them resistive to on-line cleaning (soot blowing) processes [28], they can cause severe distortion of the flow within the boiler leading to increased erosion and an increased pressure drop across the boiler [28]. It is also possible for these deposits to become detached, either due to their own weight, or from thermal shock from changes in the boiler temperature regime, resulting in damage and distortion of the superheater tubes and also the evaporator tubes in the ash hopper below [28]. This shedding of deposits can cause sudden changes in the heat flux profile of the boiler which can affect the temperature and combustion conditions within the boiler, making them difficult to control.

2.7 Summary

The fuel related problems encountered by a boiler operator will predominantly occur on the gas side of the boiler, but may indirectly affect the steam side (i.e. by reducing the heat transferred to the steam and hence reduced electrical output). These problems present themselves in three forms; slagging, fouling and corrosion, all of which are caused by deposition of minerals from within the fuel ash onto heat transfer surfaces. During the process of its formation, coal is contaminated by a number of non-combustible minerals, which, during coal combustion, form the coal ash. In the combustion zone, where temperatures can reach 1750°C, slagging is the primary concern. Here, iron, silicon and aluminium particles can be in molten or semi-molten states and adhere to the evaporator tubes on impact and form hard glassy slags. In the cooler convective section deposition occurs by a different process known as fouling. Some of the minerals which were volatilized in the combustion zone, principally the alkali metals K and Na, condense onto cooler heat transfer surfaces in the form of sulphates. Here, they form a sticky film that allows incident solid particles to adhere. These particles sinter to form a loose, porous deposit which can harden with age allowing them to grow quite large, disrupting gas flow and presenting a significant barrier to heat transfer.

Chapter 3 - High Temperature Corrosion

3.1 Introduction

As demand for electricity grew through the 1940s and 1950s, the thermal efficiency of boilers climbed from around 27% to approximately 38% [44]. During the 1960s as efficiency approached 40%, efforts were made to increase it further to around 45%. This was achieved by increasing the steam temperature from 454°C in 1948 to 565°C in 1965 [44]. This increase in steam temperature resulted in a significant increase in operating temperature of the heat transfer tubes. This meant that existing coals containing high concentrations of sulphur, chlorine and sodium began to cause problems with wastage of superheater and waterwall tubes. This problem was partly alleviated by the move away from mild steel towards chromium – molybdenum steels. However, this was not the complete solution and research began into the causes and solutions for these problems.

3.2 Steel Use in Power Station Boilers

A power station boiler is in essence an assemblage of tubes providing heat transfer between the water or steam carried within and the furnace gas [27]. In a coal fired boiler these tubes can be exposed to temperatures as high as 1100°C for superheaters in the convective pass and as high as 1425°C for superheaters in the roof or radiant section [29]. For this reason, the art of boiler design has become a balancing act between material costs and plant longevity and the choice of steel used in each part of the boiler is determined by these factors.

There are three main types of steel used in boiler tube construction [27]:

- Carbon steels
- Chromium Molybdenum alloy steels
- Austenitic and ferritic stainless steels

Steels in boiler applications are selected primarily for their creep strength but also for corrosion resistance [27]. The type of steel used is also limited by the maximum operating steel temperature. Carbon steels used in boiler applications typically contain 0.05 – 0.25% carbon and 0.4 - 0.7% manganese and have a maximum operating temperature of 450°C above which creep and scaling problems become excessive [27]. For this reason the use of carbon steels is limited to the cooler parts of the boiler such as the economiser, primary superheater and primary reheater [27].

Above 450°C low alloy ferritic steels offering more creep resistance are used, these contain additions of molybdenum, chromium and in some alloys vanadium. 12CrMo910, containing 0.12% carbon, 0.5% manganese with the addition of 2.25% chromium and 1% molybdenum and 12CrMo45 which has additions of 0.9% chromium and 0.5% molybdenum are two of the most widely used of these steels. With a maximum operating temperature of 580°C and superior creep and corrosion resistance, they are principally used for superheater and reheater tubes, pipes and headers [27].

For temperatures above 580°C, the use of low alloy ferritic steels is limited by the required wall thickness needed to achieve the desired design life. In such situations austenitic stainless steels are used. Stainless steel typically refers to those with a chromium content in excess of 12% [27], this chromium forms a protective oxide layer which provides excellent corrosion resistance. The most common types of austenitic stainless steel used in power plants are those based on the 18% chromium and 12% nickel alloys [27]. In addition they contain small quantities of other elements; AISI 316 contains 2.5% molybdenum, AISI 321 contains 0.35% titanium and AISI 347 contains 0.7% niobium, which provide higher creep resistance. Austenitic stainless steels typically have a maximum operating temperature of 650°C. However, Esshete 1250 steel which, with additions of molybdenum, vanadium, niobium and boron, offering superior creep strength and ductility, has an operating temperature of 670°C.

These stainless and specialist high temperature steels are considerably more expensive than standard grades of carbon and alloy steels. Steel prices in June 2005 show that the price of cold rolled coil steel was $649 per tonne for carbon steel [60], $2678 per tonne for type 304 stainless and $4855 per tonne for type 316 stainless [61]. A power station manager must weigh up the price of the steel against its expected lifespan and the physical and incurred cost of replacing or repairing it. In order to do this, the plant manager will need a good understanding of the processes and mechanisms that can cause failure of the steel. The principle mode of attack is fuel ash corrosion; the following discussion highlights the main causes and mechanisms of fuel ash corrosion.

3.3 Causes of Fuel Ash Corrosion

Fuel ash corrosion is also referred to as high temperature corrosion or fireside corrosion. Akturk et al [62] describe fuel ash corrosion as the oxidation of steels within the boiler by the solid, liquid or gaseous products of fossil fuel combustion. They state that this type of corrosion manifests itself as either wastage flats on the hottest exposed faces of the tubes or as deep honeycomb pits and that it primarily affects aerodynamically exposed tubes (the leading tubes of a superheater bank for example). They believe that this type of corrosion is associated with the deposits formed on boiler tubes, stating that the composition of the deposit depends upon the type of fuel burned. They also suggest that elements present as only trace amounts in the fuel can concentrate on tube surfaces and constitute the majority of corrosive deposits. They identified four elements; sodium and potassium (alkali metals) along with sulphur and chlorine, which form the majority of the corrosive deposits. They suggest that Chlorine in the coal promotes the release into the flue gas of sodium and potassium from alumino-silicate compounds. These alkali metals are then free to react with the sulphur from within the coal to form fusible sulphates. They suggest that it is these sulphates that cause the majority of corrosion. However, they also note that alkali metal release is influenced by the ash content of the coal; stating that the amount of ash affects the partition of alkali metals between the ash melt and the vapour phase. The result of this is that the higher the ash content, the greater the proportion of alkali metals rendered innocuous.

Cutler and Raask [57] postulate that the release of potassium into the flue gas occurs when sodium is absorbed by semi-molten potassium alumino-silicates in the combustion zone of the boiler. This releases potassium and allows the formation of K_2SO_4 and its subsequent deposition in the radiant and convective sections of the boiler. They tested this theory by studying synthetic mixtures of potassium silicates with varying quantities of NaCl. They found that as the NaCl content was increased up to one third of the potassium was released from the potassium silicates.

Srivastsva and Godiwalla [63] also identified alkali metals in trace quantities in the coal, stating that alkalis make up about 1% of the coal whilst sulphur, in the form of SO_3, accounts for approximately 0.2%. They also link these elements to the formation of corrosive deposits on the boiler tubes, stating that alkali sulphates have been identified in areas of boilers suffering from corrosion. Otsuka [64] also identifies alkali metals existing in trace amounts as the key cause of fuel ash corrosion. Otsuka states that coal fired in power generating boilers contains up to 3% sulphur, 0.6% chlorine with sodium present at up to 700ppm and potassium at 2500ppm. Otsuka also states that the condensation of low melting point alkali salts from the flue gas on the tube surface is the root cause for severe wastage of tube materials.

Adopting a free energy minimisation method, Otsuka calculated the thermodynamic equilibrium composition of flue gas from a typical pulverised coal at temperatures ranging from 700 – 1200°C. Using the same principle, the gases were 'cooled' to a typical metal surface temperature of 600°C to calculate the molar quantity of vapour condensate deposits. The results of this study showed that Na_2SO_4 and K_2SO_4 are vapour condensed from the flue gas whilst Fe_2O_3 accumulates by impingement or adhesion of fly ash particles. This is supported by Harb and Smith [29] who state that "The principal source of iron and aluminium is mineral matter found originally in the coal, although some of the iron may result from corrosion of the tube wall itself" [29]

3.4 The Role of Complex Alkali sulphates in Corrosion

Corey et al [65] identified the presence of alkali iron trisulphates in the deposits on wasted tubes. These findings were backed up by Cain and Nelson [66], who discovered that complex iron alkali sulphates formed within fireside deposits were corrosive when in a molten state. They suggested that the molten compounds migrate through the ash layer towards the tube surface due to the thermal gradient that exists within the deposit. During experimental work they identified the formation of complex alkali iron trisulphates by the following reaction:

$$3(K,Na)_2SO_4 + Fe_2O_3 + 3SO_3 \leftrightarrow 2(K,Na)_3Fe(SO_4)_3 \qquad (3.1)$$

By relating corrosion rate to the temperature of the deposits, Cain and Nelson identified one main corrosion zone and two minor zones. The main zone was due to the formation of complex alkali iron trisulphates of the form $(K,Na)_3Fe(SO_4)_3$, which becomes molten at 620°C. Corrosion rate was seen to increase along with temperature until about 720°C where the thermal stability limit of the complex compounds is exceeded and they begin to disassociate. This is thought to be the main cause of corrosion due to the fact that the complex sulphates are molten within the operating temperature range of the superheater tubes (600°C [29]). The two minor corrosion zones are thought to have less impact on corrosion, primarily because they fall outside this operating temperature range. The first zone occurs well above this range at about 880°C where the normal alkali sulphates K_2SO_4 and Na_2SO_4 begin to melt. However, it is thought that this will only affect non-cooled supports in high gas temperature regions. The other zone occurs below the normal operating temperature at around 315°C where pyrosulphates of the form $K_2S_2O_7$ and $Na_2S_2O_7$, which are molten at this temperature are formed. However the formation of these pyrosulphates is impeded by the competing reaction (3.1) producing the complex alkali iron trisulphates which remain solid at temperatures this low. Hendry and Lees [59] support these findings, stating that "pyrosulphates are not relevant to superheater attack at normal temperatures (those greater than 475°C) and sodium-to-potassium ratios due to the requirement for their formation of SO_3 levels far in excess of those achieved through the stoichiometric combustion of pulverised coal" [59].

In another aspect of their work, Cain and Nelson studied the effect varying potassium – sodium ratios on corrosion rate. Here, they identified a minimum melting temperature for the complex alkali iron trisulphates of 552°C at a molar ratio of between 1:1 and 2:1 potassium-to-sodium. Therefore, they suggested that given the correct conditions, the main zone of corrosion could be extended to temperatures as low as 550°C.

Following on from the work of Rahmel and Jaeger, who identified a depression in melting point to ca. 627°C when 12mol% $Fe_2(SO_4)_3$ is added to K_2SO_4, Hendry and Lees [59] adopted a ternary sodium, potassium, iron sulphate melt for their studies of fuel ash corrosion. By inspection of the binary sulphate systems Na_2SO_4-K_2SO_4, Na_2SO_4-$Fe_2(SO_4)_3$, and K_2SO_4-$Fe_2(SO_4)_3$ shown in figure 3.1, they assumed a low melting point trough to exist within the ternary system extending between the alkali metal ferric sulphate binary eutectics, with its minimum lying on the conodes through the minimum in the Na_2SO_4-K_2SO_4 liquidus curve [59].

To test this theory they created a number of compositions; keeping the ratio of Na_2SO_4 to K_2SO_4 at 4:1 at all times, they created mixtures with 5, 15, 25 and 50 wt% $Fe_2(SO_4)_3$. Measuring the melting temperature by simultaneous thermal analysis (STA), they found melting points of 806°C, 550°C, 546°C and 540°C for each test respectively. From these results they deduced that a minimum melting temperature of 530°C existed at approximately 30 wt% (14mol%) $Fe_2(SO_4)_3$ and that compositions between 15 wt% (6 mol%) and 50 wt% (30 mol%) $Fe_2(SO_4)_3$ were molten below 550°C. Using this information they were able to confirm the findings of Cain and Nelson; identifying a zone of elevated corrosion at temperatures between 565°C and 700°C. They also support the theory that the reduction in corrosion rates above 700°C is due to disassociation of ferric sulphate, stating: "the reduction in corrosion rates is due to the decomposition of ferric sulphate at low activity in the melt leaving a residue of $KNaSO_4$ and Na_2SO_4" [59].

Harb and Smith [29] claim that the formation of alkali aluminium sulphates ($KAl(SO_4)_2$) can cause the temperature at which the liquid sulphate deposit becomes unstable to increase. They show that the temperature at which metal loss from the superheater tubes ceases can be increased by up to 100°C from 650°C to 750°C when alkali aluminium sulphates are added to the melt. However they also identified calcium and magnesium as potential inhibitors to corrosion, firstly by capturing SO_3 in the flue gas, forming calcium sulphate ($CaSO_4$) and magnesium sulphate ($MgSO_4$) and secondly reducing alkali iron trisulphate formation by forming the more stable compounds $K_2Ca_2(SO_4)_3$ and $K_2Mg_2(SO_4)_3$.

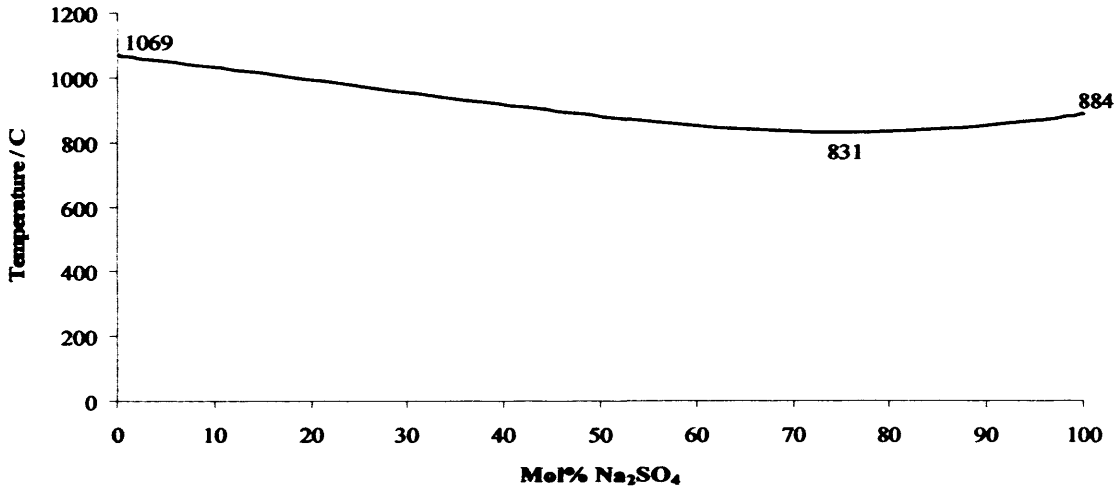

(a) Binary sulphate system Na_2SO_4-K_2SO_4

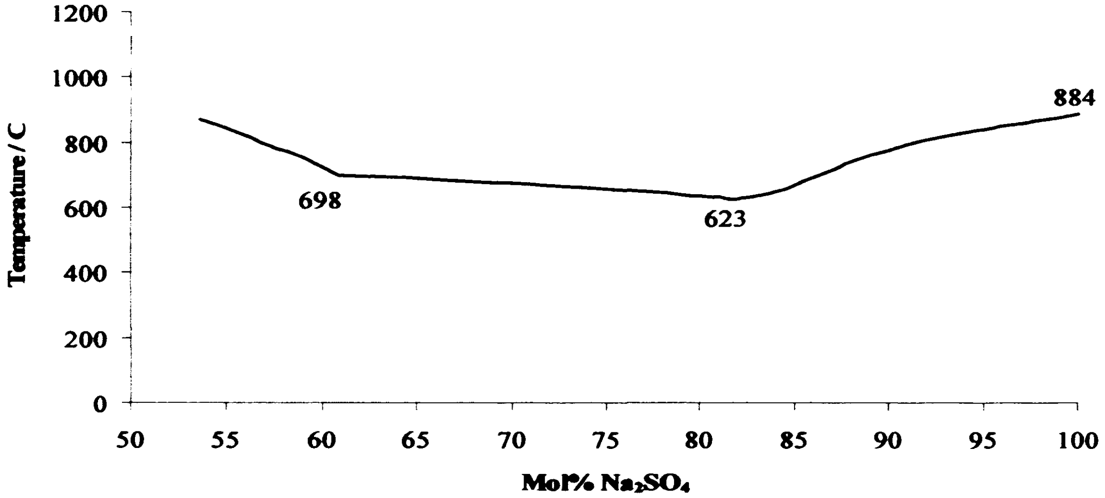

(b) Binary sulphate system Na_2SO_4-$Fe_2(SO_4)_3$

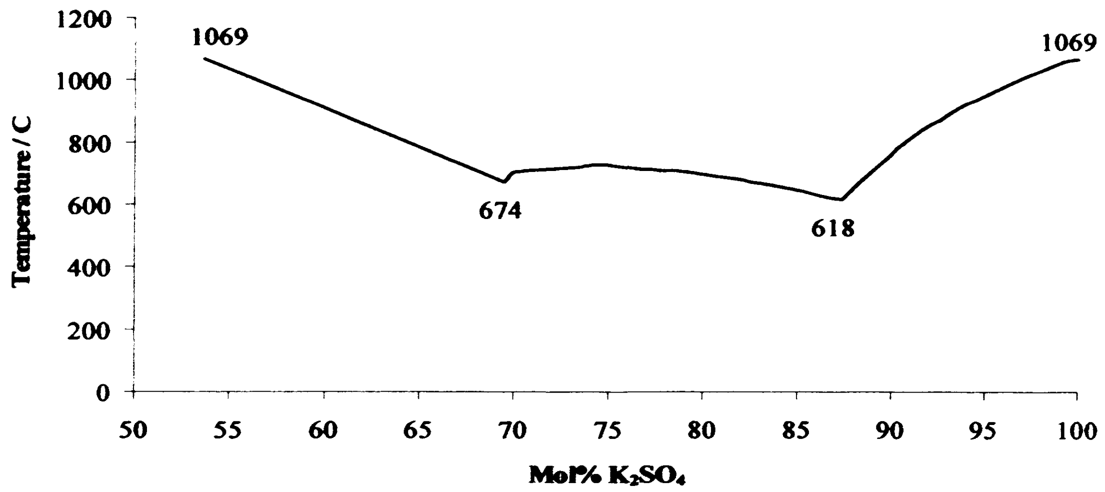

(c) Binary sulphate system K_2SO_4-$Fe_2(SO_4)_3$

Figure 3.1: Melting temperatures of binary sulphate systems

3.5 Mechanisms of Fuel Ash Corrosion.

In order to combat fuel ash corrosion, not only does a plant manager need to know what substances are causing the corrosion, but he needs to know by what mechanisms they are achieving it. What follows is an outline of how understanding of these corrosion mechanisms has developed.

Cain and Nelson [66] stated that a molten mixture of sodium and potassium sulphates along with iron or aluminium oxides and sulphur trioxide existed at the tube surface temperature. They claimed that "these liquids were capable of penetrating the protective oxide layer and preventing its regeneration. Once in contact with the metal surface they react to form a sulphide scale which is porous and non-protective and allows the corrosive reaction to proceed with much less inhibition than the equivalent thickness of oxide scale" [66]. They also identified the formation of complex alkali iron sulphates as a key step in the corrosion process.

They claimed that the corrosion process occurred as a result of the following reaction mechanism:

- Iron from the tube surface reacts with alkali iron trisulphate by the following reaction

  $9Fe + 2(K,Na)_3Fe(SO_4)_3 \rightarrow 3(K,Na)_2SO_4 + 4Fe_2O_3 + 3FeS$ (3.2)
- The Iron sulphide produced reacts with oxygen to form sulphur dioxide and magnetite

  $3FeS + 5O_2 \rightarrow 3SO_2 + Fe_3O_4$ (3.3)
- The sulphur dioxide produced in reaction (3.3) is further oxidised to produce sulphur tri-oxide

  $2SO_2 + 2O_2 \rightarrow 3SO_3$ (3.4)
- Finally this sulphur tri-oxide reacts with the alkali sulphates and hematite in the ash to form more of the alkali iron trisulphate, which is free to react with the iron at the tube surface.

  $3(K,Na)_2SO_4 + Fe_2O_3 + 3SO_3 \rightarrow 2(K,Na)_3Fe(SO_4)_3$ (3.5)

They claim that in the cycle only oxygen and tube metal are consumed with the end product being iron oxide. Therefore it is suggested that only a small amount of corrosion agent may be responsible for a large amount of corrosion.

Hendry and Lees [59] identified the inward transport of SO_3 through a molten sulphate layer as a key step in the mechanism by which corrosion takes place. They claim that "corrosion rate is dependant upon temperature in the operational range 500 – 700°C in terms of the melting behaviour of alkali iron sulphates as a function of SO_3 partial pressure" [59]. They suggest that the thickness of the molten sulphate layer is governed by its temperature gradient, claiming that the inner boundary of the layer is controlled by the steam-metal temperature and that the outer boundary is controlled by the temperature (720°C) at which ferric sulphate disassociates to Fe_2O_3 leaving a solid alkali sulphate residue.

The mechanism they have identified is as follows. Firstly a gradient of SO_3 is established within the molten sulphate layer due to inward diffusion from the flue gas. At the sulphate melt – metal oxide boundary, dissolution of the protective oxide layer occurs through the reaction

$$Fe_2O_3 + SO_3 \leftrightarrow Fe_2(SO_4)_3 \qquad (3.6)$$

As the products of reaction (3.6) diffuse outwards, the increasing SO_3 partial pressure increases the solubility of the iron trisulphate ($Fe_2(SO_4)_3$). However, this is counteracted by the effects of increasing temperature, which decreases the stability of the iron trisulphate forcing the reaction in the opposite direction until, at 720°C, it disassociates to produce Fe_2O_3 and SO_3. The iron oxide produced at the outer edge of the sulphate melt forms a non-protective oxide layer whilst the SO_3 is free to diffuse back towards the metal surface where reaction (3.6) can take place again.

The dissolution of the protective oxide layer under these conditions will increase the corrosion rate until a steady state is established, where the corrosion rate balances the dissolution of the protective oxide layer. Like Cain and Nelson, they note that as the oxide – sulphate melt interface temperature approaches 720°C, the melt becomes infinitely thin, since a molten sulphate layer containing $Fe_2(SO_4)_3$ cannot exist above this temperature. In this situation, solid residues of alkali sulphates (Na_2SO_4 and K_2SO_4) are left which have a minimum melting temperature of 830°C. they claim that "due to the lack of a molten layer to facilitate the diffusion of oxygen and sulphur to the metal surface, the corrosion rate decreases to a value equal to that controlled by bulk solid state diffusion processes" [59].

Cutler and Raask [57] have identified different corrosion mechanisms for the furnace wall tubes and the superheater tubes. They state that on the furnace wall tubes a thin layer of oxide scale is formed corresponding to the excess air level in the flue gas. Under normal oxidising conditions, they claim, "for mild steel and low chromium alloy, the corrosion rate is approximately 40nm/h" [57]. However, they state that "in the burner region of the boiler, flame impingement on the walls and the deposition of partially burnt coal particles can give rise to local regions with a reducing atmosphere" [57]. They claim, "under these conditions corrosion rates can be increased by orders of magnitude to several hundred nm/h" [57]. This is because these conditions "favour a shift in the chemical equilibrium for the sulphur species in the flue gas towards higher sulphur potentials allowing sulphidation of the metal to take place as well as oxidation, producing a thicker but less protective scale on the metal surface" [62].

They identify several major differences between this type of corrosion and that which takes place on the superheater tubes. The first of which is the fact that "as all of the combustion reactions are complete by the time the flue gas reaches the superheater region, uniform oxidising conditions are considered to prevail" [57]. Secondly, the superheaters operate at a much higher temperature (650°C). The implications of this are that a molten alkali metal sulphate layer can form at or near the tube surface. However, at the lower end of the operational temperature range normal oxidation of the metal proceeds, controlled by the growth of the protective oxide scale.

Cutler and Raask, support the transport process proposed by Hendry and Lees. This is described quite succinctly the by Harb and Smith [29]. They state that "to support a sustained corrosion mechanism, a negative solubility gradient across the deposit, allowing metal to dissolve at the metal/melt interface, is required" [29] this means that the highest solubility is at the metal-salt interface. Moving outwards through the deposit, the temperature increases which, in turn, decreases the solubility forcing the dissolved metal to re-precipitate away from the interface, avoiding saturation of the melt. However, they claim that "under isothermal conditions, the solubility of the corrosion product increases with increasing SO_3 concentration" [29]. It has already been established that the concentration of SO_3 rises as the outer edge of the melt is reached. This would result in a positive solubility gradient with the lowest solubility at the metal-melt interface and the highest solubility at the gas-melt interface; the opposite of that required for sustained corrosion. They claim however, "the presence of a temperature gradient across the melt will counteract the effects of the varying SO_3 concentration within the melt". Stating, "specifically the temperature gradient causes the solubility at the metal-melt interface to increase and that at the gas-melt interface to decrease" [29]. They claim "sustained corrosion is seen in instances where this negative solubility gradient, resulting from the temperature gradient, is sufficient to overcome the positive solubility gradient caused by the SO_3 concentration gradient" [29]. Like Hendry and Lees, Cutler and Raask believe that this will result in an increase in corrosion rate until it balances the dissolution of the protective oxide layer. This also underlines the need for the molten sulphate layer for this process to work, stating, "in areas where high temperatures cause disassociation of the iron sulphate and the solidification of the sulphate layer, the corrosion rate returns to that of normal high temperature oxidation" [58].

Akturk et al [62] support the theory of condensation of alkali sulphates onto the protective oxide layer from the hot flue gases. They agree that at a surface temperature ca. 580°C, the deposits remain molten and contain free SO_3 which stabilises the sulphate and attacks the protective oxide scale, forming iron, chromium and nickel sulphates. Again, they support the theory suggested by Hendry and Lees, stating, "the stability of the sulphates will decrease as temperature increases and they will begin to disassociate" [62]. They support the claim that the temperature gradient within the sulphate melt causes a concentration gradient for the disassociated metal ions, ensuring that dissolution is continuous, as iron, chromium and nickel diffuse out through the sulphate melt. They claim that at the hotter, outer layer of the sulphate melt, iron and chromium oxides are formed within the ash but no longer form a protective layer.

They go on to confirm that the rate of this continuous transport process determines the corrosion rate. They state, "as gas temperatures increase, so do corrosion rates and that increasing tube surface temperatures will also increase the corrosion rate due to faster reaction rates" [62]. They agree that at metal temperatures of 650°C to 700°C, the molten sulphate becomes thermodynamically unstable and that corrosion rates begin to fall as temperatures increase above this and that eventually the corrosion rate falls to that of normal high temperature oxidation, resulting in the classical bell-shaped curve shown in figure 3.2.

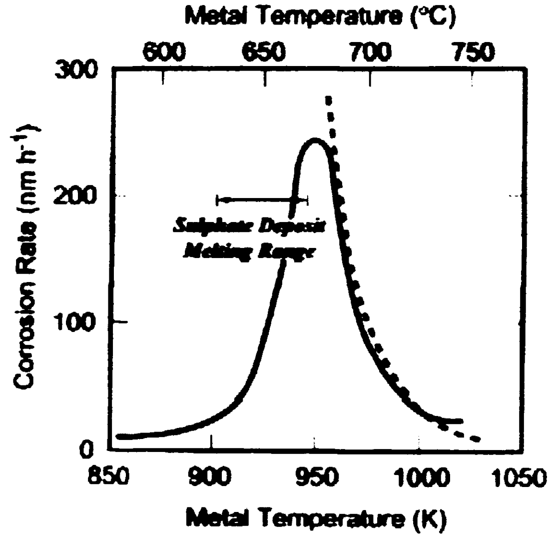

Figure 3.2: The dependence of corrosion rate on temperature [61]

Like Hendry and Lees, Srivastava and Godiwalla [63] describe separate corrosion mechanisms, the first being a low temperature pyrosulphate corrosion mechanism and the second a high temperature trisulphate mechanism. They too emphasise the requirement for high concentrations of SO_3, especially for the low temperature pyrosulphate corrosion mechanism. They state "the existence of the mechanism depends upon the availability of high concentrations of SO_3 which is produced by the catalytic oxidation of SO_2 on active surfaces" [63]. However, they state that "at least 10,000ppm SO_3 must be present for $K_2S_2O_7$ to form at 538°C and that even when burning a high sulphur (4 – 5%) coal, SO_2 concentrations in the flue gas will not exceed 3500ppm. Hence the SO_3 formed will be less than one tenth that required to form pyrosulphates at superheater temperatures (593°C)" [63]. For this reason, they claim "a consistent mechanism for pyrosulphate corrosion can only exist in the temperature range 399 – 482°C" [63].

They suggest that the mechanism begins with the deposition of alkalis on the exposed metal surfaces and their subsequent reaction with SO_3 to produce $K_2S_2O_7$ and $Na_2S_2O_7$. These pyrosulphates react with the protective oxide layer around the tubes according to the following reactions:

$$3(K,Na)_2S_2O_7 + Fe_2O_3 \rightarrow 3(K,Na)_2SO_4 + Fe_2(SO_4)_3 \qquad (3.7)$$

or

$$4(K,Na)_2S_2O_7 + Fe_3O_4 \rightarrow 4(K,Na)_2SO_4 + Fe_2(SO_4)_3 + FeSO_4 \qquad (3.8)$$

As the removal of the protective oxide layer takes place, the metal is further oxidised by reaction (3.9).

$$3Fe + 2O_2 \rightarrow Fe_3O_4 \qquad (3.9)$$

They attribute high temperature corrosion to a mechanism slightly different to those proposed in earlier works. However, like the others they maintain that alkali iron trisulphates are responsible for attack, though through slightly different reactions (3.10) – (3.13).

$$4Fe_3O_4 + 18(K,Na)_2SO_4 + 18SO_3 + O_2 \leftrightarrow 12(K,Na)_3Fe(SO_4)_3 \qquad (3.10)$$

or

$$Fe_2O_3 + 3(K,Na)_2SO_4 + 3SO_3 \leftrightarrow 2(K,Na)_3Fe(SO_4)_3 \qquad (3.11)$$

Again, as the protective oxide layer is removed the tube material is further oxidised to balance its depletion.

$$3Fe + 2O_2 \rightarrow Fe_3O_4 \qquad (3.12)$$

or

$$4Fe + 3O_2 \rightarrow 2Fe_3O_4 \qquad (3.13)$$

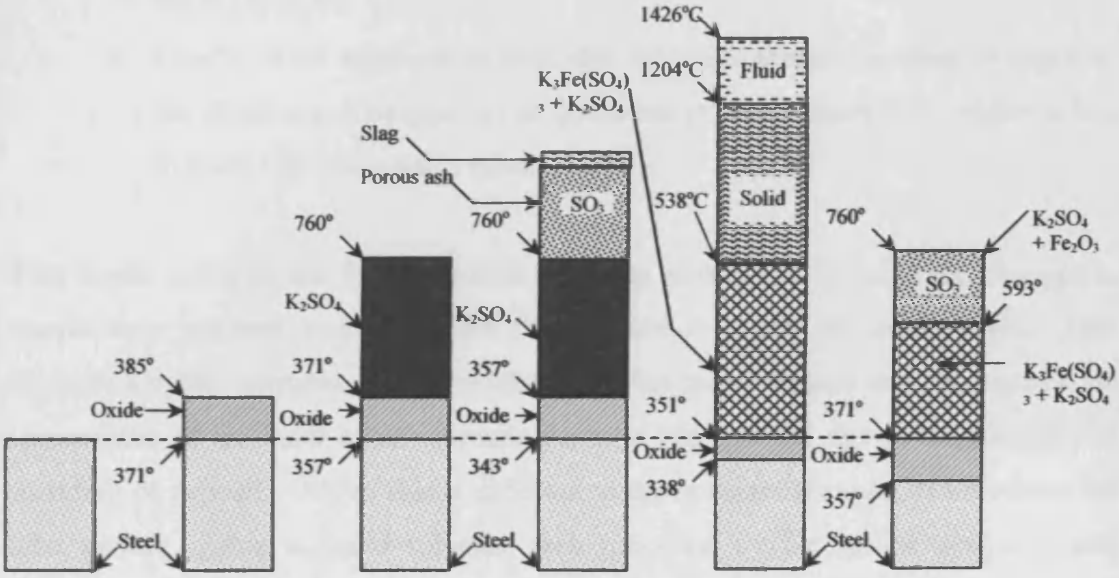

Figure 3.3: Formation of complex sulphates by removal of the protective oxide film [63]

Figure 3.3 shows a schematic representation of the process that Srivastava and Godiwalla proposed for corrosion of the superheater tubes. They suggest that the mechanism occurs as follows:

- Firstly, a solid oxide film forms on the surface of the tube.
- Alkalis such as K_2SO_4 and Na_2SO_4 from the ash and the flue gas deposit on the oxide layer
- The surface of the deposit becomes sticky as its surface temperature increases as it grows thicker.
- The sticky surface captures impacting fly ash particles where they release SO_3 by thermal dissociation as they are heated by the passing flue gases.
- The SO_3 migrates towards the cooler metal surface.
- The surface temperature of the deposit becomes so hot that the captured ash particles begin to melt and form a layer of slag on the surface.
- As the temperature of the inner deposit layer begins to fall due to the insulting effect of the outer layers of slag, the SO_3 reacts with the oxide film to form alkali iron trisulphates $K_3Fe(SO_4)_3$ and $Na_3Fe(SO_4)_3$.

- More of the tube surface is oxidised to compensate for the removal of the oxide layer.
- Finally, if the temperature suddenly increases due to shedding of deposits, the alkali iron trisulphates can dissociate releasing more SO_3, which is free to react with the oxide scale again.

This model relies on the formation and shedding of deposits to cause the changes in temperature required to produce the SO_3 needed to attack the oxide scale. This suggests a cyclic corrosion regime where corrosion rates increase and decrease as the temperature of the inner alkali sulphate deposits rise and fall due to the growth and shedding of deposit. Whilst this is different to the constant removal of iron from the tube surface within a liquid sulphate melt proposed by the earlier works, it still emphasises the importance of SO_3 and alkali metals in the process.

3.6 Summary

It has been established that high temperature corrosion is caused by the alkali metals sodium and potassium from the fuel ash and that these metals react with sulphur, volatilised in the flue gases, to form alkali sulphates. The literature suggests that the problem begins when these species condense onto the cool surface of the protective oxide layer surrounding the steel. Initial mechanisms proposed suggested where these alkali sulphates react with the iron in the oxide layer forming alkali iron trisulphates, and that this was the direct cause of corrosion [66]. However, later proposals were that the alkali metals reacted with iron from the deposited ash to form the alkali iron trisulphates. It was suggested that this was merely a process that accelerated the rate of corrosion which is caused by other processes, namely the reaction of the oxide layer with SO_3. Claims that the formation of a melt, which facilitated faster diffusion of reaction agents (SO_3) towards, and corrosion products (Fe ions or iron trisulphate) away from the tube surface, were put forward [29, 57, 60]. It has been established that addition of differing quantities of iron trisulphate to the alkali metals can have a drastic effect on the formation temperature of the melt which increases the temperature range over which the corrosion processes are effective.

All parties agreed that the temperature gradient across the melt or deposit was the driving force behind the corrosion. It was established that this temperature gradient was responsible for maintaining the differential in solubility between the inner (higher solubility) and outer (lower solubility) surfaces of the melt, which allowed the constant transport of iron, chromium and nickel away from the tube surface.

Chapter 4 - Biomass Combustion

4.1 Introduction

As has already been stated, biomass is a very diverse fuel source, certain types of which can be very similar to coal whilst others are vastly different. This variation presents powerstation managers with a range of problems when trying to predict how a particular type of biomass fuel will react within a boiler. In order to accurately predict the behaviour of biomass fuels under co-combustion conditions, it is necessary to fully understand the fuel properties and how they differ from those of coal. It is also necessary to establish how these differences will affect the behaviour of the fuel in terms of its combustion characteristics, the nature of the ash it will form, likely emissions and any fuel storage, handling and preparation problems which might occur.

4.2 Properties of Biomass Fuels

The differences between biomass fuels and coal arise due to the way they are formed; plant tissues are composed of structural and non-structural carbohydrates that are formed as a result of photosynthesis. The components of biomass include cellulose, hemicellulose, lignin, lipids, proteins, starches, simple sugars, water and hydrocarbons [4, 26]. Coal is the product of millions of years of extreme temperature and pressure on plant tissues coupled with chemical decomposition and attack from anaerobic micro-organisms, resulting in a complex polymer containing carbon, hydrogen, oxygen, nitrogen, sulphur and inorganic elements [7]. Waste derived fuels, created from unwanted residue and rubbish can contain a wide range of substances. These types of fuel range from municipal solid waste (MSW), which can contain paper, wood, yard trimmings, food scraps, food packaging (both plastic and metal) as well as metal and plastics from industrial sources [5] to agricultural wastes and sewage sludge.

When considering biomass fuels it can be useful to differentiate between plant-based fuel sources and those derived from waste. Relative to coal, plant-based biomass fuels typically have less carbon, nitrogen and sulphur and more oxygen due to their carbohydrate structure [4, 5, 7]. They will also have a lower heating value, ash content and density whilst having higher moisture content [5]. In contrast to this, wastes and agricultural residues can have high ash and nitrogen contents [3, 5, 7]. The properties of plant-based biomass fuels can also vary with growth conditions and position within the plant [5].

In general, in plant-based biomass fuels typically 30 – 50$\%_{wt}$ of dry matter is oxygen [4, 10], and 30 – 60$\%_{wt}$ is carbon. Hydrogen is the third major constituent making up some 5 – 6% of the fuel by weight [4]. This compares with an overall carbon content of 77 – 90%, an oxygen content of 3 – 15% and a hydrogen content of 4.5 – 5.5% for bituminous coal [36]. When considering the proximate analysis of these biomass fuels, volatile matter is the major constituent accounting for between 60$\%_{wt}$ and 80$\%_{wt}$ of the fuel [3, 5, 7, 10], moisture content is in the range of 5 – 50$\%_{wt}$ [10, 20], fixed carbon makes up 10 – 20% of the fuel [10] with ash accounting for between <1$\%_{wt}$ and 20$\%_{wt}$ [7, 10]. When considering the ultimate analysis of these fuels, sulphur content is from 0$\%_{wt}$ – 0.3$\%_{wt}$ [10] compared to ca. 1.3$\%_{wt}$ for coal [36] and nitrogen ranges from 0.1$\%_{wt}$ to 2$\%_{wt}$ [10] compared to 0.5$\%_{wt}$ – 2.5$\%_{wt}$ for coal [36].

In contrast to these figures, sewage sludge can contain from as little as 2$\%_{wt}$ fixed carbon [12] to as much as 50$\%_{wt}$ [14]. In addition the ash content of sewage sludge is generally much higher sometimes accounting for as much as 50 – 60$\%_{wt}$ of the mass of the fuel [11, 12]. Sewage sludge is usually dried before use leaving a moisture content of less than 10$\%_{wt}$ [20], however before drying this can be as high as 60 – 80$\%_{wt}$ [12]. The sulphur content of sewage sludge is around 0.9$\%_{wt}$ which is comparable with that of coal [14, 36] and the nitrogen content is approximately twice that of coal at up to 5$\%_{wt}$ [14].

The importance of the moisture and ash contents of biomass fuels can be seen when they are directly compared to the quantities of moisture and ash introduced by coal per megawatt. For example, in his research Prinzing found that coal will introduce ca. 2.6g of moisture per megawatt of power produced, whereas sawdust can introduce as much as much as 32.2g per megawatt [25]. This is similar for the ash content where coal will introduce ca. 4.3g of ash per megawatt of power produced, sawdust will produce as little as 0.4g and right of way trimmings (ROW) 17.2g per megawatt [25].

The high value for ROW is due to the detritus that becomes associated with the fuel during collection [25]. Such vast differences between the compositions of the fuels will inevitably have an effect on the behaviour of the composite fuel within the furnace, even at relatively low levels of substitution. The thermal properties of these fuels such as specific heat, thermal conductivity and emissivity can vary with moisture content, temperature and degree of thermal degradation by up to one order of magnitude [5].

4.3 Combustion Characteristics of Biomass Fuels

The burning profile of a fuel provides a 'fingerprint' of the complete combustion process, giving an assessment of its combustion characteristics [67]. Using this profile it is often possible to identify stages of combustion such as ignition, devolatilisation and char combustion. By comparing the burning profile of coal to those of some biomass fuels, it is possible to understand the main differences in combustion characteristics. The first part of the profile is characterised by a steady mass loss as any remaining moisture is released following drying of the fuel [14], this is followed by a sudden increase in the rate of mass loss as combustion of the fuel begins (ignition) [14]. The onset of ignition in biomass fuels often occurs at lower temperatures than it does in coal [12]. The ignition of biomass is similar to that of coal however it is more likely to be homogeneous in nature due to the high volatile content associated with biomass fuels [7]. This prevents ignition of the char particle until volatile combustion has ceased, since during this time all the available oxygen is consumed by the volatile combustion [37, 39]. Demibras found that the ignition temperatures for a range of biomass fuels including sunflower shells, pinecones, cotton refuse and olive refuse were within the range of 463 – 475K [5], Sami et al found the ignition temperature of manure to be ca. 525K [7], this compares with an ignition temperature for coal of around 675K [34], although, this can be as low as 575K for particles of 30 - 50μm and up to 700K for particles greater than 125μm [67]. These findings suggest that ignition temperature of a fuel decreases as the volatile content is increased [67]. The premature ignition of fuel is a significant consideration for powerstation managers when trying to minimise the potential for burner damage when firing biomass fuels.

In general, biomass has high volatility and reactivity [5], with combustion characteristics that most resemble those of lignite or brown coal [10]. The ratio of fixed carbon over volatile matter (FC/VM) is a measure of how well a fuel will burn [8]. Lower values indicate a fuel which will burn more readily; for coal these values vary between 1 and 4, however, for biomass they often fall below 1, with sewage sludge falling as low as 0.15 [8]. The high reactivity of biomass fuels is demonstrated by the peak temperature [5]; this is the temperature on the burning profile at which the maximum mass loss due to combustion occurs [5]. For biomass fuels this is typically 560 – 575K [5, 14], whilst for coal it is nearer 800K [68] although larger coal particles (>100μm) can demonstrate a second, earlier peak at around 725K caused by the homogeneous nature of their ignition [39, 67]. Studies by Otero et al on the co-combustion of sewage sludge with coal demonstrated that for sewage sludge, the burning profile features two distinct peaks such as those for large coal particles; one at 575K corresponding to devolatilisation and another at ca. 680K which corresponds to char combustion [14]. This indicates that these processes occur as individual events. Meanwhile, they showed that the burning profile for coal featured only one peak at ca. 800 – 900K, demonstrating that the processes of devolatilisation and char combustion overlapped during coal combustion [14]. These findings are supported by Ninomiya et al who identified temperature peaks of 475 – 500K and 675 – 700K for biomass and a single peak at 875K for coal [3]. Sami et al showed that the magnitude of mass loss rate at peak temperature was significantly higher for sewage sludge than it was for coal [7]. This suggests that the devolatilisation event occurs more quickly for sewage sludge [7], owing to the fact that the rate of volatile release in coal is limited by the high fixed carbon content [8]. Ninomiya et al support this, stating that the devolatilisation of sewage sludge occurs in the range 425 – 725K, whilst that of coal occurs at 600 – 825K [3]. The reason for this earlier release and ignition of volatile matter is that the volatiles released are much lighter (shorter chain hydrocarbons) than those of coal [3], meaning that the activation energy for the combustion reactions is lower [7].

This rapid release and combustion of volatiles in the initial stages of combustion can cause problems for powerstation managers. In coal combustion this process lasts only 10 – 100ms [7]. During this time, for bituminous coals, up to 36% of the heat energy of the fuel can be released, leaving the remaining 64% to be released over the next few seconds as the char burns out. However, in biomass fuels up to 76% of the heat contribution can come from volatile matter [5, 7]. It has already been stated that the process of volatile release in biomass is faster than that for coal; therefore, the release of such a large proportion of the fuel's energy in such short space of time can be very problematic, causing damage to the boiler tubes in the combustion zone. These sorts of phenomena can affect the temperature profile and heat distribution within the boiler leading to lower temperatures and efficiency in the convective section. Char burnout can be affected by this in one of two ways depending on the type of fuel and its specific properties; in fuels with low moisture and low ash char burnout will occur more quickly due to the smaller amounts remaining to oxidise, and the fact that the char is more porous in nature following the release of volatiles, allowing oxidation reactions to proceed at a faster rate [7, 10]. In fuels which have high moisture and ash contents the burnout can be hindered, firstly due to the increased requirement for fuel drying which can delay ignition, and secondly; following volatile release, depending on the ash content, the remaining particle can be up to 80% inorganic minerals which act as a barrier, hindering oxygen diffusion to the char surface [3]. This can result in an increase in the un-burnt carbon (UBC) in ash as the minerals agglomerate to form a porous ash network with the char trapped within [3]. If the UBC rises above 5% then powerstation managers can encounter saleability problems when trying to dispose of boiler ash [12, 17].

4.3.1 Heating Value (HV)

The heating value of the fuel is a measure of its energy content and is a very important factor for powerstation managers to consider when contemplating different fuels. Essentially, the higher the heating value of a fuel, the lower the amount of that fuel that is required to fulfil the power output requirements of the plant. Typical heating values of bituminous coals are in the range of 25.8 – 34.8 MJ/kg [36]. Table 4.1 shows the typical heating value of a selection of biomass fuels [68]

From the table it can be seen that the heating value of biomass fuels is varied, with the lowest value at around 6 MJ/kg for sewage sludge some 4 to 5 times lower than that of coal [13]. The heating values of these fuels are dictated by their moisture, ash and carbon content. Before the onset of combustion, all of the moisture within a fuel is evaporated; the evaporation of water is a strongly endothermic reaction and will require an energy input to take place [4]. This energy requirement detracts from the energy released by the fuel, thus fuels with higher moisture contents will have lower heating values [4]. The autothermal limit (self supporting combustion) for biomass is around 65% moisture; above this, the energy released by the fuel is not sufficient to satisfy the evaporation of the moisture [4]. Therefore, fuels with high moisture contents, such as wood, can suffer from ignition and combustion problems [7].

Table 4.1 - Heating values of a selection of biomass fuels

Biomass Fuel Type	Heating Value MJ/kg
Bark	10.5 – 12.1
Sawdust	10.5 – 17.6
Bagasse	8.4 – 15.1
Peat	9.2 – 11.7
Coffee Grounds	11.3 – 15.1
Nut Hulls	17.2 – 18.8
Rice Hulls	12.1 – 15.1
Corn Cobs	18.4 – 19.2
Sewage Sludge	6.0 – 12.0

High ash contents in fuels can cause similar problems since the ash does not contribute to the heat release from the fuel but will absorb heat as the fuel particles heat up [4]. Jenkins et al state that for every 1% increase in ash content of a fuel, the heating value decreases by approximately 0.2MJ/kg [4]. This is the reason that fuels such as sewage sludge, which can contain as much as 60% ash, have such low heating values. The heating value of a fuel can also be affected by the degree of oxidation prior to combustion [4]. Fuels release heat energy as the elements and compounds within them are oxidised, if a fuel is already highly oxidised then less energy will be released by oxidising reactions. Plant based biomass contains lignin and cellulose, cellulose contains more oxygen than lignin so has a lower heating value (17.3MJ/kg compared to 26.7MJ/kg for lignin) [4]. Coal is made up primarily of hydrocarbons which have much lower levels of oxidation thus giving coal its higher heating value [4]. Jenkins et al sate that for every 1% increase in the carbon content of a fuel the heating value is increased by 0.39MJ/kg [4].

Using a substitute fuel with a lower heating value will mean that the overall quantity of fuel required to obtain the desired power output will rise. Sami et al suggest that using a 10% blend of wood will reduce the heating value of the composite fuel by up to 3% [7]. The deficiencies of sewage sludge in this respect are highlighted by Gerhardt et al who suggest that three parts sewage sludge must be used to replace one part coal [12]. This is supported by Ireland et al who suggest that for every 1% of heat supplied by sewage sludge, the heating value of the composite fuel will decrease by 0.6% [8]. This need for additional fuel to match the power requirement can cause problems with ash loading within the boiler [12, 20]. Both Gerhardt and Heinzel suggest that whilst producing the same power output, a 25% substitution of sewage sludge can increase the quantity of ash entering the boiler by up to 5 times [12, 20]. The additional fuel requirement can also cause problems in the fuel supply systems and the pulverisers [15, 25].

4.3.2 Flame Temperature and Temperature Profile

The increased ash loading that comes with some biomass fuels can also have an effect on the temperature regime within the furnace. When firing sewage sludge one would expect the rapid release and combustion of volatile matter to give higher a flame temperature, however, the high ash content of the fuel absorbs much of the heat and serves to reduce the flame temperature [12]. The high ash content can also cause clouding of the atmosphere within the furnace; this serves to hinder radiant heat transfer to the furnace walls and, as a result of this, the wall temperature is reduced and the temperature in the centre of the boiler remains higher [12, 13]. Gerhardt et al found in their work that the wall temperature of the furnace was up to 100°C lower whilst the furnace exit gas temperature was some 100°C hotter as the energy remained in the dust-laden flow [12]. This can threaten the integrity of the superheaters as hotter flue gases will cause their surface temperature to rise increasing the threat of high temperature corrosion problems as discussed in Chapter 3

The stoichiometric air requirement for biomass is circa 4 to 7 kg of air for every kg of fuel burnt, this compares to around 14 to 17 kg for hydrocarbon fuels [4]. The lower the air requirement for biomass fuels, the smaller the quantity of atmospheric nitrogen that must be heated along with the combustion products to achieve the adiabatic flame temperature [4]. Most biomass fuels have an adiabatic flame temperature of 2000 – 2700K, whilst methane which has a heating value three times that of wood at 55.6MJ/kg, has an adiabatic flame temperature of only 2300K [4]. This highlights the fact that the heating value of a fuel cannot be relied upon entirely to predict temperatures within a furnace.

4.3.3 Flame Stability

As has been stated before, a stable flame is achieved by matching the fuel feed velocity with the flame velocity (rate of burning). Failure to achieve this condition will result in the point of ignition travelling in the direction of the lower velocity, causing blowoff if the fuel feed velocity is too high and flash back, which can lead to mill fires, if the fuel feed velocity is too low [39]. Flame stability is determined by the air velocity, excess air, particle size and ignition properties of the fuel [9]. By lowering the air velocity and increasing the excess air and particle size, which govern devolatilisation and heating rates, the flame is made more stable [9]. Coal flames where the concentration of volatiles varies significantly can experience some stability problems [9]. One of the primary effects of adding biomass fuels will be to change the volatile content of the composite fuel, thus stability problems may occur, especially if the supply of biomass cannot be guaranteed and therefore the type of substitute fuel is varied. In addition to this, the high moisture and ash contents of the fuel may cause ignition and flame temperature problems which could also threaten the flame stability [7]. Sami et al state that if the flame temperature is allowed to fall below 1600K then flame stability problems will be encountered [7].

4.4 Ash Nature and Deposition of Biomass Ash

The effect of a biomass fuel on the nature of the resulting ash can be as important to a boiler operator as the combustion characteristics. The fate of ash is often determined by the nature of the combustion regime within a boiler, since temperature is a critical factor in determining the nature of the ash as it passes through the system. Temperature will dictate whether the ash remains solid, becomes sticky or becomes molten. Flame temperatures can also dictate the degree of volatilisation of inorganic elements within the fuel which can be problematic further downstream.

4.4.1 Sources of Ash in Biomass Fuels

As has already been discussed, the inorganic and mineral elements that form ash during coal combustion can be split into three categories; inherent materials which are dispersed within the coal matrix, extraneous minerals which are loosely attached to the coal substance and organically-bound minerals which, formed by bacterial reaction within the coalification process are intimately dispersed throughout the material [28, 30, 44]. The minerals in the first group are formed from the substances absorbed by the plant during growth [44]. It is these elements which are most likely to be found in biomass materials since the plants are still in their growth phase when they are harvested. It is possible for extraneous matter to be included in biomass fuels such as wood, ROW and forestry residue since soil and dirt can be picked up in processing steps during harvesting [4].

The type of inorganic matter found in biomass fuels depends heavily on soil type, chemistry and nutrients used by the plant [24]. Silicon occurs in plants by absorption of silicic acid from the soil solution and is usually in granular or hydrated (dispersed) form [24]. Potassium and other nutrients correlate with metabolic growth and are found predominantly in areas of the plant where growth is most vigorous such as leaves, tips and bark and are atomically dispersed within the organic matrix making them readily volatile on combustion [18, 24]. Aluminium, iron and other minerals are introduced through soil contamination and are predominantly in the form of clays and oxides [24]. Most of these inorganics are found in coal, but are in the form of minerals, whereas in biomass fuels they exist as simple salts or are associated with the organic matrix [22, 68]. This difference in the mode of existence of inorganics between coal and biomass fuels can cause great differences in their fate during combustion, for example, in coal only 0.5 – $4\%_{wt}$ of inorganics are volatilised whilst in biomass between 30 and $75\%_{wt}$ will enter the vapour phase [68].

4.4.2 Composition and Behaviour of Inorganics in Biomass Fuel

In general, biomass ash has less Al, Fe and Ti than coal but more Si, K, Na, Ca and P [3, 5, 10, 13, 20]. In herbaceous fuels potassium and silicon are the principal ash forming constituents; for straw, silica can make up over 21% of ash, potassium can account for as much as 33% whilst phosphorous can make up between 4 and 16% [10]. Chlorine is also a major constituent of herbaceous fuel ash with levels as high as 3.6% [5]. Sewage sludge contains similar amounts of Al and Si to coal but generally more Fe, P and Ca [3, 8]. As with coal combustion, it is the vaporisation of the alkali metals within the fuel that causes boiler operators greatest concern [5, 6].

As with coal ash, once in the vapour phase these alkali metals can condense onto heat transfer surfaces causing fouling and corrosion problems or coagulate to form aerosols and fly ash particles [22, 23, 68].

The composition of the fuel ash can affect the mechanisms by which this vaporisation process occurs; in fuels with low alkali metal contents, vaporisation occurs by the breakdown of alkali sulphates forming alkali chlorides [24]. For those fuels with high alkali but low chlorine contents, hydroxides are the most abundant form of vapour whilst in fuels with high alkali and nitrogen contents cyanides are the most abundant form [24]. Chlorine is problematic because it facilitates the mobilisation of inorganic constituents, shuttling alkalis as chlorides from the fuel to the heat transfer surfaces where they react to form sulphates [4]. Generally during combustion, most of the alkali reacts with alumino silicates to form stable compounds such as $KAlSi_2O_6$ preventing deposition on the heat transfer surfaces [22], however as the biomass share increases, the aluminium share decreases due to the lower Al content in the biomass fuel. This means that less of the stable compound is formed leaving more potassium to react with chlorine to form the harmful species KCl, [22]. The KCl deposits on the heat transfer surfaces and subsequently sulphates in the solid phase to form K_2SO_4; one of the main causes of slagging, fouling and corrosion [22, 68].

The detrimental effects of alkali sulphates on ash deposits have already been discussed in Chapter 2. These theories are supported by Andersen et al [68], who suggest that straw deposits will have increased tenacity due to the higher K_2SO_4 content formed from the higher initial K_2O content of the straw ash.

When considering sewage sludge combustion, Nadziakiewicz and Koziol [19] suggest that more fine particles are formed as a result of the sewage sludge ash. This puts a greater load on dust removing equipment than pure coal which forms larger particles which impact heat transfer surfaces forming slag [19]. Ninomiya et al [3] suggest that calcium provides the foundation of the ash layer for sewage sludge with the formation of $CaPO_4$/Al-Si which is more efficient at capturing trace elements and, as a result, less zinc and boron is vaporised, allowing more alkali substances to volatilise which will form the initial layers of deposit [3]. This differs from the structure of coal ash proposed by Frandsen et al [21] who suggest that the supporting structure for the deposit is formed by 'fingers' of iron created as large Fe particles impact the heat transfer surface and disrupt the thermal boundary layer, allowing them to stay molten and capture other smaller aluminosilicate particles. They go on to describe how the structure of straw deposits loses this orderliness and assumes the form of large randomly scattered particles of mainly Ca and Si [21].

4.4.3 Softening and Melting Temperatures of Biomass Ashes

Figure 4.1 shows the critical temperature points in the ash fusion test. This is used to measure the softening and melting behaviour of ashes [36].

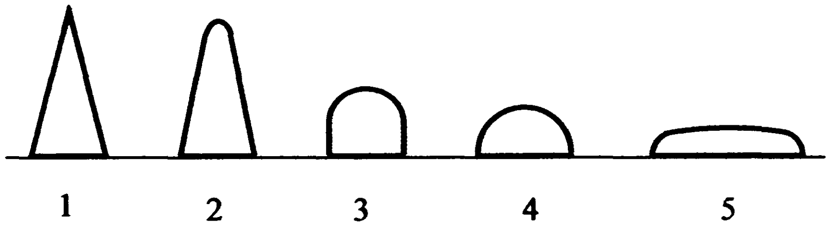

1	Cone before heating
2	IT (or ID) Initial deformation temperature (initial deformation of the cone tip)
3	ST Softening temperature (height is equal to base width)
4	HT Hemispherical temperature (height is equal to one half base width)
5	FT Fluid temperature (height is equal to one sixteenth base width)

Figure 4.1: Critical temperature points of ash [36]

These temperatures provide a convenient way to assess the effects of biomass fuels on ash behaviour. Typically, high rank coals will have a softening temperature (ST) of circa 1250 – 1300°C and a fluid temperature (FT) of around 1350 – 1450°C [11]. The ST of wood ashes is some 50°C lower at 1200 – 1250°C with a FT some 100°C lower at 1250 – 1350°C [11]. For straw and energy crops there is a larger range with ST from as low as 750°C to 1100°C and FT from around 1000°C to 1350°C [11]. Sewage sludge has a ST of around 1200°C and a FT of 1300°C [20]. When considering blends of coal and biomass, Heinzel et al [20] found that biomass blends of up to 25%$_{th}$ had very little effect on the lower critical temperatures such as initial deformation temperature (IT), however, the upper critical temperatures such as FT were greatly reduced by the addition of biomass. They suggest that "blends of coal and biomass containing high alkali contents may not influence initial deposit formation temperatures, but may promote slagging at considerably lower temperatures than in coal-only firing" [20]. They believe that fusion and slag formation is affected by the fluxing properties of the biomass components and therefore initial deformation temperatures are not affected but the formation of slag will occur at lower temperatures [20].

4.4.4 Deposition Experience in Large Scale Biomass Co-firing Tests and Facilities

Experimental data from large-scale co-firing tests and facilities seems to be heavily biased towards straw co-firing. There were numerous accounts in the literature of straw co-firing experience. Commenting on studies carried out in the 11MW stoker-fired boiler, a 80MW circulating fluidised bed boiler and the 330MW_{th} Vestkraft PF boiler, Hansen et al [23] described how the high concentrations of chlorine and potassium in straw were responsible for severe slagging and corrosion problems in stoker and fluidised bed boilers but only produced "limited fouling and slightly increased corrosion rates in pulverised-fuel fired boilers" [23]. This is supported by the findings of Frandsen [21], who suggests that potassium chloride could present a problem in grate-fired boilers but not in pulverised fuel fired boilers, but goes on to state that the amount and tenacity of deposits does increase with straw share [21]. Frandsen reported that a $10\%_{th}$ straw share yielded few or no problems whilst $20\%_{th}$ presented high problems, suggesting that at low straw shares, the effects of the straw ash were dominated by the coal ash, however, at higher straw shares, large incompletely burnt straw particles could cause slagging at lower temperatures due to the lower melting point of straw ash [21].

These findings are supported by Andersen et al [68], who, following their studies at the 150MW_e Studstrup power station, state that "deposit amount and tenacity increased with increased exposure time, increased straw share and increased flue gas temperature" [68]. They also observed that during the $20\%_{th}$ trial, deposition in the secondary superheater and reheater was higher than in the $10\%_{th}$ test. However, during both the $10\%_{th}$ and $20\%_{th}$ trials, platen superheater deposits remained unchanged. They also observed a hard plate like formation of slag in the burner region during the $10\%_{th}$ test which was absent when firing a $20\%_{th}$ straw share [68]. This suggests that the deposition problems are displaced further along the gas stream as straw share is increased.

Sondreal et al [10] also reported increased deposition when co-firing 20%$_{th}$ straw with bituminous coal in Denmark, and that co-combustion was suspended owing to technical problems including ash deposition problems and ash saleability problems where the maximum UBC in ash for the concrete industry was exceeded. They state that the "ash deposits from straw co-firing are characterised by high levels of potassium aluminosilicates and small amounts of K_2SO_4" [10]. They also report on a 20%$_{th}$ co-firing test in Illinois, where computer controlled scanning electron microscopy (CCSEM) revealed an ash "characterised by low viscosity liquid phases enriched in potassium-iron aluminosilicates" [10]. They report that potassium enrichment at lower temperatures indicates that it was condensed from the vapour phase onto particle surfaces either as a sulphate or a chloride [10], consistent with the vapour deposition mechanism highlighted in Chapter 2.

Sami et al [7] report that no adverse effects were observed during the co-firing of switch grass in a 40MW boiler whilst Savolainen [15] reported no adverse effects on slagging and fouling during sawdust co-firing of up to 25% by mass. During their work at the 138MW$_e$ unit 2 and 190MW$_e$ unit 3 at the Shawville power station, Prinzing and Hunt [25] observed that the mills and feeders were the limiting factor when co-firing up to 3%$_{wt}$ sawdust, suggesting that deposition problems were a secondary factor. Skrifvars et al [69] found an ash enriched with alkali, sulphur and chlorine in their wood firing tests, meanwhile, Steenari and Lindqvist [18] state that phosphorous in pure coal ash is less than 1% but this rises to ca. 4% when wood is co-fired at 70% in a 30MW circulating fluidised bed (CFB) boiler at 35 – 40% load. They state that this is due the fact that wood ash can be as much as 9% phosphorous whilst the ash of coal contains only 0.8% [18].

Following their investigations of sewage sludge co-combustion, Gerhardt et al [12] and Nadziakiewicz and Koziol [19] noted the increased amounts of harmful trace metals such as mercury, selenium and arsenic being released into the atmosphere with the combustion gases. Meanwhile other trace elements such as lead, cadmium, zinc, chromium and barium, among others, are retained in the solid residue which can affect its saleability and, therefore, limits the amount of sludge that can be used [19].

Gerhardt et al discovered that the fusion temperatures of ash when co-firing sewage sludge dropped by some 85°C, promoting the earlier formation of slag [12].

Following work at the 315MW$_{th}$ Naantali combined heat and power (CHP) plant, Savolainen [15] claims that the unburned carbon in the ash increases as the wood share increases. Savolainen found that by increasing the wood share form 25%$_{vol}$ to 33%$_{vol}$, the UBC increased by 1% [15]. As stated earlier, if this value rises above 5%, the marketability of the ash can be reduced.

4.4.5 Corrosion Experience in Large Scale Biomass Co-firing Tests and Facilities

The majority of the literature concerning corrosion experience is related to the co-firing of coal and straw. Sondreal et al [10] reported that during 20% straw co firing, in regions of the boiler where heat transfer surface temperatures exceeded 580°C, high temperature corrosion by sulphates was seen, however, none was seen during the 10% straw co-firing tests [10]. Frandsen [21] supports these findings, reporting that during 10%$_{th}$ straw co-firing at the 330MW$_{e}$ Vestkraft plant no increase in corrosion was seen. He states that the majority of the potassium in the ash was found to be insoluble in water and was, therefore, assumed to be in the form of potassium aluminosilicates [21]. However, he goes on to state that "straw fired boilers suffer extensive high temperature corrosion problems and as a result steam temperatures of less than 500°C are used to alleviate the problem" [21]. Hansen et al [23] state that no difference was observed between the corrosion test materials during 10%$_{th}$ straw co-firing and pure coal firing; suggesting that corrosion therefore occurs by the same mechanism [23]. However, they did indicate that the corrosion rate increased by 50% during the straw co-firing [23]. They suggest the reason for this is that the increased share of potassium in the straw ash is more readily volatilised which allows a higher rate of formation of harmful alkali-iron trisulphates which attack the metal surface [23].

4.5 Fuel Handling, Grindability and Size Distribution of Biomass Fuels

Power station managers are not only presented with problems inside their combustion equipment; careful consideration has to be given to the effect of biomass co-firing on external fuel handling and storage systems. Size distributions of biomass fuels can vary, Hein and Bemtgen [11] suggest that wood needs to be milled to less than 1mm to burn satisfactorily within the residence times of a modern PF boiler. Savolainen

[15] supports this saying that the critical particle size for wood is 1mm but states that with modern burners, particle sizes of 100%<8mm and 30-40%<1mm can be accepted [15]. Sewage sludge can be milled as coal and will therefore attain a similar size distribution to that of coal (mean particle diameter of 30μm) [12, 15]. However, straw can be up to 20 cm long and still achieve complete combustion in some larger PF-fired plants [15].

Typically, when firing biomass, higher fuel feed rates will be required due to the lower calorific value of biomass fuels [7, 25]. Prinzing and Hunt [25] state that 1m^3 of coal is equivalent to 5m^3 of sawdust 7m^3 of ROW and 10m^3 of SRWC (short rotation woody crop). This will impact on several aspects of the fuel delivery system. Firstly, larger storage areas will be required, fuel conveyor capacity may need to be increased as blocking and clogging may occur exacerbated by the higher moisture content of biomass [8] and fuel mill capacity may be exceeded.

There are indeed several documented instances where the fuel mills have been the limiting factor that controls the maximum share of biomass fuel that can be fired [15, 25]. Sondreal et al [10] state that the maximum fraction of biomass that can be fed through coal pulverisers before a separate fuel feed is required is 4%$_{wt}$. This compares to 5-8% quoted by Bain et al [6] specifically for wood firing. Bain also goes on to suggest that the maximum feasible wood share for PF combustion is 15% and that wood shares higher than this are only suitable for fluidised bed combustion [6]. Savolainen [15] supports this, stating that above 16%$_{wt}$ wood share the mill drying capacity was inadequate and that at 25%$_{wt}$ sawdust the boiler capacity was reduced to 75% due to the limitations of the mills [15].

There are several reasons for these limitations. Firstly it could be that the mill feeders are incapable of coping with the increased volume of fuel required to meet the desired thermal capacity [15, 25]. Prinzing and Hunt [25] found that during trials at the Shawville plant, Unit 2, which is equipped with ball mills and table feeders, was limited by the feeder capacity. During 3% wood co-firing trials, whilst the mills had no difficulty attaining the correct grind (80% through a 200μm mesh), the feeder was running at 119% capacity [25]. This rose to 130% capacity when using ROW clippings [25]. Meanwhile, in unit 3, which is equipped with paddle feeders, feeder speed was not a problem however operators struggled to maintain the required mill outlet temperatures of 66 to 71°C, resulting in a forced reduction in capacity of 3MW (1.6%) when firing $3\%_{wt}$ sawdust and up to 15MW (8%) when co-firing ROW [25]. This problem occurs because the mills act as a dryer for the fuel before entering the boiler, the increased mass of fuel due to the lower calorific value of wood plus the additional moisture in the wood requires a greater heat input to remove the moisture. This means that more hot air needs to be fed into the pulveriser, increasing the internal pressure. To prevent damage to bearings and surrounding machinery by 'puffing' of the fuel, the pulverisers are run at a slight negative pressure, therefore, the mill pressure cannot exceed atmospheric. This means that if mill pressure is too high and temperature is still too low, then the only recourse is to decrease the fuel feed rate and hence the boiler output [25].

In addition to feeder and thermal limitations, the coal grind can be affected by feeding biomass and coal through the same mills. Savolainen [15] states that when grinding wood (sawdust) within the coal mills, coal fineness remains relatively un-affected by wood shares of up to $25\%_{vol}$ ($2.5\%_{th}$) but at shares greater than this the coarsening of the coal grind becomes significant. This can be explained by the relative difficulty of grinding wood compared to coal. The Hardgrove gindability index (HGI) value of a material is a measure of how easily it can be ground; the higher the value, the easier the material is to grind. Coal has a HGI value of around 80 whilst wood has a HGI of only 1 or 2, this means that by adding as little as $3\%_{wt}$ wood can reduce the HGI value of the overall fuel by up to 6 points [25].

The higher volatile matter content of biomass fuels can also present problems to powerstation managers. These manifest themselves as fires and smoke in the fuel handling system [8]. They are particularly prevalent in cases of wood co-firing where sawdust is flattened into flakes in the mills [15]. When these flakes come into contact with the hot primary air in the windbox they begin to smoke and can even ignite in extreme cases [15]. The lower flash point of sewage sludge also poses an increased risk of explosion over coal in the fuel handling system and mills [12]. For fuels such as sewage sludge it is also important to consider the storage and conveyance implications posed by such a fuel. It is possible that odour and dust may need to be contained and that special storage bunkers and covered/sealed conveyors may be required [12].

Many of the above problems can be solved by implementing separate fuel feed systems, Sami et al [7] state that whilst joint feed lines increase the risk of blockage, they give excellent fuel mixing resulting in higher efficiencies and lower emissions. However, they also state that using separate feed lines, but firing through a single burner, can produce yet higher efficiencies and further reduce emissions but at the expense of potential damage to burner swirl vanes as one fuel must be fired through the secondary air inlet [7]. He concedes that using completely separate fuel supply systems will allow greater degrees of substitution but fuel mixing will be compromised resulting in lower efficiencies and increased emissions [7]. Sami et al estimate the cost per kW of retro-fitting a joint fuel supply system to an existing boiler of \$40 – \$50 per kW of power generated by the biomass, whilst to fit an entirely new biomass fuel supply system this cost rises to ca. \$175 - \$200 [7]. A powerstation manager must weigh up the perceived fuel cost savings of higher levels of substitution against the cost incurred through fitting a separate fuel supply system for the biomass fuel.

4.6 The Effect of Co-firing Biomass Fuel on Gaseous Emissions

The emissions of NO_x and SO_x can be reduced by up to 20% during most biomass co-firing techniques [5, 7, 8]. NO_x emissions are reduced by two factors. Firstly, many biomass fuels contain less nitrogen than coal, so the amount of NO_x created by oxidation of fuel nitrogen is reduced, secondly, less atmospheric nitrogen, introduced with the combustion air, is oxidised due to the staging effect of the earlier volatile release and burnout during biomass combustion, caused by its lower activation energy [10, 14]. The enveloping flame acts as a shroud by consuming oxygen, preventing it from reaching the char particle and nitrogen gas [7]. This effect can be countered if the high volatile burnout leads to a concentrated temperature peak thus, increasing the quantity of thermal NO_x produced [7]. Sami et al [7] reported on work by Aerts et al that saw this type of NO_x reduction during trials with switch-grass in a 50MW pulverised coal-fired boiler, resulting in a 20% reduction when co-firing $10\%_{th}$ switch-grass. They conclude that this is principally because of the lower nitrogen content of the biomass fuel (60% less by weight and 13% less by heat) [7]. They also report on work by Cristensen and Jespersen who documented a 20% NO_x reduction with $22\%_{wt}$ biomass share in straw co-firing trials [7].

Sami et al also suggested that burner configuration was important in reducing the quantities of NO_x produced. They suggest that by firing the biomass fuel through the centre of the burner with the coal entrained in secondary air, fed through an annular orifice around the outside, NO_x emissions can be reduced [7]. This occurs as the coal, containing more nitrogen is pushed into an oxygen lean zone by the biomass fuel, inhibiting the formation of NO [7]. SO_x emissions are lower in most biomass co-firing systems simply due to the lower fuel sulphur content [11, 15]. This is aided by the higher alkali content which retains the sulphur in the ash in the form of alkali sulphates and tri-sulphates [11]. Emissions of CO and CO_2, in relation to heat release, are similar to that of lignite [10] and therefore, compare favourably against bituminous coal.

Waste fuels such as sewage sludge and RDF usually contain similar or higher amounts of fuel nitrogen and sulphur [8, 11, 17, 19]. Sewage sludge in particular has high nitrogen content at up to 5% of the fuel [14], with sulphur at around 1%, comparable to that of coal. As a result of this, it is likely that NO_x emissions will increase during sewage sludge firing [8, 17, 19]. SO_x emissions will only increase slightly due to the larger quantity of fuel required per unit heat stemming from the lower calorific value of the sewage sludge [8]. Gerhardt et al support this stating that the input of nitrogen can be up to 8 times higher and the input of sulphur up to 3.6 times higher for every megajoule of heat produced by sewage sludge rather than coal [12]. These effects can be reduced by using air and fuel staging [11] however, the powerstation manager would need to weigh up the cost of retrofitting these staging systems and improving the NO_x and SO_x scrubbers with the perceived benefits of firing the sewage sludge.

4.7 Summary.

Given the diverse nature of biomass and waste derived fuels, there are a great number of factors that a powerstation manager must consider before going ahead with a biomass co-firing scheme. Principal concerns he must face are; whether the co-firing scheme is going to result in damage or failure of the boiler and heat transfer systems, the cost of modifications that may be needed to the boiler and ancillary plant to facilitate the proposed scheme and finally, any environmental and legislative issues that may arise from the use of biomass or waste fuels within the boiler.

The combustion characteristics and the effect they will have on the regime inside the boiler are one of the most important factors for a boiler operator to consider. The earlier and more extensive devolatilisation phenomena encountered with biomass fuels can cause early ignition, this presents the threat of burner damage and flashbacks which could cause mill fires. On the other hand the increased moisture and ash content of some biomass fuels could cause delayed ignition, resulting in lower flame temperatures or flame 'blowoff' leading to loss of output. The changes encountered in the heat release profile or burning profile of the fuel could cause temperature problems and reduced efficiency due to lower temperatures in the convective section since most of the heat is released in the very early stages of biomass combustion. Contrary to this, clouding of the combustion chamber, reducing radiant heat transfer can cause elevated temperatures at the furnace exit which puts superheaters and reheaters at risk of damage through corrosion.

High levels of substitution will be required to see significant benefits from biomass co-firing. Biomass fuels in general have a lower heating value than coal and therefore higher fuel feed rates will be required; this introduces problems with the fuel storage, preparation and supply systems which will require significant financial investment to accommodate the biomass fuel supply.

It is easy to predict the repercussions of each of these factors individually, however it is when trying to assess the outcome of all of the combined factors where a powerstation manager requires assistance. This is where prediction tools can become very useful and, as can be seen in the next chapter, much work has gone into trying to produce a tool that will reliably predict these effects for a wide range of fuels and boilers.

Chapter 5 - Modelling Techniques for the Prediction of Combustion Regimes

5.1 Nomenclature

a	Constant derived from boundary conditions	(dimensionless)
A, F	Area	(m^2)
A^r	Ash content of the fuel	(dimensionless)
B	Constant (6.2x10^{-5})	(dimensionless)
$\overline{B}$	Dimensionless fuel flowrate relative to the total fuel flowrate	(dimensionless)
b	Constant derived from boundary conditions	(dimensionless)
c	Constant	(dimensionless)
C	Minimum deposition rate constant	(dimensionless)
C_a	Air factor	(dimensionless)
C_b	Burner factor	(dimensionless)
C_f	Fuel factor (no units)	
$C_{p,m}$	Concentration of molten particles	(dimensionless)
$C_{p,s}$	Concentration of solid particles	
C_{sr}	Ash removal factor	(dimensionless)
d_p	Particle diameter	(m)
e_v	Constant of restitution	(dimensionless)
f	Deposition rate	(kg/m^2/s)
f_s	Severity factor	(dimensionless)
FS	The slagging index	(K)
g_i	Gas density	(kg/m^3)
h	Height	m)
k	Constant (no units), thermal conductivity	(W/m)
l_i	Deposit thickness	(m)
$\dot{m}$	Deposition rate	(kg/m^2/s)
m_i	Mass per unit area	(kg)
$M_{l,xy}$	Mass flux of particles	(kg/s)
m_p	Mass of impacting particle	(kg)

$M_{w,xy}$	total windward mass deposited	(kg)
m_{xy}	flux of particles entering the deposition zone	(kg/s)
$\overline{N}$	Number of fragments	(dimensionless)
p	Pressure, Partial pressure	(Pa)
P	Probability	(dimensionless)
q	Heat loss	(W/m^2)
Q	Heat energy	(kJ/kg)
Q_{Lxy}	Initial leeward deposition rate	($kg/m^2/s$)
R	Empirically derived rate constant	(dimensionless)
$R_{b/a}$	The base-to-acid ratio	(dimensionless)
R_{TS}	The slagging factor	(K)
R_{90}	Dust fineness	(dimensionless)
SR	The silica ratio	(dimensionless)
T	Temperature	(K)
t_n	Timestep	(s)
u^i_p	Velocity of the impacting particle	(m/s)
V	Gas velocity	(m/s)
V^c	Volatile content of the fuel	(dimensionless)
V_l, V_s	Volume	(m^3)
w	Gas velocity	(m/s)
x	Thickness	(m)
α	Air ratio (excess)	(dimensionless)
β	Angle of impact	(degrees),
β	fraction of fuel burned	(dimensionless)
β_i	Mass transfer coefficient	(dimensionless)
β_j	Burnout rate	(kg/s)
δ_p	Thickness of the sticky layer on the particle	(m)
$\delta\alpha$	Excess air ratio	(dimensionless)
ε	Emissivity	(dimensionless)
ε_A	Angle factor	(dimensionless)
ε_I	Impact efficiency	(dimensionless)
ε_S	Sticking probability	(dimensionless)
η	Viscosity	(Pa s)

μ	Coefficient of friction	(dimensionless)
ξ	Sticking Probability	(dimensionless)
ρ, ρ_p	Density	(kg/m^3)
σ	Stefan-Boltzmann constant	(dimensionless)
Φ	Deposit porosity	(dimensionless)
χ	Surface Tension	(N/m)
Ψ	Coefficient of thermal efficiency	(dimensionless)

5.2 Introduction

There are four main techniques that a powerstation manager can use for predicting the effect a change in fuel type will have on the operation of a pulverised fuel fired boiler. These are; the use of empirical indices derived form operator experience, in situ measurements in Bench, pilot and full scale combustion facilities, the use of computational fluid dynamics (CFD) to predict combustion and flow regimes and the development of bespoke prediction tools unique to a particular boiler, usually derived from experimental data, scale up from laboratory tests or the result of numerical analysis.

5.3 Empirical Predictive Indices

Empirical predictive indices have been used to predict ash behaviour and deposition tendencies for many years and have provided the basis of the majority of boiler designs. They are based upon experience of a wide range of coals in a number of different boilers, and are still one of the most secure bases for decision making, particularly if used in conjunction with pilot scale testing [28]. Many indices utilise laboratory ash chemistry and combustion intensity to assess the deposit forming potential of a fuel. Presented below is an outline of some of the major predictive indices.

5.3.1 The Base/ Acid Ratio ($R_{b/a}$) [30]

The base/acid ratio is most suited to lignitic ash (%CaO + %MgO > %Fe_2O_3) and is defined on a weight basis where the ash composition is normalised on a sulphate free basis.

$$R_{b/a} = \frac{Fe_2O_3 + CaO + MgO + K_2O + Na_2O}{SiO_2 + Al_2O_3 + TiO_2} \qquad (5.1)$$

The higher $R_{b/a}$, the greater the tendency of the fuel towards deposition problems since increases in the basic oxide components on the top of the formula will result in a higher $R_{b/a}$, and hence, more slagging. The following limits can be applied to the base / acid ratio:

<0.5	Low slagging propensity
0.5 – 1.0	Will begin to encounter slagging problems
1.0 – 1.75	Severe slagging problems will be encountered

This model can be adapted to account for the importance of FeS_2 in the slagging process by multiplying the product by the total sulphur in the fuel expressed as a weight %. This is known as the slagging factor and is denoted R_s, it is more suited to bituminous coal ash (%CaO + %MgO < %Fe_2O_3) and is defined by the following limits [36]:

<0.5	Low slagging propensity
0.6 – 2.0	Medium slagging propensity
2.0 – 2.6	High slagging propensity
>2.6	Severe slagging propensity

5.3.2 The Silica Ratio (*SR*) [30]

The content of iron and calcium is believed to strongly influence the slagging propensity of a fuel [30]; the silica ratio is a good way of assessing this.

$$SR = \frac{SiO_2}{SiO_2 + Fe_2O_3 + CaO + MgO} \qquad (5.2)$$

As the iron and calcium contents are decreased, the ratio tends to 1; therefore, a lower value will indicate an increased tendency towards slagging. The following limits determine the severity of the slagging problem [30].

0.50 – 0.65	High slagging
0.65 – 0.72	Some slagging
0.72 – 0.80	No slagging

5.3.3 The Iron / Calcium Ratio [36]

This is simply the ratio of Fe_2O_3 content to CaO content in the fuel expressed as weight %. Values below 0.31 and above 3.0 will give a low tendency towards slagging. A fuel yielding a value in the range 0.31 – 3.0 will present medium to severe slagging deposits [36].

5.3.4 Other Indices Based on Ash Chemistry

Sodium content can be used to assess fouling potential. Skorupska [36] states that for lignitic ash a value of <2.0 will present low fouling, 2.0 – 6.0 will present medium fouling and >6.0 will give high to severe fouling. For bituminous ash, a value of <0.5 will give low fouling, 0.5 – 1.0 will give medium fouling and >1.0 will present high to severe fouling [36]. The total alkaline metal content can also be used in this way, the sum of the Na_2O and K_2O contents expressed as a percentage will yield a value of <0.3 for a fuel with low fouling potential, 0.3 – 0.4 for medium fouling potential and >0.4 for high to severe fouling potential [36].

5.3.5 The Slagging Index (*FS*) [30]

This index is based upon the initial deformation temperature (IT) and the hemispherical temperature (HT) and is defined as follows:

$$FS = \frac{4(IDT) + HT}{5} \quad \text{(Units of °C or K)} \qquad (5.3)$$

Here, the lower the value of *FS*, the higher the threat of slagging and fouling. This index has the following limits for bituminous coal:

<1325	Severe slagging
1325 – 1504	High slagging
1505 – 1615	Medium slagging

5.3.6 Ash Viscosity

There are several indices that use ash viscosity as an indicator of slagging potential. The simplest of these is the T_{250} of the ash; this is simply the temperature at which the ash has a viscosity of 250 poise (25 Ns/m^2) [36].

The model has the following limits:

<1204	Severe slagging
1246 – 1121	High slagging
1399 – 1149	Medium slagging
>1302	Low slagging

The second is the viscosity slagging factor as described by Bott [30], here, the temperatures at which the ash viscosity is 25, 200 and 1000 Ns/m^2 are calculated and used in the following formula to calculate the viscosity slagging factor (R_{TS}):

$$R_{TS} = \frac{T_{25} - T_{1000}}{9.75 \times f_s} \qquad (5.4)$$

Where, T_{25} and T_{1000} are the temperatures at which the coal ash acquires a viscosity of 25 and 1000 Ns/m^2 and f_s is the severity factor depending upon the T_{200} at which the ash has a viscosity of 200 Ns/m^2 shown in table 5.1

Table 5.1: Severity factors f_s for R_{TS}

T_{200} / °C	f_s
1000	0.9
1100	1.3
1200	2.0
1300	3.1
1400	4.7
1500	7.1
1600	11.4

The required temperatures can be found using the following correlation:

$$T = \left(\frac{10^7 m}{\log \eta - c} \right)^{\frac{1}{2}} + 150 \qquad (5.5)$$

Where:

$m = 0.00835SiO_2 + 0.00601Al_2O_3 - 0.109$,

$c = 0.0415SiO_2 + 0.0192Al_2O_3 + 0.0276Fe_2O_3 + 0.0160CaO - 3.92$

and η is the required viscosity. The slagging propensity in terms of R_{TS} is given below:

<0.5	Low slagging propensity
0.1 – 1.0	Medium slagging propensity
1.0 – 2.0	High slagging propensity
>2.0	Severe slagging propensity

This index relies upon the assumption that at the specified temperature, the coal ash is completely fluid, which is not always the case in practice [30].

It is important to note that each of these indices has its own limitations and can only be used to give an indication of the potential of a fuel for slagging and fouling and therefore, should be used with caution [30]. This is particularly important for fuels where little is known of their performance characteristics; fuels such as biomass and waste derived fuels.

5.4 Computational Fluid Dynamics (CFD)

In order to gain a more detailed view of the effects a particular fuel may have on the combustion regime within a boiler, powerstation managers can turn to computational fluid dynamics (CFD) to provide the answer. CFD requires the discretisation of the boiler geometry into a number of control volumes, known as a mesh, across which time averaged conservation equations for the gas phase are numerically solved in a Eulerian fashion by an iterative process, whilst the particle phase is solved against the Lagrangian frame of reference [70, 71]. A greater the number of control volumes for a particular model will produce a more detailed solution; however a larger number of control volumes will require the solution of more equations which increases the run time of the model, leading to a trade off between detail and solution time. Below are some examples of how CFD can be used to simulate combustion.

5.4.1 Combustion Simulation Using CFD Codes

An example of how the greater detail produced by a CFD model can be beneficial to a boiler operator is highlighted in work carried out by Vanormelingen et al using the FLUENT CFD code [72]. Whilst analysing the 230MW$_e$ Langerlo boiler to assess the influence of co-firing secondary fuels (cheaper coals, petroleum cokes, sludges etc) on the overall combustion performance [72], they were able to identify individual burners which were causing emissions problems. In this instance, a number of burners were firing as a jet burner, mainly due to a high core air momentum, this was leading to the destruction of the inner recirculation zone where NO_X formation is suppressed leading to high NO_x production rates [72]. Optimisation of the core air momentum could lead to a decrease in NO_x emissions at the furnace exit and hence a financial saving in de-NO_x costs [72]. It is also noted in the work that the oxygen and unburned carbon profiles were predicted in good agreement with values observed in the field [72]. Instances of CFD simulation of full scale powerstation boilers in the literature are few due to the size of the mesh required to provide a detailed solution.

Gera et al [70] have used modified char oxidation sub-models, derived from experimental data, to simulate biomass combustion in smaller boilers. These models were able to predict, with good accuracy, the level of unburned carbon (UBC) loss and UBC in ash in a 30 kW downfired boiler as well as temperature and NO_x in a 150 kW pilot scale furnace [70]. With these models they were able to confirm the 'fireball' effect of high volatile yield in biomass combustion as well as decreased UBC in ash as biomass share is increased [70].

Sheng et al [71] have also modelled a 150kW pilot scale furnace. They have used a two mixture fraction probability density function (PDF) approach to track two different coal streams within the furnace to assess the effects of coal blends [71]. They have compared this to a single mixture fraction approach with weighted average properties of the component fuels [71]. Their findings were that the two mixture fraction approach was able to predict the non-additive effects of the properties of the different fuels where the single mixture fraction approach failed [71]. Blackreedy et al [73] have achieved a similar result by tracking pine sawdust and coal separately using a species transport type approach, allowing them to define separate devolatilisation and combustion models for both the coal and the sawdust streams. This approach can account for the greater volatile release during the early stages of biomass combustion since the kinetic rates of the combustion reactions can be set manually [73]. This type of model also allows for tracking of the coal and biomass streams separately in the discrete phase, allowing the effect of the larger (750μm) biomass particles on overall burnout to be assessed [73].

Kurose et al [74] have used a CFD code to investigate the effects of fuel moisture content on flame temperature and flue gas composition. They discovered that as moisture content increases, flame temperature and NO_x concentration decrease whilst O_2 concentration increases in the near-burner region [74]. In other work Kurose has used a CFD code to model an advanced low-NO_x burner [75]. Using this model Kurose was able to identify a high temperature recirculation zone near the burner outlet where coal particles are trapped for some time, promoting volatile release and advancing char combustion [75]. Kurose states that this leads to oxygen depletion in the hottest region, limiting the formation of thermal NO_x [75]. Kær et al have used a stand-alone CFD code to model the gas temperatures and species concentrations of a straw-fired grate boiler. They were able to gain good agreement with experimental results form the 33MW Masnedø plant in Denmark [76].

Kurniawan, [77], Scribano [78] and Carrieri [79] at Cardiff University have produced simulations of pilot and bench scale furnaces for the Powerflam projects. Carrieri was able to validate his results against experimental data taken as part of the Powerflam project and found that the CFD software was able to predict temperatures within the ENEL 500kW down-fired pilot scale furnace to within 75°C, and chemical composition of the combustion gases was also predicted with a good degree of accuracy [79].

Another focus for CFD work is the development of sub-models and sub-routines to improve prediction in specific aspects of combustion. Within the remit of the

Powerflam project Svensson [80] and Kurniawan [77] have produced sub-models to improve particle fragmentation modelling. Both Kurniawan and Svensson's models utilised a particle scalar update macro to interrupt the discrete (particle) phase iteration at each timestep. The models used the following equation (5.6) to calculate the number of fragments formed, based on changes in the mass of the particle stream caused by the degree of burning and devolatilisation:

$$\overline{N} = a + b(\overline{\mu} + k) + c\frac{1}{(\overline{\mu} + k)} \tag{5.6}$$

Where $\overline{N}$ is the number of fragments, a and b are constants derived from the boundary conditions, c and k are constants and $\overline{\mu}$ is the mass ratio (current mass divided by initial mass).

The number of particles flowing per second in a particle stream is known as its strength, as fragmentation occurs, the number of particles and hence the strength of the stream increases [80]. At a given timestep (t_n), the model will calculate the number of fragments based on particle mass. During the fragmentation step, the mass of the particle stream is set as its current mass multiplied by the ratio of the number of fragments in the last time step to that in the current timestep (t_{n-1}/t_n), which will always be <1, therefore, the mass decreases. Since the mass flowrate is kept constant during the fragmentation step, the code automatically increases the strength of the particle stream to compensate for the reduction in mass, giving the fragmentation [80]. Svensson showed that using this model peak magnitude of char reaction was some 8 times higher than without whilst peak temperatures increased by some 27% [80]. Using a more advanced version of this model, Kurniawan has successfully modelled particle fragmentation in a cement kiln [77].

5.4.2 Deposition Simulation Using CFD Codes

Wang and Harb [81] have derived a technique whereby they apply a succession of models to a converged combustion simulation to simulate particle deposition within the 85 MW_e Goudey boiler. Following successful convergence of the combustion simulation using the PCGC-3 code, a statistical particle cloud model was used to assess particle impaction rates [81]. The particle cloud model divides the particle stream into 300 'computational parcels', which were assumed to contain particles with identical properties, once the mean location of the particle cloud contacts the boiler wall, the entire parcel is assumed to have impacted [81]. This approach allowed them to reduce the simulation time from several months for individual particle tracking to several days [81]. Once the particle rates were established, a second model was used to calculate the particle sticking probability for a representative number of particles. This model used the impaction rates along with physical characteristics (viscosity) of both the approaching particle and the deposition surface to determine whether the particle sticks or not [81]. In order to save on computation time, they did this at 150 locations within the boiler and used linear interpolation to determine deposition at areas in between [81]. Due to the fact that deposition affects the combustion regime, after prolonged deposition the initial converged combustion solution became invalid and therefore, the simulations were repeated in an iterative process until a "quasi semi-state" was reached [81]. Using this approach they were able to accurately predict deposit growth on a deposition panel in a pilot scale furnace but were unable to validate their findings in the full-scale utility boiler due to lack of deposit information.

Lee et al [47] have also developed a deposition model for use with CFD, however, they have adopted a different approach for their work, using the local area around a single heat exchanger tube for their computational domain. The smaller size of the domain has allowed them to use individual particle tracking to assess particle trajectories. Their work comprised a very detailed consideration of particle impact dynamics and physical state during impact which may make the model difficult to apply to a full scale boiler. They developed a model which predicted particle sticking probability (ξ) based upon particle viscosity, surface tension, impact angle and impact velocity [47]. The basis of the model was that a sticky layer of sodium sulphate formed on the particle surface. The thickness of this sticky layer was also considered along with the possibility of multiple impacts by a single particle incident upon a rough surface [47]. They were able to validate the model, which is defined in equation (5.7), using experimental data [47].

$$\xi = \frac{2\chi A}{\frac{1}{2}m_p\left\{e_v u_p^i\left(1-\frac{12\rho_{Na_2SO_4}\delta_p^2\sin^2\beta\left(1+\frac{\mu}{\tan\beta}\right)}{\rho_p d_p^2}\right)^{\frac{1}{2}}\right\}^2} \qquad (5.7)$$

Where χ is the surface tension of sodium sulphate, A is the contact area between the particle and the surface, m_p is the mass of the impacting particle, e_v is a constant of restitution for the velocity, u^i_p is the velocity of the impacting particle, ρ and ρ_p are the density of sodium sulphate and the particle respectively, δ_p is the thickness of the sticky layer on the particle, β is the angle of impact, μ is the coefficient of friction between the particle and the deposit surface and d_p is the diameter of the impacting particle [47].

Fan et al [82] have employed a particle impaction model as a post processor. Using this model, they have been able to evaluate how turbulent velocity fluctuations in the gas phase influence particle trajectories. They have modeled particle capture efficiency as a function of particle temperature and sticking probability, which is in turn defined as a function of particle viscosity [82]. This is a more simplistic approach to particle sticking than those described above, however, once particle sticking is determined, Fan goes on to model deposit growth and structure [82]. Crucial factors in determining this are deposit porosity (Φ), deposit thickness, (l_i), fluidity and thermal conductivity, of which, porosity and thickness are considered to be critical [82]:

$$\Phi = 1 - \left[(1-\Phi_0) + \frac{V_l}{V_s}(1-\Phi_0)\right] \qquad (5.8)$$

Where Φ_0 is the initial deposit porosity, V_l is the volume of the liquid fraction and V_s is the volume of the solid fraction of the deposit.

$$l_i = \frac{m_i}{\left[\rho_p\left(1-\Phi_i\right)\right]} \tag{5.9}$$

Where m_i is the mass per unit area, ρ_p is the solid particle density and Φ_i is the porosity (*i* denotes the current time step).

The model was used to predict the flow field, temperature regime, particle transport and deposit behaviour in a 300MW PF boiler [82]. A staged approach to modeling was used here also; the flow field was solved first which was then used to calculate particle trajectories, temperature and burnout histories [82], this process was iterated until the no change was observed in the flow field. Fan then applied the deposition models in a 5 step iterative process and was able to predict mass of particles, deposit porosity and deposit thickness along the centerline of the front wall of the boiler [82].

Lee and Lockwood [83] have successfully combined a CFD simulation with experimental data to predict the slagging potential of three UK coals. In a similar approach to those of Lee and Fan, the model first solves the flow field and temperature and momentum equations before applying an impaction rate, sticking probability, and deposit build up model [83]. The wall conditions are re-calculated over a given time interval to reveal new deposit and wall temperatures, and deposit surface conditions, as above, the CFD simulation can be repeated in an iterative fashion to account for these changes. They stress the importance of including erosion effects in the deposit growth model which allowed them to attain reasonable agreement with experimental results from the simulated furnace [83].

Pyykönen and Jokiniemi [84] have used the FLUENT CFD code to model aerosol deposition of sodium chloride on superheater tubes, they have used two different boundary layer models; the first is a general CFD-based model and the other is a one dimensional boundary layer theory model for the stagnation point. The computational domain was localized around a single superheater platen with the boundary conditions coming from industrial experience [84]. The work is introduced as a test case, and it is stressed that in no way are they producing a predictive tool, they state that the work is an exercise to assess the feasibility of aerosol deposition models in CFD combustion simulations. The particles under consideration are so small (submicron) that inertial effects, gravity and other external forces are neglected [84]. The modeling consists of three models using three grids; the first is the solution of the boundary layer aerosol dynamics and deposition rates, the second is the simulation of deposit growth and transformation and the third is the transportation of gaseous species which assist in deposition phenomena [84]. Pyykönen and Jokiniemi stress that the solution is purely illustrative and is not representative of a particular boiler.

The modeling showed that alkali chloride deposition appears not to be influenced by tube angle with little variation between surfaces parallel and perpendicular to the flow [84]. These findings suggest that deposition has occurred by one of three mechanisms each of which can be significant depending on conditions [84]. The first mechanism is condensation of alkali chlorides onto submicron fume particles and their subsequent transportation to the tube surface by thermophoresis, secondly is the deposition of alkali chlorides by vapor diffusion and finally the homogenous nucleation of alkali chloride to form new particles which are transported to the surface by thermophoresis [84]. Pyykönen and Jokiniemi state that in PF-fired boilers, nucleation is not as important due to the higher concentration of submicron fume particles [84]. They also suggest that following a soot-blowing cycle, when the surface temperature is lowest, alkali chloride is deposited mainly in condensed form on submicron fume particles, however, they suggest as deposit surface temperatures rise, vapor diffusion becomes more significant, until the point where soot-blowing begins and the two mechanisms share equal importance [84].

The above models demonstrate the power of CFD as a predictive tool; with the range of applications spanning full scale boiler simulation to modeling individual particle impact phenomena and fragmentation. However, the examples also serve to highlight some of the main detractors from CFD as a tool for combustion simulation; principally the length of time required to run large scale models and the fact that to accurately represent pulverized coal combustion it is often necessary to deviate from the original code using user defined functions for models which simulate aspects of PF combustion not covered by the original code.

5.5 Other Modelling Techniques

There are many examples in the literature of bespoke numerical models developed for the prediction of combustion phenomena and, in particular, ash deposition. What follows is an outline of how various models within the literature tackle the problem of simulating combustion and ash deposition PF boilers.

5.5.1 Mathematical modelling

Kouprianov [85] claims that the computational time required to run comprehensive combustion and CFD models is too great for them to be a useful tool when designing new or retrofit boiler plant, suggesting an advanced zonal computational method (AZCM) instead. This model works by dividing the boiler into a series of control volumes across which the energy balance equation is calculated to give outlet temperature and heat flux for each zone [85]. An iterative technique is used for convergence of the predicted temperature at the zone outlet [85]. Each burner row is considered as a separate zone into which fuel flows at the rate B_i where i is the zone number, therefore the total fuel input B_r is:

$$B_r = \sum_{i=1}^{m} B_I \quad \text{or} \quad \sum_{i=1}^{m} \overline{B}_i = 1 \tag{5.10}$$

where $\overline{B}$ is a dimensionless fuel flowrate relative to the total fuel flowrate and m denotes the last zone with a burner input [85]. Kouprianov expresses the air that enters each zone as a fraction of the excess air ratio (α_{bi}) where i denotes the burner zone number, therefore, the total air entering a zone (α_t) is expressed as:

$$\alpha_t = \sum_{i=1}^{m} \alpha_{bi} \overline{B}_i + \sum_{j=1}^{n} \Delta\alpha_j + \Delta\alpha_f \tag{5.11}$$

Where n denotes the final zone and a_j is the tertiary air fraction, where j denotes the number of a zone where tertiary air is entered and α_f is the air leakage into the furnace [85].

Kouprianov claims that key to the model is the estimation of the burnout rate of the fuel as it passes along the furnace, given as β_j [85]:

$$\beta_j = \frac{1}{1-0.01q_4} \times \frac{\bar{h}_j}{\bar{h}_j + 0.01q_4} \qquad (5.12)$$

Where $\bar{h}_j$ is the height from the bottom plane of the first zone to the top plane of the arbitrary j^{th} zone, and q_4 is the value of heat loss due to unburned carbon [85]:

$$q_4 = 0.52C_fC_bC_{sr}\left[1.5 + C_a(\delta\alpha)^{1.2}\right]\frac{\left(A^r R_{90}\right)^{0.9}}{\left(V^c\right)^{1.5}} \qquad (5.13)$$

C_f, C_b, C_{sr}, and C_a are the fuel, burner, ash removal and air factors which are determined by the boiler and fuel type, $\delta\alpha$ is the excess air ratio, A^r is the ash content of the fuel, R_{90} is the dust fineness and V^c is the volatile content [85].

Finally, Kouprianov gives the calculation of the temperature of the 1st zone as [85]:

$$\vartheta_1'' = \frac{\beta_{b1}Q_1^r + Q_{a1} + i_1 + Q_{rg1} - (Q_6)_1}{(VC)_1''} - \frac{\sigma_0\varepsilon_{f1}\left(T_1''\right)^4}{B_r\left(VC_1\right)''}(\Psi F)_1 \qquad (5.14)$$

Where β is the fraction of fuel burned (1 denotes the first zone and b denotes burner), Q_l^r is the lower heating value of the fuel, Q_{al} is the heat introduced by the air, i_l is the sensible heat of fuel delivered into the zone, Q_{rgl} is the heat introduced by flue gas recirculation, $(Q_6)_l$ is the heat removed by bottom ash and like $(VC)_1''$, the specific heat of the flue gas, is derived based on the amount of fuel burned, σ_0 is the emissivity of the black body and ε_f is the effective emissivity of the furnace, T is the temperature, Ψ is the coefficient of thermal efficiency and F is the area of the furnace [85]. This gives the following for the *j*th zone [85]:

$$\vartheta''_j = \frac{\beta_{bj} Q_1^r + i_j + Q_{rgj} - Q_{6j}}{(VC)''_j} + \frac{(VC)''_{j-1}}{(VC)''_j} \vartheta''_{j-1} - \frac{\sigma_0 \varepsilon_{fj} (T''_j)^4}{2B_r (VC)''_j} \left[\left(\frac{T''_{j-1}}{T''_j} \right)^4 + 1 \right] \times \left[(\Psi_{av} F_w)_j + (\Psi'' - \Psi')_j F_{cs} \right] \tag{5.15}$$

where, *w* denotes walls and *cs* denotes cross-sectional [85]. Kouprianov emphasises the fact that the calculation for the *j*th zone considers the degree of burnout achieved in the previous (*j*-1th) zone [85]. The model was compared with experimental data taken from a 500MW boiler furnace, the calculation error for the model was found to be less than 2% for the burner zones and 4% for the other zones in the boiler, which equates to a temperature error of around 50°C [85].

Tomeczek et al [55] base their model on the condensation of alkali sulphates (K_2SO_4 and Na_2SO_4) onto tube surfaces using the viscosity of molten ash. They suggest that three types of deposition occur; molten particles, solid particles and condensing vapour. The following three equations were used to describe the deposition [55]:

$$\dot{m}_1 = B P_1 P_2 C_{p,m} w \qquad (5.16)$$

$$\dot{m}_2 = P_1 P_3 C_{p,s} w \qquad (5.17$$

$$\dot{m}_{d,i} = \beta_i \frac{p_i - p_{s,i}}{p} \rho_g \qquad (5.18)$$

where $\dot{m}_1$, $\dot{m}_2$ and $\dot{m}_{d,i}$ are the deposition rates of molten particles, solid particles and vapour condensed species, *i*, respectively, B is a constant ($6.2\text{x}10^{-5}$), $C_{p,m}$ and $C_{p,s}$ are the concentrations of molten and solid particles in the gas stream respectively, w is the gas velocity, p is the gas pressure, p_i is the partial pressure of gaseous component *i*, $p_{s,I}$ is the saturation pressure of gaseous component *i* at the surface temperature, β_i is the mass transfer coefficient and g_i is the density of the gas.

P_1 is the probability of a particle hitting the heat transfer surface, P_2 is the sticking probability and P_3 is the probability of a solid particle hitting a sticky surface being retained. These are defined as follows [55]:

$$P_1 = \frac{A_{duct} - A_{free}}{A_{duct}}, \quad P_2 = 0 \text{ for } T < 1450\text{K}, P_2 = 0.1 \text{ for } 1450\text{K} < T < 1800\text{K},$$

$$P_2 = 0.1 + \frac{10(T_p - T_m)}{T_m} \text{ for } 1800\text{K} < T < 1950\text{K } P_2 = 1 \text{ for } T > 1950\text{K},$$

$$P_3 = S\dot{m}_d$$

where A_{duct} is the area of the boiler duct, A_{free} is the area of the duct minus the cross-sectional area of the heat transfer tubes, T and T_p are the particle temperature, T_m is the melting temperature $\dot{m}_d$ is the deposition rate of vapour condensed species and S is and experimental value of 6.2 $(\text{kg/m}^2\text{s})^{-1}$. Tomeczek et al were able to use this model to predict the deposit build up in an industrial scale boiler over a period of nine months. They predicted large deposit formation on the leading edge of the first superheater pendant which migrated downstream as the deposit built up due to the deposit surface temperature exceeding the saturation temperature of condensing alkali sulphates [55].

Erickson et al [86] have developed a model for deposit growth based on the adhesion of sticky particles to either sticky or dry deposits, and the adhesion of non-sticky particles to a sticky deposit. Under slagging conditions, they propose the following; the fraction of sticky particles impacting the deposit surface (f) is:

$$f = \frac{A_s}{A} \tag{5.19}$$

Where A_s is the flux of sticky particles to the surface and A is the total flux of particles to the surface [86]. They suggest that if W_s is the fraction of the wall that is sticky, then the total flux of particles adhering to the wall (F_s) is given as follows:

$$F_s = A_s + \left(A - A_s\right)W_s \qquad \text{(5.20}$$

Thus the fraction of particles that adhere is given by:

$$\frac{F_s}{A} = f + \left(1 - f\right)\delta f \qquad (5.21)$$

Where δ is the fraction of A_s that is still sticky at the wall temperature [86]

They go on to state that the deposit growth cycle can only be fully described if changes in thermal properties and conditions over the deposit depth profile are considered [86]. Therefore, the heat flux (q_{dirty}) after deposit build-up is given by [86]:

$$\begin{aligned} q_{dirty} &= \varepsilon_d \sigma \left(T_{gas}^4 - T_{depositsurface}^4\right) \\ &= \left(\frac{k_d}{\Delta x_d}\right)\left(T_{depositsurface} - T_i\right) \qquad (5.22) \\ &= \left(\frac{k_i}{\Delta x_i}\right)\left(T_i - T_{tube}\right) \end{aligned}$$

Where σ is the Stefan-Boltzmann constant, ε_d is the effective emissivity, T_{gas}, $T_{deposit\ surface}$, T_i and T_{tube} are the temperatures of the gas, deposit surface, inner deposit layer and tube surface respectively, k_d is the mean thermal conductivity of the bulk deposit and Δx_d is thickness whilst k_i and Δx_i apply to the inner deposit layer [86]. Using this, they were able to account for the degradation of heat flux over time [86]. These models were applied to a 'coal quality expert' computer programme along with a more complex fouling model which used impact efficiency and sticking probability to determine deposit growth. In this model, they propose that deposition on the windward face of a heat exchanger tube is caused by inertial impaction and can be defined by equations (5.23) and (5.24) [86].

$$Q_{w,xy} = (\varepsilon_I \varepsilon_S \varepsilon_A) \times m_{xy} \qquad (5.23)$$

$$M_{w,xy} = \int_{t_0}^{t} \frac{Q_{w,xy} f_{\Delta T}}{(t+1)^n} + C \qquad (5.24)$$

Where $Q_{w,xy}$ is the initial windward deposition rate, ε_I, ε_S and ε_A are the impact efficiency, sticking probability and angle factor respectively, m_{xy} is the flux of particles entering the deposition zone, $M_{w,xy}$ is the total windward mass deposited, $f_{\Delta T}$ is the change in deposition rates due to temperature change as a result of deposition, t_0 and t are the initial and final time, n is the growth rate degradation constant (empirically derived) and C is the minimum deposition rate constant.

They also stated that deposition on the leeward face of the heat exchanger tubes was caused by small particles (<10μm) by thermophoresis and could be described by equation (5.26) [86]:

$$Q_{l,xy} = \frac{V^2}{T} RM_{l,xy} \qquad (5.26)$$

Where $Q_{l,xy}$ is the initial leeward deposition rate, $M_{l,xy}$ is the mass flux of particles <10μm, V is the gas velocity, T is the gas temperature and R is an empirically derived rate constant [86].

The slagging model was validated using experimental data from a pilot scale furnace and was able to successfully predict the change in heat flux over time as deposit build-up increased [86]. The fouling model has been validated using ash data taken from a full scale utility boiler and was found to be able to predict, to a reasonable degree of accuracy, the composition of the deposits [86].

5.5.2 Thermochemical Modelling

Another popular technique for assessing the slagging and fouling potential of fuels is the use of thermochemical software to solve thermodynamic equilibrium equations for the fuel to assess ash composition and melting points. This type of modelling is in essence a model of the fuel itself rather than a boiler, i.e. the model assesses the effects of different conditions on the chemical behaviour of the fuel rather than how the fuel behaves in a boiler under different conditions. The software works by "calculating the concentrations of chemical species when specified elements or compounds react or partially react to reach a state of chemical equilibrium" [87]. The software uses the minimisation of Gibb's free energy to do this [87]. The user can define the reactants, select the possible compound and solution products and set the final conditions (temperature, pressure etc) for the system under consideration [87].

Jak [88] has used a version of this software (F*A*C*T) to model the Al-Ca-Fe-O-Si system in order to asses the relationship between ash fusion temperature and phase equilibria of coal ash slags. Results of the model were compared to high temperature ash fusion tests [88]. The software was used to calculate multi-phase equilibria, liquidus temperatures and the proportions of solid and liquid phases in a specified atmosphere for the above system [88]. In the study, some 23 coals were used to develop correlations between liquidus temperature and ash fusion temperature, which showed excellent agreement with the predictions made by the software [88].

Jak has followed up this work using a later version of the software (FactSage) to investigate viscosity modelling [89]. The model uses a specially developed FactSage database for the Al_2O_3-CaO-FeO-Fe_2O_3-SiO_2 slag system which predicts its melting behaviour alongside a viscosity model which calculates the viscosities of completely molten (homogeneous) and part crystalline (heterogeneous) slags based upon their composition and the operating temperature [89]. The FactSage software is used to calculate the proportions of solids and the composition of the remaining liquid phase [89]. Jak states that this type of work is particularly relevant to slagging boilers; since the slag is tapped off in a molten state, it is essential that the viscosity of the slag remains low enough (5 – 25 Pa.s) that it does not freeze in the tapping system [89]. The model showed that starting from iron free slags, as FeO is added, the liquidus temperature at first decreases followed by a gradual increase [89]. This corresponds to a steady decrease in slag viscosity up to 50% FeO [89]. Jak states that as the fraction of solids in the slag increases above 20%, they become increasingly hard to tap and that in those situations this type of modelling can be very valuable [89].

Thompson and Argent [90] have used this software to assess the mobilisation of sodium and potassium from the fuel ash during combustion. In their modelling they have used the following species C, H, O, N and S from the coal and oxidant and Al, Si, Na, K, Ca, Mg, Fe, Mn, Ti, Cl and P as the major inorganic species [90]. Cooling of the combustion gases has been modelled in two ways; firstly by simulating rapid cooling with no intermediate equilibrium steps (similar to hot gas encountering a cold superheater tube) and by cooling in 10° steps with the condensed products removed at each step [90]. The results indicated that under combustion conditions, the alkalis were mobilised to a small extent, which agreed with the published data [90]. The model suggested that the alkalis present in the gas phase would begin to deposit as a salt melt at around 1100K [90]. They also suggest that variation in the mineral composition can affect partitioning between the solid and gaseous phases in a very complex manner, and as such, it is possible for mobility to be much higher than expected [90].

Turn et al [91] have used a similar process to that above to study the fouling characteristics of processed biomass. They have used a 2 step modelling system whereby an initial equilibrium calculation is performed at a higher temperature (1000 – 1500°C) to simulate the combustion zone, followed by a second at a lower temperature (500 – 800°C) to simulate the superheater region [91]. In the first calculation, element ratios based on fuel and air input are used resulting in the formation of solid, liquid and gaseous phases [91]. The gaseous products of the first calculation are then used as the input to the second calculation at the lower temperature [91]. The resulting solid phase product from the second calculation is assumed to be representative of the deposit formed in the superheater region and has been compared to samples taken using a cooled deposition probe, from tests in a coal and bagasse-fired boiler at a sugar factory in Pu'unene, Maui, Hawaii [91].

The chemical equilibrium model did not predict the formation of deposits containing Al, Si, Ti or Ca due to them not being present in the gaseous products of the first calculation; analysis of the deposit samples showed them to be depleted in Al and Si compared to the grate material, this suggests that they are deposited there as solid material carried through from the combustion zone [91]. The model was able to predict the deposition of Fe, Na, K, P and S which were present as $K_3Na(SO_4)_2$, Fe_2O_3, Na_2SO_4 and FeO_4P [91]. The model predicted sodium concentrations in the range of 9% – 15% whilst the experimental results showed 3% – 18%, predictions for potassium were in the range 26% – 42% with the deposit samples yielding 7% – 26% [91], sulphur was predicted in the range 20% – 25% with the experiment giving 17% – 18% at higher concentrations [91]. The model was also able to predict iron contents to within 5% absolute [91]. However, predictions for phosphorous were approximately one order of magnitude lower at 0.2% – 0.5% compared to 2% – 4% in the tests [91]. Turn states that this is not unreasonable considering the low concentration (<0.1%) of phosphorous in the fuels [91]. The concentration of Mg in the deposits as $MgSO_4$ and $Mg_3P_2O_8$ was also under predicted by some 2 orders of magnitude over those found in the deposits [91]. Overall, these predictions were in reasonably good agreement with the compositions of the deposit samples collected from the boiler [91]. The model shows that this type of calculation can be used to begin to predict the composition of deposits formed on superheater tubes through vapour deposition.

5.6 Summary

The models outlined in the preceding pages demonstrate many different approaches to the modelling of pulverised coal and biomass fuel combustion, each of which has its own merits and drawbacks. Empirical predictive indices are essentially a prediction of fuel behaviour rather than boiler performance, they are very simple with little data needed for input offering a quick and easily comparable answer making comparison of fuel types like for like very simple. However, they also rely on some very fundamental assumptions, and because of this, cannot always be relied upon for their accuracy; many of the indices are based upon experience with existing fuels (principally coals) and whilst they may provide reasonable results when interpolating between them, extrapolating to predict the effects of new or largely unused fuels can be potentially dangerous.

CFD codes are able to accurately predict the temperature and flow fields within PF boilers and can produce results accurate to within a few degrees Celsius. CFD models are also able to model separate fuel streams making them ideal for studying co-

combustion. With the addition of user defined sub-models they are also capable of accurately predicting particle combustion, fragmentation, burnout and deposition. However, in addition to the expertise required and time taken to prepare the simulation, as several of the authors stated, CFD models can at best take several hours or days to run and at worst weeks or even months. This makes it very difficult and time consuming to compare results between fuel types. This is compounded by the way results are presented; contour plots make direct comparison more difficult, requiring a degree of interpretation before an answer is achieved. These models are also based upon a specific boiler geometry and therefore quite detailed information regarding the size, shape, and capacity of the boiler along with fuel and air flowrates is required before the simulation can be run.

It is difficult to assess the value of bespoke models as they are often boiler specific and do not lend themselves easily to comparison. As in the examples above, they often involve complex calculations and some degree of computer processing, especially if numerical methods are utilised. They often require a considerable amount of setting up or preparation to adapt the model to the boiler concerned. Kouprianov's model [85] demonstrates this; starting from scratch with a new boiler would require a considerable amount of work to sub divide the boiler into its zones and to calculate fuel and air proportions entering through the burners. It also highlights the fact that these models often require data which may be difficult to measure or obtain, for example, Kouprianov's model uses several factors; C_f, C_b, C_{sr}, and C_a which are the fuel, burner, ash removal and air factors which all need to be calculated before the model can be used. However, the main advantage these models offer, once they have been fully developed, is that they can be almost as effective as CFD simulations but far more time efficient, offering results much more readily. Tomeczek's model [55] shows similar traits, requiring one-dimensional modelling of the gas flows within the boiler before the deposition models can be applied.

In a similar fashion to CFD simulation, these models require quite detailed knowledge of both the fuels under investigation and the boiler they will be fired in. These models are in essence boiler performance evaluators as they consider the boiler geometry and inputs in order to evaluate the thermal conditions within the boiler before applying the deposition model.

The thermochemical analysis method, like the empirical indices, moves away from the physical representation of the boiler in question and concentrates on modelling fuel behaviour based upon its chemistry. This requires detailed knowledge of the fuel composition, however, since boiler geometry is not considered, this is often the only input. This modelling technique can be approached as in Turn's work [91]; basic assumptions on the range of thermal conditions a fuel will experience within a boiler are made and the software is used to produce results in the form of a relationship which can be applied to a subsequent boiler model such as the viscosity model of Jak's work [89]. The time taken to run the software is negligible compared to CFD codes and development and set-up is minimal in comparison to bespoke or numerical modelling techniques. However, as the output of these models is usually an ash composition and a prediction of its phase, an element of interpretation will be required before the results become directly applicable to the needs of a boiler operator.

As is always the case, each of the above modelling techniques has advantages and disadvantages which become more or less prevalent as the scope of the work being carried out changes. For example the time and effort required to produce a full scale CFD simulation might be worthwhile to assess the effects of proposed structural changes to a boiler, whilst a thermochemical approach may be more appropriate if the user is interested in the effects on slag viscosity of a new fuel and the development of a boiler specific bespoke modelling tool might be considered valuable to an operator who wants to continually asses the deposition of a particular fuel ash and its effects on the thermal output of the boiler. It is this type of model that has been proposed by the PowerFlam consortium as a solution to predicting the effects of biomass co-combustion in its members' boilers. As each of the members will have different boiler configurations, they are interested in a tool that can be easily adapted for use in different boilers. Presented in subsequent chapters are the author's experiences of CFD, thermochemical and bespoke modelling techniques in an attempt to combine aspects of each to produce one such universal boiler performance prediction tool.

Chapter 6 - The Development of a Universal Prediction Tool

6.1 Nomenclature

B, b	Thermal percentage of the boiler output to be supplied by the substitute fuel	(dimensionless)
C_d	Constant	(dimensionless)
C_g	Constant	(dimensionless)
c_{pj}	Specific heat capacity of species, j	(J/kgK)
f	Mixture fraction	(dimensionless)
$\overline{f'^2}$	Mean mixture fraction variance	(dimensionless)
f_{fuel}	Mixture fraction of the fuel stream	(dimensionless)
f_{ox}	Mixture fraction of the oxidiser stream	(dimensionless)
f_{sec}	Mixture fraction of the secondary stream	(dimensionless)
G	Gibbs free energy	(kJ)
H	Specific enthalpy	(kJ/kg)
H^*	Instantaneous enthalpy	(J/kg)
h_1	Enthalpy of the water or steam as it enters the heat exchanger	(kJ/kg)
h_2	Enthalpy of the water or steam as it leaves the heat exchanger	(kJ/kg)
h_f	Enthalpy of the fluid at the saturated liquid line	(kJ/kg)
h_g	Enthalpy of the fluid at the saturated vapour line	(kJ/kg)
h^0_j	Standard state enthalpy of formulation for species j	(J/kg)
i_{ef}	Fraction of species i in the equivalent fuel	(dimensionless)
i_p	Fraction of species i in the parent fuel	(dimensionless)
i_s	Fraction of species i in the substitute fuel	(dimensionless)
k	Mass transfer coefficient	(units vary)
k	Thermal conductivity	(W/mK)
$\dot{m}$	Mass-flowrate	(kg/s)
m_{fuel}	Mass of the fuel stream	(kg)
m_j	Mass of species j	(kg)
m_{ox}	Mass of the oxidiser stream	(kg)

m_{sec}	Mass of the secondary stream	(kg)
m_{total}	Combined mass of fuel, secondary and oxidiser streams	(kg)
p_{sec}	Normalised secondary mixture fraction	(dimensionless)
Q	Heat energy	(J)
S	Specific entropy	(kJ/kgK)
S_m	Source term due to the transfer of mass into the gas phase from the reacting particles	(dimensionless)
S_{user}	Source term introduced by the user	(dimensionless)
T	Temperature	(K)
$\vec{v}$	Overall velocity vector	(m/s)
x_p	Mass fraction of parent fuel	(dimensionless)
x_s	Mass fraction of substitute fuel	(dimensionless)
ε	Turbulent dissipation rate	(m^2/s^3)
λ	Equivalence Ratio	(dimensionless)
μ_t	Turbulent viscosity	(Pa s)
ρ	Density	(kg/m^3)
σ_t,	Constant	(dimensionless)
ϕ_{i1}, ϕ_{i2}	Thermochemical scalars	(dimensionless)

6.2 Introduction

As has already been established in the preceding chapters, despite the significant greenhouse gas reductions over the past decade, the power generation sector is under significant pressure from the UK and European governments to further reduce emissions. One way the industry might look to alleviate this pressure is through the co-combustion of alternative fuels (mainly biomass and waste derived fuels) in its existing coal-fired power plants. Whilst this can produce significant reductions in harmful emissions, it poses a number of problems that need to be addressed by the boiler operator to allow the continued smooth running of the facility. Many of these problems are ash related, and key to solving them is an understanding of how the ash will behave under boiler operating conditions. In order to make these schemes financially viable, operators need to ensure that minimal modifications to combustion plant are needed and that electrical output remains unaffected whilst maintaining running costs at the existing level. This is where prediction tools can be useful;

allowing the boiler operator to make an informed decision on how and to what degree an alternative fuel can be used.

6.3 The PowerFlam Consortium

Some of these prediction techniques have been discussed in Chapter 5, where the need to develop a fast, effective and above all easy to use prediction tool was highlighted. To this end, power generators are investing in research programmes with universities and industrial research organisations in an attempt to fulfil this goal. The EU sponsored PowerFlam consortium is one such group of investors. The consortium comprises 4 industrial partners, Laborelec, Electricitie De France (EDF) and ENEL Produzione; major Belgian, French and Italian power generators along with VGB; a trade organisation for power utility companies with over 400 members. Working alongside these are three industrial research organisations; The International Flame Research Foundation Research Station (IFRF-RS), The International Flame Research Foundation (IFRF Net) and The Institute of Power Engineering (IEn) along with three universities, University of Wales, Cardiff, University of Wales Glamorgan and The Institute of Process Energy and Fuel Technology – TU Clausthal. The proposal seeks to develop an integrated package of methodologies which will allow operators of large pulverised coal fired utility boilers to increase the use of diverse biomass fuels co-fired in existing boilers, thus reducing emissions of greenhouse gases.

The work included the use of several pilot and bench scale combustion rigs and a drop tube furnace to examine the behaviour of biomass fuels under co-combustion conditions. Alongside the experimental work there is a programme of modelling and simulation, which includes the use of CFD to predict the behaviour of fuels in the experimental rigs. In addition to this, one of the requirements was to develop a prediction tool, which can be used by boiler operators to assess the effect on boiler performance when using biomass fuels in a full scale boiler. When creating the specification for the prediction tool, the industrial partners identified the following capabilities that the tool should include:

- Ease of use – The tool should be easy to use and require no training other than the instructions provided with it.

- Accessible – Anybody wanting to use the tool should be able to do so on a normal desk or lap top personal computer without the need for special software or high processing power.
- Transferable – The tool should not be specific to a particular boiler; the user should be able to quickly and easily create models for different boilers.
- Minimal input data – The tool should require the minimum of input data.
- No gas-side measurements – The tool should not rely on gas side measurements to perform its calculations due to the difficulties associated with taking them.
- Wide range of application – The tool should be capable of handling predictions for a wide range of regular and unconventional fuels.
- Simple results – Boiler operators may want to run many simulations and compare results, therefore, the results should be in a simple form that require little or no interpretation.

To try to meet these criteria, the initial proposal was a spreadsheet based system which can be run using Microsoft Excel. The spreadsheet uses a series of empirically derived relationships, calculated for a number of coals and biomass fuels covering a large range of operating conditions to predict the performance of the boiler in a number of areas, this is outlined schematically in figure 6.1:

6.4 Data Input by the User

The data required by the user for input into the spreadsheet can be divided into three main groups; fuel based data, boiler data and process control data.

6.4.1 Fuel Based Data

Fuel based data is all the information required regarding the parent and substitute fuels, including proximate, ultimate and ash analyses along with the calorific value of each of the fuels. The proximate and ultimate analyses of the fuels are entered on an as received basis as a weight percentage of the total fuel. The spreadsheet automatically normalises the entries and converts them to a dry basis as required by the correlations used to calculate fuel energy release (see Section 6.6.1).

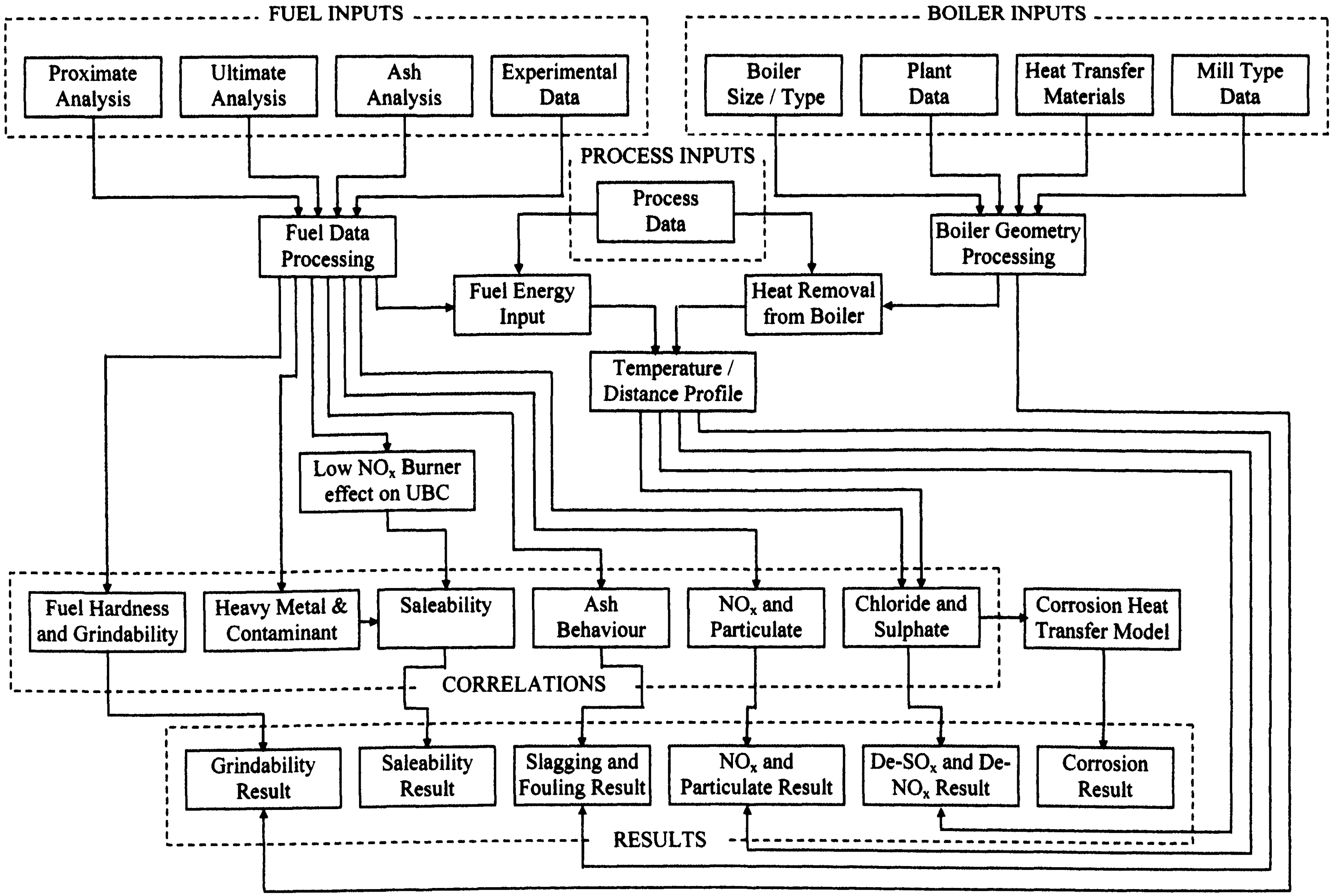

Figure 6.1: Initial prediction tool proposal for the PowerFlam Consortium.

Tables 6.1 and 6.2 are typical of those used to enter the data into the spreadsheet. The ash analysis is entered into the spreadsheet as a percentage of the total ash, these values are also normalised to ensure that the values total 100%. Table 6.3 is an example of those used to enter the ash analysis into the spreadsheet. The final fuel input is the lower calorific value of both the parent and substitute fuels.

Table 6.1: Typical proximate and ultimate analyses and LCV for a medium volatile coal used in the PowerFlam project

Proximate Analysis	As Received / $\%_{wt}$	Dry Basis / $\%_{wt}$
Moisture	4.20	-
Fixed Carbon	51.00	34.76
Volatile Content	33.30	53.24
Ash Content	11.50	12.00
Total	100.00	100.00
LCV / MJ/kg	28.860	-

Ultimate Analysis	As Received / $\%_{wt}$	Dry Basis / $\%_{wt}$
Carbon	67.23	70.18
Hydrogen	5.15	5.38
Oxygen	9.86	10.29
Nitrogen	1.31	1.37
Sulphur	0.75	0.78
Ash	11.50	12.00
Moisture	4.20	-
Total	100.00	100.00

Table 6.2: Proximate and ultimate analyses and LCV for a typical sewage sludge used in the PowerFlam project

Proximate Analysis	As Received / $\%_{wt}$	Dry Basis / $\%_{wt}$
Moisture	11.72	-
Fixed Carbon	2.75	3.12
Volatile Content	36.72	41.59
Ash Content	48.81	55.29
Total	100.00	100.00
LCV / MJ/kg	10.935	-

Ultimate Analysis	As Received / $\%_{wt}$	Dry Basis / $\%_{wt}$
Carbon	19.12	21.66
Hydrogen	4.16	4.71
Oxygen	12.77	14.47
Nitrogen	2.65	3.00
Sulphur	0.77	0.87
Ash	48.81	55.29
Moisture	11.72	-
Total	100.00	100.00

Table 6.3: Ash analyses for medium volatile coal and typical sewage sludge used in the PowerFlam project

Medium Volatile Coal	$\%_{wt}$ of total ash	Normalised	Typical Sewage Sludge	$\%_{wt}$ of total ash	Normalised
Na_2O	0.87	0.88	Na_2O	0.70	0.71
K_2O	1.47	1.48	K_2O	1.94	1.97
CaO	3.48	3.51	CaO	7.85	7.99
Al_2O_3	20.32	20.48	Al_2O_3	12.42	12.63
MgO	1.99	2.01	MgO	1.74	1.77
Fe_2O_3	7.60	7.66	Fe_2O_3	14.00	14.24
SiO_2	58.86	59.33	SiO_2	55.61	56.57
SO_3	3.21	3.24	SO_3	0.50	0.51
Mn_3O_4	0.14	0.14	Mn_3O_4	0.24	0.24
TiO_2	0.98	0.99	TiO_2	0.68	0.69
P_2O_5	0.23	0.23	P_2O_5	2.31	2.35
ZnO	0.03	0.03	ZnO	0.10	0.10
Li_2O	0.03	0.0	Li_2O	0.03	0.03
B_2O_3	0.00	0	B_2O_3	0.18	0.18
Total	99.21	100.00	Total	98.30	100.00

6.4.2 Boiler Geometry Input

Information regarding the geometry of the boiler is also required, this includes physical dimensions, the location and number of heat exchangers (superheaters, reheaters, economisers, etc) and also details of the mean tube diameter, thickness, length and number along with the type of steel used for each. For the purpose of illustration, data from the Langerlo boiler, a 618 MW_{th} wall fired pulverised coal boiler, run by the Belgian utility company, Laborlec has been used to populate figures and tables.

6.4.21 Physical Dimensions

Key physical dimensions for the boiler are entered into the spreadsheet via diagrams similar to those in figures 6.2 and 6.3. The diagram shown in figure 6.2 is used to input the overall height and width of the boiler as well as describe its basic shape. Figure 6.3 is similar to the diagram used to locate the heat exchange plant and burner rows within the boiler. The current version of the spreadsheet is set up solely for a standard wall fired pulverised fuel fired boiler with combustion chamber, top pass and down pass. Due to the 1 dimensional nature of the calculation, this can easily be adapted for tangentially fired boilers. Boiler equipment beyond the economiser stages such as air and water pre-heaters are neglected by the calculation and therefore, no provision has been made to allow the input of data concerning them.

The heat exchange equipment is identified by the user in Table 6.4. The first column of the table contains numbers corresponding to heat exchanger IDs as identified in figure 6.3. The plant names are entered into the table in the order in which they encounter the combustion gases. The entry for number 8 will always correspond to the waterwalls, leaving the remaining 7 entries to form any combination of superheaters, reheaters and economisers. The heat exchange equipment can be given any name the user desires, for the purposes of this document the convention used is as follows; heat exchangers are numbered in the order in which the process water/steam passes through them, for example, the first superheater the water/steam encounters becomes superheater 1, the second is then superheater 2.

The spreadsheet cannot accommodate any more than 7 additional heat exchangers (to the water walls) therefore, if more are required the user may have to combine some of the heat exchangers. In terms of water/ steam flow, two of these heat exchangers are upstream of the water walls as water heaters (economisers) and the remaining five must be situated downstream of the waterwalls and can form any combination of superheaters and reheaters. The spreadsheet can accommodate between one and six burner rows, these are identified automatically by the spreadsheet. Due to the one dimensional nature of the calculation, the spreadsheet does not account for the number of burners in each burner row, therefore, each burner row is treated as a single fuel entry point. The remaining cells in table 6.4, showing the position of the plant along the centreline of the boiler, are populated automatically by the spreadsheet in a process described in Section 6.5.2, the Boolean logic functions used to do this are shown in Appendix A.

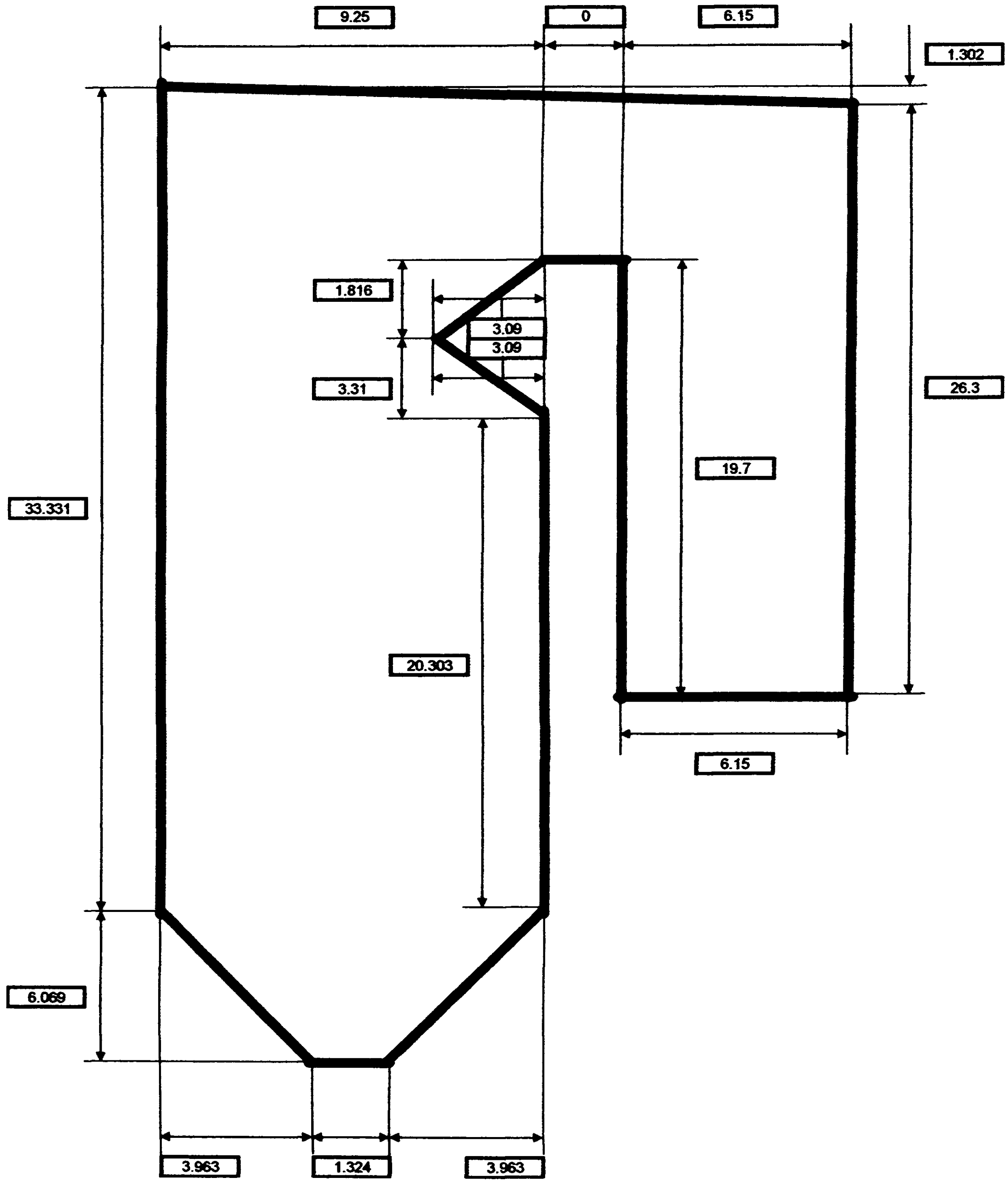

Figure 6.2: Input of general basic dimensions

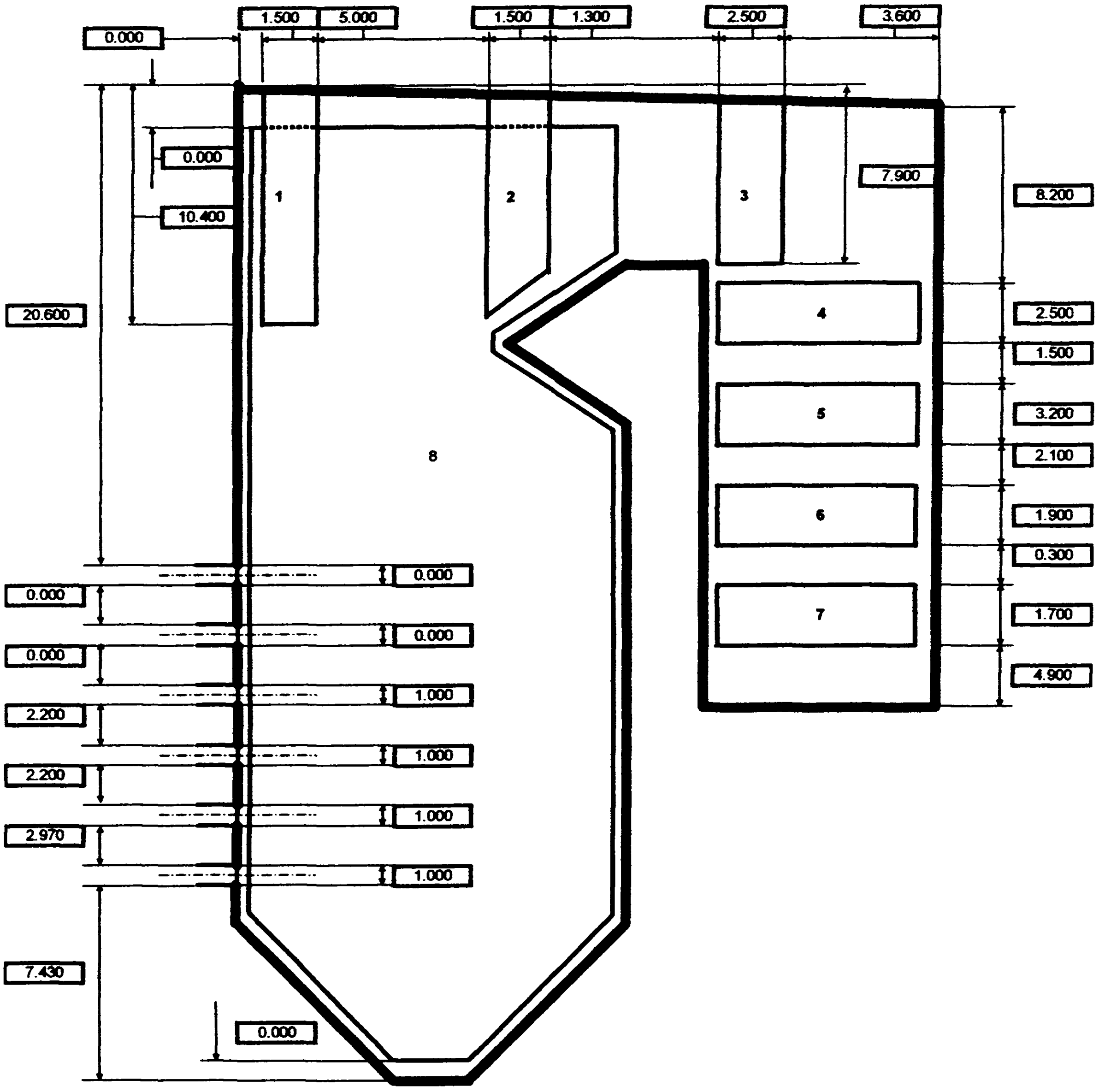

Figure 6.3: Input of plant and burner locations

Table 6.4: Identification of heat exchange plant within the boiler

Plant Number	Plant Name	Plant Start / m	Plant Finish / m
N/A	Burner Row 1	7.430	8.430
N/A	Burner Row 2	11.400	12.400
N/A	Burner Row 3	14.600	15.600
N/A	Burner Row 4	17.800	18.800
N/A	Burner Row 5	18.800	18.800
N/A	Burner Row 6	18.800	18.800
8	Water Walls	0.000	38.246
1	Superheater 2	29.272	32.409
2	Superheater 3	34.775	36.668
3	Reheater 2	38.262	39.082
4	Superheater 1	46.223	48.723
5	Reheater 1	50.223	53.423
6	Economiser 2	55.523	57.423
7	Economiser 1	57.723	59.423

Table 6.5: Geometry input of heat exchange equipment

Plant	Number o f tubes	Mean tube length / m	Mean outside tube diameter / m	Mean inside tube diameter / m	Type of steel used*
Superheater 2	28	16	0.038	0.029	B
Superheater 3	58	10	0.042	0.030	B
Reheater 2	110	8	0.051	0.042	B
Superheater 1	110	6	0.051	0.042	B
Reheater 1	110	6	0.0635	0.0515	A
Economiser 2	110	6	0.051	0.040	A
Economiser 1	110	6	0.051	0.040	A

* Steel A – Carbon steels (e.g. ST45.8) Steel B – Carbon alloy steels (e.g. 13CrMo45 or 10CrMo910)
Steel C – Stainless steel grades AISI 316, 321 & 347 Steel D – Stainless steel grade AISI 310.

Information describing the geometry of the heat exchange equipment is entered via a table similar to table 6.5 above. Only basic information is required; giving the total number of tubes, their mean length and mean internal and external diameters along with the type of steel used for their construction.

6.4.3 Process Control Data Input

The final data set required is all of the information describing the process and operation of the boiler. It is here that the user can decide the degree of substitution required by entering the percentage of overall thermal output that is to be met by the substitute fuel.

The excess air is entered as the ratio of the total air entering the boiler to the stoichiometric air requirement, known as the equivalence ratio (λ); this means that stoichiometric combustion is entered as a value of 1. Should 20% excess air be required, then a value of 1.2 would be entered. The spreadsheet presents the user with an estimate of the O_2 percentage in the flue gas to allow fine tuning of the excess air value. It is also possible to set the air preheat temperature here, in degrees Celsius. The value entered will apply to primary, secondary and tertiary air supplies and no provision is made for differentiation between streams, therefore, it may be necessary to calculate a mean air temperature to be entered here.

The user is also able to define the thermal output of the boiler at this stage by entering the fuel mass flowrate into the boiler in kg/s. If the user has specified that a blend of parent and substitute fuel is to be fired, the spreadsheet will use the calorific value of each of the fuels to calculate the mass flowrate of each whilst maintaining a constant thermal output. These mass flowrates are also displayed to the user. Table 6.6 shows the fuel flowrates and thermal output for the Langerlo boiler using a blend of $90\%_{th}$ coal and $10\%_{th}$ sewage sludge.

Table 6.6: Fuel Flowrate data for the Langerlo boiler

Coal Injected (kg/s)	21.800
Total Coal Flowrate (kg/s)	19.620
Total Substitute Fuel Flowrate (kg/s)	5.754
Equivalent Fuel Flowrate (kg/s)	25.374
Thermal Output (MW)	629.148

The proportion of fuel fired through each burner row can be defined, and is entered as the fraction of the total fuel entering the boiler in a table such as table 6.7, showing the fuel distribution between burner rows for the Langerlo boiler.

Table 6.7: Distribution of fuel between burners for the Langerlo boiler

Fuel fired in Burner Row 1 (%)	25.00
Fuel fired in Burner Row 2 (%)	25.00
Fuel fired in Burner Row 3 (%)	25.00
Fuel fired in Burner Row 4 (%)	25.00
Fuel fired in Burner Row 5 (%)	0.00
Fuel fired in Burner Row 6 (%)	0.00

It is also possible to enter, in kg/s, the mass flowrate of steam through each individual piece of heat exchange equipment, this allows the user to account for bleeding of water or steam from the system for pre-heat or other purposes.

The final set of process data required is the thermodynamic data for the water and steam. This comprises temperature and pressure data before and after each of the heat exchange stages such as that shown in table 6.8 for the Langerlo boiler.

Table 6.8: Thermodynamic data for the steam side of the Langerlo boiler.

Heat Exchanger	Temperature Before (°C)	Temperature After (°C)	Pressure Before (bar)	Pressure After (bar)
Economiser 1	236.00	265.00	136.00	134.00
Economiser 2	265.00	310.00	134.00	132.00
Water Walls	310.00	330.00	132.00	134.00
Superheater 1	330.00	390.00	132.00	129.00
Superheater 2	390.00	415.00	129.00	126.00
Superheater 3	415.00	535.00	126.00	123.00
Reheater 1	339.00	431.50	25.00	24.50
Reheater 2	431.00	524.00	24.50	24.00

As table 6.8 shows, the spreadsheet does not allow for changes in temperature or pressure between heat transfer stages, this means that heat losses from pipes and conduits cannot be assessed, however there is a provision for an overall global loss which can include these losses along with heat transfer losses. This is entered as a percentage of the overall thermal output of the boiler.

6.5 Data Processing

The spreadsheet will automatically process the data entered by the user to prepare it for use in the embedded calculations and correlations that are used to provide the user with the information required.

6.5.1 Fuel Data Processing

Following input into the spreadsheet, the fuel data is processed to produce an estimate of the flue gas composition following complete combustion of the fuel. This is done by creating an 'equivalent fuel' which is formed by assuming additive behaviour between the parent and substitute fuels by the following equation (6.1):

$$i_{ef} = \frac{(x_p \times i_p) + (x_s \times i_s)}{(x_p + x_s)} \qquad (6.1)$$

Where i_{ef} is the fraction of species i in the equivalent fuel, x_p is the mass fraction of parent fuel, i_p is the fraction of species i in the parent fuel, x_s is the mass fraction of substitute fuel and i_s is the fraction of species i in the substitute fuel.

The mass fractions of parent and substitute fuels are calculated by the following equation (6.2):

$$\frac{x_p}{x_s} = \left\{\frac{100 - B}{LCV_p}\right\} \times \left\{\frac{B}{LCV_s}\right\}^{-1} \qquad (6.2)$$

Where B is the thermal percentage of the boiler output to be supplied by the substitute fuel, LCV_p is the lower calorific value of the parent fuel and LCV_s is the lower calorific value of the substitute fuel.

Using equations (6.1) and (6.2), proximate, ultimate and ash analyses are calculated for the equivalent fuel and flue gas composition is calculated based upon these results.

6.5.1.1 Calculation of the Flue Gas Composition

A hidden worksheet embedded within the spreadsheet automatically calculates the flue gas composition based upon the equivalent fuel composition and the equivalence ratio (λ). The spreadsheet has the capability to deal with equivalence ratios of less than 1 by considering a two-stage combustion of carbon and sulphur to monoxides by reactions (1) and (2) and then further combustion to dioxides by reactions (3) and (4).

$$2C + O_2 \rightarrow 2CO \qquad (1)$$

$$2S + O_2 \rightarrow 2SO \qquad (2)$$

$$2CO + O_2 \rightarrow 2CO_2 \qquad (3)$$

$$2SO + O_2 \rightarrow 2SO_2 \qquad (4)$$

$$2H_2 + O_2 \rightarrow 2H_2O \qquad (5)$$

This method has limited accuracy at sub-stoichiomeric equivalence ratios, as no attempt is made to account for differences in reaction rates between the oxidation reactions for Carbon and Sulphur.

For equivalence ratios of less than 1, the calculation works by first converting all of the carbon and sulphur to CO and SO by reactions (1) and (2) and all of the hydrogen to H_2O by reaction (5). The amount of O_2 remaining is then calculated and is used to convert CO and SO to CO_2 and SO_2 until all of the O_2 has been consumed. Equal proportions of CO and SO will be converted into dioxides as no consideration is given to reaction rates and energies. For equivalence ratios greater than 1, the model assumes that no CO or SO are present in the flue gas, therefore, all carbon and sulphur are converted straight to dioxides.

The assumed resultant flue gas is made up of a combination of CO, CO_2, SO, SO_2, H_2O, N_2, O_2 and ash. The CO, CO_2, SO and SO_2 come from reactions (1) to (4), the H_2O comes from a combination of reaction (5) and the moisture already present within the coal. The N_2 is present as the nitrogen from the coal and also that introduced with the combustion air (which is assumed to be 23.3% O_2 and 76.7% N_2 by mass). It is assumed that the nitrogen does not oxidise to form nitrous oxides. The oxygen present is due to that introduced in the excess air; during stoichiometric and sub-stoichiometric combustion no O_2 is present in the flue gas. The flue gas composition is calculated in tables similar to 6.9 and 6.10, which show the flue gas composition for the Langerlo boiler firing a 10% sewage sludge blend under normal excess air conditions. Table 6.9 shows the calculation of the mass of flue gas products per kg of wet coal fired and table 6.10 shows the flue gas composition as a mole fraction. For illustrative purposes table 6.11 and 6.12 show the flue gas composition for the Langerlo boiler operating with an equivalence ratio of 0.95.

Table 6.9: Calculation of mass fraction of combustion products for the Langerlo boiler

Species	Ultimate Analysis / $\%_{wt}$	Oxidation Reaction	Mass of O_2 required / kg	Mass of Products / kg
Carbon	64.45	$2C + O_2 \rightarrow 2CO$	0.000	0.000
		$2CO + O_2 \rightarrow 2CO_2$	1.719	2.363
Hydrogen	4.66	$2H_2 + O_2 \rightarrow 2H_2O$	0.373	0.491
Oxygen	11.61	Consumed	-0.116	0.000
Nitrogen	1.24	No Reaction	0.000	0.012
Sulphur	0.81	$2S + O_2 \rightarrow 2SO$	0.000	0.000
		$SSO + O_2 \rightarrow 2SO_2$	0.008	0.016
Moisture	8.68	No Reaction	0.000	0.087
Ash	8.53	No reaction	0.000	0.085
Total	99.99	n/a	1.983	2.983
Oxygen introduced in excess air				0.417
Nitrogen introduced in combustion air				7.900
Total mass of combustion products				11.300

Table 6.10: Calculation of flue gas composition for the Langerlo boiler

Product	Mass per kg wet fuel /kg	Molecular weight	Moles per kg of wet fuel / mol	Mole fraction / $\%_{mol}$
CO	0.000	28	0.0000	0.00
CO_2	2.363	44	0.0537	14.22
H_2O	0.506	18	0.0281	7.44
O_2	0.417	32	0.0130	3.45
N_2	7.912	28	0.2826	74.82
SO	0.000	48	0.0000	0.00
SO_2	0.016	64	0.0003	0.07
Total	11.215	n/a	0.3777	100.00

Table 6.11: Calculation of mass fraction of combustion products for the Langerlo boiler with λ = 0.95

Species	Ultimate Analysis $\%_{wt}$	Oxidation Reaction	Mass of O_2 required / kg	Mass of Products / kg
Carbon	64.45	$2C + O_2 \rightarrow 2CO$	0.099	0.173
		$2CO + O_2 \rightarrow 2CO_2$	1.521	2.092
Hydrogen	4.66	$2H_2 + O_2 \rightarrow 2H_2O$	0.373	0.419
Oxygen	11.61	Consumed	-0.116	0.000
Nitrogen	1.24	No Reaction	0.000	0.012
Sulphur	0.81	$2S + O_2 \rightarrow 2SO$	0.000	0.001
		$SSO + O_2 \rightarrow 2SO_2$	0.007	0.014
Moisture	8.68	No Reaction	0.000	0.087
Ash	8.53	No reaction	0.000	0.085
Total	99.99	n/a	1.884	2.884
Oxygen introduced in excess air				0.000
Nitrogen introduced in combustion air				6.203
Total mass of combustion products				9.087

Table 6.12: Calculation of flue gas composition for the Langerlo boiler with λ = 0.95

Product	Mass per kg wet fuel /kg	Molecular weight	Moles per kg of wet fuel / mol	Mole fraction / $\%_{mol}$
CO	0.173	28	0.0062	0.00
CO_2	2.092	44	0.0475	14.22
H_2O	0.506	18	0.0281	7.44
O_2	0.000	32	0.0000	3.45
N_2	6.215	28	0.2220	74.82
SO	0.001	48	0.0000	0.00
SO_2	0.014	64	0.0002	0.07
Total	9.002	n/a	0.3040	100.00

The information contained in the above tables is used to provide the spreadsheet with an estimate of the mass of combustion products passing through the boiler at any given time. This data will be used by the spreadsheet during the calculation of the temperature profile for the boiler. In addition to this data, the flue gas analysis worksheet also calculates the composition of the equivalent fuel in $\%_{mol}$ in readiness for input into correlations used to predict the temperature-enthalpy relationship for the fuel.

6.5.2 Boiler Geometry Data Processing

Due to the one-dimensional nature of the calculation, the spreadsheet uses the data entered into the boiler geometry diagrams (shown in figures 6.2 and 6.3) to calculate a theoretical centreline within the boiler shown in figure 6.4. The overall length of the centreline is calculated along with where on that centreline the heat exchange equipment begins and ceases to influence the temperature of the flue gases passing along it.

The centreline is produced using the data from figure 6.2 and simple geometric calculations to calculate its length (see Appendix A). It is split into 8 sections at positions where the boiler cross-section or the direction of gas flow changes. This information is combined with the locations of the boiler plant and heat exchange equipment from figure 6.3 to calculate in which section they cross the centreline.

If the heat exchange equipment does not cross the centreline, such as superheater 2 in figure 6.3, then an assumed position where the heat exchanger begins and ceases to influence the flue gas is calculated. This is done by using simple logic statements and geometric calculations to compare the position of the heat exchange plant to the sections of the centreline (see Appendix A). There are limits to where each heat exchanger can fall on the centreline; these are displayed in table 6.11, which shows the first and last section along the centreline that each heat exchanger can influence for example, heat exchanger 1 can influence any section from section 1 to section 7. It is also not possible for heat exchangers to overlap (i.e. heat exchanger 2 cannot begin to influence the flue gas before heat exchanger 1 has ceased influencing it). This is the case for all heat exchangers with the exception of the water walls.

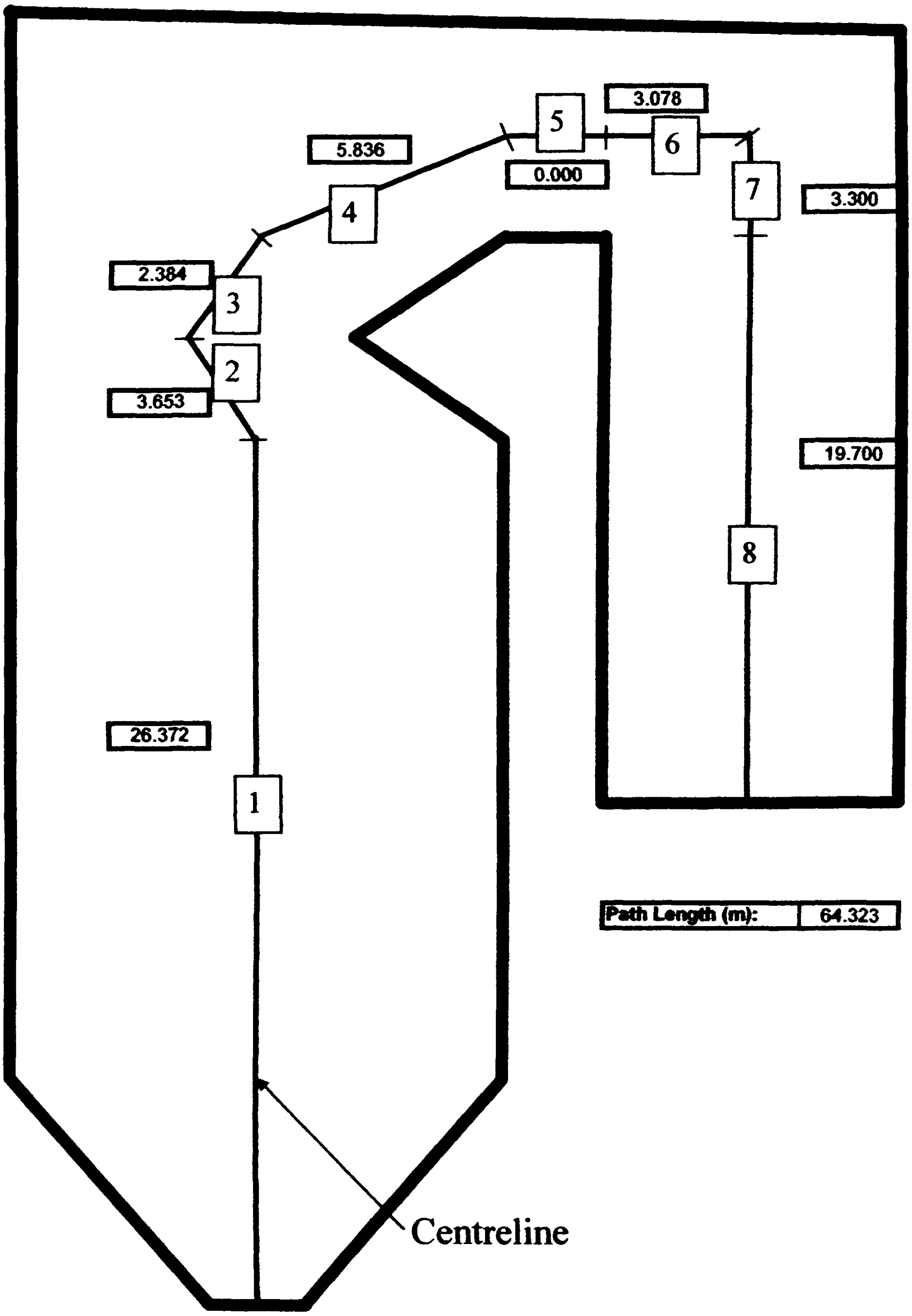

Figure 6.4: The theoretical centreline for the Langerlo boiler

Table 6.13: Limits of influence of heat exchange equipment

Heat Exchanger ID from fig. 12	Heat Exchanger Name (Langerlo)	First Section to influence	Last Section to influence
1	Superheater 2	1	7
2	Superheater 3	4	7
3	Reheater 2	5	7
4	Superheater 1	7	8
5	Reheater 1	7	8
6	Economiser 2	8	8
7	Economiser 1	8	8
8	Water Walls	1	4

The plant start and plant finish columns of table 6.4 show the results of the calculation process described above. The data describing the position of these heat exchangers is fundamental to the calculation of the temperature profile which is the keystone of many of the calculation processes within the spreadsheet.

6.5.3 Processing of the Process Control Data

The majority of the process control data can be used in its raw state however, it is necessary to calculate the heat energy change of the water/steam across each of the heat exchangers for use in further calculations within the spreadsheet. This is done using equation (6.3), the steady flow energy equation.

$$Q = \dot{m}(h_2 - h_1) \qquad (6.3)$$

Where Q is the heat energy gained by the water or steam as it passes through the heat exchanger, $\dot{m}$ is the mass flow-rate of the water/steam, h_2 is the enthalpy of the water or steam as it leaves the heat exchanger and h_1 is the enthalpy of the water or steam as it enters the heat exchanger.

The process of calculating these values has been automated to prevent the user having to calculate or extract the values from steam tables each time he wants to perform a calculation. The information required to make the conversion is contained in tabular form in Thermodynamic and Transport Properties of Fluids by Rogers and Mayhew

[92]. It was necessary to convert these tables into a format which could be used in the spreadsheet to calculate the enthalpy of the steam based on any temperature or pressure entered by the user. Therefore, simple equations were derived relating temperature to specific enthalpy for saturated liquid and saturated vapour and also temperature to specific enthalpy at a given pressure for superheated steam. The spreadsheet uses these equations to convert the temperature and pressure values entered in table 6.8 into the enthalpy of the steam before and after each heat exchanger within the boiler. The curves of specific enthalpy as a function of temperature for the saturated liquid line, the saturated vapour line and the superheat region can be seen in figures 6.5 to 6.7.

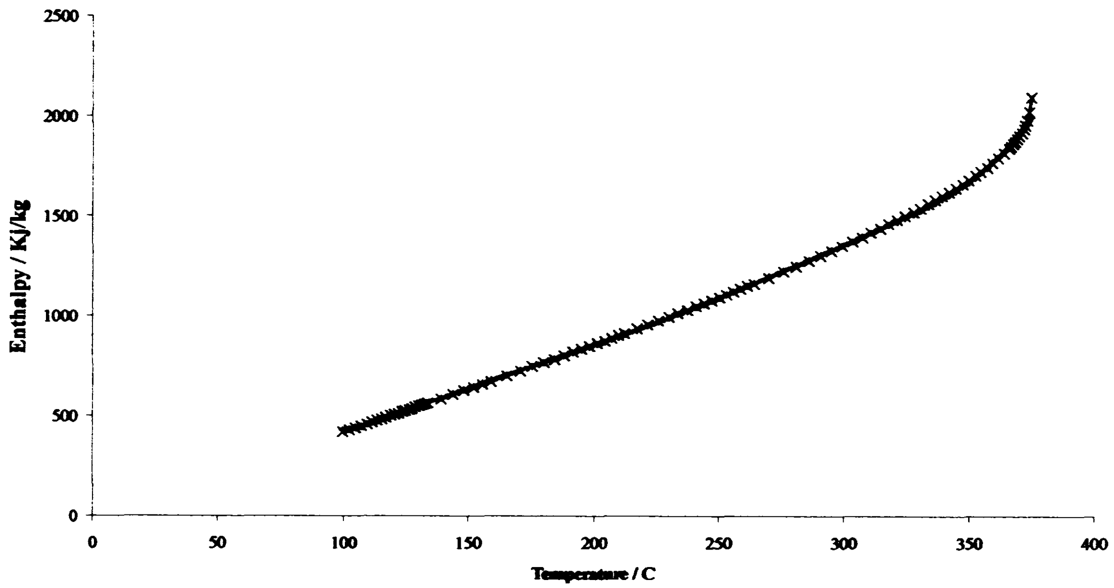

Figure 6.5: Specific enthalpy as a function of temperature for saturated liquid [93]

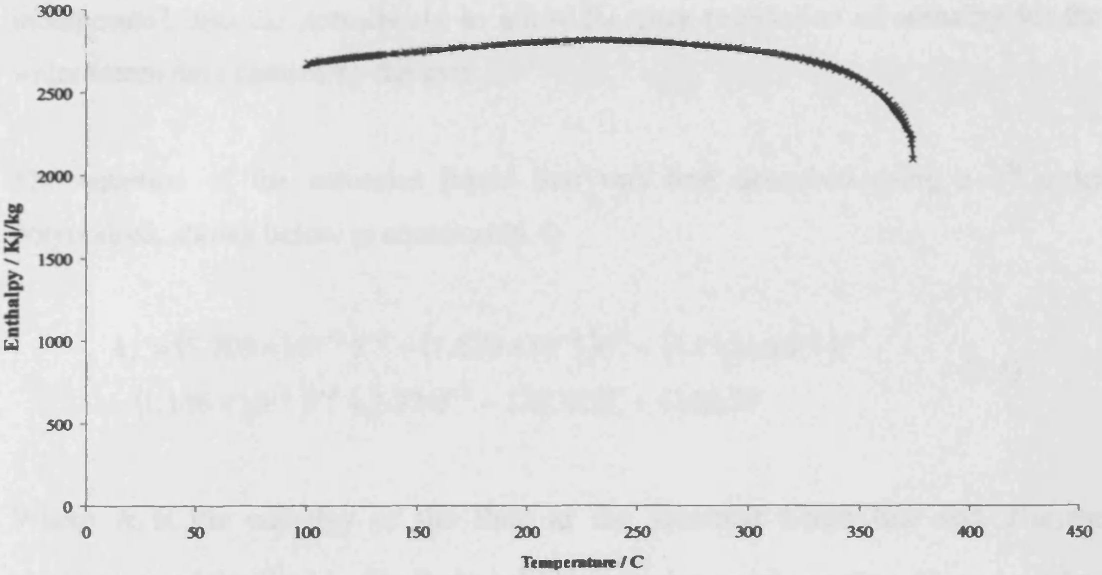

Figure 6.6: Specific enthalpy as a function of temperature for saturated vapour [93]

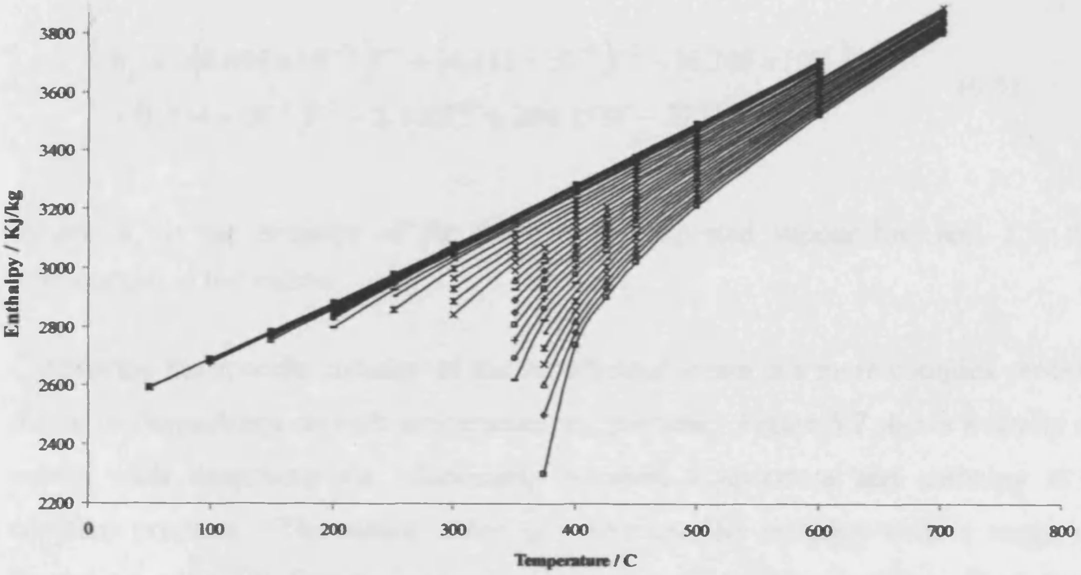

Figure 6.7: Specific enthalpy as a function of temperature at discrete pressure values for superheated steam [92]

Figures 6.5 and 6.6 show the relationship between specific enthalpy and temperature for saturated liquid and saturated vapour respectively. Figure 16 shows a family of curves describing the relationship between specific enthalpy and temperature for superheated steam at a series of discrete pressure values between 0.006112 and 220 bar. The trend line function available in Microsoft Excel has been used to derive the equation of each of the curves in polynomial form. These equations have been incorporated into the spreadsheet to allow the easy calculation of enthalpy for the water/steam data entered by the user.

The equation of the saturated liquid line was best described using a 6th order polynomial, shown below as equation (6.4)

$$\begin{aligned} h_f &= \left(5.703\times10^{-11}\right)T^6 - \left(7.620\times10^{-8}\right)T^5 + \left(4.117\times10^{-5}\right)T^4 \\ &- \left(1.146\times10^{-2}\right)T^3 + 1.731T^2 - 129.921T + 4162.59 \end{aligned} \tag{6.4}$$

Where h_f is the enthalpy of the fluid at the saturated liquid line and T is the temperature of the liquid. Similarly a 6th order polynomial equation 43 was used to describe the saturated vapour curve.

$$\begin{aligned} h_g &= -\left(8.695\times10^{-11}\right)T^6 + \left(4.117\times10^{-7}\right)T^5 - \left(6.245\times10^{-5}\right)T^4 \\ &+ \left(1.734\times10^{-2}\right)T^3 - 2.165T^2 + 204.153T - 3771.860 \end{aligned} \tag{6.5}$$

Where h_g is the enthalpy of the fluid at the saturated vapour line and T is the temperature of the vapour.

Calculating the specific enthalpy of the superheated steam is a more complex process due to its dependence on both temperature and pressure. Figure 6.7 shows a family of curves each describing the relationship between temperature and enthalpy at a constant pressure. The steam tables give the specific enthalpy over a range of temperatures for 39 discrete pressure values, the task of incorporating all of these curves into the spreadsheet would have been too complex. Therefore, five pressure ranges were used instead, they are as follows:

- $0.1 \leq \text{Pressure} \leq 4.0$ bar
- $4.0 \leq \text{Pressure} \leq 15.0$ bar
- $15.0 \leq \text{pressure} \leq 70.0$ bar
- $70.0 \leq \text{Pressure} \leq 160.0$ bar
- $160.0 \leq \text{Pressure} \leq 221.2$ bar

The curves for the limits of these ranges are shown in figure 6.8 and their equations have been calculated in the same manner as those for the saturated liquid and vapour lines.

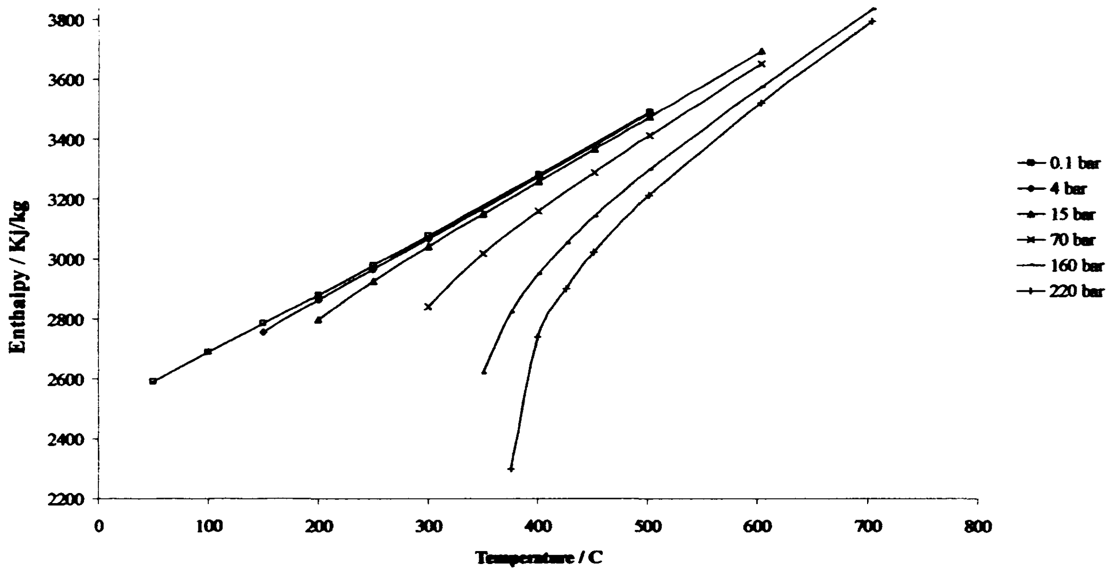

Figure 6.8: Curves of temperature versus enthalpy for the constant pressure values used within the spreadsheet

The equation of each of these isobars has been embedded within the spreadsheet and allows the user to calculate the enthalpy of superheated steam. The equation of each of the curves is given below in equations (6.6) to (6.11).

At 0.1 bar $$h = 1.985T + 2487.7 \tag{6.6}$$

At 4 bar $$h = 2.082T + 2443.0 \tag{6.7}$$

At 15 bar $$h = 2.220T + 2365.4 \tag{6.8}$$

At 70 bar $$h = \left(1.084\times10^{-5}\right)T^3 - \left(1.655\times10^{-2}\right)T^2 + 10.755T + 821.56 \tag{6.9}$$

At 160 bar $$h = \left(2.754\times10^{-5}\right)T^3 - \left(5.041\times10^{-2}\right)T^2 + 33.352T + 4296.80 \tag{6.10}$$

At 221.2 bar $$h = \left(2.774\times10^{-5}\right)T^3 - \left(4.837\times10^{-2}\right)T^2 + 30.417T + 3270.2 \tag{6.11}$$

Nested Boolean logic statements embedded within the spreadsheet are used to identify which pressure range the steam cycle data entered by the user falls within. The spreadsheet calculates the upper and lower bounds for the temperature entered then interpolates between the two values based upon the pressure entered to give the enthalpy of the steam. Enthalpy values calculated in this manner have proved to be within 1.9% of the value calculated using data from the steam tables [92].

There are a number of limits applied to the calculation dictated by the data provided in the steam tables [92]. The equations for the saturated water and vapour lines can only be applied to temperatures within the range 99.6 °C to 374.15 °C.

For superheated steam, each pressure range has its own temperature limits. They are as follows:

- $0.1 \leq \text{Pressure} \leq 4.0$ bar $50 \leq T \leq 500$ °C
- $4.0 \leq \text{Pressure} \leq 15.0$ bar $200 \leq T \leq 600$ °C
- $15.0 \leq \text{pressure} \leq 70.0$ bar $200 \leq T \leq 600$ °C
- $70.0 \leq \text{Pressure} \leq 160.0$ bar $350 \leq T \leq 700$ °C
- $160.0 \leq \text{Pressure} \leq 221.2$ bar $400 \leq T \leq 700$ °C

If temperatures or pressures are entered which are outside these ranges, an error message will appear in the enthalpy field reading "Out of Range".

Assumptions have been made regarding the water/steam conditions at each point within the steam cycle. The saturated liquid line is used to calculate the enthalpy for the two heat exchangers upstream of the water walls as well as for the water entering the water walls. It is assumed that upon exiting the water walls the water has become saturated vapour and thus, the saturated vapour line is used to calculate the enthalpy of the steam at this point. Finally, it is assumed that the steam entering the first heat exchanger downstream of the water walls is still saturated and has not been superheated, however, steam exiting that heat exchanger is assumed to be superheated and will remain in a state of superheat even after expansion through high or low pressure turbines and within subsequent reheat stages. The data is presented to the user in a table similar to that shown below.

Table 6.14: Heat energy gained by steam and removed from flue gas

	Temperature Before / °C	Temperature After / °C	Pressure Before / Bar	Pressure After / Bar	Heat Energy Gained by Steam / MJ	Energy Removed From Flue Gas / MJ
Water Walls	310.00	330.00	132.00	132.00	248.481	282.365
Superheater 2	390.00	415.00	129.00	126.00	21.610	24.557
Superheater 3	415.00	535.00	126.00	123.00	70.272	79.855
Reheater 2	432.00	524.00	24.50	24.00	40.560	46.091
Superheater 1	330.00	390.00	132.00	129.00	55.848	63.463
Reheater 1	339.00	432.00	25.00	24.50	42.137	47.883
Economiser 2	265.00	310.00	134.00	132.00	46.282	52.593
Economiser 1	235.00	265.00	136.00	134.00	29.223	33.208
			Total / MJ		554.413	630.015
			Heat Loss / %		n/a	12.00%

Table 6.14 shows a discrepancy between the heat energy gained by the steam and that removed from the flue gas. This discrepancy arises due to the heat loss during heat transfer as defined by the heat transfer coefficient. The user can identify this heat loss factor by adjusting the heat loss value shown in the bottom row of the table until it matches the thermal energy provided by the fuel (see Section 6.4.3), this allows the user to identify the global heat loss for their particular boiler. Shown here is the heat loss for the Langerlo boiler firing $10\%_{th}$ sewage sludge and $90\%_{th}$ coal.

6.5.4 Summary

The outcome of the above processes is to take the fuel, boiler geometry and process control data and use it to calculate the enthalpy change of the flue gases across the various heat exchangers within the boiler. This data is projected onto a theoretical boiler centreline to produce a 'heat removal profile' for the boiler.

6.6 Development of a Temperature – Enthalpy Change Relationship for the Fuel Blend

In order to be used in the correlations and equations required to predict slagging, fouling and corrosion, the 'heat removal profile' needs to be converted into a temperature profile. This has been done by correlating the enthalpy of the flue gases at any point within the boiler to the temperature at that point. Two approaches have been used to try to achieve this outcome:

1. Derivation of empirical correlations to predict temperature
2. Development of an artificial neural network (ANN) to predict temperature

The derivation of empirical correlations was carried out by the author at Cardiff University. This approach was expanded upon by C. K. Tan of The University of Glamorgan who, within the scope of the PowerFlam project, developed an artificial neural network (ANN) to predict the relationship between temperature and enthalpy for the fuel blend.

The thermodynamic principles behind both approaches are the same with the ANN being used to provide solutions for a wider range of parent and substitute fuels; therefore, a description of how the empirical correlations were derived is given for the purposes of this document. An appraisal of the ANN method can be found in Section 6.10.

6.6.1 FLUENT PrePDF

FLUENT is a commercial computational fluid dynamics (CFD) code often used for the study of combustion and combustion equipment. In order to provide the broadest range of applications, a variety of combustion models are used within the code. One such model is the probability distribution function (PDF) approach which is particularly suited to non-premixed combustion such as particulate coal combustion where fuel and air streams are mixed within the combustion environment producing a turbulent flame. The model is a pre-processor which uses the proximate and ultimate analyses of the fuel to produce look-up tables that are accessed by the CFD code during its calculation process.

6.6.1.1 Basic Theory Behind the PrePDF Model

The model inputs are split into three streams: the fuel stream which consists entirely of solid carbon, the secondary stream, which comprises the volatiles (gaseous carbon, hydrogen, nitrogen, oxygen and sulphur) and the oxidiser stream which is the combustion air (79%$_{mol}$ nitrogen and 21%$_{mol}$ oxygen). The model solves transport equations for two conserved scalars, the fuel and secondary streams, rather than for individual species. The species concentrations are calculated from the predicted mixture fraction fields [93] and the interaction of turbulence and chemistry is accounted for with a probability density function (PDF) [93].

The FLUENT user manual states that "under a certain set of simplifying assumptions, the instantaneous thermochemical state of the fluid is related to a conserved scalar known as the mixture fraction (*f*)" [93]. The mixture fractions for the fuel and secondary streams are simply the mass fractions of those streams such that:

$$f_{fuel} + f_{sec} + f_{ox} = 1 \tag{6.12}$$

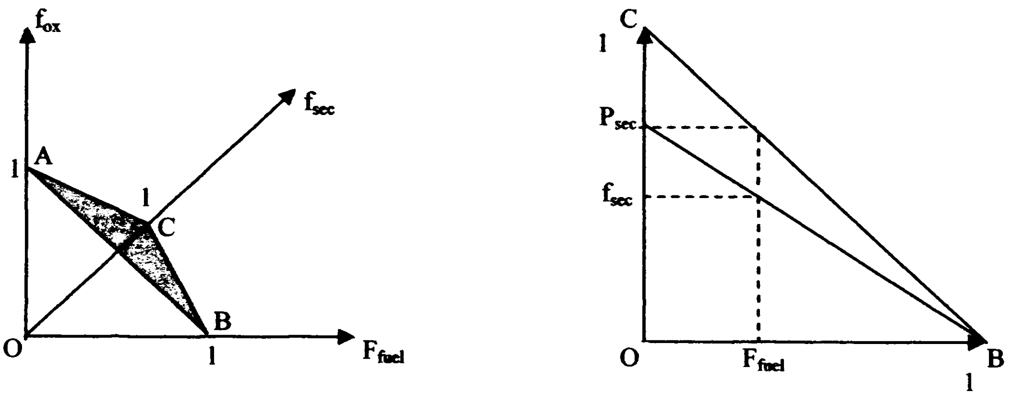

(a) f_{fuel}, f_{sec} **and** f_{ox}

(b) f_{fuel}, f_{sec} **and** P_{sec}

Figure 6.9: The relationship of f_{fuel}, f_{sec} **and** f_{ox} **and the relationship of** f_{fuel}, f_{sec} **and** P_{sec}

Equation (6.12) dictates that only points on the plane ACB in figure 6.9(a) are valid for the mixture fraction and, as a consequence, f_{fuel} and f_{sec} cannot vary independently and are only valid if their values are within the triangle OCB [93]. FLUENT discretizes triangle OCB as shown in figure 6.9(b) where the fuel mixture fraction is allowed to vary between zero and one whilst the secondary mixture fraction lies on lines with the following equation [93]:

$$f_{sec} = p_{sec} \times \left(1 - f_{fuel}\right) \tag{6.13}$$

Where p_{sec} is the normalised secondary mixture fraction and is the value at the intersection of a line with the secondary mixture fraction axis [93]. It is generally accepted that for turbulent flows, species have equal diffusivities as turbulent convection overwhelms molecular diffusion [93]. Therefore the time averaged mixture fraction equation is as follows:

$$\frac{\partial}{\partial t}\left(\rho \bar{f}\right) + \nabla \cdot \left(\rho \vec{\upsilon} \bar{f}\right) = \nabla \cdot \left(\frac{\mu_t}{\sigma_t} \nabla \bar{f}\right) + S_m + S_{user} \tag{6.14}$$

and the mean mixture fraction variance $\overline{f'^2}$ is given by:

$$\frac{\partial}{\partial t}\left(\rho \overline{f'^2}\right) + \nabla \cdot \left(\rho \vec{\upsilon} \overline{f'^2}\right) = \nabla \cdot \left(\frac{\mu_t}{\sigma_t} \nabla \overline{f'^2}\right) + C_g \mu_t \left(\nabla^2 \bar{f}\right) - \\ C_d \rho \frac{\varepsilon}{k} \overline{f'^2} + S_{user} \tag{6.15}$$

where

$$f' = f - \bar{f} \tag{6.16}$$

f is the mixture fraction of either the fuel or secondary stream, constants σ_t, C_g and C_d are equal to 0.85, 2.86 and 2.0 respectively, S_m is a source term due to the transfer of mass into the gas phase from the reacting particles, S_{user} is any source term introduced by the user, ρ is the flow density (kg/m^3), $\vec{v}$ is the overall velocity vector (m/s), μ_t is the turbulent viscosity (Pa s), ε is the turbulent dissipation rate (m^2/s^3) and k is the mass transfer coefficient (units vary) [93].

Since the system chemistry is reduced to two conserved mixture fractions, all thermochemical scalars (species mass fraction, density and temperature) are related to the mixture fractions [93]. Therefore, "given a description of the reacting system chemistry, the instantaneous mixture fraction at each point in the flow field can be used to calculate the instantaneous values of individual species mole fractions, density and temperature" [93]. In a non-adiabatic system these instantaneous values will depend upon the fuel mixture fraction, the secondary partial fraction and instantaneous enthalpy [93]:

$$\phi_{i1} = \phi_{i2}\left(f_{fuel}, p_{secondary}, H^*\right) \tag{6.17}$$

Where ϕ_{i1} represents one thermochemical scalar, ϕ_{i2} represents another thermochemical scalar and H^* is the instantaneous enthalpy (J/kg) given by:

$$H^* = \sum_j m_j H_j = \sum_j m_j \left[\int_{T_{ref,j}}^{T} c_{p,j}\,dT + h_j^0\left(T_{ref,j}\right)\right] \tag{6.18}$$

Where m_j is the mass of species j (kg), $c_{p,j}$ is the specific heat capacity of species j (J/kgK), T is the temperature (K) and h^0_j is the standard state enthalpy of formulation for species j (J/kg) [93].

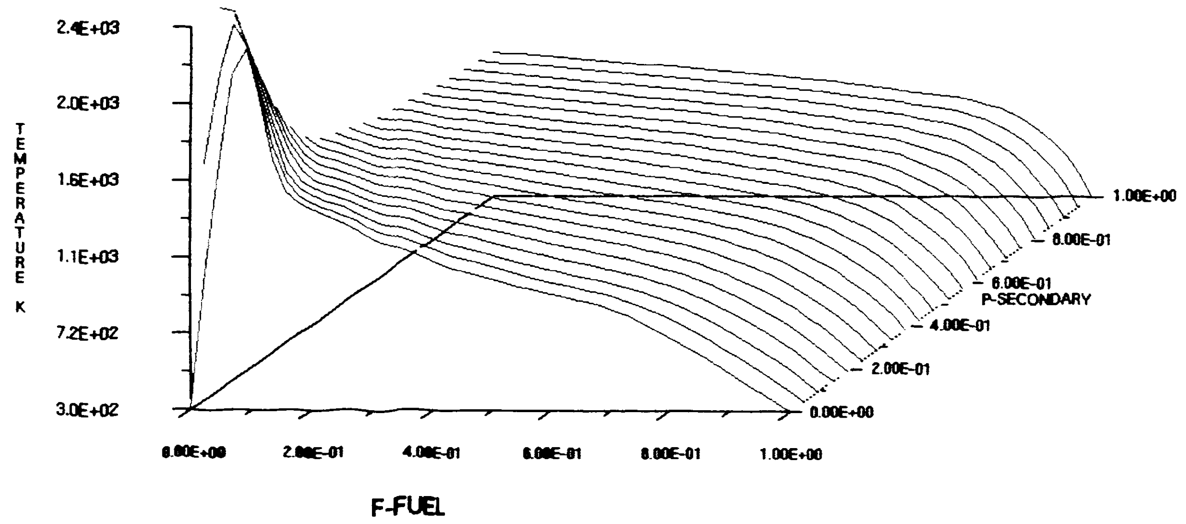

Figure 6.10: A typical look-up table for a constant value of enthalpy of zero (adiabatic)

In a non-adiabatic system, the enthalpy is not linearly related to mixture fraction as it depends upon wall heat transfer and radiation. Therefore, using equations (6.17) and (6.18), the software will produce a series of look-up tables relating temperature to f_{fuel} and $p_{secondary}$ at discrete values of instantaneous enthalpy which are called up by the FLUENT CFD code (ref. figure 6.10). It is these look-up tables that have been utilised in the development of the spreadsheet.

6.6.1.2 Application of FLUENT PrePDF to the Development of the Spreadsheet

For coal combustion, the equilibrium of the following 13 species system is considered: C_{solid}, $C_{gaseous}$, CH_4, CO, CO_2, H, H_2, H_2O, N, N_2, O, O_2 and OH. As already stated the software divides the fuel input into three streams; the fuel stream consists of pure solid carbon and, therefore, has a mole fraction of 1 for C<s> (solid carbon). The secondary stream comprises the fuel volatiles (C<g>, H, O and N) which must be entered as a mole fraction of the entire volatile content; therefore, the sum of the mole fractions in the secondary stream must also be equal to 1. The final stream is the oxidiser stream, which is entered as a mass fraction of O_2 and N_2. Other information required is the L.C.V. and specific heat of the volatile stream along with the density of the pure char.

Look-up tables were generated for discrete enthalpy values between -2400 kJ/kg and 1000 kJ/kg. These look-up tables were used to calculate the gas temperature at each of the discrete enthalpy values in the range, thus producing a relationship between gas temperature and the enthalpy change of the gas within the system. In order to find each temperature value, it was necessary to establish the working point within each look-up table by determining f_{fuel} and p_{sec} for the system, equations (6.19) to (6.22) were used to do this [93].

$$f_{fuel} = \frac{m_{fuel}}{m_{total}} \qquad (6.19)$$

Where f_{fuel} is the fuel mixture fraction, m_{fuel} is the mass of fuel stream (kg), m_{ox} is the combined mass of the stoichiometric and excess air streams (kg) and:

$$m_{total} = m_{fuel} + m_{ox} \qquad (6.20)$$

For the secondary partial fraction:

$$f_{sec} = \frac{m_{sec}}{m_{total}} \qquad (6.21)$$

Where f_{sec} is the secondary mixture fraction and m_{sec} is the mass of secondary stream (kg),

$$p_{sec} = \frac{f_{sec}}{\left(1 - f_{fuel}\right)} \tag{6.22}$$

Where p_{sec} is the secondary stream partial fraction.

Using the alpha-numerical menu within the software, it was possible to access the data used to generate the tables. Linear interpolation was used between data points to give the instantaneous flame temperature for that enthalpy value at the working point (f_{fuel}, p_{sec}). Figure 6.11 shows the temperature - enthalpy change relationship generated by this process.

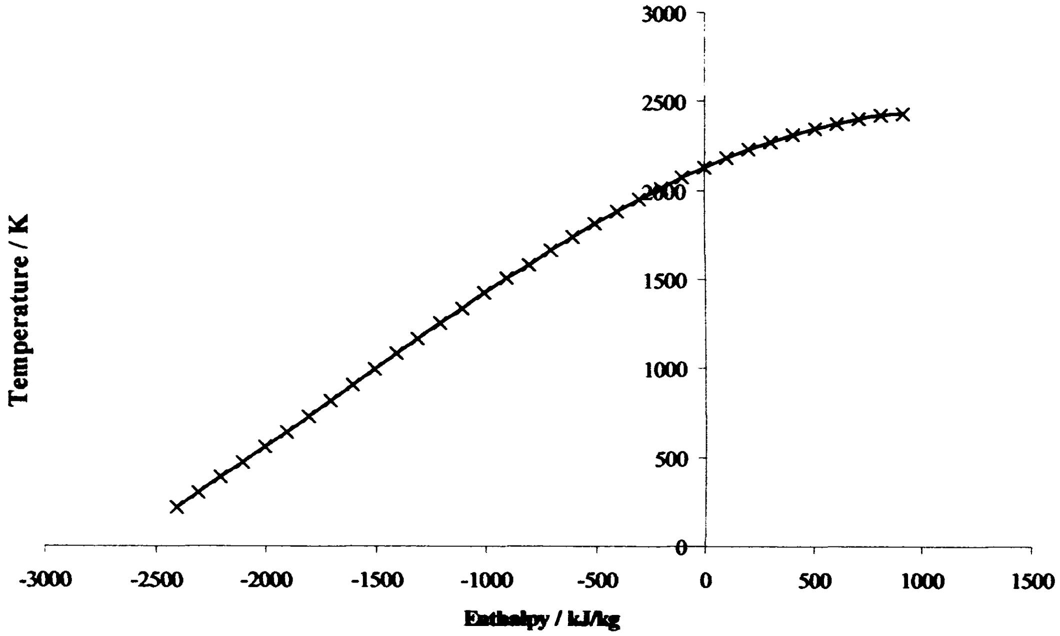

Figure 6.11: Temperature - enthalpy change relationship for Colombian medium volatile bituminous coal

The trendline function in Excel was used to derive an equation which describes the relationship within the specified range (ref. equation 6.23)

$$\begin{aligned} T = &-\left(4.204\times10^{-8}\right)\left(H^*\right)^3 + \left(1.947\times10^{-4}\right)\left(H^*\right)^2 + 0.546\left(H^*\right) \\ &+ 2120.300 \end{aligned} \tag{6.23}$$

Where T is temperature (K) and H^* is the instantaneous enthalpy, which is equivalent to the enthalpy change of the system (kJ/kg).

Look-up tables were generated in this way for a range of fuel blends between 0 and 50%$_{th}$ sewage sludge for a typical medium volatile bituminous coal (ref. table 6.15 and a typical sewage sludge (ref. table 6.16). Appendix B shows the model inputs and the data extracted from the PrePDF model for each blend.

Table 6.15: Proximate and ultimate analysis for a typical medium volatile bituminous coal

Proximate Analysis (dry)	As Received / %$_{wt}$
Fixed Carbon	59.51
Volatile Content	38.80
Ash Content	1.69
Total	100.00
LCV / MJ/kg	30.99

Ultimate Analysis (dry)	As Received / %$_{wt}$
Carbon	79.71
Hydrogen	5.18
Oxygen	11.21
Nitrogen	1.54
Sulphur	0.67
Ash	1.69
Total	100.00

Table 6.16: Proximate and ultimate analysis for a typical sewage sludge (Belgian)

Proximate Analysis (dry)	As Received / %$_{wt}$
Fixed Carbon	3.12
Volatile Content	41.59
Ash Content	55.29
Total	100.00
LCV / MJ/kg	8.41

Ultimate Analysis (dry)	As Received / %$_{wt}$
Carbon	21.66
Hydrogen	4.71
Oxygen	14.47
Nitrogen	3.00
Sulphur	0.87
Ash	55.29
Total	100.00

Working points were calculated for each equivalent fuel and the adiabatic flame temperature was calculated for each one. A relationship between maximum adiabatic flame temperature and fuel blend was established (Ref fig. 6.12)

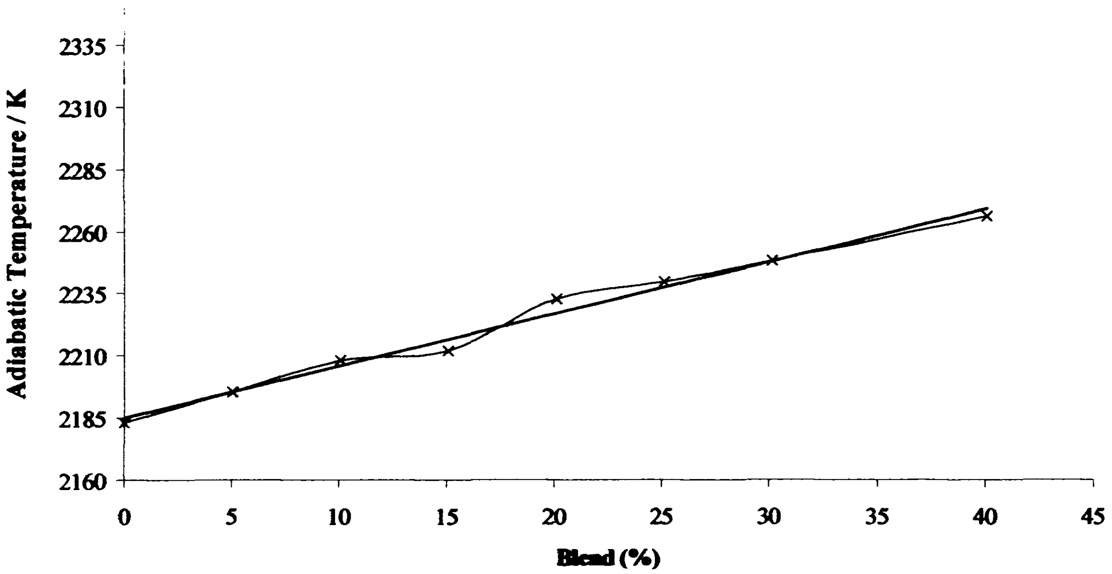

Figure 6.12: Variation in adiabatic flame temperature as $\%_{th}$ substitute fuel increases

The relationship between adiabatic flame temperature and blend is described by a straight line shown as equation (6.24).

$$T_a = 2.101B + 2185.2 \qquad (6.24)$$

Where T_a is the adiabatic temperature at the working point and B is the blend ($\%_{th}$ of the final output provided by the substitute fuel).

The adiabatic flame temperature is the temperature when the constant value of enthalpy is zero i.e. when no energy has been added to or removed from the combustion gases. This value is effectively the intercept with the temperature axis for the temperature – enthalpy change relationship. Therefore, replacing the intercept of the original temperature – enthalpy change relationship equation (6.23) with equation (6.24) will give the required variation in the temperature – enthalpy relationship as the fuel blend changes. This relies on the major assumption that equation (6.24) is valid for the entire temperature – enthalpy change relationship.

Combining equations (6.23) and (6.24) yields:

$$\begin{aligned} T = &-\left(4.204\times10^{-8}\right)\left(H^{*}\right)^{3} + \left(1.947\times10^{-4}\right)\left(H^{*}\right)^{2} + 0.546\left(H^{*}\right) \\ &+ \left(2.101B + 2185.2\right) \end{aligned} \qquad (6.25)$$

Equation (6.25) defines the temperature – enthalpy change relationship for blends of a typical medium volatile coal and a typical sewage sludge up to a limit of $40\%_{th}$ sewage sludge. This relationship is critical for calculating the temperature profile of the boiler, which provides the basis for the prediction of the fuel ash composition and corrosion effects.

6.7 Calculation of the Temperature Profile for the Boiler

The temperature profile provides the backbone of the spreadsheet giving a basis from which the fuel ash composition can be calculated, along with estimates of the potential for damage to the heat exchangers from high temperature corrosion. The creation of the profile requires the coming together of three of the data sets calculated by the spreadsheet so far:

- The enthalpy change of the combustion gases as they pass through each heat exchanger from the processing of the process control data
- The temperature – enthalpy change relationship of the combustion products for the fuel blend from FLUENT Pre-PDF and the fuel data processing.
- The position of each piece of boiler plant on the centre line of the boiler along which the combustion gases are assumed to travel from the boiler geometry data processing.

6.7.1 Division of the Boiler into Zones for 1-Dimensional Modelling

A 1-dimensional model has been used to generate the temperature profile by dividing the centreline of the boiler into zones, the heat gained by or removed from the combustion gases in each zone is calculated and the enthalpy change across that zone is found, the temperature – enthalpy change relationship is then used to calculate the temperature change within that zone caused by the change in enthalpy. The centreline was zoned in the following manner, figure 6.13 shows how the boiler has been divided into zones:

- The region between the bottom of the boiler and the first burner row is denoted zone 1.
- Burner row 1 is denoted zone 2.
- Zone 3 is the region between burner row 1 and burner row 2
- Burner row 2 is denoted zone 4.

- The remaining 4 burner rows are zoned in this fashion creating zones 5 to 12.
- The distance between the top burner row and the exit of the combustion chamber (vertical plane above the boiler nose) is divided into 6 equal zones creating zones 13 – 18.
- Zone 19 is the region between the combustion chamber exit and the start of the downward pass in the convective section.
- Each of four pieces of plant in the downward pass was allocated a zone each creating zones 20 – 23.

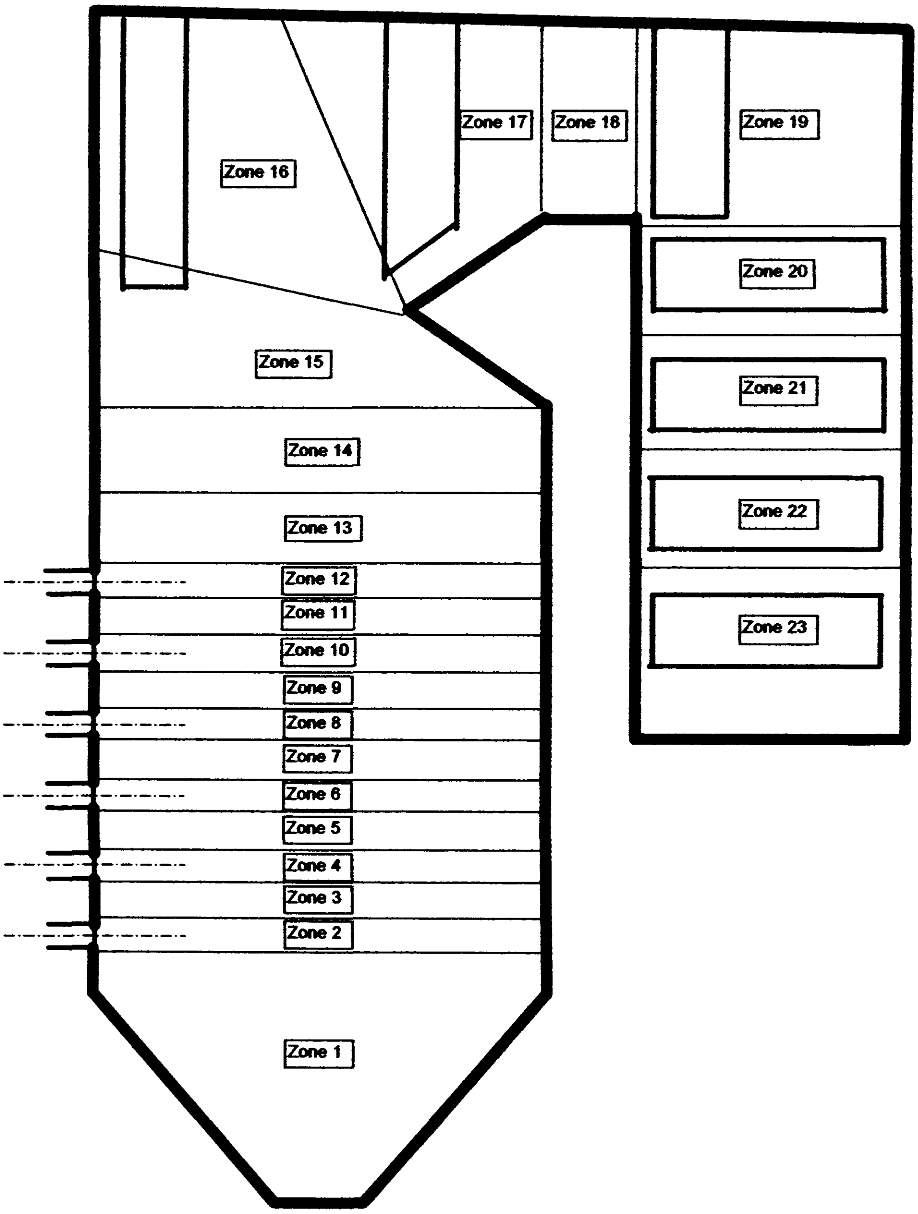

Figure 6.13: Division of the boiler into zones for 1-D modelling

Each of the zones will vary in size depending on the measurements entered by the user. A description of how the boiler is zoned in accordance with the boiler geometry data entered by the user can be found in table C1.1 in Appendix C). Heat exchangers 1 and 2 from figure 6.3 can fall in any zone from 13 to 19 and heat exchanger 3 must fall within zone 19. Boolean logic functions are used to assess which zone is influenced by which heat exchanger depending upon their location within the boiler (see Appendix C).

6.7.2 Modelling Assumptions

The output from the fuel data processing (Section 6.5.1) carried out by the spreadsheet is used to calculate the mass of combustion products passing through the heat exchangers at any given time. Several fundamental assumptions are made which allow the model to use this data in the calculation of the temperature profile:

- The flow of gas through the boiler is generated by pressure gradients caused by the evolution of combustion gases from the burning fuel. Therefore the mass of gas passing an arbitrary point in the boiler over a time interval t is equivalent to that produced by the complete combustion of the fuel that enters the boiler in that time.
- Combustion occurs within the zones defined by the burner rows producing combustion gases at the adiabatic flame temperature.
- The combustion products follow a path along the centreline of the boiler.
- The only heat energy removed from the gases is that removed by the heat exchangers. There are no other losses in the system.
- The heat energy removed by each heat exchanger is done so uniformly along its entire length.

Due to the fact that the flue gases are not all evolved in the same zone, a convention has been applied to the mixing of the existing combustion gases and those evolved at each burner zone:

- As previously stated, combustion gases produced by the combustion of the fuel are at adiabatic flame temperature.

- These gases mix with the gases already in the boiler travelling up from the preceding zones. It is assumed that this mixing occurs at the burner zone where the gas is evolved. For example, gases resulting from the injection of fuel through burner row 2 in zone 4 will mix with the gases from burner row 1 at the bottom of zone 4 before passing through zone 5 and mixing with the gases from burner row 3 at the bottom of zone 6.
- The resulting mixed gas stream will assume the mean enthalpy of the two component streams.
- Gases resulting from the injection through burner row 1 split into 2 streams, stream 1 passes round zone 1 before mixing with stream 2 at the bottom of zone 2 and then passing on to zone 3. This allows the prediction of the temperature within the ash hopper.

6.7.3 Producing the Temperature Profile

Given the relative positions of each of the heat exchangers within the boiler and the locations of the divisions between the zones, Boolean logic functions have been used to calculate which zones are influenced by which heat exchanger. This allows the spreadsheet to calculate what fraction of the total heat exchange for the boiler system occurs in each zone (see Appendix C).

The calculation begins at burner row 1 where half of the flue gas produced circulates zone 1 and half remains in zone 2. The gas enters the zone 1 with an enthalpy change of zero and is therefore at the adiabatic flame temperature. Knowing how much heat energy is removed from the combustion gases in zone 1, (Q_1) and the mass flowrate of the gases circulating in the zone it is possible to calculate the enthalpy change, (Δh_1) of those gases using the steady flow energy equation (6.3). This enthalpy change allows the temperature of the flue gases leaving the zone to be calculated using the temperature – enthalpy change relationship (equation (6.28). Upon leaving zone 1 and re-entering zone 2 the gases mix with the other half of the gases produced from burner row 1. Here the gases mix and equation (6.29) is used to calculate the mean temperature of the two gas streams

$$T_2 = \frac{T_1\left(\frac{\dot{m}_1}{2}\right) + T_a\left(\frac{\dot{m}_1}{2}\right)}{\dot{m}_1} \qquad (6.29)$$

where T_2 is the temperature of the gases at the beginning of zone 2 (°C), T_1 is the temperature of the gases at the end of zone 1 (°C), T_a is the adiabatic flame temperature (°C) and $\dot{m}_1$ is the mass flow-rate of gases produced by the combustion of the fuel injected through burner row 1 (kg/s).

Following this, the mixed stream flows through zone 2, where the heat energy removed in zone 2, (Q_2), is used to calculate the enthalpy change across zone 2, (Δh_2), and hence, the temperature of the flue gases exiting zone 2 (T_{2exit}). And through zone 3, where the temperature change is calculated by the same process, exiting zone 3 with temperature T_{3exit}. Here, the gases mix with those produced by the combustion of gases injected through burner row 2 and assume the mean temperature of the two gas streams (T_4) (equation (6.30))

$$T_3 = \frac{\dot{m}_1 T_{3exit} + \dot{m}_2 T_a}{\dot{m}_1 + \dot{m}_2} \qquad (6.30)$$

Where $\dot{m}_2$ is the mass flow-rate of gases produced by combustion of the fuel injected through burner row 2 (kg/s).

This process continues for all six burner rows producing T_{12}, the temperature of the mixed gas stream of the combustion products of burner rows 1 to 6 (equation (6.31))

$$T_{12} = \frac{T_{11exit}\sum_{n=1}^{n=5}\dot{m}_n + \dot{m}_6 T_a}{\sum_{n=1}^{n=6}\dot{m}_n} \qquad (6.31)$$

Where n denotes the burner row, $\dot{m}_6$ is the mass flow-rate of gases produced by combustion of the fuel injected through burner row 6 (kg/s) and T_{11exit} is the temperature of the flue gas stream at the exit of zone 11 (°C).

Following this, the heat energy removed in each zone (Q_n), the steady flow energy equation (6.3) and the temperature - enthalpy change relationship (6.28) are used to calculate the temperature of the flue gas exiting each zone hence producing the temperature profile for the boiler (Ref. figure 6.14). The profile also includes the location of the heat exchange equipment as dashed lines so that their influence on the gas temperature can be easily visualised.

Since the gas temperature is related only to the energy removed by each heat exchanger and not the temperature of the water or steam within, it is possible for the spreadsheet to predict gas temperatures below the temperature of the water or steam within said heat exchanger. This phenomenon is most likely to occur in the economisers and reheaters in the downward pass and clearly, in reality, should not be possible. In these situations Boolean logic is used to compare the gas temperatures to the temperature of the steam. If the gas temperature at a particular heat exchanger falls below the temperature of the water or steam within said heat exchanger, then the profile temperature is set equal to the steam temperature and not the temperature calculated by the spreadsheet. When this occurs a warning is provided to alert the user that the target temperature has not been reached within that heat exchanger (ref. figure 6.15 and Appendix C).

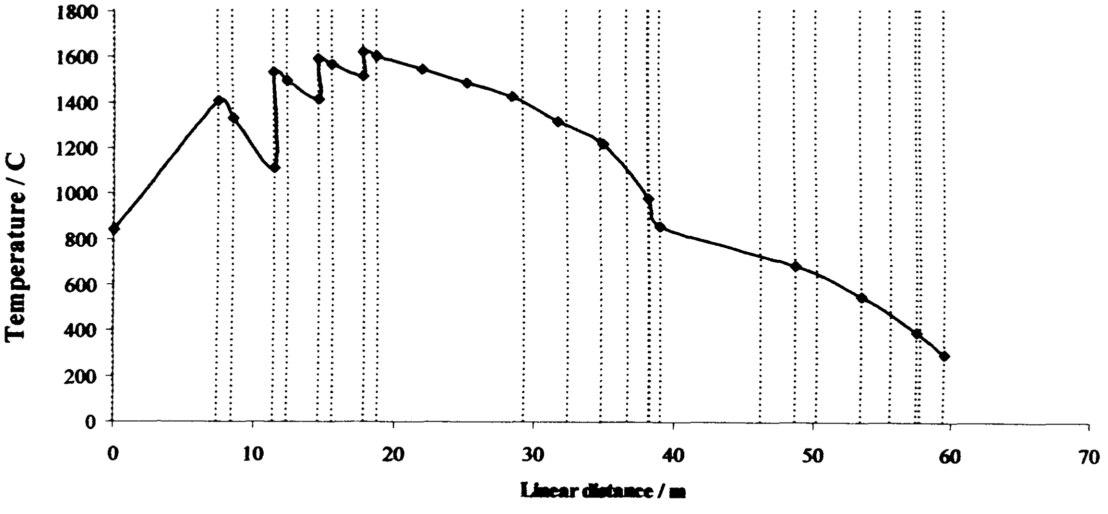

Figure 6.14: Temperature profile for the Langerlo boiler firing 90%$_{th}$ medium volatile coal and 10%$_{th}$ sewage sludge

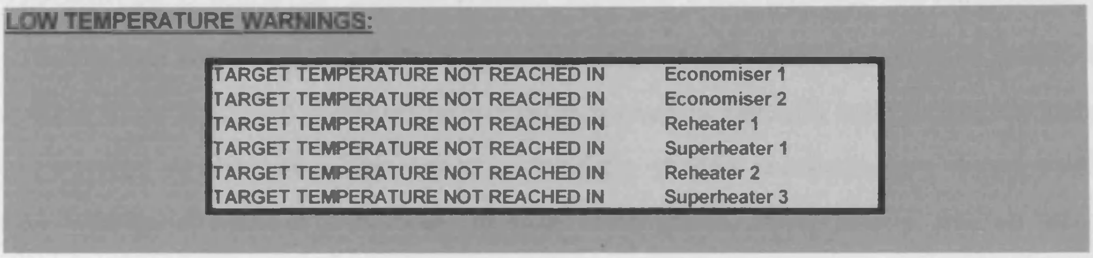

```
LOW TEMPERATURE WARNINGS:
TARGET TEMPERATURE NOT REACHED IN        Economiser 1
TARGET TEMPERATURE NOT REACHED IN        Economiser 2
TARGET TEMPERATURE NOT REACHED IN        Reheater 1
TARGET TEMPERATURE NOT REACHED IN        Superheater 1
TARGET TEMPERATURE NOT REACHED IN        Reheater 2
TARGET TEMPERATURE NOT REACHED IN        Superheater 3
```

Figure 6.15: Example of the temperature warnings displayed to the user when steam temperatures are not met

If these warning flags appear, then the fuel is not producing enough heat energy to satisfy the heat removed by the heat exchangers and the temperature profile is flawed. The user should adjust the settings until the warnings do not appear.

6.8 Creation of a Relationship Linking Gas Temperature to Ash Deposition

In a similar fashion to the creation of the temperature – enthalpy change relationship, this process has been approached in two ways:

1) The creation of empirical correlations between the temperature of the flue gas and the composition of the combustion products
2) The training of an ANN to predict the relationship between gas temperature and the composition of the combustion products.

Similarly, the empirical correlations were derived by the author at Cardiff University and were later expanded upon to create an ANN, by C. K. Tan of The University of Glamorgan, within the scope of the PowerFlam project. The derivation of empirical correlations will be presented for the purposes of this document and an appraisal of the ANN method can be found in Section 6.10.

The relationship between the temperature of the flue gases, the percentage substitution and the potential for slagging and fouling was derived using a thermochemical software and database package called FactSage. "This is the fusion of the FACT-Win / F*A*C*T and ChemSage software packages which consists of a series of information, database, calculation and manipulation modules that enable the user to access and manipulate pure substances and solution databases" [87].

The software features the 'equilib' module, which is a tool that uses the minimisation of Gibbs free energy (Ref. equation (6.32)) to calculate the concentrations of chemical species when specified elements or compounds react or partially react to reach a state of chemical equilibrium. This can be in the form of ideal solutions (gas, liquid, solid and aqueous phases) or non-ideal solutions (real gases, slags, mattes, molten salts, ceramics, alloys etc) [87].

$$\Delta G = \Delta H - T\Delta S \tag{6.32}$$

Where ΔG is the change in Gibbs free energy (kJ), ΔH is the enthalpy (energy) change (kJ/kg), T is the absolute temperature (K) and ΔS is the entropy change (kJ/kgK). Gibbs free energy (G) is the component of the total energy of a system that can do work at a constant temperature and pressure, every system will seek to achieve a minimum of free energy. Hence, if ΔG is equal to zero then the reaction or system is in equilibrium. The software calculates ΔG using a series of pre-defined databases which are selected by the user as the model is created to find an solution as close to equilibrium as possible for the given system.

6.8.1 FactSage model set-up

The 'equilib' module of the software was used to predict the mass of combustion products for a range of temperatures and fuel blends providing a set of correlations between the mass of harmful species evolved and the temperature of the combustion environment. Two separate spreadsheets have been created; one for blends with sewage sludge as the substitute fuel and the second with blends of sawdust. A description of the creation of the sewage sludge spreadsheet will be given.

The fuel data is entered into the software as the mass of combustion products (in grams) per kg of fuel burned. Combustion products are used since the purpose of the calculation is to assess how the combustion products react to form deposits on the heat exchange surfaces and not to predict the combustion process itself. Table 6.15 shows the fuel data used to create the correlations. Along with the fuel data, the temperature and pressure of the system is required. The software was run with system temperatures varying from 127°C (400K) to 1727°C (2000K) at 100°C intervals at atmospheric pressure for each of the fuel data sets shown in table 6.15. The software allows the use of a range of databases which have been created to predict the formation of certain species. The FACT-SLAG-A database was used to predict the formation of liquid slags containing, among others, the main elements of interest for coal combustion: alkali metals and phosphorous, which as stated in Chapter 2 are known to cause slagging and fouling, along with silicon, iron and aluminium which can be molten at elevated temperatures.

Table 6.17: Fuel data inputs for the creation of slagging and fouling correlations

Coal $\%_{th}$	100%	95%	90%	85%	80%	75%	50%	0%
Sewage Sludge $\%_{th}$	0%	5%	10%	15%	20%	25%	50%	100%
CO_2 (grams)	2465.00	2251.00	2067.00	1907.00	1766.00	1642.00	1188.00	701.00
H_2O (grams)	506.00	504.00	502.00	501.00	500.00	499.00	495.00	491.00
N_2 (grams)	8479.00	7805.00	7224.00	6719.00	6276.00	5885.00	4454.00	2922.00
SO_2 (grams)	15.00	15.00	15.00	15.00	15.00	15.00	15.00	15.00
O_2 (grams)	444.00	408.00	377.00	352.00	329.00	308.00	233.00	151.00
Na_2O (grams)	1.01	1.37	1.67	1.92	2.13	2.31	2.92	3.48
K_2O (grams)	1.70	2.47	3.17	3.82	4.41	4.95	7.08	9.63
CaO (grams)	4.03	6.49	9.01	11.48	13.89	16.19	26.00	38.98
Al_2O_3 (grams)	23.56	31.31	37.28	41.96	45.67	48.63	57.01	61.67
MgO (grams)	2.31	3.17	3.89	4.50	5.03	5.48	7.07	8.64
Fe_2O_3 (grams)	8.81	13.56	18.23	22.72	26.99	31.03	47.87	69.52
SiO_2 (grams)	68.23	94.58	116.99	136.29	153.09	167.83	220.85	276.13
SO_3 (grams)	3.27	4.66	5.22	5.53	5.66	5.68	4.86	2.48
TiO_2 (grams)	1.14	1.53	1.84	2.08	2.29	2.46	2.98	3.38
P_2O_5 (grams)	0.27	0.78	1.42	2.10	2.82	3.53	6.80	11.47

6.8.2 Manipulation of the FactSage model outputs

Following the calculation, a table listing all of the products of the calculation and their mass in grams is displayed. The products are displayed as being solid, liquid, gaseous or having been produced by one of the selected databases. For the data sets entered in this case, the table included over 800 different species, some of which occurred in very small quantities. It was necessary to filter out any species which occurred in quantities smaller than 1 milligram in order to keep the result data set to a manageable size.

These results were used to derive a set of correlations which would describe the mass of harmful products as a function of fuel blend and flue gas temperature. For the purposes of describing the process, the derivation of these correlations for solid, gaseous and molten phases of sodium will be discussed. Plots for the potassium, phosphorous, iron, silicon, aluminium and aluminosilicates can be found in Appendix D. The first step of this process was to plot the total mass of solid, gaseous and molten (slag) species containing sodium, potassium, phosphorous, silicon, iron and aluminium as a function of the system temperature. This produced a relationship between the mass of these elements in each phase and the temperature of the flue gases. Plots of these relationships were created for each of the eight blends shown in table 6.17.

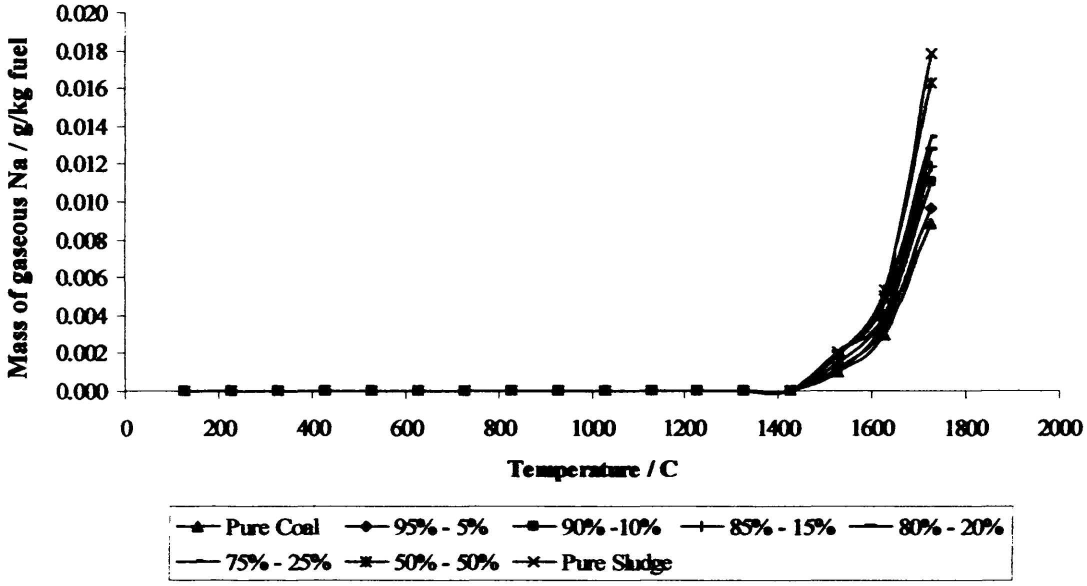

Figure 6.16 - Variation of gaseous Na with temperature for each of the eight blends

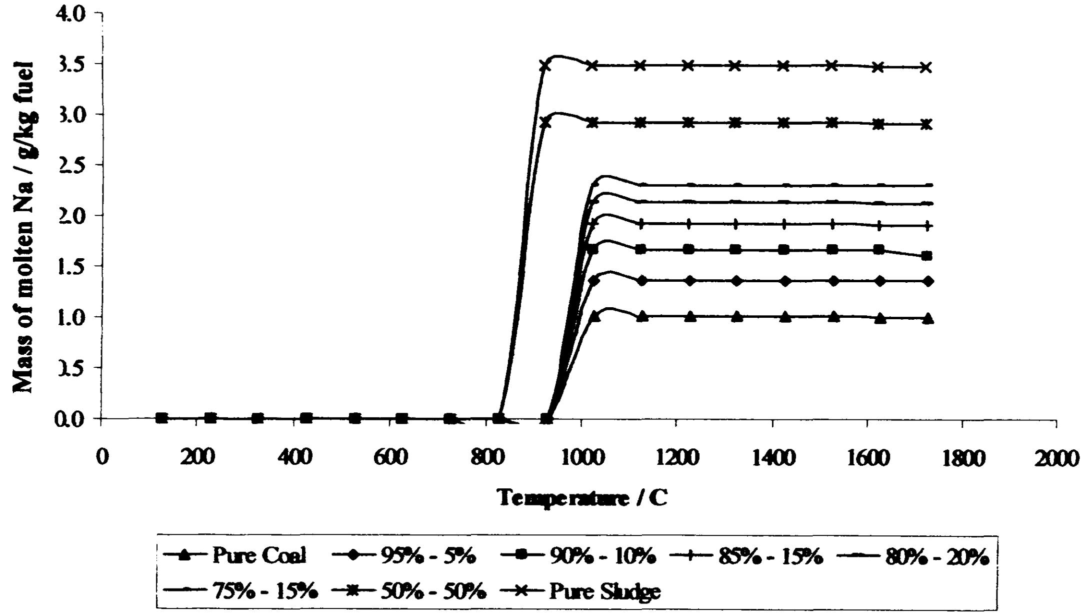

Figure 6.17: Variation of molten Na with temperature for each of the eight blends

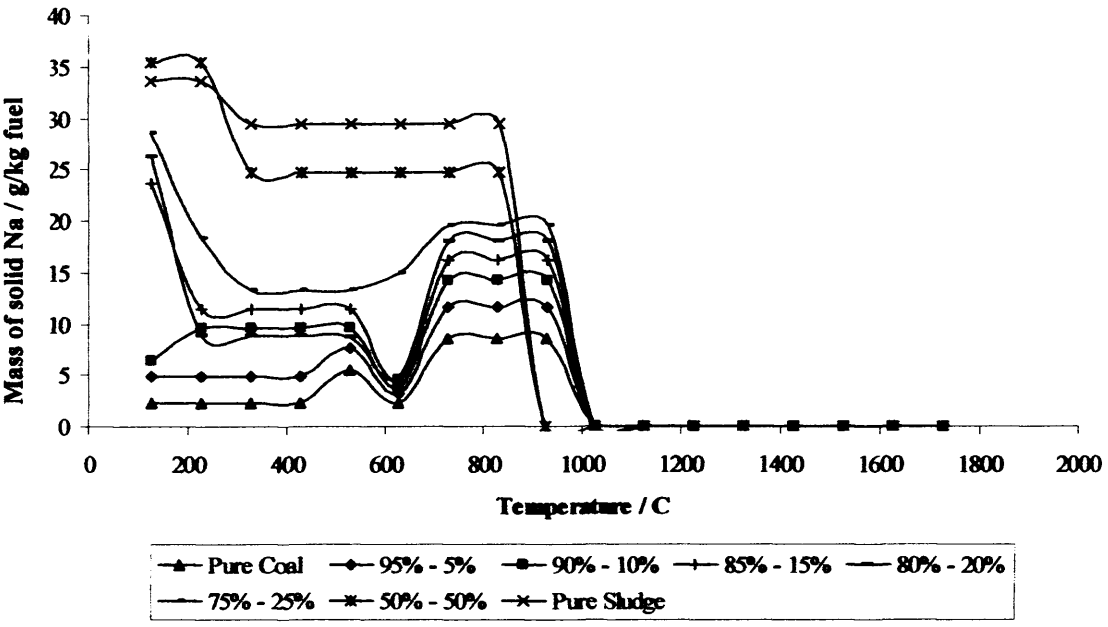

Figure 6.18: Variation of solid Na with temperature for each of the eight blends

Following this, the mass of each product was plotted as a function of fuel blend for each discrete temperature value. The equations of the resulting curves were derived using the trend line function in Excel, giving the mass – blend relationship for each species at discrete temperature values. Some of the more complex plots, in this case the variation of solid Na as a function of temperature (Ref. figure 6.17), were simplified so that fewer equations would be required to describe the system. Figure 6.19 shows this simplification.

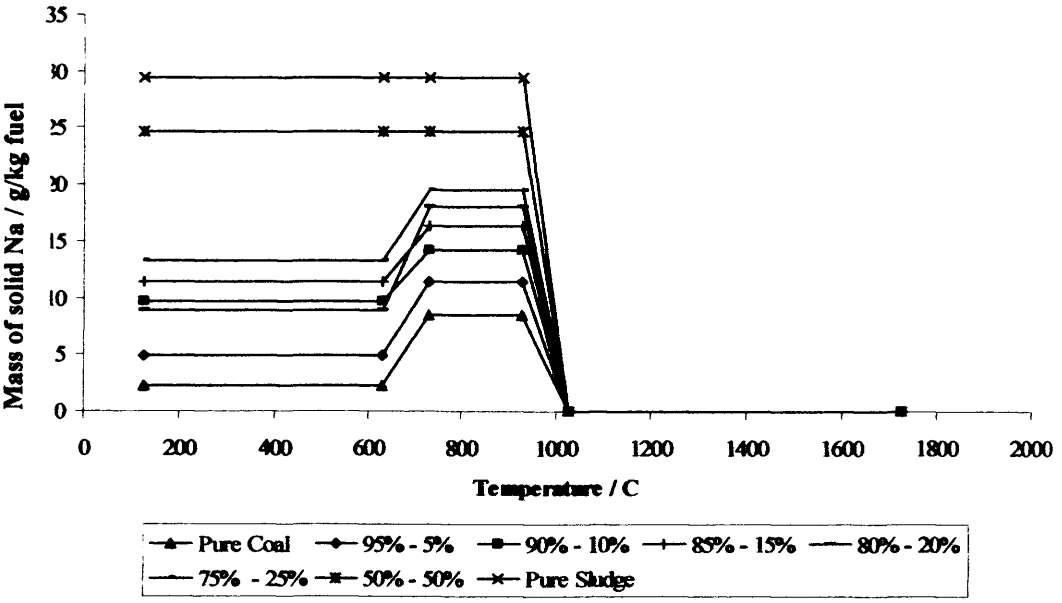

Figure 6.19: Simplification of the variation of solid Na with temperature for each of the 8 blends

The simplification process was implemented by identifying temperature ranges where the mass of products was constant or near constant for every blend, then calculating the mean mass for each blend and applying it across that temperature range. The plots for solid Na, solid K, solid Si, solid Al and solid AlSi species were simplified in this manner. Figures 6.20 and 6.21 show how this simplification reduces the number of mass versus blend plots and hence the number and complexity of the correlations derived. Without simplification, the prediction of the formation of solid Na products as a function of blend and temperature would have required around 15 – 20 equations, however, following the simplification process, only three are needed (equations. (6.38) to (6.40)).

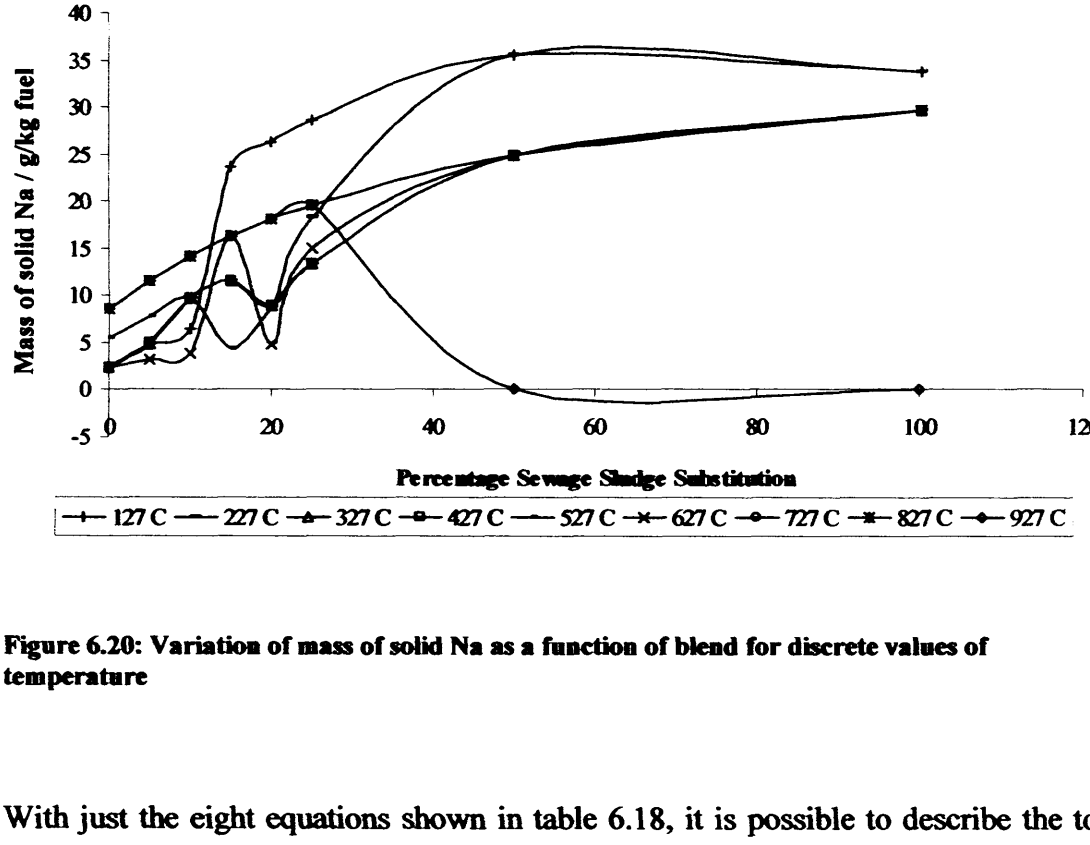

Figure 6.20: Variation of mass of solid Na as a function of blend for discrete values of temperature

With just the eight equations shown in table 6.18, it is possible to describe the total mass of sodium compounds produced for blends of fuel ranging from pure coal to pure sewage sludge within the temperature range 127 to 1727°C. Equations 6.33 to 6.40 are the equations of the curves shown in figures 6.21 to 6.23. The equations derived for potassium, phosphorous, silicon, iron and aluminium can be found in tables D4.4 to D4.16 in Appendix D.

Table 6.18: Mass - blend correlations for sodium compounds

Product and phase	Sewage Sludge Blend / $\%_{th}$	Temperature (Range) / °C	Equation	
Gaseous Na	0 – 100%	1527°C	$m = (8.947\times10^{-9})b^3 - (1.605\times10^{-6})b^2 + (8.319\times10^{-5})b - (7.792\times10^{-4})$	(6.33)
Gaseous Na	0 – 100%	1627°C	$m = (7.712\times10^{-9})b^3 - (1.614\times10^{-6})b^2 + (1.059\times10^{-4})b - (2.835\times10^{-3})$	(6.34)
Gaseous Na	0 – 100%	1727°C	$m = (6.422\times10^{-9})b^3 - (1.941\times10^{-6})b^2 + (2.198\times10^{-4})b - (9.008\times10^{-3})$	(6.35)
Molten Na	25 – 50%	927°C	$m = (1.168\times10^{-1})b - 2.920$	(6.36)
Molten Na	50 – 100%	927°C	$m = (4.090\times10^{-6})b^3 - (8.784\times10^{-4})b^2 + (7.151\times10^{-2})b - 1.024$	(6.37)
Molten Na	0 – 100%	1027 – 1727°C	Equation (6.37)	
Solid Na	0 – 20%	127 – 627°C	$m = -(4.469\times10^{-3})b^3 + (9.588\times10^{-2})b^2 + (1.969\times10^{-1})b + 2.297$	(6.38)
Solid Na	20 – 50%	127 – 627°C	$m = (5.056\times10^{-1})b + 0.394$	(6.39)
Solid Na	50 – 100%	127 – 627°C	$m = (3.490\times10^{-5})b^3 - (7.491\times10^{-3})b^2 + (6.085\times10^{-1})b + 8.611$	(6.40)
Solid Na	0 – 100%	727 – 1027°C	Equation (6.40)	

Where m is the mass of the sodium product (kg) and b is the fuel blend in $\%_{th}$

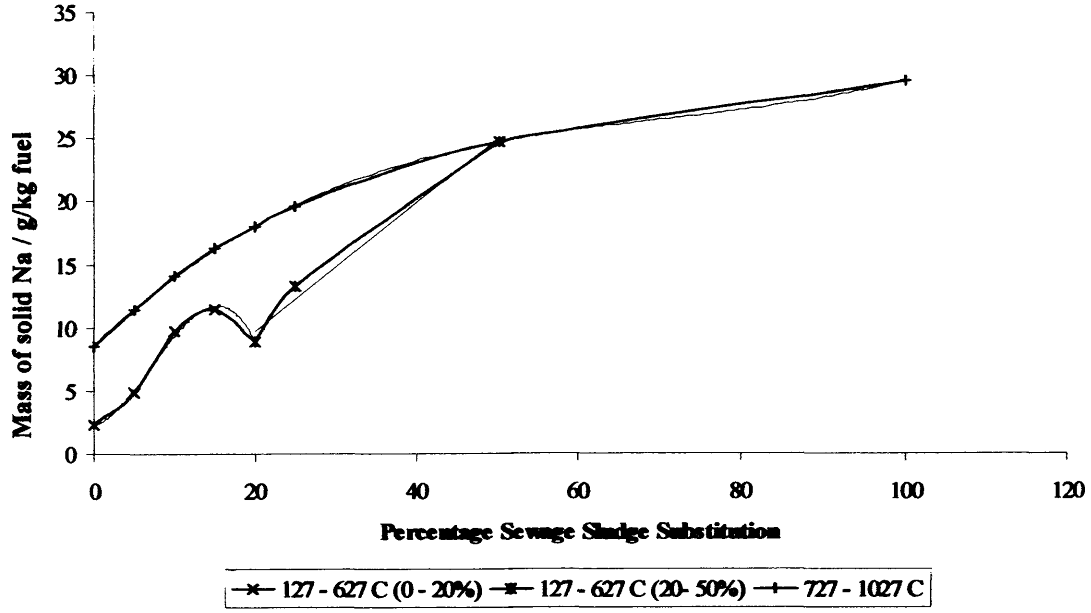

Figure 6.21: Variation of mass of solid Na as a function of blend for discrete values of temperature after simplification

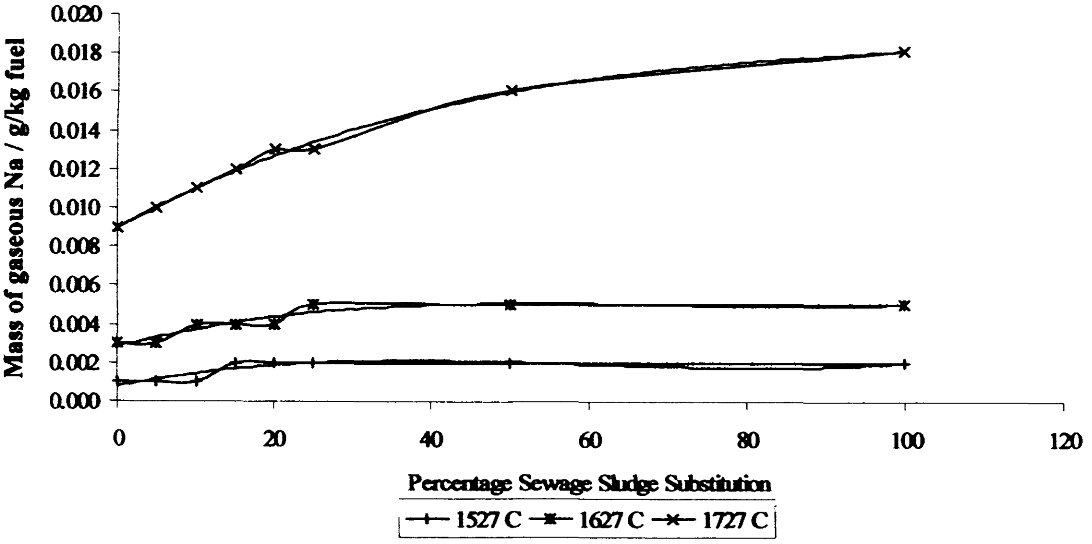

Figure 6.22: Variation of mass of gaseous Na as a function of blend for discrete values of temperature

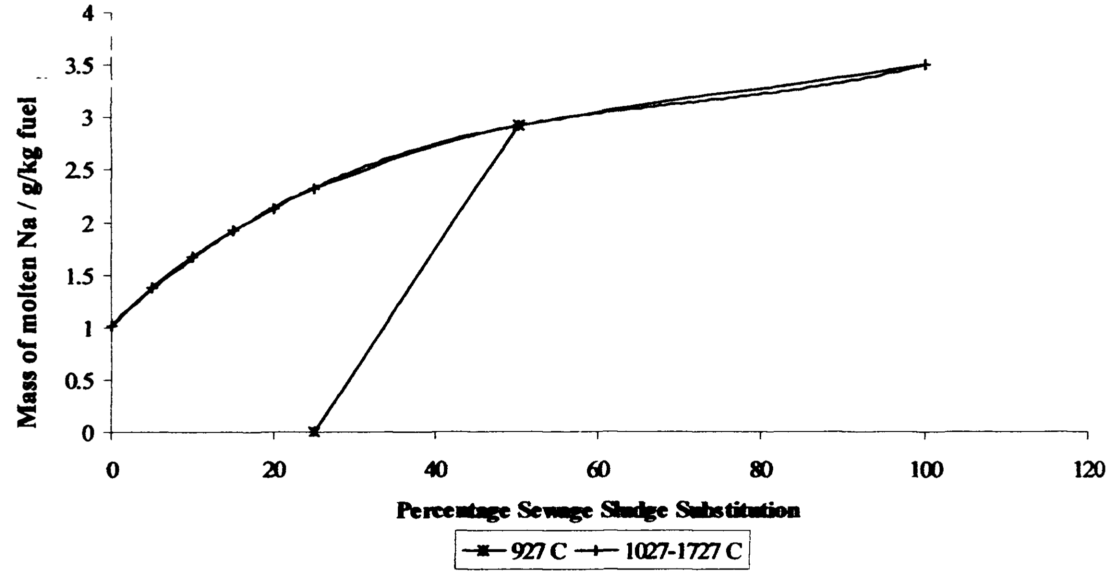

Figure 6.23: Variation of mass of molten Na as a function of blend for discrete values of temperature

6.8.3 Applying the Correlations to the Inputs Entered in the Spreadsheet

The correlations are embedded in the spreadsheet in the slagging worksheet. The spreadsheet generates a mass profile for each phase of sodium, potassium, phosphorous, silicon, iron and aluminium. This is done by calculating the mass of each product for each temperature point in the temperature distance profile. An additional 7 data points at the leading edge of each heat exchanger have been included in the profile to allow better prediction of the mass of products in the heat exchangers. The leading edge of the heat exchangers has been chosen for these data points, rather than the centre, as it is typically the leading edge of a heat exchanger that sees the highest gas temperatures.

For each data point on the profile, the spreadsheet uses Boolean logic functions to select the appropriate correlation to use. This is done by comparing the temperature range that each of the correlations is valid for against the predicted gas temperature at that data point. Once the correct correlation has been identified, the spreadsheet will enter the blend value in $\%_{th}$ of substitute fuel set by the user to give the mass of products produced at that data point. Each of the correlations is valid either for a range of temperatures (for example, equation (6.38) is valid for temperatures between 127°C and 627°C), or for a single discrete temperature (for example, equations (6.33), (6.34) and (6.35) are only valid for 1527°C, 1627°C and 1727°C respectively). If the temperature is outside one of these ranges, or between discrete temperature values, then the spreadsheet will calculate the mass of product using the correlations for the next temperature above and the next temperature below and linearly interpolate between them to give the mass for that particular temperature. This is also done using Boolean logic functions.

After the correlations have been applied, a number of graphs are displayed for reference by the user, these are as follows:

- Solid, molten, gaseous and total sodium species as a function of linear distance along the boiler centreline.
- Solid, molten, gaseous and total potassium species as a function of linear distance along the boiler centreline.
- Solid, gaseous and total phosphorous species as a function of linear distance along the boiler centreline.
- Solid, molten and total silicon species as a function of linear distance along the boiler centreline.
- Solid, molten and total aluminium species as a function of linear distance along the boiler centreline.
- Solid aluminosilicates as a function of linear distance along the boiler centreline.
- Solid, molten, gaseous and total iron species as a function of linear distance along the boiler centreline.
- Comparison of total solid, molten and gaseous species.

In addition to these graphs, warning flags are presented to the user. Figure 6.24 shows an example of these warning flags for a 10%$_{th}$ blend of a typical medium volatile bituminous coal and a typical sewage sludge in the Langerlo boiler, Appendix D shows the functions used to create them. These warning flags are based upon information from the 7 calculation points at the leading edge of each heat exchanger.

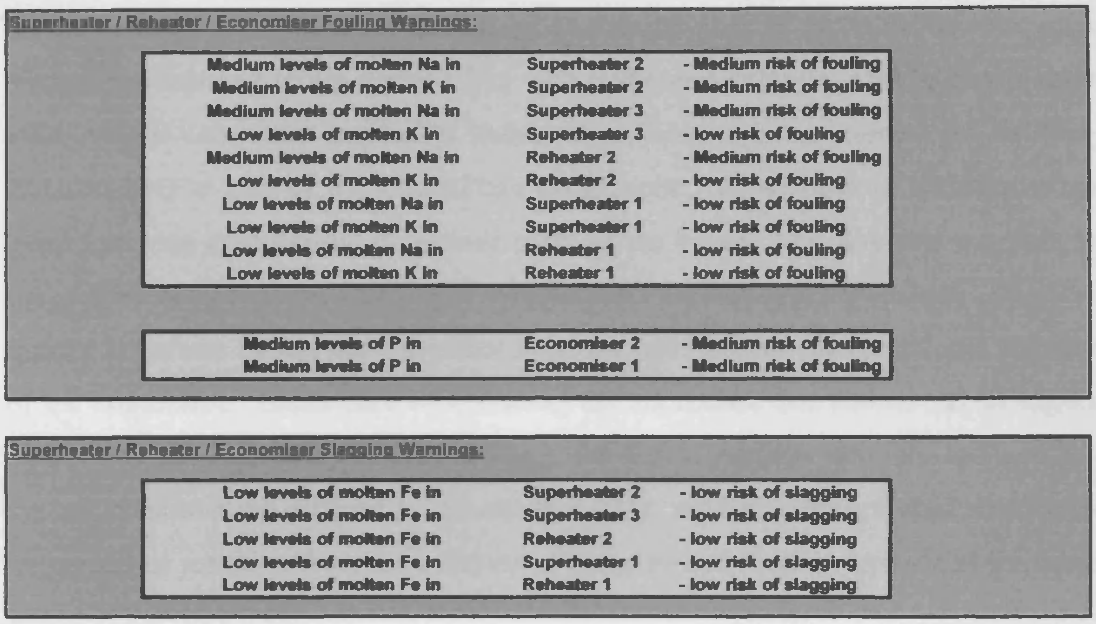

Superheater / Reheater / Economiser Fouling Warnings:

Medium levels of molten Na in	Superheater 2	- Medium risk of fouling
Medium levels of molten K in	Superheater 2	- Medium risk of fouling
Medium levels of molten Na in	Superheater 3	- Medium risk of fouling
Low levels of molten K in	Superheater 3	- low risk of fouling
Medium levels of molten Na in	Reheater 2	- Medium risk of fouling
Low levels of molten K in	Reheater 2	- low risk of fouling
Low levels of molten Na in	Superheater 1	- low risk of fouling
Low levels of molten K in	Superheater 1	- low risk of fouling
Low levels of molten Na in	Reheater 1	- low risk of fouling
Low levels of molten K in	Reheater 1	- low risk of fouling

Medium levels of P in	Economiser 2	- Medium risk of fouling
Medium levels of P in	Economiser 1	- Medium risk of fouling

Superheater / Reheater / Economiser Slagging Warnings:

Low levels of molten Fe in	Superheater 2	- low risk of slagging
Low levels of molten Fe in	Superheater 3	- low risk of slagging
Low levels of molten Fe in	Reheater 2	- low risk of slagging
Low levels of molten Fe in	Superheater 1	- low risk of slagging
Low levels of molten Fe in	Reheater 1	- low risk of slagging

Figure 6.24: An example of the warning flags used to identify areas of concern to the user

The flags identify to the user when there is a low, medium, or high risk of fouling in the superheaters, reheaters and economisers. They also show whether a low, medium or high risk of slagging is present in the superheaters and reheaters. In accordance with the deposition mechanisms for slagging and fouling offered by several authors [43, 44, 47, 55], and presented in Chapter 2, fouling potential in the superheaters and reheaters has been determined by the presence of molten alkali metals in the combustion products. It is believed that these materials coalesce to form aerosol mists of molten alkali salts. These aerosols, deposited on heat transfer surfaces by thermophoresis, form a sticky glue layer which allows the adhesion of larger solid iron and silicon particles to the heat transfer surface. In the economisers, fouling potential is determined by the phosphorous concentration in the combustion products. Slagging potential in the superheaters and reheaters is governed by the presence of molten iron species in the combustion products. As stated in Chapter 2, it is thought that slagging occurs due to the inertial impaction of molten iron rich particles on the heat transfer surfaces [53, 54].

The warnings are triggered when the values of these molten species reach or exceed thresholds set in the spreadsheet. These thresholds have been identified based upon operational experience, provided by Laborelec, gained with the Langerlo boiler, firing blends of sewage sludge and medium volatile bituminous coal. This was supplemented by the expertise gained by co-firing blends of up to 20%$_{th}$ of sewage sludge, sawdust and refuse derived fuel with pulverised coal in a 150kW bench-scale twin cyclone combustor at Cardiff University. This work was carried out by Abd-Rahman [94] as part of the PowerFlam programme. In addition to the knowledge gained on slag composition in various parts of the boiler, Abd-Rahman was able to make observations on the quantity of slagging and fouling deposits formed within the system at various blends and the effect these deposits had on the operational stability of the combustor. Experience of operating the combustor has shown that at higher blends (10, 15 and 20%$_{th}$ sewage sludge), far more deposits were formed and the system became more difficult to operate smoothly; suffering from forced shutdowns by blockages resulting from the build-up of slagging and fouling deposits in the latter stages of the combustor.

In light of these findings, the thresholds were set by simulating a 5%$_{th}$ blend of sewage sludge and medium volatile bituminous coal within the Langerlo boiler using the spreadsheet, and noting the mass of molten sodium, potassium and iron products. These masses were then used to set the threshold between low and medium risk of slagging and fouling problems. This was possible as experience of co-combustion of sewage sludge in 2.5%$_{th}$ and 5%$_{th}$ blends at the Langerlo boiler has shown no significant problems caused by slagging and fouling [95]. From the work that was carried out by Abd-Rahman at Cardiff University [94], it was possible to deduce the thermal blends of sewage sludge and coal of 10% or more would begin to present significant problems for the boiler operator. Therefore, using the same fuels for the Langerlo boiler in the spreadsheet, a blend of 10%$_{th}$ sewage sludge was simulated using the spreadsheet and the masses of the molten sodium, potassium and iron were noted. These masses were set as the threshold between a medium and a high risk of slagging and fouling problems occurring.

The fouling thresholds were set as follows:

Fouling within the superheaters and reheaters due to the presence of molten sodium (g/kg fuel burned):

- $Na_{molten} < 1.0$ Low risk of fouling due to the presence of Na
- $1.0 < Na_{molten} < 1.2$ Medium risk of fouling due to the presence of Na

• $1.2 < Na_{molten}$	High risk of fouling due to the presence of Na

Fouling within the superheaters and reheaters due to the presence of molten potassium (g/kg of fuel burned):

• $K_{molten} < 0.3$	Low risk of fouling due to the presence of K
• $0.3 < K_{molten} < 1.0$	Medium risk of fouling due to the presence of K
• $1.0 < K_{molten}$	High risk of fouling due to the presence of K

Fouling within the economisers due to the presence of phosphorous (g/kg of fuel burned)

• $P_{total} < 1.0$	Low risk of fouling due to the presence of P
• $1.0 < P_{total} < 2.0$	Medium risk of fouling due to the presence of P
• $2.0 < P_{total}$	High risk of fouling due to the presence of P

Slagging within the superheaters and reheaters due to the presence of molten iron (g/kg of fuel burned)

• $Fe_{molten} < 5.0$	Low risk of slagging due to the presence of Fe
• $5.0 < Fe_{molten} <10.0$	Medium risk of slagging due to the presence of Fe
• $10.0 < Fe_{molten}$	High risk of slagging due to the presence of Fe.

6.9 Development of a High Temperature Corrosion Model.

In conjunction with the slagging model, the spreadsheet uses the temperature profile to predict the potential for boiler damage caused by high temperature corrosion. A model has been developed which predicts the formation of corrosive species known to attack the heat transfer surfaces, particularly in the high temperature regions of the boiler such as the platen superheater banks.

6.9.1 The High Temperature Corrosion Mechanism

The discussions in Chapter 3 have led to the selection of the following mechanism to model the high temperature corrosion within the boiler; this is based upon the corrosion mechanism suggested by Srivastava and Godiwalla [63] and takes in aspects of the work done by Hendry and Lees [59] and Cain and Nelson [66]. Figure 6.25 shows schematically how the mechanism works.

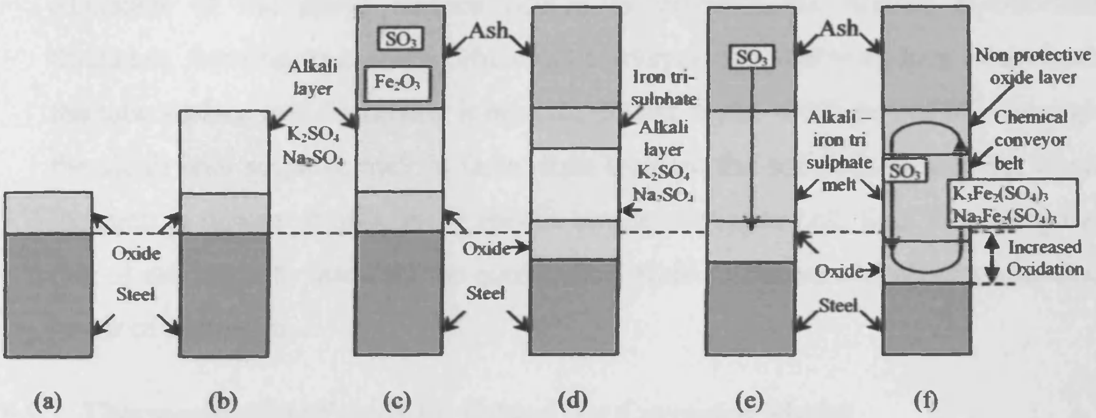

Figure 6.25 - Schematic showing the progression of the high temperature corrosion model

(a) A metal oxide film is formed on the outer surface of the heat exchanger tube.

(b) Alkali sulphates (K_2SO_4 and Na_2SO_4 originating from the alkalis in the fuel ash and sulphates in the boiler atmosphere) deposit on the oxide layer. As this layer grows, its outer surface temperature approaches their melting temperature and the deposit becomes sticky.

(c) Particles of fly ash are captured by the sticky layer and are heated to the point where SO_3 is released through thermal dissociation of sulphur compounds in the ash. This SO_3 reacts with the iron oxide (Fe_2O_3) on the metal surface to form iron trisulphate $Fe_2(SO_4)_3$. As the oxide layer reacts with the SO_3, further oxidation of the metal surface occurs to provide the normal equilibrium thickness of scale

(d) In sufficient quantities, (approx $25\%_{mol}$), when mixed with the alkali salts K_2SO_4 and Na_2SO_4 adjacent to the ash layer, the iron trisulphate will react to form the alkali iron trisulphates $K_3Fe(SO_4)_3$ and $Na_3Fe(SO_4)_3$. These species melt at a considerably lower temperature than the alkali salts and therefore provide a better medium for SO_3 diffusion from the flue gas to the metal surface than the solid alkali salts.

(e) As the thickness of the melt increases, so does the temperature of its outer surface. As this temperature approaches 720°C, the alkali iron trisulphates begin to dissociate releasing SO_3, iron oxide and alkali sulphate. The iron oxide forms a non-protective oxide layer between the ash layer and the alkali iron trisulphate melt.

(f) The SO_3 released by this process then diffuses back towards the cooler metal surface where it reacts with the oxide to form more iron trisulphate. Again, oxidation of the metal surface occurs to maintain the normal equilibrium thickness, forming in essence 'chemical conveyor belt' carrying iron away from the tube surface and depositing it beneath the ash layer. Diffusion of SO_3 through the alkali iron sulphate melt is faster than through the solid alkali salts so, when the melt is present it effectively speeds up the conveyor belt, thus increasing the rate of oxidation to maintain the equilibrium scale thickness and causing elevated levels of corrosion.

6.9.2 Thermochemical Principles Behind the Corrosion Model

From the discussions in Chapter 3 it is evident that the most important causal factor of elevated corrosion is the alkali iron trisulphate melt. It is important to note that without the alkali iron trisulphate melt corrosion still occurs, but the corrosion rate is much lower (equal to that caused by gaseous oxidation controlled by bulk solid state diffusion of SO_3 through the alkali salts). When the alkali iron trisulphate melt is present, the corrosion rate increases and is controlled by the rate at which SO_3 can be transported through the melt, which is in turn governed by the local partial pressure of SO_3.

The model aims to predict the formation of the alkali iron trisulphate melt based upon the composition of the deposited ash. In this instance, the FactSage thermochemical software package has been used to generate empirical correlations which predict the composition of the deposits on the heat exchanger tubes. The predicted composition of the deposit is combined with the liquidus temperature of the ternary system: Na_2SO_4-K_2SO_4-$Fe_2(SO_4)_3$ to determine the phase of the alkali-iron sulphate mix. If the mix is in a solid state then the corrosion levels remain normal, however, if it is molten then elevated levels of corrosion will be seen. The severity of corrosion is based purely on the composition and not the quantity of the deposits as composition is the critical factor that determines the formation of the alkali iron trisulphate melt.

6.9.2.1 The ternary system Na_2SO_4-K_2SO_4-$Fe_2(SO_4)_3$

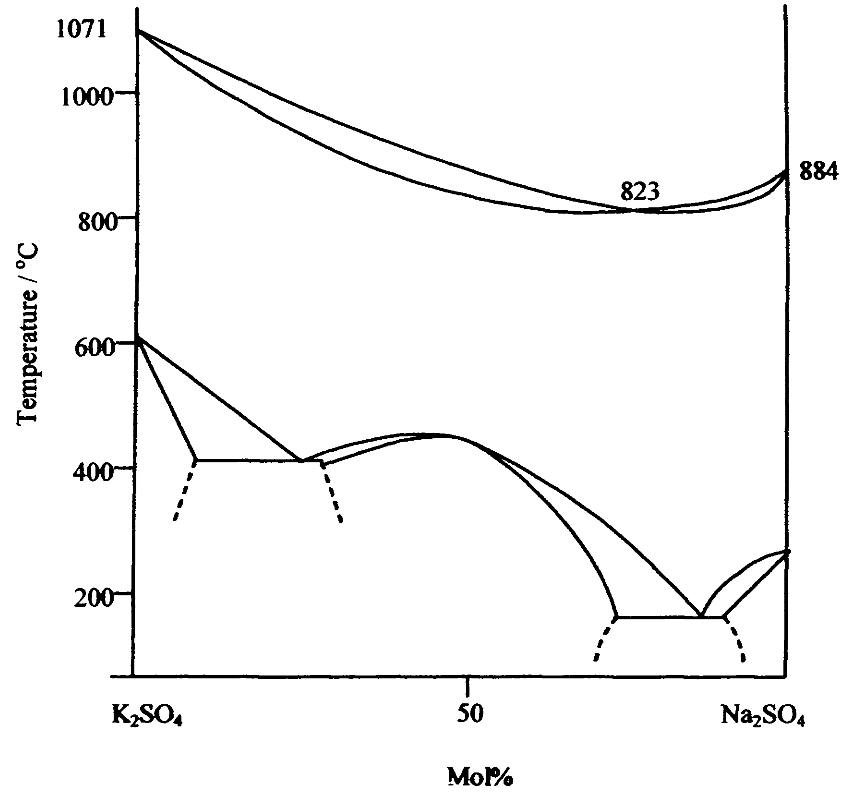

Figure 6.26: The phase diagram for the binary system Na_2SO_4 – K_2SO_4

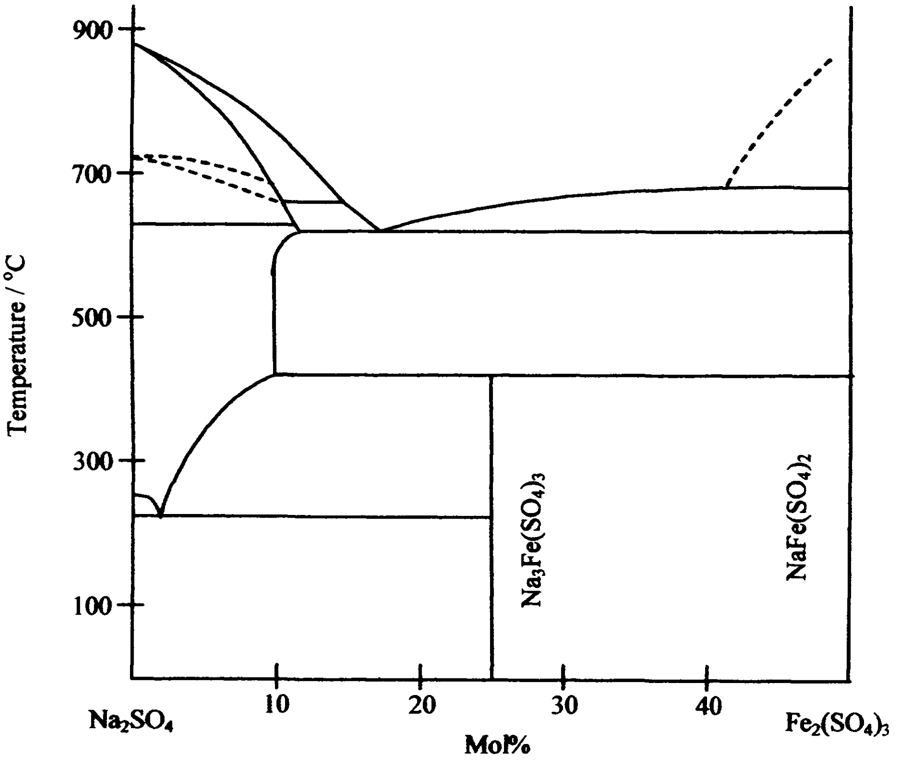

Figure 6.27: The phase diagram for the binary system Na_2SO_4 – $Fe_2(SO_4)_3$

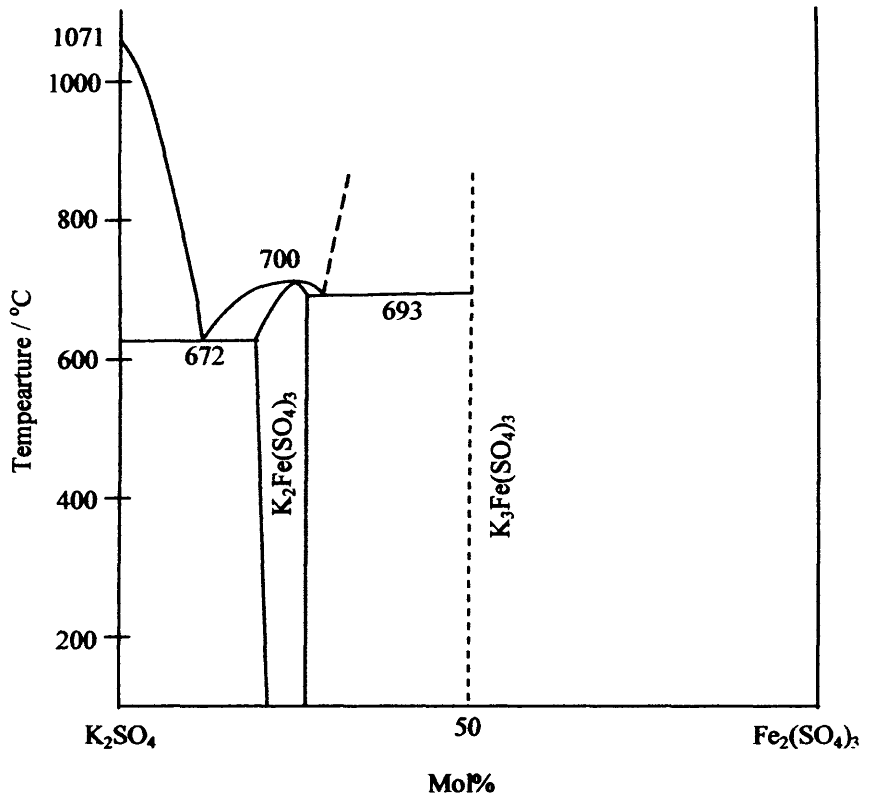

Figure 6.28: The phase diagram for the binary system $K_2SO_4 - Fe_2(SO_4)_3$

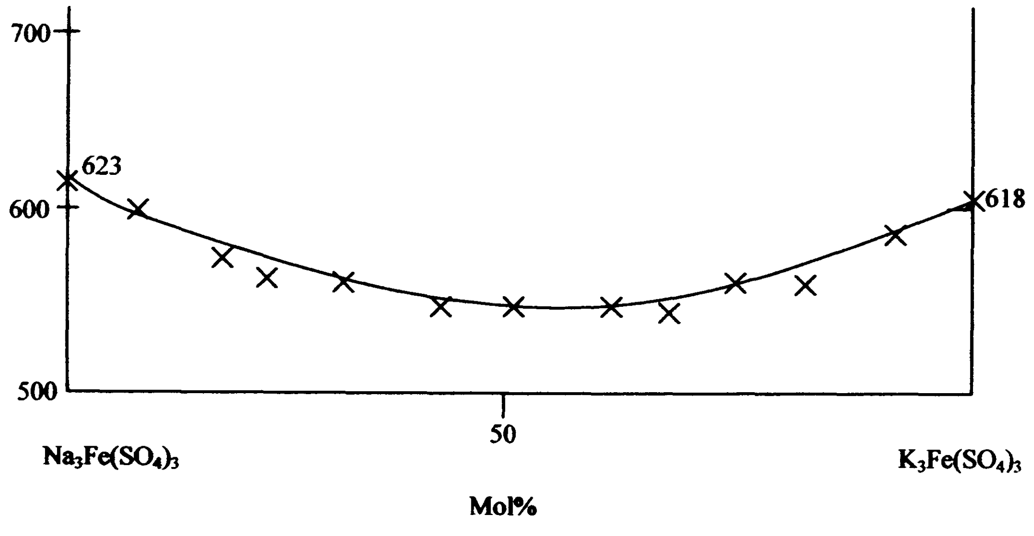

Figure 6.29: Experimentally derived melting temperature for the binary system $Na_3Fe(SO_4)_3 - K_3Fe(SO_4)_3$ [59]

The FactSage thermochemical software package has been used to calculate the melting temperature of the three binary sulphate systems Na_2SO_4-K_2SO_4, Na_2SO_4-$Fe_2(SO_4)_3$ and K_2SO_4-$Fe_2(SO_4)_3$ as shown in figure 3.1 (page 41). This has been combined with the binary tri-sulphate system $Na_3Fe(SO_4)_3$-$K_3Fe(SO_4)_3$. Figures 6.27 and 6.28 show the phase diagrams for the Na_2SO_4-$Fe_2(SO_4)_3$ system and the K_2SO_4-$Fe_2(SO_4)_3$ system respectively. From the Na_2SO_4-$Fe_2(SO_4)_3$ diagram, it can be seen that the molten alkali iron trisulphate $Na_3Fe(SO_4)_3$ forms at approximately $18.5\%_{mol}$ Na_2SO_4 - $81.5\%_{mol}$ $Fe_2(SO_4)_3$, with a melting temperature of 623°C. The K_2SO_4-$Fe_2(SO_4)_3$ diagram reveals that the alkali iron trisulphate $K_3Fe(SO_4)_3$ forms at approximately $12.5\%_{mol}$ K_2SO_4, $87.5\%_{mol}$ $Fe_2(SO_4)_3$, with a melting temperature of 618°C.

The melting temperature of the Na_2SO_4-K_2SO_4 system is shown in figure 6.26, this reveals a melting temperature for pure Na_2SO_4 of 884°C and 1071°C for pure K_2SO_4. There is a minimum melting temperature of 830°C at $74.5\%_{mol}$ Na_2SO_4, $25.5\%_{mol}$ K_2SO_4. This has been combined with figure 6.29 which shows the results of experimental work done by Hendry and Lees [59]. Their work has revealed the melting temperatures of sodium and potassium iron trisulphates at 623°C and 618°C respectively. The work shows the melting points of various mixtures of the alkali iron trisulphates, measured in a simulated flue gas atmosphere. Furthermore, Figure 6.29 reveals a minimum melting temperature of around 550°C for a 1:1 to 2:1 mix of $K_3Fe(SO_4)_3$ to $Na_3Fe(SO_4)_3$.

Using the above binary systems, a family of curves has been created (see Appendix E). These curves are estimates of the melting temperature for a range of sodium sulphate – potassium sulphate ratios from 100% Na_2SO_4 to 100% K_2SO_4 as $Fe_2(SO_4)_3$ concentration varies. They have been created by interpolating between the Na_2SO_4-$Fe_2(SO_4)_3$ system and the K_2SO_4-$Fe_2(SO_4)_3$ system along the liquidus curves for the Na_2SO_4-K_2SO_4 system and the $Na_3Fe(SO_4)_3$-$K_3Fe(SO_4)_3$ system. Essentially, the correlations describe the melting temperature of the system as a function of $Fe_2(SO_4)_3$ for discrete Na_2SO_4-K_2SO_4 compositions. These relationships have been inserted into the spreadsheet, in essence, providing a 'melting temperature map' for compositions of sodium and potassium salts mixed with up to $50\%_{mol}$ iron trisulphate.

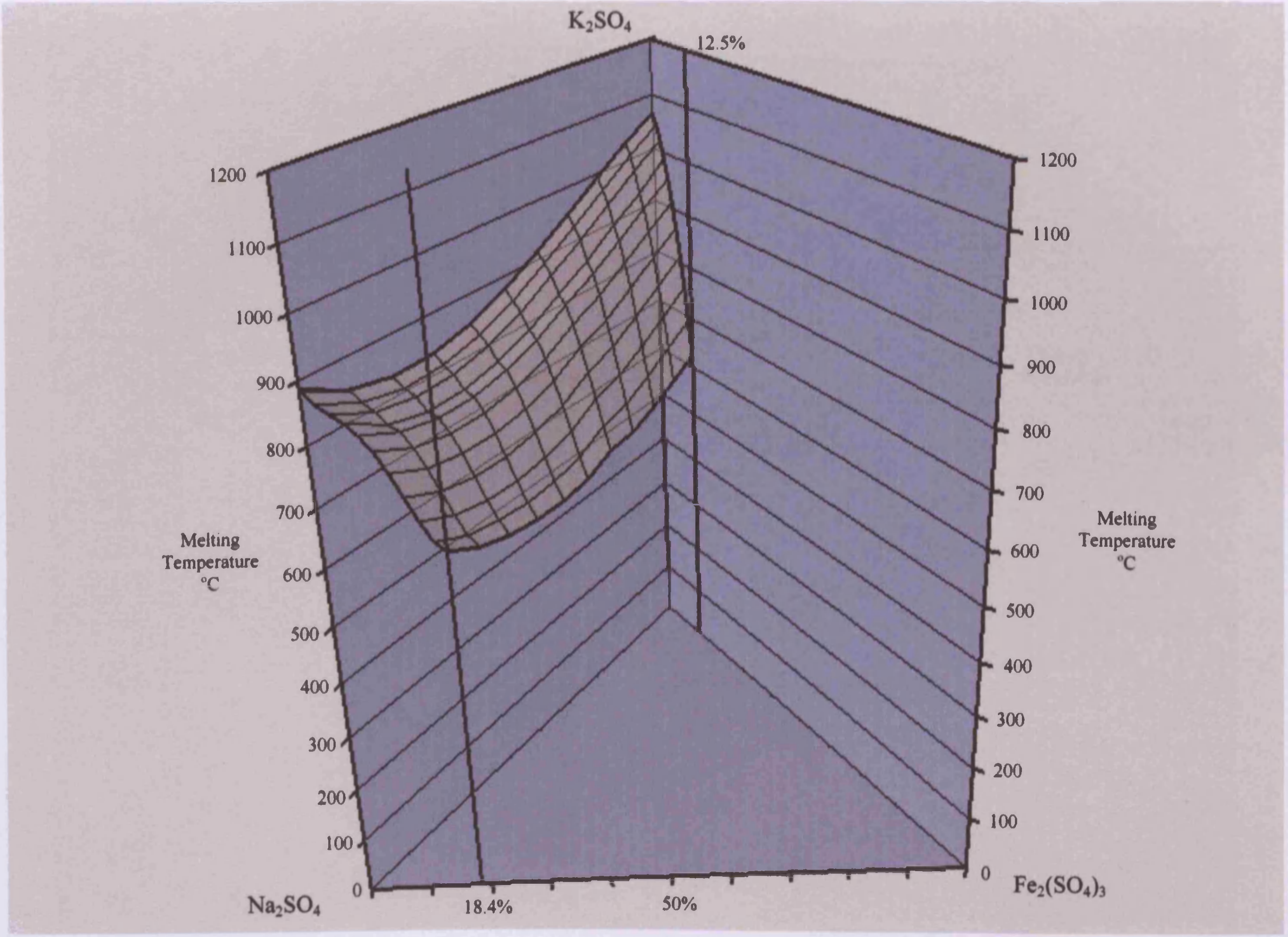

Figure 6.30: Region A of the 'melting temperature map' for the ternary system Na_2SO_4-K_2SO_4-$Fe_2(SO_4)_3$

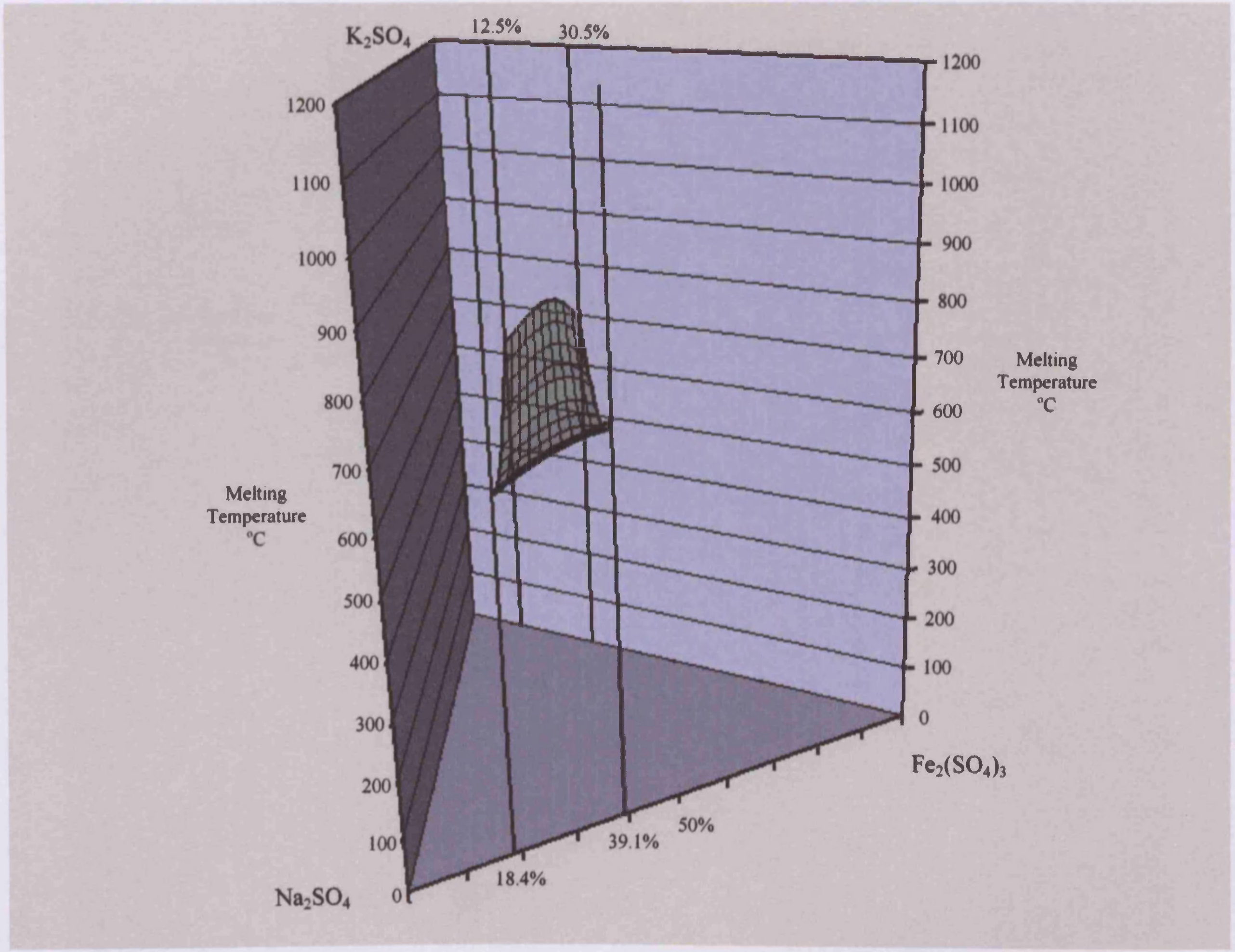

Figure 6.31: Region B of the 'melting temperature map' for the ternary system Na_2SO_4-K_2SO_4-$Fe_2(SO_4)_3$

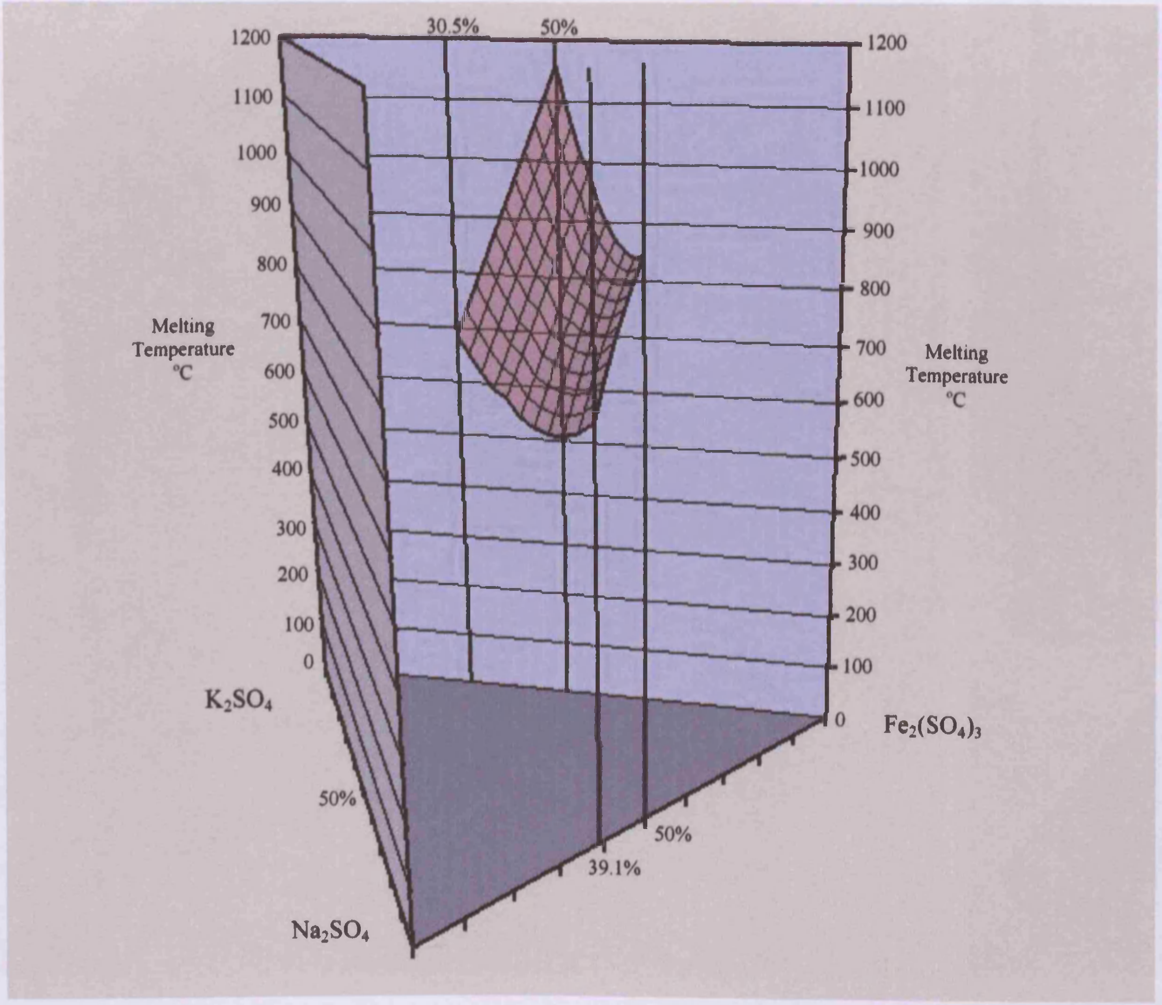

Figure 6.32: Region C of the 'melting temperature map' for the ternary system Na_2SO_4-K_2SO_4-$Fe_2(SO_4)_3$

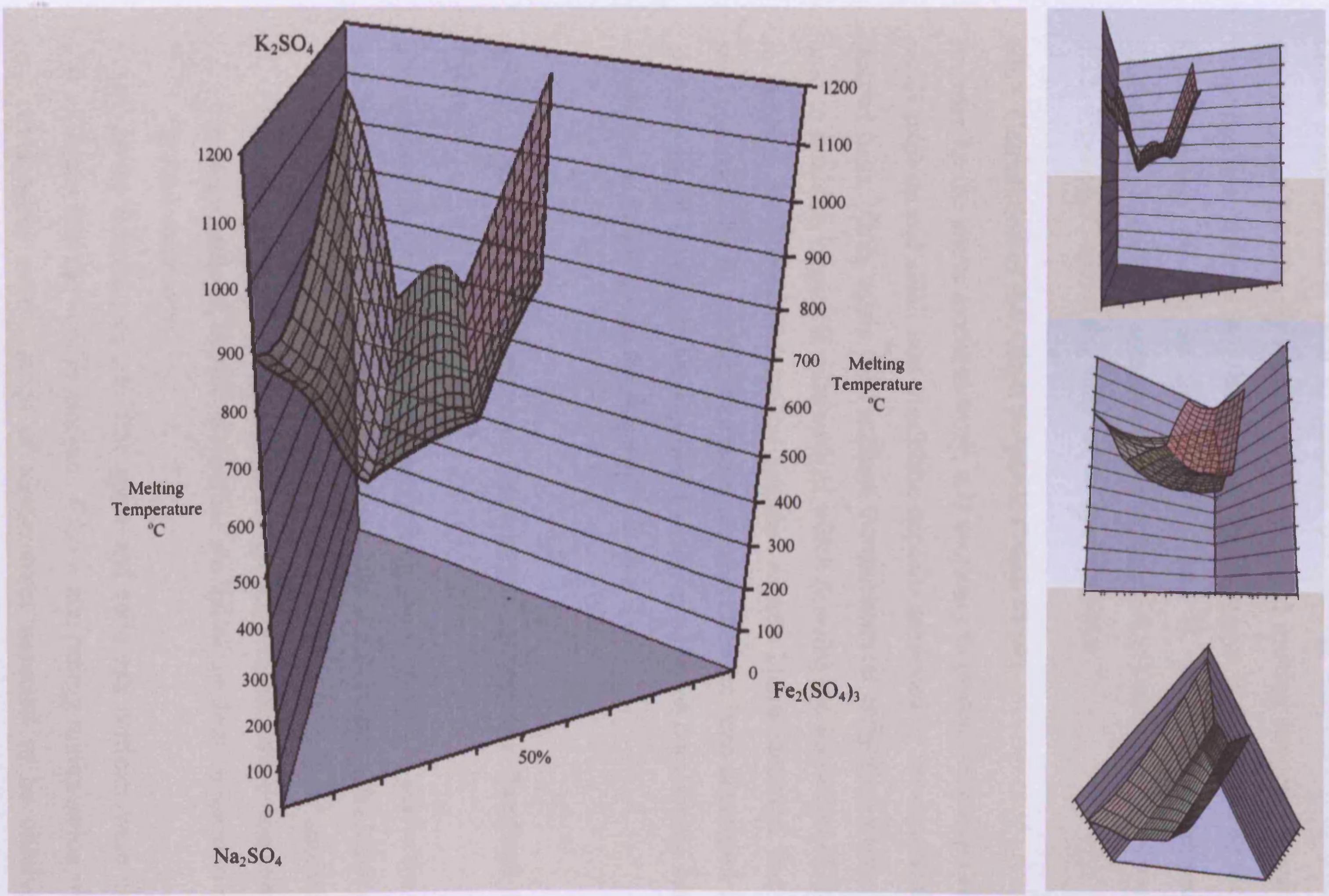

Figure 6.33: The 'melting temperature map' for the ternary system Na_2SO_4-K_2SO_4-$Fe_2(SO_4)_3$

The spreadsheet uses this 'map' shown in figures 6.30 to 6.33 to establish whether an alkali sulphate melt will occur for any particular composition of alkali salts and iron trisulphate produced by the combustion of the fuels entered into the spreadsheet. Linear interpolation is used to calculate the melting temperature of compositions which do not fall directly on one of the estimated melting temperature curves. The 'map' has been divided into three zones, zone A which is dominated by the Na_2SO_4-K_2SO_4 system (shown in figure 6.30), zone B which is dominated by the $Na_3Fe(SO_4)_3$-$K_3Fe(SO_4)_3$ system (shown in figure 6.31) and zone C shown in figure 6.32. Figure 6.33 shows the 'map' of the entire system.

6.9.3 Calculation of the Alkali Sulphate Composition

In order for the above model to work, it is necessary to predict the composition of the alkali sulphate and alkali iron trisulphate deposits produced by the combustion of the desired fuels. Once again the FactSage thermochemical software package has been used to establish empirical relationships which describe the formation of the species in question for blends of a typical medium volatile bituminous coal and a typical sewage sludge. In its present state the spreadsheet has not been developed to include an ANN model to replace the empirical indices, as has been done for the temperature – enthalpy relationship and the slagging indices.

6.9.3.1 Development Empirical Correlations Using the FactSage Software Package

The FactSage thermochemical software package has been used to derive the empirical indices using a vapour deposition technique. This is a three step calculation process:

- In the first step, the coal, air and ash compositions were entered into the FactSage equilib module. Gibb's free energy minimisation was carried out at a temperature of 1600°C to simulate the initial combustion reaction of the coal in the burner zone.
- In the Second step, the flue gases and solid ash particles were used at the inputs into the equilib module. Gibb's free energy minimisation was carried out again over a range of temperatures expected to be observed in the convective pass of a boiler. This range was from 1400°C typically seen by the

platen superheaters in the radiant section to 350°C experienced in the latter stages of the economiser section, producing a typical flue gas composition for that particular temperature.

- The third step of the process sees a range of estimated steel tube surface temperatures from 650°C to 300°C used to simulate vapour deposition. This was achieved by using the gas phase species from the second step of the process as the input into the equilib module, and performing Gibb's free energy minimisation at temperatures within the range 650°C to 300°C to simulate the flue gases coming into contact with the superheater tubes. Any solid species formed during this process are assumed to have formed by the condensation of species from the gas phase. It was assumed that all of these species adhered to the tube surface thus allowing the prediction of the deposit composition.
- During this last step several specific databases were used which dealt specifically with the formation of alkali salts and trisulphates. These were:
    - FACT SALT - predicts the formation of liquid salts of K and Na among other species
    - FACT CSOB - predicts the formation of solid alkali salts including Na_2SO_4 and K_2SO_4.
    - FACT NKSO - predicts the formation of solid Na_2SO_4 and K_2SO_4 at low temperatures in high Na_2SO_4 mixtures.
    - FACT KSO - predicts the formation of solid Na_2SO_4 and K_2SO_4 at low temperatures in high K_2SO_4 mixtures.
    - FACT KNSO - predicts the formation of $K_3Na(SO_4)_2$.
    - FACT SSUL – predicts the formation of solid Na_2SO_4.

Predictions of flue gas composition were made in step two for temperatures in the range 1400°C to 350°C at 50°C intervals. Step 3 was carried out at each of these discrete temperature points, whereby the gases were cooled to temperatures in the range 650°C to 300°C again at 50°C intervals. For each temperature point in step 3, the mass of deposited species was noted along with the mass of SO_3. This process was carried out for a range of blends of pure coal, 5%, 10%, 15%, 20%, 25% and 50% sewage sludge.

These masses were then used to derive empirical correlations relating the mass of deposited alkali salts and iron trisulphate to the temperature of the combustion gases for each discrete tube surface temperature value. Figures 6.34 to 6.39 show examples of these curves for Na_2SO_4, K_2SO_4 and $Fe_2(SO_4)_3$ at a 10%$_{th}$ blend of sewage sludge and medium volatile bituminous coal. Curves for the remaining blends and tube temperatures can be found in Appendix E.

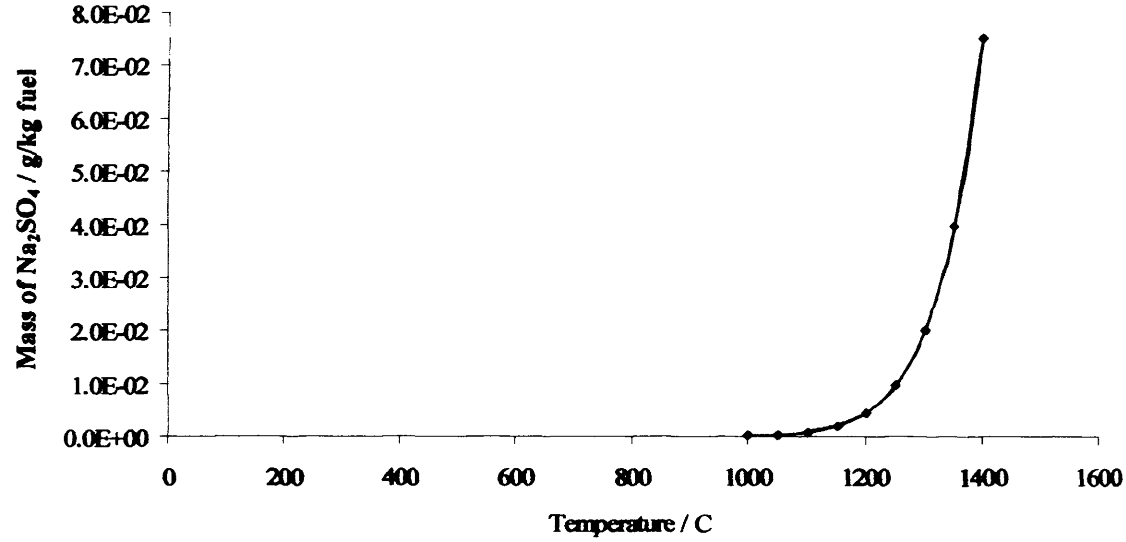

Figure 6.34: Variation of deposited Na_2SO_4 with temperature for tube temperatures of 650°C to 350°C at flue gas temperatures above 1000°C for a 10%$_{th}$ sewage sludge blend

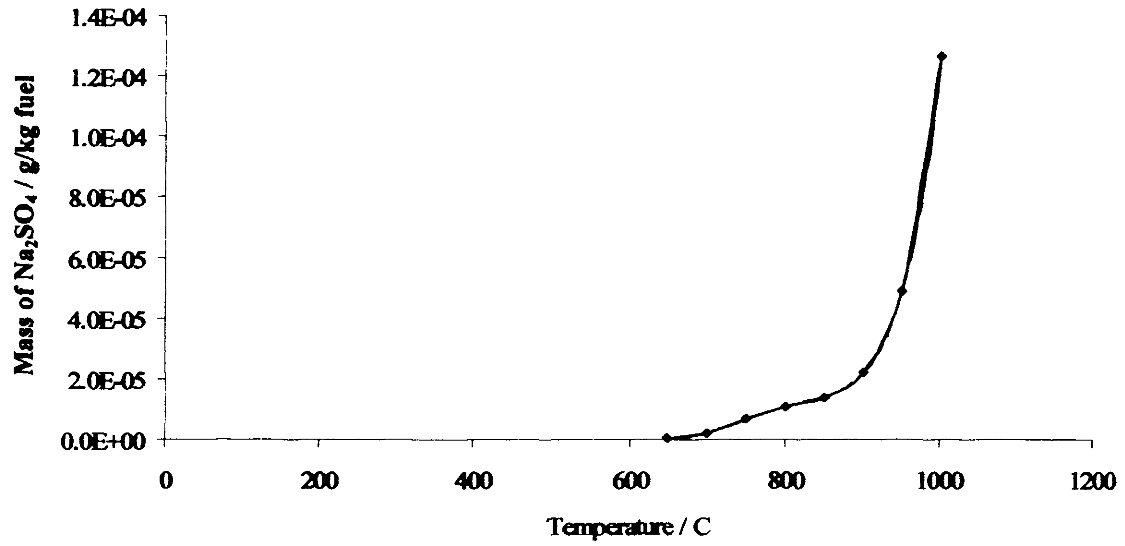

Figure 6.35: Variation of deposited Na_2SO_4 with temperature for tube temperatures of 650°C to 350°C at flue gas temperatures below 1000°C for a 10%$_{th}$ sewage sludge blend

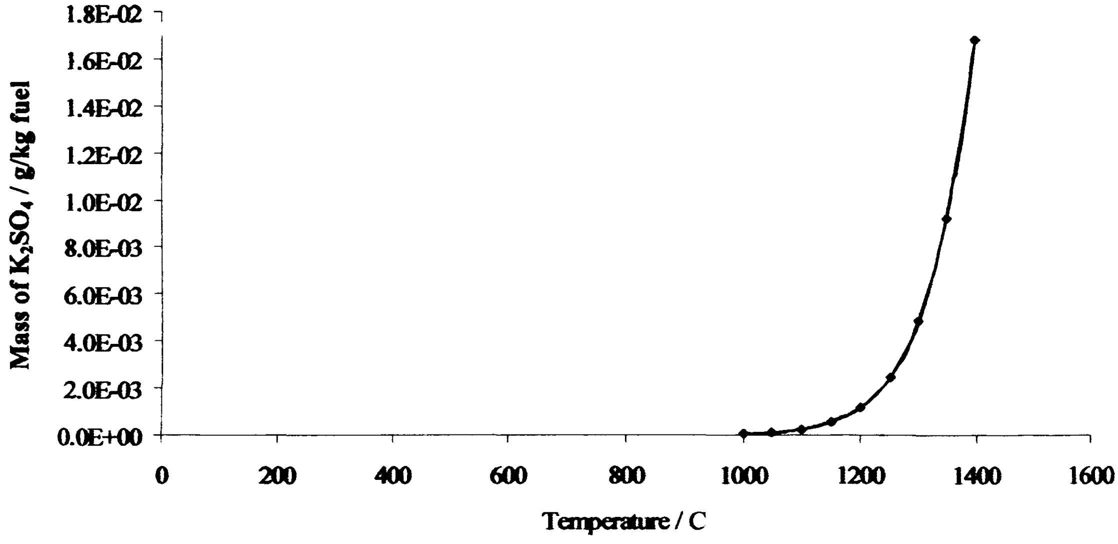

Figure 6.36: Variation of deposited K_2SO_4 with temperature for tube temperatures of 650°C to 350°C at flue gas temperatures above 1000°C for a 10%$_{th}$ sewage sludge blend

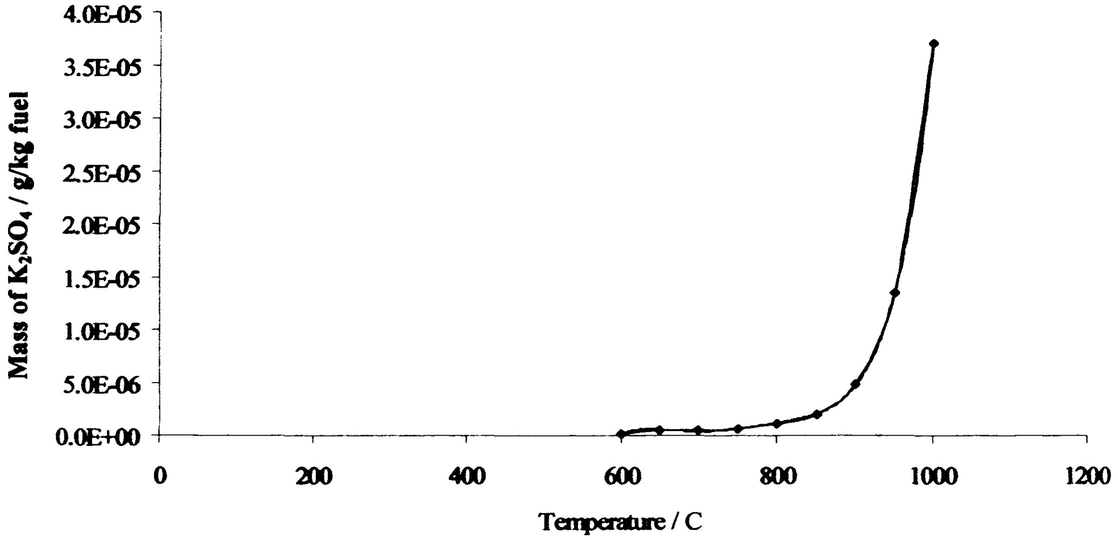

Figure 6.37: Variation of deposited K_2SO_4 with temperature for tube temperatures of 650°C to 350°C at flue gas temperatures below 1050°C for a 10%$_{th}$ sewage sludge blend

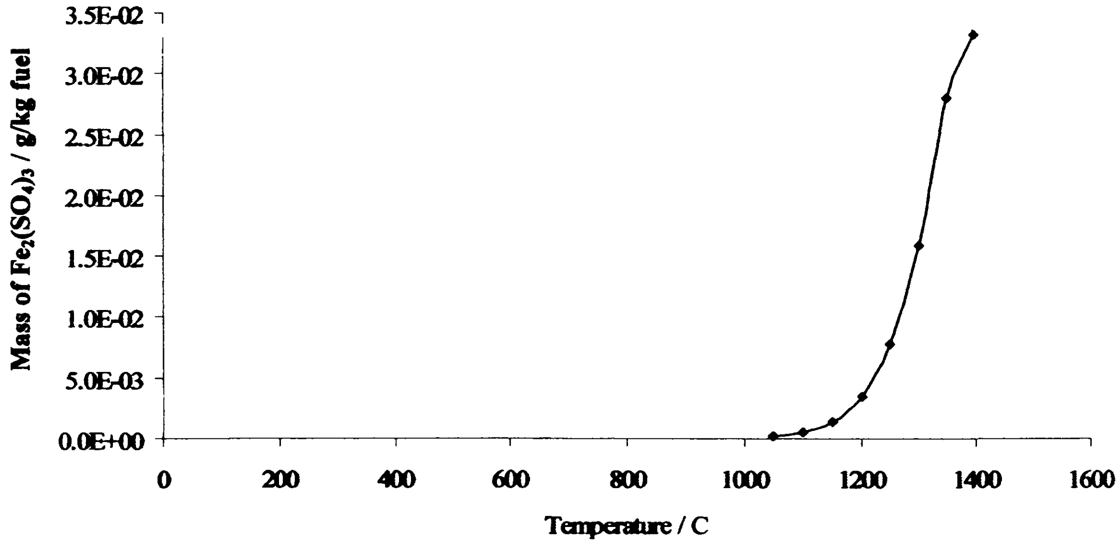

Figure 6.38: Variation of deposited $Fe_2(SO_4)_3$ with temperature for tube temperatures of 550°C to 300°C at flue gas temperatures above 1050°C for a 10%$_{th}$ sewage sludge blend

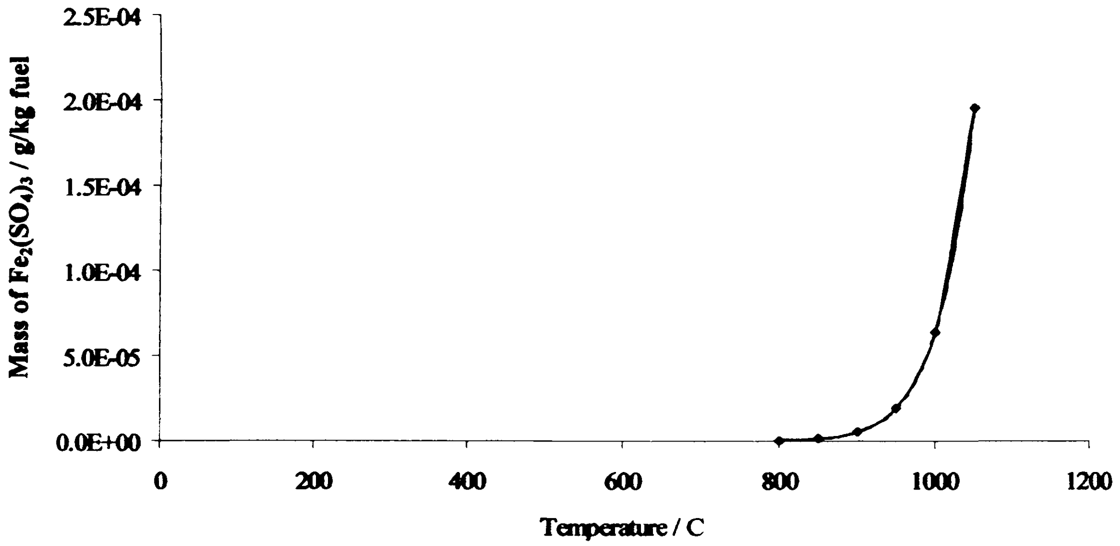

Figure 6.39: Variation of deposited $Fe_2(SO_4)_3$ with temperature for tube temperatures of 550°C to 300°C at flue gas temperatures below 1050°C for a 10%$_{th}$ sewage sludge blend

Microsoft Excel's trend line function was used to establish polynomial equations for each of the curves, (equations (6.41) to (6.46) in table 6.19). These equations represent only a small selection of the total number of equations derived, which can be seen as equations E5.34 to E5.104 in Appendix E.

Table 6.19: Equations of curves describing the formation of species for blends of $10\%_{th}$ sewage sludge with bituminous coal.

Species	Gas Temperature Range / °C	Tube Temperature Range / °C	Equation	
Na_2SO_4	1000°C – 1400°C	350°C - 650°C	$m = 8.075\times10^{-12}T^4 - 3.5699\times10^{-8}T^3$ $+5.9253\times10^{-5}T^2 - 4.3735\times10^{-2}T + 12.1066$	(6.41)
Na_2SO_4	650°C – 500°C	350°C - 650°C	$m = 1.2025\times10^{-16}T^5 - 4.4163\times10^{-13}T^4$ $+6.4493\times10^{-10}T^3 - 4.6792\times10^{-7}T^2$ $-1.6867\times10^{-4}T - 2.4169\times10^{-2}$	(6.42)
K_2SO_4	1000°C – 1400°C	350°C - 650°C	$m = 1.5531\times10^{-12}T^4 - 6.8202\times10^{-9}T^3$ $+1.1253\times10^{-5}T^2 - 8.2620\times10^{-3}T + 2.2763$	(6.43)
K_2SO_4	650°C – 500°C	350°C - 650°C	$m = 3.5554\times10^{-17}T^5 - 1.3228\times10^{-13}T^4$ $+1.9634\times10^{-10}T^3 - 1.4525\times10^{-7}T^2$ $+5.3538\times10^{-5}T - 7.8636\times10^{-3}$	(6.44)
$Fe_2(SO_4)_3$	1050°C – 1400°C	300°C – 550°C	$m = 1.3807\times10^{-9}T^3 - 4.4964\times10^{-6}T^2$ $+4.8884\times10^{-3}T - 1.7737$	(6.45)
$Fe_2(SO_4)_3$	800°C – 1050°C	300°C – 550°C	$m = 5.6431\times10^{-16}T^5 - 2.4469\times10^{-12}T^4$ $+4.2496\times10^{-9}T^3 - 3.6940\times10^{-6}T^2$ $+1.6068\times10^{-3}T - 2.7973\times10^{-1}$	(6.46)

The equations derived for each of the discrete blends of fuel, mentioned above, have been embedded within the spreadsheet to be used to calculate the composition of alkali sulphates and iron trisulphates that are deposited on the heat exchanger tubes for the desired blend of fuel specified by the user.

6.9.4 Implementation of the high temperature corrosion model within the spreadsheet.

The model is implemented in several steps:

1) Calculation of the heat exchanger tube surface temperatures
2) Prediction of the formation of alkali sulphates and iron trisulphates
3) Calculation of the deposit composition and melting temperature
4) Comparison of the deposit melting temperature to the tube surface temperature.

6.9.4.1 Calculation of the Heat Exchanger Surface Temperature

One of the essential inputs into the model is the surface temperature of the heat exchanger tubes within the boiler in question. These temperatures are calculated by estimating the thermal conductivity of the heat exchanger steel and assessing the heat transfer to the steam within them. Equation (6.47), taken from Engineering *Thermodynamics: Heat and Work Transfer by Rogers and Mayhew* [96] has been used to calculate the surface temperature of the heat exchanger elements.

$$T_{Surface} = T_{Steam} - \left\{\frac{Q/N}{2\pi kl}\right\}\ln\left(\frac{r_o}{r_i}\right) \tag{6.47}$$

Where $T_{surface}$ is the mean surface temperature of the heat exchanger elements (°C), T_{steam} is the mean steam temperature passing through the heat exchanger (°C), q is the heat energy gained by the steam as it passes through the heat exchanger (J), n is the number of elements within the heat exchanger, k is the thermal conductivity of the element material (W/m°C), l is the mean length of the heat exchanger elements (m), r_o is the mean outer diameter of the heat exchanger elements (m) and r_i is the mean internal diameter of the heat exchanger elements (m).

It is important to note that k varies significantly for different types of metal and also with the temperature of that metal. For this reason several typical metals used for the manufacture of heat exchangers in power station boilers have been selected and their thermal conductivity has been plotted as a function of their temperature (see figure 6.40). The metals were:

- ST45.8 – A carbon steel used for low temperature regions towards the end of the convective pass.
- 13CrMo45 – A Carbon alloy steel with a higher melting temperature than carbon steels.
- 10CrMo910 - A Carbon alloy steel with a higher melting temperature than carbon steels.
- AISI 310, AISI 316, AISI 321, AISI 347 – Stainless steels with differing alloys to provide better thermal, strength and creep resistance.

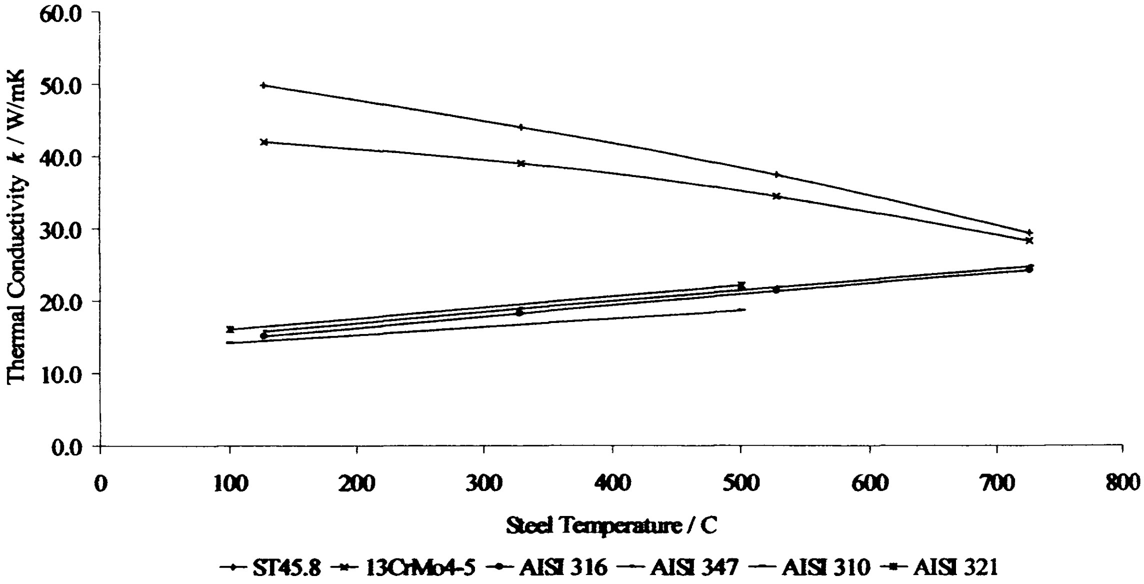

Figure 6.40: Variation of thermal conductivity (*k*) with temperature for various types of steel [27]

The trend line function within Excel has been used to estimate the equations of these curves; equations (6.48) to (6.53) shown in table 6.20.

Table 6.20 Thermal conductivity relationships as a function of temperature for a number of typical superheater steels

Steel type	Equation	
ST45.8	$k = -(1.4375\times10^{-6})T^2 - (2.1774\times10^{-2})T + (5.2763\times10^{1})$	(6.48)
13CrMo4-5	$k = -(2.1250\times10^{-5})T^2 - (4.8525\times10^{-3})T + (4.2959\times10^{1})$	(6.49)
AISI 310	$k = (1.1250\times10^{-2})T + (1.3075\times10^{1})$	(6.50)
AISI 316	$k = -(1.250\times10^{-6})T^2 - (1.6067\times10^{-2})T + (1.3180\times10^{1})$	(6.51)
AISI 321	$k = -(1.8750\times10^{-6})T^2 - (1.6451\times10^{-2})T + (1.3736\times10^{1})$	(6.52)
AISI 347	$k = (1.500\times10^{-2})T + (1.4600\times10^{1})$	(6.53)

These equations have been used in an iterative process to calculate the surface temperature of the heat exchangers. An initial surface temperature of 1000°C is assumed. The spreadsheet calculates two *k* values:

- The thermal conductivity of the heat exchanger metal at the point where the steam enters ($k_{0(min)}$), based upon the mean of the surface temperature (1000°C) and the steam temperature ($T_{0(min)}$).

- The thermal conductivity of the heat exchanger material at the point where the steam exits ($k_{0(max)}$) based upon the surface temperature (1000°C) and the steam temperature ($T_{0(max)}$).

The spreadsheet then uses equation (6.47) to calculate the two surface temperatures ($T_{0(min)}$ and $T_{0(max)}$) based upon $k_{0(min)}$ and $k_{0(max)}$. These surface temperatures are then used in a second iteration to calculate $k_{1(min)}$ and $k_{1(max)}$ which in turn are used to calculate new surface temperatures. The process is repeated for five iterations yielding $T_{5(min)}$ and $T_{5(max)}$. Boolean logic functions are used to ensure that the thermal conductivity is calculated for the correct type of steel. This process is used to calculate the minimum and maximum heat exchanger surface temperatures ($T_{5(min)}$ and $T_{5(max)}$) for each of the heat exchangers in the boiler.

6.9.4.2 Prediction of the Formation of Alkali Sulphates and Iron Trisulphates

A database is generated showing the formation of Na_2SO_4, K_2SO_4 and $Fe_2(SO_4)_3$ for each blend (0, 5, 10, 15, 20, 25 and 50%$_{th}$) of sewage sludge for each of the heat exchanger surface temperatures based upon the gas temperature at the leading edge each heat exchanger. The correlations described in Section 6.6.3.1 are used to do this as follows:

Several correlations have been created for each species for a number of gas temperature ranges. The temperature profile is used to provide the gas temperature at the leading edge of the heat exchanger, which is compared to these temperature ranges using Boolean logic functions (see Appendix E), and the correct correlation for the range in which it falls is applied. The mass of deposit formed is calculated for the entire range of heat exchanger tube surface temperatures. A second table is generated, which compares the minimum and maximum heat exchanger surface temperatures ($T_{5(min)}$ and $T_{5(max)}$) to the heat exchanger surface temperature ranges and uses Boolean logic to select the correct correlation and hence, the correct mass of deposit for each blend of fuel. Linear interpolation is then used to calculate the mass of deposit formed for the exact blend of fuel under examination.

6.9.4.3 Calculation of the Deposit Composition and Melting Temperature

The above process is carried out for each of the species Na_2SO_4, K_2SO_4 and $Fe_2(SO_4)_3$ giving the mass of each species deposited and hence, calculating the deposit composition. The melting temperature 'map' for the ternary system Na_2SO_4-K_2SO_4-$Fe_2(SO_4)_3$ described in Section 6.9.2.1 is used to calculate the melting temperature of the deposits formed. The melting temperature 'map' comprises the correlations shown in Appendix E which describe the melting temperature of the deposits as a function of $Fe_2(SO_4)_3$ for discrete Na_2SO_4-K_2SO_4 compositions. The percentage Na_2SO_4 is used as the driver for the calculation in the following way:

The percentage of Na_2SO_4 within the Na_2SO_4 - K_2SO_4 system is identified, and the nearest correlations above and below that value are used to calculate the melting temperature based upon the percentage of $Fe_2(SO_4)_3$ within the deposit. Linear interpolation is then used to identify the melting temperature of the system for the exact value of the Na_2SO_4 component. This gives the melting temperature (T_m) for that particular system composition.

6.9.4.4 Comparison of the Deposit Melting Temperature (T_m) to the Tube Surface Temperature

The melting temperature of the system (T_m) calculated by the process described above is evaluated against the heat exchanger tube surface temperature ($T_{5(min)}$ and $T_{5(max)}$), from Section 6.9.4.1, using Boolean logic functions. If $T_{5(min)}$ or $T_{5(max)}$ are above T_m then the existence of an alkali-iron sulphate melt is deemed to be possible as is the risk of increased corrosion which is carried with it. The threat of increased corrosion is conveyed to the user using warning flags such as those shown in figure 6.41. It is also possible to differentiate between the threat posed to the hottest and coolest parts of the heat exchanger since predictions are made based upon the minimum and maximum heat exchanger tube surface temperatures. The warning flags indicate to the user three possible situations:

1. The alkali and iron sulphate deposits are solid, in which case normal levels of corrosion prevail.
2. The alkali and iron sulphate deposits are molten, in which case there is the possibility of increased levels of corrosion, or
3. No alkali iron sulphate deposits are formed meaning that no corrosion will occur as a result of alkali sulphate deposition.

It can be seen from figure 6.4.1 that a $10\%_{th}$ blend of a typical medium volatile coal and a typical sewage sludge produces an elevated risk of corrosion in the hottest parts of superheater 3, for superheater 1, reheater 1 and the economisers there are no corrosive species deposited, whilst for all other regions of the boiler normal corrosion levels are dominant.

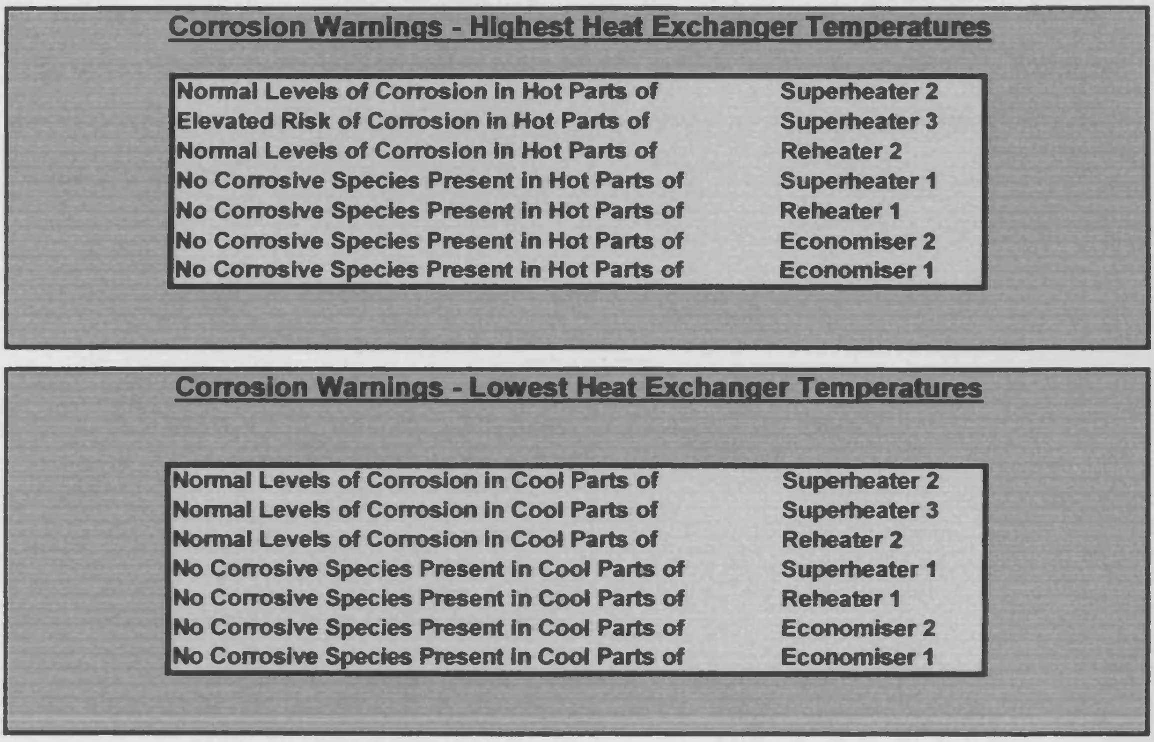

Corrosion Warnings - Highest Heat Exchanger Temperatures

Normal Levels of Corrosion in Hot Parts of	Superheater 2
Elevated Risk of Corrosion in Hot Parts of	Superheater 3
Normal Levels of Corrosion in Hot Parts of	Reheater 2
No Corrosive Species Present in Hot Parts of	Superheater 1
No Corrosive Species Present in Hot Parts of	Reheater 1
No Corrosive Species Present in Hot Parts of	Economiser 2
No Corrosive Species Present in Hot Parts of	Economiser 1

Corrosion Warnings - Lowest Heat Exchanger Temperatures

Normal Levels of Corrosion in Cool Parts of	Superheater 2
Normal Levels of Corrosion in Cool Parts of	Superheater 3
Normal Levels of Corrosion in Cool Parts of	Reheater 2
No Corrosive Species Present in Cool Parts of	Superheater 1
No Corrosive Species Present in Cool Parts of	Reheater 1
No Corrosive Species Present in Cool Parts of	Economiser 2
No Corrosive Species Present in Cool Parts of	Economiser 1

Figure 6.41 - Corrosion warning flags for a $10\%_{th}$ blend of sewage sludge with a typical medium volatile bituminous coal for the Langerlo boiler

6.10 The Use of Artificial Neural Networks Within the Predictor

The models described in this chapter so far have been empirical models based upon correlations created using thermochemical software that have been embedded within the spreadsheet. These models principally rely upon relationships derived specifically for one type of fuel. Using the empirical correlations described above, the spreadsheet is able to make predictions for a medium volatile bituminous coal and typical sewage sludge. The spreadsheet may be used to predict the behaviour of similar coals however, predictions of behaviour for different substitute fuels such as sawdust and RDF would not be valid.

It is for these reasons that, as has been mentioned in Sections 6.6 and 6.8, artificial neural network (ANN) models have been developed to replace the empirical correlations within the spreadsheet, and in its latest form have been used to replace the temperature – enthalpy correlations and the slagging correlations.

6.10.1 Basics of an ANN

An artificial neural network is a processing paradigm composed of a high number of inter-connected processing elements (neurons), which work in unison to solve a specific problem. ANNs are able to learn from example. Figure 6.42 shows a basic model of a neuron.

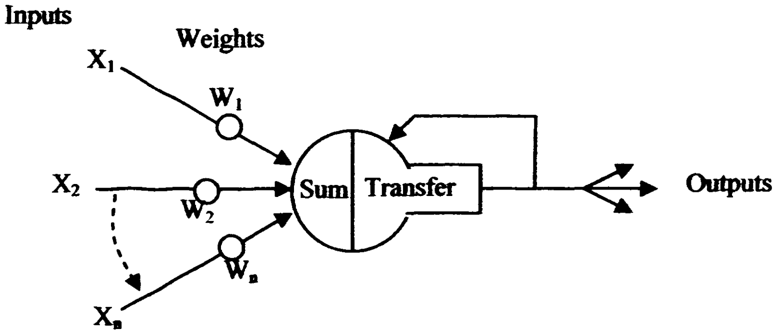

Figure 6.42 Simple model of an ANN neuron [97]

In its simplest form, the neuron works by taking the inputs (X_1 to X_n), multiplying them by their relative weightings (W_1 to W_n) and passing their sum through a 'transfer function' to give an output. A set of inputs and their prospective outputs is used as the training data for the network, generating the 'transfer function'. This transfer function can then be used to interpolate the correct output for any input data within the limits of the training data set. This is the process that has been used to create the ANNs utilised in the latest version of the spreadsheet.

6.10.2 Creating the ANNs for Use in the Spreadsheet.

The ANNs used in the spreadsheet have been developed by C. K. Tan of The University of Glamorgan, with help from the author in generating the training data.

6.10.2.1 Training Data

Training data was created for 5 different coals and three different substitute fuels, the ash, proximate and ultimate analyses of which are shown in table 6.21.

Table 6.21 Fuels used to generate the training data for the ANNs

	Coal 1	Coal 2	Coal 3	Coal 4	Coal 5	Sewage Sludge	Sawdust	RDF
	Proximate Analysis (%)							
Moisture	4.29	1.00	1.70	12.90	53.80	11.72	34.90	4.70
Ash	11.53	10.83	5.00	17.45	2.80	48.81	0.70	8.90
Volatiles	33.33	32.94	34.00	27.50	26.90	36.72	55.00	72.70
Fixed Carbon	51.04	55.22	59.30	42.15	16.50	2.75	9.40	13.70
	Ultimate Analysis (%)							
Carbon	67.23	73.94	77.90	59.53	29.90	19.12	32.10	41.20
Hydrogen	5.15	4.88	4.60	3.79	2.20	4.16	3.90	6.40
Oxygen	9.74	6.74	7.50	6.20	10.40	12.77	28.20	37.00
Nitrogen	1.31	1.53	1.77	1.80	0.61	2.65	0.26	0.60
Sulphur	0.75	1.05	0.88	1.11	0.39	0.77	0.01	0.04
LCV (kJ/kg)	27240	28860	30662	24150	10073	8410	10935	16558
	Ash Analysis (%)							
Na_2O	1.82	0.86	2.10	0.44	1.20	1.10	2.30	2.00
K_2O	6.50	3.22	1.00	3.80	0.80	2.70	9.80	1.90
CaO	1.98	5.80	8.10	1.80	18.20	11.50	40.00	22.90
Al_2O_3	34.45	24.70	24.90	25.30	5.20	12.20	4.10	23.70
MgO	3.22	3.80	1.90	2.40	7.70	2.10	4.80	2.70
Fe_2O_3	9.19	10.20	21.10	9.10	17.00	19.00	1.60	2.30
SiO_2	43.23	43.70	34.10	46.20	40.10	34.90	23.70	39.80
SO_3	1.05	5.70	4.90	1.90	10.00	0.80	1.90	1.60
TiO_2	1.82	0.92	0.70	0.89	0.50	0.80	0.40	2.10
P_2O_5	0.36	0.27	1.20	0.09	0.00	14.50	2.10	1.00

6.10.2.1a Training data for the temperature – enthalpy ANN

The above fuels were used to generate 300 training cases using the FLUENT PrePDF non-premixed combustion pre-processor, undergoing the same process as described in Section 6.6.1.2. Fuel blends of up to $20\%_{th}$ were used with oxidiser temperatures varying from 300 to 700K and equivalence ratios of 1 to 1.25. Tan was able to create a computer program which would extract the data from the pre-processor and calculate the enthalpy profile thus greatly reducing the magnitude of this task. The 300 prePDF input data sets and their corresponding temperature – enthalpy profiles were used to train the ANN such that it can predict the temperature – enthalpy relationship for any blend of fuel which falls within the following limits:

Table 6.22 Limits of operation for the temperature – enthalpy ANN inputs

Parameter	Maximum	Minimum
Oxidiser Temperature / K	719	300
f-fuel (see Section 6.6.1.1)	0.05762047	0.01719498
p-sec (see Section 6.6.1.1)	0.08279875	0.02113665
C (mole fraction)*	0.4032038	0.0949395
H (mole fraction)*	0.7229858	0.4490175
O (mole fraction)*	0.2160267	0.0400407
N (mole fraction)*	0.0364819	0.0065099
Volatile matter**	79.05	30.57
Fixed C**	69.43	20.95
Volatile LCV* / kJ/kg	39783.05	15650
Fuel LCV* / kJ/kg	35004.15	21955.5

*dry, ash free

** As received

6.10.2.1b Training Data for the Slagging and Fouling ANN

The fuels shown in table 6.21 were also used to generate the training data for the slagging and fouling ANN using the FactSage thermochemical software package, undergoing the same process as that described in Section 6.8.1. Some 600 input data cases and their corresponding ash compositions were created for fuel blends of up to $20\%_{th}$ sewage sludge, sawdust and RDF for each of the 5 coals with equivalence ratios of 1.00 to 1.25, and at temperatures in the range 400 – 1900K. This data was then used to train the slagging and fouling ANN to predict the mass of species in gaseous, molten and solid phases containing Na, K, P, Si, Al and Fe containing species. It was not possible to train the ANN to predict the formation of individual species as many of the species produced occurred on fewer than the minimum 20 occasions required to train the ANN.

6.10.3 Implementing the ANNs Within the Spreadsheet

The user inputs for this version of the spreadsheet remain the same as those for the previous version which utilised the empirical correlations. The ANNs are located on hidden pages within the spreadsheet and are activated by the use of a macro which is run by the user.

6.10.3.1 The Temperature – Enthalpy ANN

The temperature – enthalpy ANN is located on the hidden sheet Nnet and is activated by running the macro 'Enthalpy-Temperature' which was written by C. K. Tan. The spreadsheet automatically collates the required input data and sorts it in a table such as that shown below

Table 6.23 Temperature – enthalpy ANN inputs for a 10%$_{th}$ blend of sewage sludge and medium volatile bituminous coal for the Langerlo boiler

Parameter	Value
Oxidiser Temperature / K	473
f-fuel	0.04022412
p-sec	0.03547060
C mole fraction*	0.2282137
H mole fraction*	0.6500522
O mole fraction*	0.1012363
N mole fraction*	0.0204978
Volatile matter*	45.83
Fixed C*	54.16
Volatile LCV* / kJ/kg	26477.99
Fuel LCV* / kJ/kg	29953.40

The outputs of the ANN are a temperature – enthalpy relationship such as those shown in figure 6.43 and a temperature – enthalpy profile for the boiler based upon the calculated enthalpy change of the flue gases as they pass through each zone such as those shown in figure 6.44

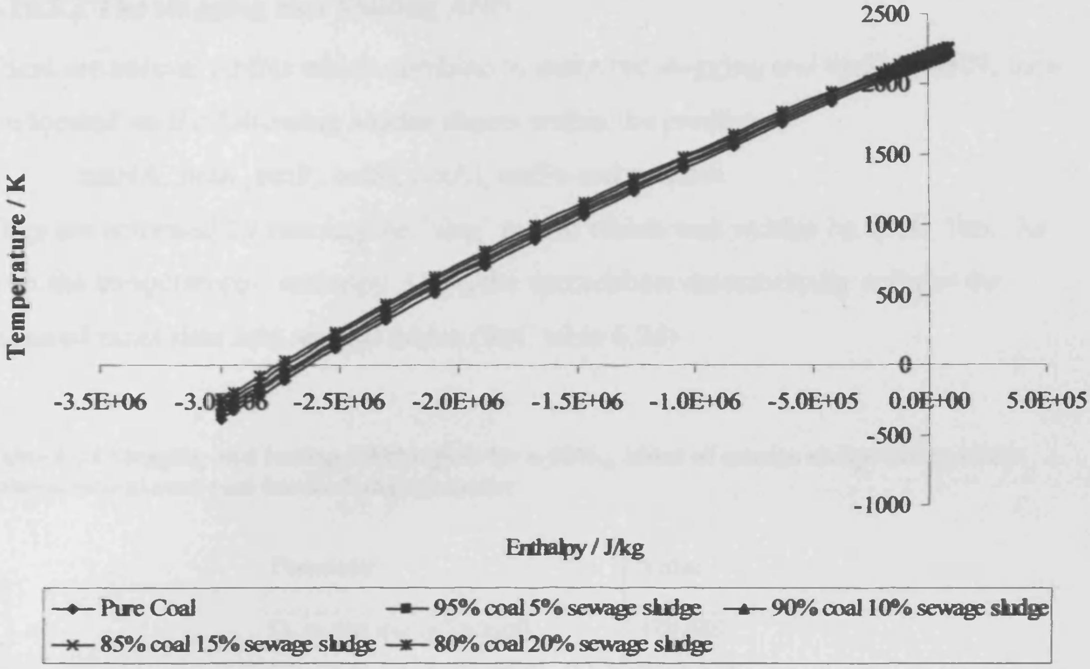

Figure 6.43 Temperature – enthalpy relationships produced using the ANN for a range of blends of sewage sludge and a medium volatile bituminous coal

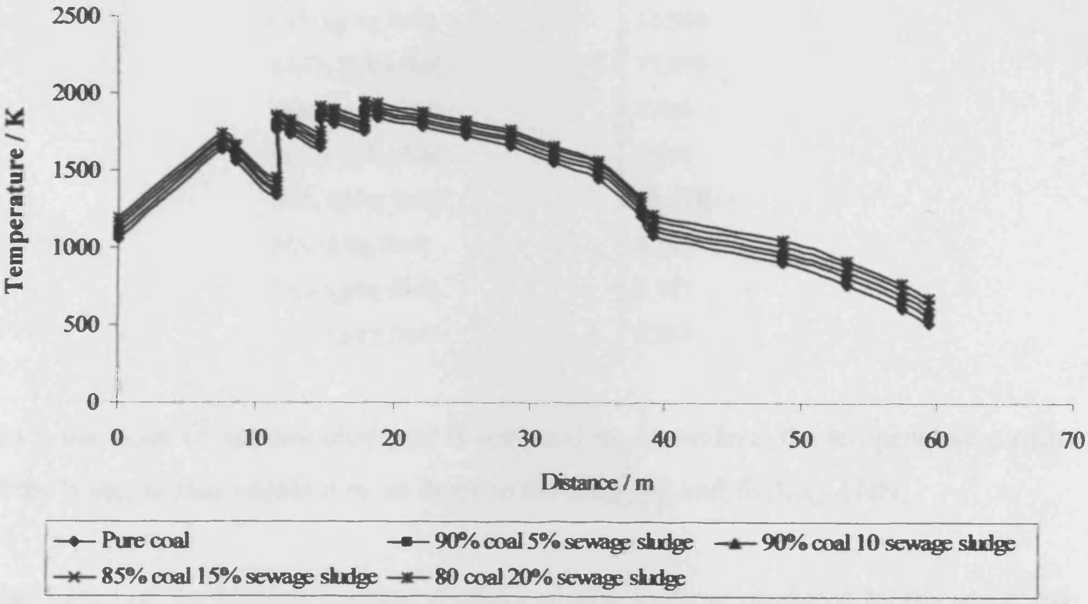

Figure 6.44 Temperature profiles produced using the ANN for a range of blends of sewage sludge with a medium volatile bituminous coal for the Langerlo boiler.

6.10.3.2 The slagging and Fouling ANN

There are several ANNs which combine to make the slagging and fouling ANN, these are located on the following hidden sheets within the predictor:

netNA, netK, netP, netSi, netAl, netFe and netAlSi

They are activated by running the 'slag' macro which was written by C. K. Tan. As with the temperature – enthalpy ANN, the spreadsheet automatically collates the required input data into several tables (Ref. table 6.24)

Table 6.24 Slagging and fouling ANN inputs for a 10%$_{th}$ blend of sewage sludge and medium volatile bituminous coal for the Langerlo boiler

Parameter	Value
O_2 in flue gas (g/kg fuel)	420.489
CO_2 in flue gas(g/kg fuel)	2363.264
H_2O in flue gas (g/kg fuel)	506.070
SO_2 in flue gas (g/kg fuel)	16.284
N_2 in flue gas (g/kg fuel)	7925.786
Na_2O (g/kg fuel)	1.012
K_2O (g/kg fuel)	4.021
CaO (g/kg fuel)	11.566
Al_2O_3 (g/kg fuel)	17.091
MgO (g/kg fuel)	3.436
Fe_2O_3 (g/kg fuel)	7.040
SiO_2 (g/kg fuel)	33.419
SO_3 (g/kg fuel)	4.129
TiO_2 (g/kg fuel)	0.717
P_2O_5 (g/kg fuel)	0.584

Since the mass of species produced is temperature dependant, the temperature profile of the boiler is also required as an input to the slagging and fouling ANN.

The output of the ANN is a series of tables similar to those produced by the empirical correlations detailing the mass of solid, molten and gaseous Na, K, P, Si, Al and Fe at each calculation point on the temperature profile and also at the leading edge of each heat exchanger. Figures 6.45 and 6.46 show the difference in predicted molten species formation between pure coal and a 10%$_{th}$ sewage sludge blend.

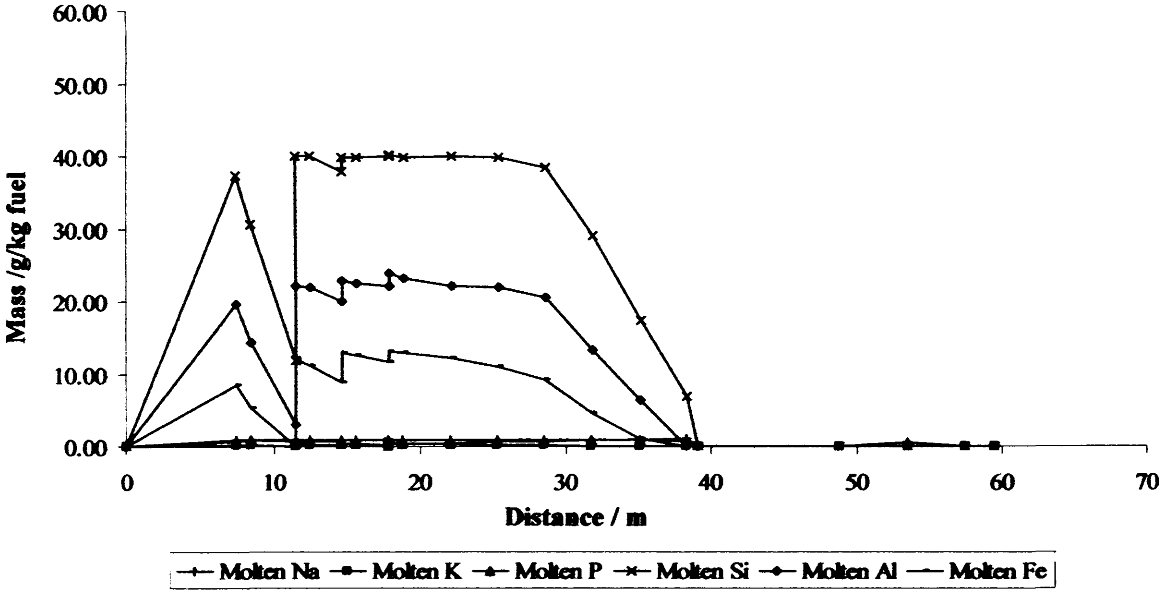

Figure 6.45 Mass of molten species as a function of distance for pure coal in the Langerlo boiler calculated using the slagging and fouling ANN

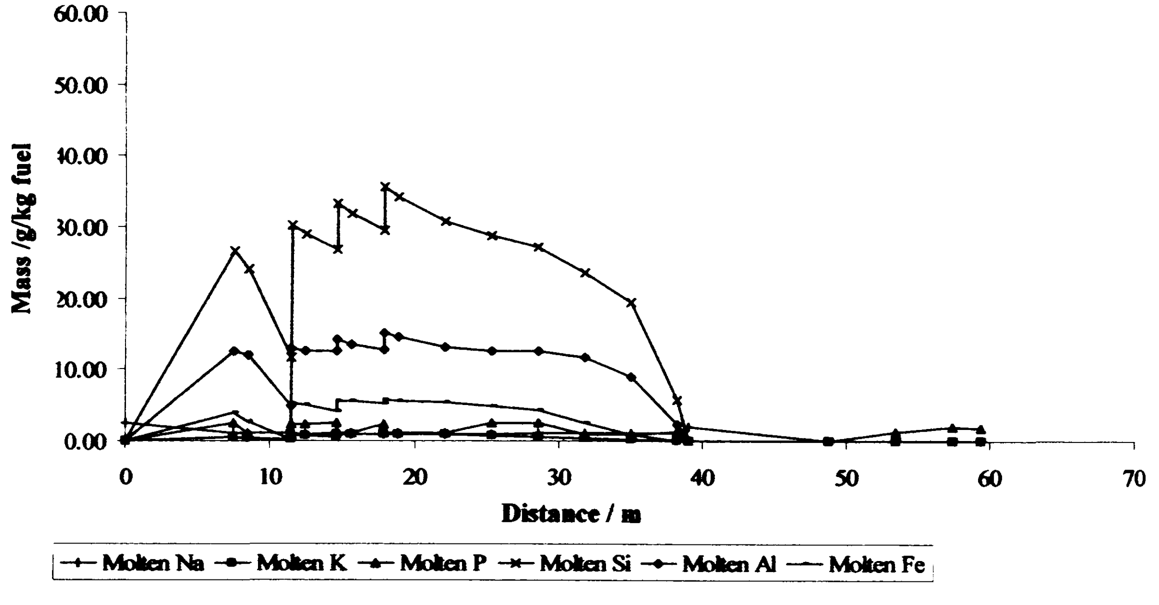

Figure 6.46 Mass of molten species as a function of distance for A 90% coal – 10% sewage sludge blend in the Langerlo boiler calculated using the slagging and fouling ANN

6.11 Summary

A prediction tool has been developed for assessing the likelihood of increased slagging, fouling and corrosion problems caused as a result of co-firing blends of a typical medium volatile bituminous coal and a typical Belgian sewage sludge. A user interface was developed which allows the boiler operator to enter all of the relevant data regarding the parent and substitute fuels, boiler dimensions and geometry and process and operation settings for the boiler they wish to analyse. Steam cycle data has been embedded within the prediction tool, which automatically calculates the heat removal rates for each of the heat exchangers in the boiler based upon the data entered by the user.

A simple two-stage combustion reaction is used within the spreadsheet to predict a theoretical flue gas composition. The mass flowrate of the flue gas is used, along with the heat removal rates to calculate the enthalpy change of the flue gas as it passes through the boiler. Empirical correlations, derived from a pre-processing package for the FLUENT CFD software package, have been used to equate the enthalpy change of the flue gases to their temperature, creating a temperature profile for the boiler. The temperature profile forms the backbone of the prediction tool and is used in each of the slagging, fouling and corrosion models.

Empirical correlations have been derived for fuel blends of up to 50%$_{th}$ substitute fuel using the FactSage thermochemical software package. These correlations relate the mass of gaseous, solid and molten combustion products formed, based upon the fuel blend specified by the user, to the flue gas temperature. The temperature profile is used to assess the composition of the combustion products at the leading edge of each of the heat exchangers within the boiler. The level of gaseous and molten sodium and potassium (alkali) containing species is calculated at each of these points and is compared against thresholds set using industrial experience and experimental data to assess whether there is a high, medium or low risk of slagging or fouling occurring at each of the heat exchangers.

A similar technique has been used to assess the formation of corrosive species within the deposits and the effect of fuel blend on corrosion levels within the boiler. A thermal model has been adopted to assess the surface temperature of the heat exchanger tubes based upon the heat energy being removed by them. FactSage thermochemical software has been used to simulate vapour deposition of alkali salts and iron sulphates from the flue gases onto the cooler heat exchanger tubes. Correlations have been created, which relate the mass of each species deposited to the flue gas temperature for a range of heat exchanger surface temperatures and fuel blends. The heat exchanger surface temperatures predicted by the thermal model are used to assess the composition of deposits formed at each heat exchanger. A melting temperature 'map' for the ternary Na_2SO_4-K_2SO_4-$Fe_2(SO_4)_3$ system has been embedded into the spreadsheet which will calculate the temperature of formation of the 'sulphate melt' which increases the rate of corrosion for any melt composition up to 50% $Fe_2(SO_4)_3$. This melting temperature map is used to assess the temperature of formation of the sulphate melt for the composition of deposits predicted by the correlations for each heat exchanger. This melting temperature is compared to the predicted surface temperature of each of the heat exchangers to assess whether a 'sulphate melt' occurs and the levels of corrosion are increased.

In the latest version of the spreadsheet, the temperature – enthalpy and slagging and fouling empirical correlations have been replaced by artificial neural networks which allow the prediction of potential slagging and fouling problems for a far wider range of fuels than the empirical indices can cater for.

All of the predictions are relayed to the user via warning flags which are displayed on the front page of the spreadsheet. It is important to note that the spreadsheet does not make quantitative predictions of slagging, fouling and corrosion levels but instead identifies changes in deposit formation and uses those changes to identify potential problems.

Chapter 7 - CFD Simulation of the ENEL 500kW$_{th}$ Downfired Furnace

7.1 Nomenclature

A	Empirical constant equal to 4	(dimensionless)
A_g	Specific internal surface area of the particle	(m^2)
A_p	Particle surface area	(m^2)
A_r	Kinetic rate parameter	(dimensionless)
A_1, A_2	Kinetic rate parameters	(dimensionless)
B	Empirical constant equal to 0.5	(dimensionless)
$C_{j,r}$	Molar concentration of each reactant and product species j in reaction r	(kgmol/m^3)
C_1	Constant	(dimensionless)
D_e	Effective diffusion coefficient in the particle pores	(dimensionless)
$D_{i,m}$	Diffusion coefficient for species i in the mixture	(dimensionless)
d_p	Particle diameter	(m)
$d_{p,0}$	Original particle diameter	(m)
D_t	Turbulent diffusivity	
D_0	Diffusion rate coefficient	(dimensionless)
$D_{0,r}$	Diffusion rate coefficient for reaction r	(dimensionless)
E_r	Kinetic rate parameter	(dimensionless)
E_1, E_2	Kinetic rate parameters	(dimensionless)
f_{comb}	Combustible fraction of the particle	(dimensionless)
$f_{v,0}$	Fraction of volatiles in the particle at time 0	(dimensionless)
$\vec{J}_i$	Diffusion flux of species i	(kg/m^{2}s)
k	Mass transfer coefficient	(units vary)
k_i	Intrinsic reactivity of the char	
$k_{b,r}$	Reaction rate constants for reaction r	(dimensionless)
$k_{f,r}$	Reaction rate constants for reaction r	(dimensionless)

m_a	Ash content of the particle	(dimensionless)
m_p	Particle mass	(kg)
$m_{p,0}$	Mass of the particle at time 0	(kg)
$m_v(t)$	Volatile yield up to time t	(kg)
$M_{w,i}$	Molecular weight of reactant i	(kg/kgmol)
$M_{w,R}$	Molecular weight of a particular reactant R	(kg/kgmol)
N	Total number of species	(dimensionless)
N_r	Number of reactants in reaction r	(dimensionless)
N_r	Apparent order of reaction r	
p_n	Bulk partial pressure of the gas phase species	(Pa)
R	Gas-law constant (8314.47 J/kgmol-K)	(J/kgmol-K)
R	Chemical reaction rate	
R_i	Net rate of production of species i	(kg/s)
$R_{j,r}$	Rate of particle surface species reaction per unit area	(kg/m^{2}s)
$\overline{R_{j,r}}$	Rate of particle surface species depletion	(kg/s)
$R_{kin,r}$	Kinetic rate of reaction	
R_1, R_2	Kinetic rate	(units vary)
S_b	Stoichiometric requirement of the surface burnout reaction	(dimensionless)
Sc_t	Schmidt number	
S_i	rate of creation of species i by addition from the dispersed phase plus any user defined sources	(kg/s)
T	Temperature	(K)
U	Fractional degree of burnout	(dimensionless)
$\vec{v}$	Overall velocity vector	(m/s)
Y_i	Mass fraction of species i	(dimensionless)
Y_j	Mass fraction of surface species j in the particle	(dimensionless)
Y_P	Mass fraction of any product species, P	(dimensionless)
Y_R	Mass fraction of a particular reactant R	(dimensionless)
E	Turbulent dissipation rate	(m^2/s^3)
A	Burning mode constant	(dimensionless)

a_1, a_2	Yield constants	(dimensionless)
ε	Turbulent dissipation rate	(m^2/s^3)
Γ	Net effect of third bodies on the reaction rate	(dimensionless)
$\eta'_{j,r}$	Forward rate component for each reactant and product species *j* in reaction *r*	(dimensionless)
$\eta''_{j,r}$	Backward rate component for each reactant and product species *j* in reaction *r*	(dimensionless)
η_r	Effectiveness factor	(dimensionless)
λ	Equivalence ratio	(dimensionless)
μ_t	Turbulent viscosity	(Pa s)
$\nu'_{i,r}$	Stioichiometric coefficient for reactant *i* in reaction *r*	(dimensionless)
$\nu''_{j,r}$	Stoichiometric coefficient for product *j* in reaction *r*	(dimensionless)
$\nu'_{R,r}$	Stoichiometric coefficient of a particular reactant *R* in reaction *r*	(dimensionless)
ρ	Density	(kg/m^3)

7.2 Introduction

As has already been highlighted in Chapter 5, CFD (Computational Fluid Dynamics) software is potentially a very useful tool for assessing the impact of co-firing bio-fuels and wastes in coal fired utility boilers. CFD can be used to provide highly detailed in-depth analysis of one aspect of a combustion system on the microscopic scale, for example, simulating particle deposition on an isolated boiler tube. However, it is also capable of providing an overall view of a complete combustion system on the macroscopic scale, for example modelling of full scale industrial boilers.

7.3 The Use of CFD as an Aid to Developing the Prediction Tool

This chapter will outline attempts to use CFD as a method of validation for the boiler performance prediction tool outlined in Chapter 6. The modelling of the combustion chamber of a 500kW single burner, down fired furnace, firing different blends of coal and sewage sludge has been undertaken to try to achieve this. The aim of this exercise is to examine the effect of the substitute fuel on flame temperature and ignition time and also the composition of the flue gases. It was hoped that this data could be used to validate the initial flue gas composition model, combustion model and adiabatic flame temperatures calculated by the predictor. It was also hoped to study the deposition characteristics of the blended fuel on deposition probes within the model with a view to developing a deposition model within the predictor.

7.4 The ENEL 500kW$_{th}$ Downfired Furnace.

In order to gain valid comparisons between the spreadsheet predictions and the CFD exercise, it is desirable to have some experimental data with which to validate the CFD model. ENEL have conducted some co-firing trials using their 500kW$_{th}$ pilot-scale facility for which the results data was made available [98].

7.4.1 The Furnace and Combustion System

ENEL's 500kW$_{th}$ test furnace (Ref. figure 7.1) consists of a vertical, down fired refractory lined combustion chamber some 3.5m long with and internal cross section of 0.84m x 0.84m. Beyond the combustion chamber the section narrows to 0.3m x 0.3m over a distance of 0.5m into a 1m long ash pot giving an overall height of 5m. At the half way point of the convergence a 0.3m x 0.3m duct carries flue gases away at right angles to the burner axis through a transfer duct some 3.1m long. From here, the flue gases are transported along ductwork and through two heat exchangers totalling 40m in length (not modelled).

Located 0.5m from the end of the transfer duct is an orifice to allow the insertion of a 300mm x 25mm diameter slag deposition probe. The combustion chamber also features a total of 8 similar sized orifices at distances of 0.25m, 0.69m, 1.13m, 1.79m, 2.23m, 2.67m and 3.27m from the burner outlet in addition to 8 smaller orifices equally spaced within 1.4m of the burner for near burner measurements. Finally, heat removal in the combustion chamber is regulated by 48 water cooled lances connected in parallel and mounted on the walls of the chamber, which remove heat from the combustion zone [99]. The furnace is designed to have a residence time of approximately 1.5s which is comparable to that between the burner levels and the first rows of the superheater in a full scale boiler.

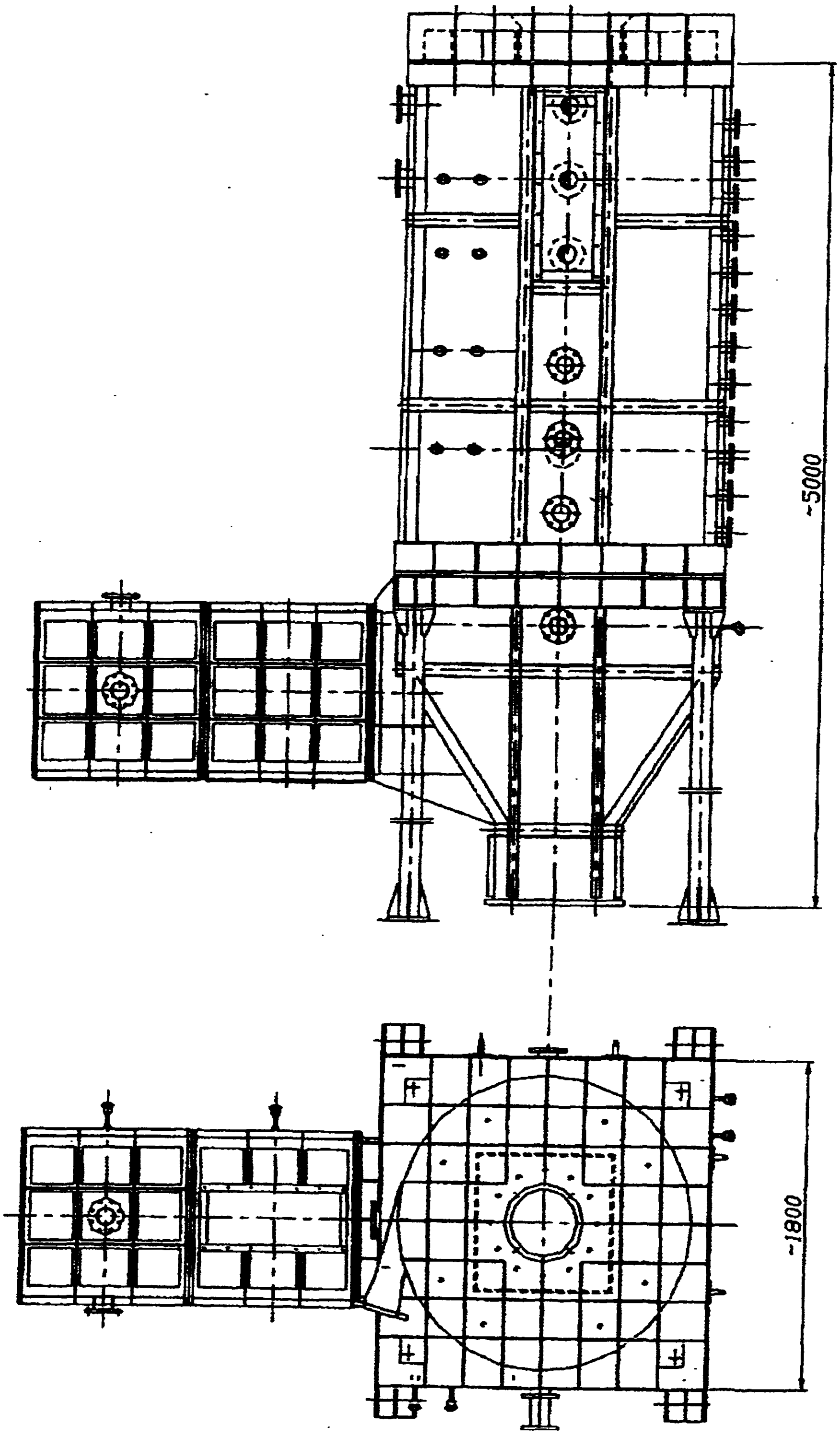

Figure 7.1: The ENEL 500kW$_{th}$ furnace

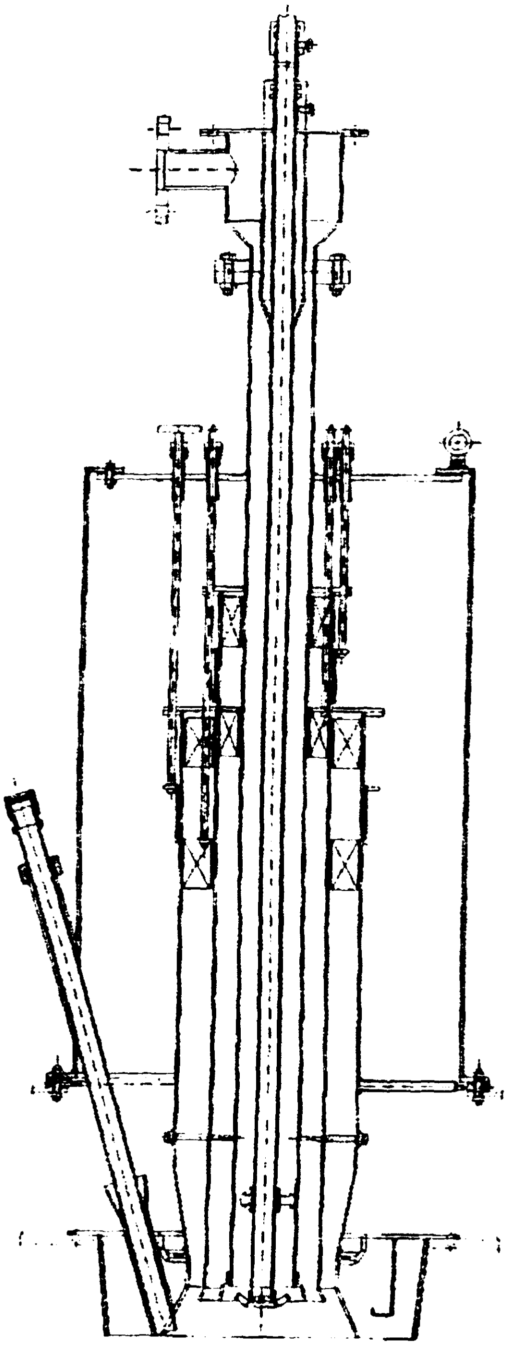

Figure 7.2: The low-NO$_x$ burner used in the ENEL 500kW$_{th}$ furnace.

7.4.2 The burner

The furnace is equipped with a single down firing burner, centrally mounted at the top of the combustion chamber. "The burner, (Ref. figure 7.2) is a scaled version (according to Slavi-Payne criteria) of the low-NO$_x$ burner T.E.A. jointly developed by ENEL and Ansaldo" [99]. The burner can be operated with gas, liquid and solid fuels such as extra-heavy oils, coal, coal-water emulsions and blends of coal and different substitute fuels. A torus shaped primary air duct of internal diameter 30mm and external diameter 70mm by 700mm long is used to carry pulverised coal and primary air to the combustion chamber. Secondary air is supplied via an 80mm internal diameter, 130mm external diameter duct with anticlockwise swirl as viewed from below. Finally tertiary air is supplied via a 140mm internal diameter, 176mm external diameter duct with clockwise swirl as viewed from below.

Each of the air ducts features a diffuser; at the point of entry to the furnace, the primary air duct has an internal diameter of 40mm and an external diameter of 100mm, the secondary air duct has internal diameter of 110mm and an external diameter of 150mm and the tertiary air duct has an internal diameter of 160mm and an external diameter of 228mm. The primary air duct also features two diffuser rings of 50mm mean diameter and 70mm mean diameter to deflect the fuel particles into the secondary and tertiary air streams.

7.4.3 The ENEL Combustion Trials

A number of combustion trials have been carried out by ENEL using their 500kW downfired furnace. Various blends of pulverised coal and sewage sludge were fired at differing equivalence ratios.

7.4.3.1 Fuel Data

The fuels used in the ENEL combustion trials were; a high volatile Colombian coal and a pulverized Belgian sewage sludge provided by LABORELEC. Characterisation of these fuels was carried out using the IFRF Plug Flow Reactor [100], details of this characterisation can be seen in tables 7.1 to 7.4. The Rosin-Rammler particle size distribution data for the coal, sewage sludge and the two fuel blends is shown in table 7.5.

Table 7.1: Executive summary of the fuel characterisation for the Colombian coal [100]

Colombian Coal PF1	Proximate Analysis $\%_{wt}$ (dry)			Proximate Analysis $\%_{wt}$ (dry, ash free)	
	Ash	Volatiles	Fixed Carbon	Volatiles	Fixed Carbon
Fuel	6.0	39.0	55.0	41.5	58.5
Char	16.1	6.2	77.7	7.4	92.6

Colombian Coal PF1	Ultimate Analysis $\%_{wt}$ (dry, ash free)					LCV / MJ/kg_{dry}
	C	H	O	N	S	
Fuel	77.8	5.5	1.7	14.3	0.8	29.9
Char	89.9	1.8	1.9	5.8	0.6	27.1
Volatiles	72.0	7.2	1.6	18.3	0.9	31.7

Table 7.2: Executive summary of the fuel characterisation for the Belgian sewage sludge [100]

Belgian Sewage Sludge PF1	Proximate Analysis $\%_{wt}$ (dry)			Proximate Analysis $\%_{wt}$ (dry, ash free)	
	Ash	Volatiles	Fixed Carbon	Volatiles	Fixed Carbon
Fuel	42.6	52.3	5.1	91.1	8.9
Char	89.1	6.9	4.1	62.8	37.2

Colombian Coal PF1	Ultimate Analysis $\%_{wt}$ (dry, ash free)					LCV / MJ/kg_{dry}
	C	H	O	N	S	
Fuel	47.4	7.0	6.6	34.7	1.5	11.6
Char	42.2	2.4	2.3	51.8	1.3	1.4
Volatiles	48.0	7.5	7.0	36.0	1.6	20.8

Table 7.3: Executive summary of the fuel characterisation for the 95% Colombian coal – 5% Belgian sewage sludge blend [100]

Colombian Coal PF1	Proximate Analysis %$_{wt}$ (dry)			Proximate Analysis %$_{wt}$ (dry, ash free)	
	Ash	Volatiles	Fixed Carbon	Volatiles	Fixed Carbon
Fuel	10.1	40.4	49.5	45.0	55.0
Char	24.0	9.1	66.9	12.0	88.0

Colombian Coal PF1	Ultimate Analysis %$_{wt}$ (dry, ash free)					LCV / MJ/kg$_{dry}$
	C	H	O	N	S	
Fuel	75.5	5.6	2.1	16.0	0.9	27.8
Char	87.3	2.2	1.7	8.3	0.5	24.1
Volatiles	69.5	7.3	2.2	20.0	1.0	30.7

Table 7.4: Executive summary of the fuel characterisation for the 90% Colombian coal – 10% Belgian sewage sludge blend [100]

Belgian Sewage Sludge PF1	Proximate Analysis %$_{wt}$ (dry)			Proximate Analysis %$_{wt}$ (dry, ash free)	
	Ash	Volatiles	Fixed Carbon	Volatiles	Fixed Carbon
Fuel	13.7	41.7	44.6	48.4	51.6
Char	30.2	8.7	61.1	12.5	87.5

Colombian Coal PF1	Ultimate Analysis %$_{wt}$ (dry, ash free)					LCV / MJ/kg$_{dry}$
	C	H	O	N	S	
Fuel	73.3	5.7	2.4	17.7	0.9	26.1
Char	87.3	2.2	1.7	8.3	0.5	22.6
Volatiles	66.0	7.5	2.8	22.5	1.1	29.4

Table 7.5: Particle size distribution Rosin-Rammler data for the fuels used in the ENEL combustion trials [100]

Fuel / blend (%$_{th}$) sewage sludge	Colombian Coal	Belgian Sewage Sludge	5% Sewage Sludge	10% Sewage Sludge
Maximum Particle Diameter (μm)	150	>500	>500	>500
Minimum Particle Diameter (μm)	32	<1	<1	<1
Mean Particle Diameter (μm)	52	13.9	45	38
Spread Parameter	1.19	0.85	1.05	1.01

7.4.3.2 Operational Process Data

Data has been provided for 6 of the combustion trials conducted in the ENEL furnace with varying levels of sewage sludge and equivalence ratios (λ):

1. Pure Colombian coal with a λ of 1.05
2. Pure Colombian coal with a λ of 1.20
3. 95%$_{th}$ Colombian coal – 5%$_{th}$ Belgian sewage sludge with a λ of 1,26
4. 95%$_{th}$ Colombian coal – 5%$_{th}$ Belgian sewage sludge with a λ of 1.27
5. 90%$_{th}$ Colombian coal – 10%$_{th}$ Belgian sewage sludge with a λ of 1.23
6. 90%$_{th}$ Colombian coal – 10%$_{th}$ Belgian sewage sludge with a λ of 1.65

During the combustion trials, the ENEL furnace operated at a nominal 500kW$_{th}$. The standard burner configuration is to run 13% primary (transport) air with entrained coal particles, 43% secondary air and 44% tertiary air with minimum swirl in the secondary and tertiary air streams and bluff body swirl in the primary air stream. Details of the fuel and air flowrates and other process parameters during each of the runs are shown in table 7.6.

Table 7.6: Furnace input controls for the ENEL combustion trials

Trial		1	2	3	4	5	6
Coal Flowrate	kg/h	67.50	66.90	62.48	57.77	59.45	52.33
Sludge Flowrate	kg/h	0.00	0.00	7.70	7.70	15.50	15.50
Thermal Power Coal	kW$_{th}$	511	507	473	438	450	396
Thermal Power Sludge	kW$_{th}$	0	0	25	25	50	50
Thermal Power Total	kW$_{th}$	511	507	498	463	500	446
Primary Air Flowrate	kg/h	78.51	80.48	83.43	80.53	83.95	78.50
Secondary Air Flowrate	kg/h	605	693	618	572	518	639
Primary Air Temperature	°C	25	28	25	28	25	30
Secondary Air Temperature	°C	400	400	400	400	400	400
Number of Cooling Lances		42	42	43	42	42	42
Heat Absorbed by Lances	kW	235	231	241	193	231	178

7.4.3.3 Key Results of the ENEL Combustion Trials

Table 7.7 shows the principal measurements from the ENEL combustion trials.

Table 7.7: Key measurements made during the ENEL combustion trials

Trial		1	2	3	4	5	6
Combustion Chamber Temperature	°C	1123	1202	1090	1063	1026	895
Transfer duct Temperature	°C	788	837	769	803	770	732
O_2 Transfer duct	%$_{mol}$	4.18	5.66	5.23	7.55	5.90	8.00
CO Transfer duct	ppm	193	50	225	74	144	109
CO_2 Transfer duct	%$_{mol}$	14.59	13.22	12.75	11.75	12.95	8.91
NO_x Transfer duct	ppm	557	674	587	665	707	581

7.5 The FLUENT CFD Software Package.

The FLUENT CFD software package has been used for the simulation of the combustion systems described in this chapter. The FLUENT package comprises Gambit, a pre-processor for geometry modelling and mesh generation, PrePDF, a pre-processor for modelling non-premixed combustion and the FLUENT solver itself.

For all flows, FLUENT solves the governing integral equations for the conservation of mass and momentum, if heat transfer is involved, an additional equation for energy conservation is solved. Flows involving species mixing or reactions require the solution of a species conservation equation and if the non-premixed combustion model is used, conservation equations for the mixture fraction and its variance are solved. Additional transport equations are also solved when the flow is turbulent [93].

The solution is carried out by the following three steps [93]:

1. Division of the domain into discrete control volumes using a computational grid.
2. Integration of the governing equations across each control volume to construct algebraic equations for the "discrete dependant variables" or unknowns such as temperature, pressure, velocity and other scalars.
3. Linearization of the discretised equations and solution of the resultant linear equation system to yield updated values of the dependant variables.

Two different numerical methods are available within FLUENT to achieve the solution; the segregated solver, which solves the conservation equations sequentially or the coupled solver, which solves them simultaneously. The segregated solver with implicit formulation is used for combustion problems as it, unlike the coupled solver, supports features such as the non-premixed combustion prePDF model used for particulate combustion [93].

As the governing equations are non-linear and coupled, several iterations of the solution loop must be completed before a converged solution is achieved. Each iteration comprises the following steps [93]:

1. The fluid properties are updated based upon the current solution (or initialized solution if the calculation has just started).
2. The *u*, *v* and *w* momentum equations are solved using current values for pressure and control volume face mass fluxes to update the velocity field.

3. As the new velocities from step 2 may not satisfy the continuity equation locally, a pressure correction equation is derived which is solved to obtain the necessary corrections to the pressure and velocity fields and the control volume face mass fluxes such that the continuity equation is satisfied.
4. Equations for other scalars such as energy, species, turbulence and radiation are solved using updated values of the other variables.
5. Where interphase coupling (transfer of mass between the continuous gas phase and the solid discrete phase, for example) is to be used, the source terms in the appropriate continuous phase equations may be updated by a discrete phase trajectory calculation.
6. A check for convergence of the equation set is made.

These steps are iterated until the convergence criteria are met.

7.6 Previous CFD Work on the ENEL 500kW$_{th}$ Furnace

Initial work on this subject was carried out by Carrieri [79], who created a simple 2D model of the furnace using the FLUENT 6.1 CFD software package. Carrieri used a coarse grid of 6792 triangular cells to model the combustion chamber, transfer duct and the refractory walls of the furnace using a simplified representation of the burner. The non-premixed combustion model was used to simulate fuel combustion. This utilises the PrePDF pre-processor within the software which is discussed in detail in section 6.6.1.1. Devolatilisation was modelled using the two competing rates model and char combustion using the intrinsic combustion model, the Reynolds stress model was used for turbulence modelling along with the P1 radiation model [79].

Carrieri produced results that compared well with the experimental data provided by ENEL; wall temperatures were predicted within 5% of measured values, O_2 and CO_2 levels within the flue gases were predicted to within 4% and CO and NO_x to within 30% [79]. However due to the two dimensional nature of the model, Carrieri was unable to predict particle deposition on the deposition probe in the transfer duct of the furnace.

7.7 The ENEL 500kW$_{th}$ Furnace CFD Model

Following on from Carrieri's work, a three dimensional model of the ENEL 500kW$_{th}$ furnace has been constructed, it is hoped that solution of the combustion system in three dimensions will enable the prediction of particle trajectories and moreover, the estimation of impaction rates on deposition probes situated within the furnace.

7.7.1 Development of the 3D Computational Grid

The FLUENT pre processor, Gambit, has been used to model the geometry of the ENEL 500kW$_{th}$ furnace in three dimensions. The computational grid underwent several evolutions during the problem solving process.

7.7.1.1 Version 1 of the Computational Grid.

A representation of the computational domain can be seen in figure 7.3. Despite being symmetrical in the X-Y plane, the entire furnace has been modelled as it is believed that given the turbulent nature of the flow regime within the furnace, the flame and combustion conditions would not exhibit symmetry.

It is important to note that unlike in Carrieri's 2D models, the refractory lining of the furnace has not been modelled. It was deemed that the refractory played no significant part in accurately predicting the flow characteristics and particle trajectories within the furnace. Whilst its insulating properties would be important for predicting the temperature regime, these properties could be more efficiently modelled as boundary conditions.

The first version of the computational grid comprised approximately 98000 cells, the majority of which were hexahedral cells in main combustion zone, with wedge, pyramid and tetrahedral cells used to model the more complex parts of the combustion domain (burner, deposition probe and convergence). The advantage of using a tetrahedral cell structure in these situations over a hexahedral (six sided) cell structure is that it allows complex geometries to be meshed relatively easily, allowing cells to be clustered in areas of the flow domain where a finer mesh may be required. If a fine mesh is required in a certain area of the domain, using structured hexahedral meshes often forces a fine mesh to be situated in an area where it is not needed, greatly increasing computational time [93].

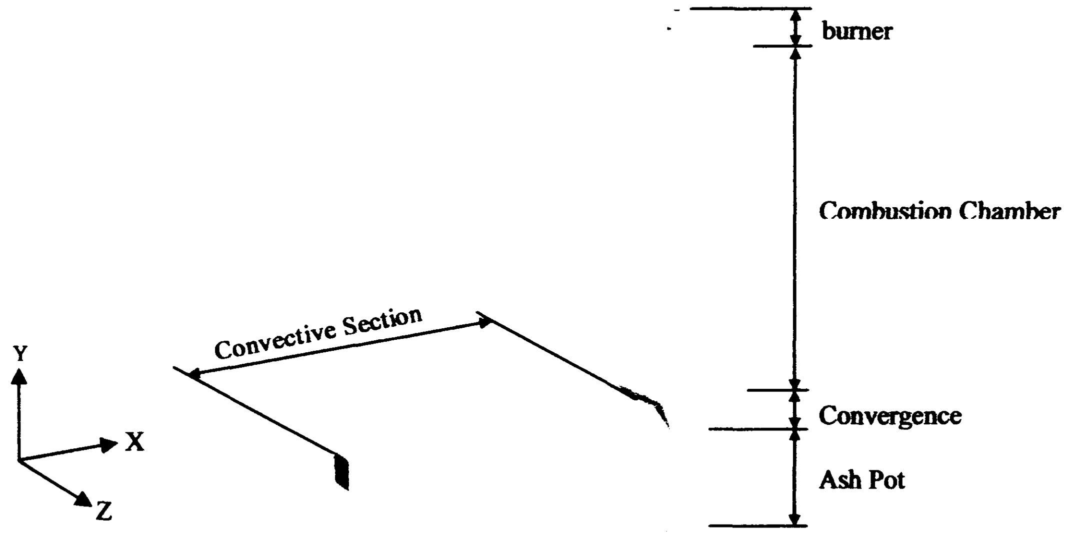

Figure 7.3: The computational domain boundaries of the ENEL 500kW$_{th}$ furnace

7.7.1.2 Version 2 of the Computational Grid

In version 2, the grid was refined to better model the burner, allowing a more accurate representation of the flow regime of the transport and combustion air as it entered the furnace (Ref. figure 7.4). The burner was modelled as three separate inlets for the primary, secondary and tertiary air respectively. The diffuser in the primary air stream was also modelled to promote better mixing of the fuel with the secondary and tertiary air. The second version of the computational grid has been constructed using approximately 215000 four-sided tetrahedral cells. Another feature of this grid was a division of the combustion chamber into three sections; near burner, central and lower region. This promoted more accurate representation of heat removal through the boiler walls, allowing the use of local heat removal rates rather than using a single global heat flux value.

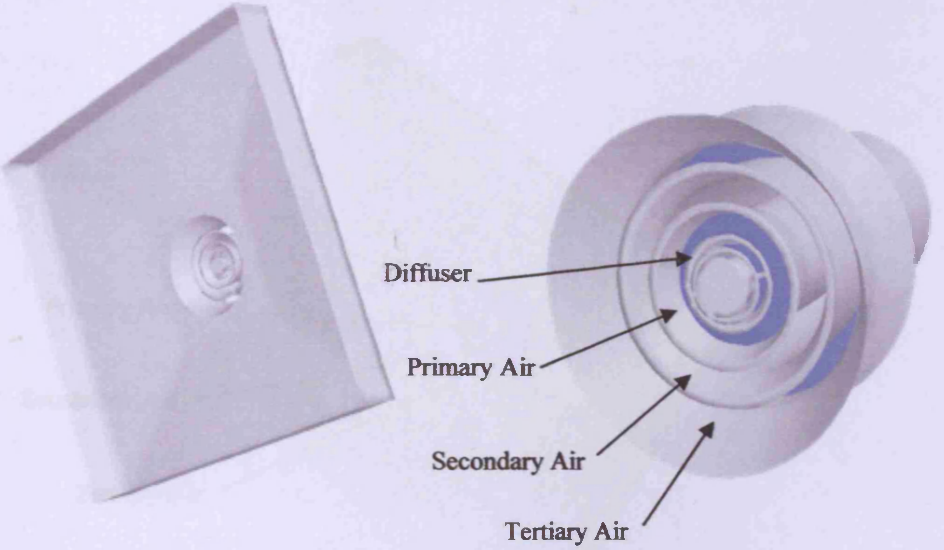

Figure 7.4: The computational domain boundaries around the burner region in version 2 of the computational grid.

7.7.1.3 Version 3 of the Computational Grid

In a final evolution of the computational grid an entirely hexahedral cell structure was used. Hexahedral cells, despite causing more difficulties during mesh creation, offer a significant performance advantage over tetrahedral cells; hexahedral cells permit much larger aspect ratios than tetrahedral cells, a large aspect ratio in a tetrahedral cell will affect the skewedness of the cell more so than in a hexahedral cell. The skewedness is a key factor in assessing the quality of a mesh, as cells with low skewedness will produce more accurate results and faster convergence [93].

Other changes in the computational grid include reverting to a simpler burner geometry to reduce computation time (Ref. figure 7.5) and the division of the furnace wall to allow modelling of individual cooling lances (ref. figure 7.6).

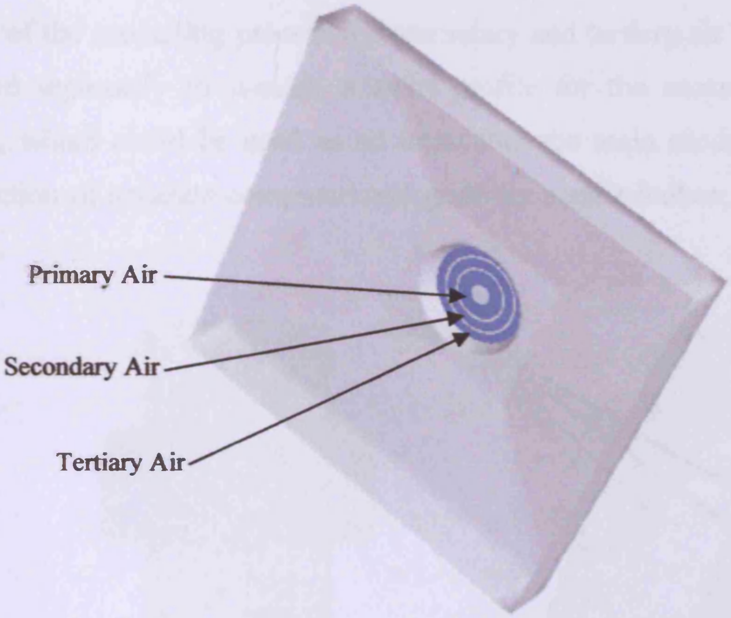

Figure 7.5: The simplified burner geometry used for the version 3 computational grid

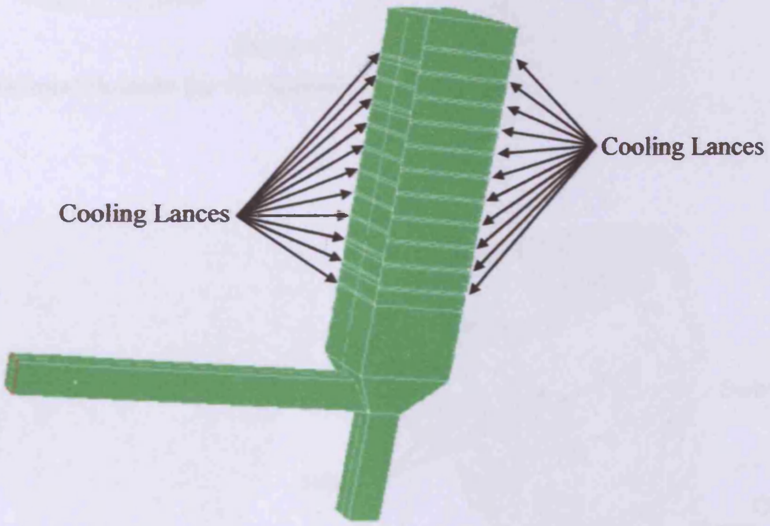

Figure 7.6: The boundaries of the computational domain of version 3 of the computational grid showing the cooling lances modelled separately

7.7.1.4 The Secondary and Tertiary Air Windboxes

As part of the modelling process the secondary and tertiary air windboxes were each modelled separately to provide a swirl profile for the secondary and tertiary air streams, which could be used as an input into the main model. This required the construction of separate computational grids for each windbox, shown in figures 7.7 and 7.8.

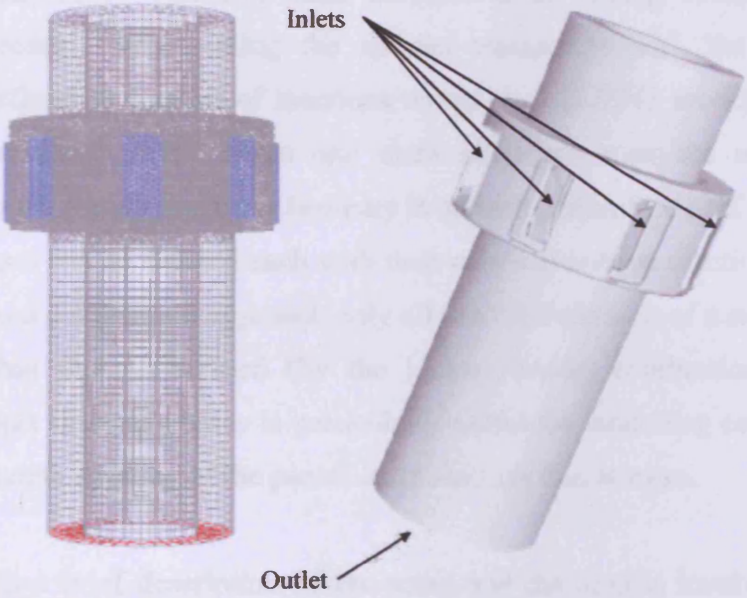

Figure 7.7: Computational domain for the secondary air windbox

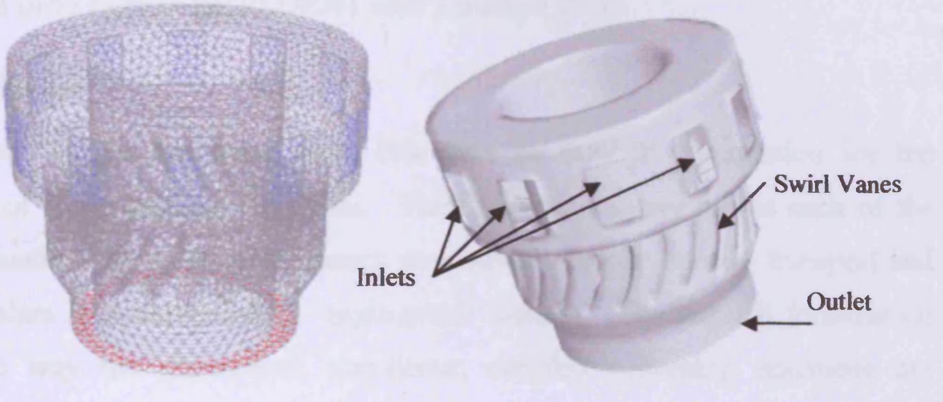

Figure 7.8: Computational domain for the tertiary air windbox

7.7.2 Model Setup

Two different combustion approaches have been used during the modelling process; the non-premixed combustion prePDF model and the species transport model. The main difference between these models is how the combustion chemistry is treated. The non-premixed combustion model, as is explained in section 6.6.1.1, uses a pre-processor which generates lookup tables based upon the fuel inputs to define the combustion chemistry. FLUENT then accesses these lookup tables during the calculation process. When using the species transport model, the combustion chemistry is defined as a series of reactions within the FLUENT model setup itself. The species transport model holds one main advantage over the non-premixed combustion model; the combustion chemistry is defined within FLUENT, any number of discrete phases can be defined each with their own combustion reactions, whereas, the non-premixed combustion approach only allows the definition of a single discrete phase which has the pre-defined (by the lookup tables) combustion chemistry. Defining multiple discrete phases is particularly useful for modelling co-combustion as it allows separate tracking of the parent and substitute fuel streams.

What follows is a brief description of the setup and the models involved with the reasons behind the choices made. For a full list of the FLUENT inputs and model settings, refer to Appendix F. For detailed descriptions of the models used and the theory behind them refer to the FLUENT user's manual [93].

7.7.2.1 The Solver

The segregated solver has been used, this uses an implicit formulation for the linearization of the governing equations. The segregated solver solves each of the governing equations for continuity (mass), momentum, energy, species transport and any other scalars in a sequential or 'segregated' fashion. The implicit formulation refers to the way the discretised, non-linear, coupled governing equations are linearised to allow their solution. The implicit formulation sees unknown variables in each cell computed using existing and unknown values from neighbouring cells. Therefore, each unknown will appear in more than one equation in the system allowing the equation set to be solved simultaneously to find the values of the unknowns.

The current simulation is in a 3D computational domain, therefore, the 3D setting has been chosen for the spatial discretisation. The ENEL 500kW$_{th}$ furnace is to be modelled under steady-state conditions as the combustion conditions are considered to be constant. For this reason the simulation can be carried out as a steady-state event and the governing equations will have no time dependant terms within them. The SIMPLE pressure-velocity coupling algorithm has been used. This is recommended for complex steady state flows as it has a more conservative under relaxation value [93]. The gradient option is used to define how the derivatives of a given variable are used to discretise the convection and diffusion terms of the equations of motion, the FLUENT default of cell-based has been chosen here.

7.7.2.2 The Energy Model

"The flow of thermal energy from matter occupying one region of space to matter occupying a different region of space is known as heat transfer" [93]. Modelling of heat transfer is fundamental to combustion simulations, for this reason, it is necessary to use the energy equation. Once the energy equation is activated, it is necessary to define thermal boundary conditions at inlets, exits and walls (see Appendix F).

7.7.2.3 The Radiation Model

The P-1 radiation model has been selected owing to its ability to simulate radiative heat exchange between the gas and particulate phase. "The P-1 radiation model is based upon the more general P-N model which uses the expansion of radiation intensity onto an orthogonal series of spherical harmonics" [93]. It is capable of predicting interphase radiative heat transfer and can model scattering effects over large optical thicknesses (optical thickness is given by multiplying a suitable length scale for the domain, i.e. furnace diameter, by the absorption coefficient). It is suited to complex geometry, however, has a tendency to over predict heat fluxes if the optical thickness is too small or a localised heat source or sink is used.

7.7.2.4 The Viscous Model

Turbulent flows are characterised by fluctuating velocity fields, these mix transported quantities such as momentum, energy and species concentration, causing them to fluctuate also [93]. Due to the small scale and high frequency of these fluctuations, direct simulation of them is too computationally expensive. Instead the instantaneous equations are time-averaged, removing the small scale. These modified equations contain additional unknowns requiring a turbulence model to solve them. "The Reynolds stress model closes these Reynolds-averaged Navier-Stokes equations by solving transport equations for the Reynolds stresses together with an equation for the dissipation rate" [93]. FLUENT recommends using the Reynolds stress models for highly swirling combusting flows such as those in the near burner region of the ENEL 500kW$_{th}$ furnace.

7.7.2.5 The Species Model

Throughout the course of the modelling exercise, two different species models have been used. As previously mentioned, initial simulations were carried out using the non-premixed combustion model however, in later simulations the species transport model was introduced, allowing the simulation of two different fuel streams.

7.7.2.5a The Non-premixed Combustion Model

In non-premixed combustion, fuel and oxidiser enter the furnace as two distinct streams (mixing refers to the molecular level rather than physical mixing of the streams). In the non-premixed combustion model, FLUENT reduces the thermochemistry of the system to a single parameter; the mixture fraction, which is defined as "the mass that originated form the fuel stream" i.e. the local mass of burnt and unburnt fuel stream elements (C, H etc) in the species (CO_2, H_2O etc) [93]. A more detailed description of the non-premixed combustion model has previously been given in section 6.6.1.1.

7.7.2.5b The Species Transport Model

The species transport model is the simulation of the mixing and transport of chemical species by the solution of conservation equations for convection, diffusion and reaction sources for each component species. Multiple simultaneous reactions can be modelled, taking place in the bulk phase or on wall and particle surfaces [93]. The conservation equation takes the general form [93]:

$$\frac{\partial}{\partial t}(\rho Y_i)+\nabla\cdot(\rho\vec{v}Y_i)=-\nabla\cdot\vec{J}_i+R_i+S_i \qquad (7.1)$$

Where ρ is the density of species i (kg/m^3), Y_i is the mass fraction of species i, $\vec{v}$ is the overall velocity vector (m/s), $\vec{J}_i$ is the diffusion flux of species i (kg/m^{2}s). R_i is the net rate of production of species i (kg/s) and S_i is the rate of creation of species i by addition from the dispersed phase plus any user defined sources (kg/s).

This equation is solved for $N - 1$ species where N is the total number of species, since the sum of mass fractions must sum to unity the N^{th} mass faction is calculated as 1 minus the sum of the solved $N - 1$ mass fractions. FLUENT recommends that the N^{th} is that with the highest overall mass fraction (N_2 in coal combustion with air) [93].

For turbulent flows such as those being solved here, the diffusion flux ($\vec{J}_i$) is described by the following equation [93]:

$$\vec{J}_i = -\left(\rho D_{i,m} + \frac{\mu_t}{Sc_t}\right)\nabla Y_i \qquad (7.2)$$

Where $D_{i,m}$ is the diffusion coefficient for species i in the mixture, μ_t is the turbulent viscosity (Pa s) and Sc_t is the Schmidt number (μ_t / ρD_t where D_t is the turbulent diffusivity).

FLUENT suggest that "turbulent diffusion generally overwhelms laminar diffusion and that the specification of detailed laminar diffusion properties in turbulent flows is not warranted" [93].

The reaction rates that appear in equation (7.1) as source terms are computed by FLUENT using one of three models. In this case, the eddy dissipation model has been chosen to do this. Here, reaction rates are assumed to be controlled by turbulence, so the computationally expensive Arrhenius rate calculations used by the finite rate model are not required. It is important to note that for this model only one or two step heat release mechanisms can be used [93].

The eddy dissipation model:

The eddy dissipation model assumes that most fuels are fast burning and, as such, it is the turbulent mixing that controls reaction rates rather than chemical kinetic reaction rates. In non-premixed flames, it is assumed that turbulence slowly convects/mixes reactants into the reaction zone where they burn quickly. In such cases, combustion is said to be mixing limited and the complex chemical kinetic rates can be neglected [93]. FLUENT provides a turbulence-chemistry interaction model where the net rate of production of species i due to reaction r, $R_{i,r}$ is given by the smaller (limiting value) of the two expressions below (equations (7.3) and (7.4)) [93]:

$$R_{i,r} = \nu'_{i,r} M_{w,i} A \rho \frac{\varepsilon}{k} \min_{R} \left(\frac{Y_R}{\nu'_{R,r} M_{w,R}} \right) \tag{7.3}$$

$$R_{i,r} = \nu'_{i,r} M_{w,i} A B \rho \frac{\varepsilon}{k} \frac{\sum_{P} Y_P}{\sum_{j}^{N} \nu''_{j,r} M_{w,j}} \tag{7.4}$$

Where $\nu'_{i,r}$ is the stioichiometric coefficient for reactant i in reaction r, $M_{w,i}$ is the molecular weight of reactant i (kg/kgmol), A is an empirical constant equal to 4, ρ is the density of the flow (kg/m^3), ε is the turbulent dissipation rate (m^2/s^3), k is the mass transfer coefficient (units vary), Y_R is the mass fraction of a particular reactant R, $\nu'_{R,r}$ is the stoichiometric coefficient of a particular reactant R in reaction r, $M_{w,R}$ is the molecular weight of a particular reactant R (kg/kgmol) , B is an empirical constant equal to 0.5, Y_P is the mass fraction of any product species, P, $\nu''_{j,r}$ is the stoichiometric coefficient for product j in reaction r [93].

In equations (7.3) and (7.4), the chemical reaction rate is governed by the large eddy mixing timescale k / ε. Combustion proceeds whenever turbulence is present (k / ε > 0), and an ignition source is not required. This is usually acceptable for non-premixed combustion, however, it is possible, especially when premixed, for ignition to occur as soon as the reactants enter the domain. To combat this FLUENT uses the finite rate/eddy dissipation model, here, the Arrhenius equation (equation (7.5)) is calculated along with the eddy dissipation equations (equations (7.3) and (7.4)), giving the molar rate of creation/destruction of species i in reaction r, producing product j [93].

$$\hat{R}_{i,r} = \Gamma\left(\nu''_{i,r} - \nu'_{i,r}\right)\left(k_{f,r}\prod_{j=1}^{N_r}\left[C_{j,r}\right]^{\eta'_{j,r}} - k_{b,r}\prod_{j=1}^{N_r}\left[C_{j,r}\right]^{\eta''_{j,r}}\right) \qquad (7.5)$$

Where Γ represents the net effect of third bodies on the reaction rate, $k_{f,r}$ and $k_{b,r}$ are reaction rate constants for reaction r, N_r is the number of reactants in reaction r, $C_{j,r}$ is the molar concentration of each reactant and product species j in reaction r (kgmol/m^3), $\eta'_{j,r}$ is the forward rate component for each reactant and product species j in reaction r and $\eta''_{j,r}$ is the backward rate component for each reactant and product species j in reaction r [93].

The net reaction rate is then taken as the minimum of these three equations. The Arrhenius rate acts as a kinetic 'switch' preventing instantaneous combustion by controlling the reaction rate at the point of entry to the domain. Once ignition has occurred, the eddy dissipation rate is generally smaller and the reactions become mixing limited [93].

7.7.2.6 The Discrete Phase Model

In addition to the transport equations for the continuous phase, FLUENT can solve a second discrete phase, in a Lagrangian frame of reference, consisting of spherical particles. FLUENT calculates the trajectories of these particles along with heat and mass transfer between them and the continuous phase and the effect this has on both particle trajectories and continuous phase flow. When the fluid flow is turbulent, FLUENT will predict the trajectories of particles using the mean continuous phase velocity, however, a stochastic method can be used to give the instantaneous gas velocity, allowing the prediction of particle dispersion due to turbulence. This works by integrating the individual particle trajectory calculations using the instantaneous gas velocity along the particle path during the integration [93]. "By computing the trajectories in this way for a suitable number of particles, the random effects of turbulence on particle dispersion may be accounted for" [93]. The length scale is the distance the particle travels before its motion equations are solved again, the shorter this distance, the more accurate the predictions will be [93]. This has been set to 0.01 for all simulations.

The interaction with the continuous phase option has been used, as recommended by FLUENT, to account for the transfer of mass, momentum and energy between the discrete and continuous phases. The particle radiation interaction has also been switched on, allowing the effects of radiative heat transfer to/from the particles to be included. FLUENT solves a defined number of continuous phase iterations before updating the discrete phase models. Increasing this number will increase the stability of the simulation, but will also increase convergence time [93]. This value is initially set to 50 for all models.

7.7.2.7 Combustion of Discrete Phase Particles

All of the particles in the models are combusting, therefore, the combusting particle option within FLUENT has been used. In doing this, the following laws are activated:

1) The inert heating law

Whilst the particle temperature is below the specified vaporisation temperature, T_{vap} or after the volatile fraction of the particle has been consumed, the inert heating law is applied, i.e. there is no reaction or mass transfer between the particle and the continuous phase [93].

2) The devolatilisation law

This is applied to the particle once it has reached the vaporisation temperature and remains in effect until the mass of the particle no longer exceeds the mass of non-volatiles within the particle [93].

The Kobayashi two competing rates devolatilisation model has been used. Kobayashi suggested that two rates controlled the devolatilisation; a slow rate, R_1 (equation (7.6)) at low temperatures and a fast rate, R_2 (equation (7.7)) at high temperatures [93]:

$$R_1 = A_1 e^{(E_1/RT_P)} \tag{7.6}$$

$$R_2 = A_2 e^{(E_2/RT_P)} \tag{7.7}$$

These kinetic rates are weighted to yield an expression for the devolatilisation as follows [93]:

$$\frac{m_v(t)}{(1-f_{v,0})m_{p,0} - m_a} = \int_0^t (\alpha_1 R_1 + \alpha_2 R_2)\exp\left(-\int_0^t (R_1 + R_2)dt\right)dt \tag{7.8}$$

Where A_1, A_2, E_1 and E_2 are kinetic rate parameters to be input by the user, R is the gas-law constant (8314.47 J/kgmol-K), T_P is the particle temperature (K), $m_v(t)$ is the volatile yield up to time t, $f_{v,0}$ is the fraction of volatiles in the particle at time 0, $m_{p,0}$ is the mass of the particle at time 0, m_a is the ash content of the particle and a_1 and a_2 are yield constants also set by the user [93]. FLUENT recommends that a_1 for the slow rate reaction be set to the volatile content as calculated by proximate analysis and that a_2 be set to 1 or close to unity to represent the high-temperature volatile yield [93].

3) The surface combustion law

Once the entire volatile component of the particle has been evolved, the surface combustion model begins. Following the complete combustion of the combustible fraction (f_{comb}) of the particle, there may be residual ash left within the particle, if this is the case, the inert heating law is invoked again [93].

With the exception of the multiple surface reactions model, surface combustion is governed by the stoichiometric requirement, S_b of the surface burnout reaction [93]:

$$Char(s) + S_b oxidiser(g) = Products(g) \tag{7.9}$$

Two different models have been used for the solution of surface combustion during the course of this modelling exercise; the intrinsic model and the multiple surface reactions model.

3a) The Intrinsic Combustion Model

The intrinsic model assumes the surface reaction rate includes the effects of both bulk diffusivity and chemical reaction. "The model uses equation (7.10) to calculate the diffusion rate coefficient, D_0, however the chemical rate, R, is expressed purely in terms of the intrinsic chemical and pore diffusion rates" (equation (7.11)) [93].

$$D_0 = C_1 \frac{\left[(T_P + T_\infty)/2\right]^{0.75}}{d_p} \qquad (7.10)$$

Where C_1 is a constant, T_P and T_∞ are the particle temperature and the temperature at infinity respectively (K), d_p is the particle diameter (m) [93].

$$R = \left\{\frac{3}{\phi^2}(\phi \coth \phi - 1)\right\} \frac{d_P}{6} \rho_p A_g k_i \qquad (7.11)$$

Where :

$$\phi = \frac{d_P}{2}\left[\frac{S_b \rho_p A_g k_i p_{ox}}{D_e \rho_{ox}}\right] \qquad (7.12)$$

Where d_p is the particle diameter (m), ρ_p and ρ_p are the particle and oxidant densities respectively (kg/m^3), A_g is the specific internal surface area of the particle (m^2), k_i is the intrinsic reactivity of the char (which is in the Arrhenius form such as equations (7.6) and (7.7) where A and E are FLUENT defaults), S_b is the stoichiometric requirement of the burnout reaction, p_{ox} is the density of the oxidant in the bulk gas (kg/m^3) and D_e is the effective diffusion coefficient in the particle pores [93].

To allow more accurate description of char particle size during combustion the burning mode a can be set, relating the particle diameter to the fractional degree of burnout, U [93]:

$$\frac{d_p}{d_{p,0}} = (1-U)^a \tag{7.13}$$

Where d_p and $d_{p,0}$ are the current and original particle diameters (m) and $U = (1-(m_p/m_{p,0}))$ where m_p and $m_{p,0}$ are the current and original particle masses (kg). With a set to 0, the particle size remains constant whilst the density reduces, with a set to 1/3, particle size decreases whilst density remains constant and with a set to 0.25 both particle size and density decrease. This mode has been found to work well with a variety of chars [93].

3b) The Multiple Surface Reaction Model

The multiple surface reaction model allows individual chemical reactions to be defined when modelling particle combustion. In this model, FLUENT uses the following equation to describe the rate of reaction, r of a particle surface species, j reacting with the gas phase species, n [93]:

Particle species j (s) + gas phase species n → products

$$\overline{R_{j,r}} = A_p \eta_r Y_j R_{kin,r}\left(p_n - \frac{R_{j,r}}{D_{0,r}}\right)^{N_r} \tag{7.14}$$

Where $\overline{R_{j,r}}$ is the rate of particle surface species depletion (kg/s), A_p is the particle surface area (m^2), η_r is the effectiveness factor, Y_j is the mass fraction of surface species j in the particle, $R_{kin,r}$ is the kinetic rate of reaction, p_n is the bulk partial pressure of the gas phase species (Pa), $R_{j,r}$ is the rate of particle surface species reaction per unit area (kg/m^{2}s), $D_{0,r}$ is the diffusion rate coefficient for reaction r and N_r is the apparent order of reaction r [93].

$D_{0,r}$ is given by equation (7.10) as in the intrinsic combustion model and the kinetic rate of reaction is in Arrhenius form as shown in equation (7.15) [93]:

$$R_{kin,r} = A_r T^{\beta_r} e^{-(E_r/RT)} \tag{7.15}$$

Where A_r and E_r are kinetic rate parameters, T is the temperature (K) and R is the gas-law constant (8314.47 J/kgmol-K) [93].

7.7.3 Initial Test Models (Simulations 1 and 2)

Two models were run initially as a test of FLUENT's 3-Dimensional modelling capabilities, combustion trials 1 and 5 have been modelled (simulations 1 and 2 respectively), using version 1 of the computational grid.

7.7.3.1 Model Details for Simulations 1 and 2

A non-premixed combustion model was selected for the initial models and combined with the Reynolds stress viscous model and the P1 radiation model. Eight discrete phase injections were equally spaced around the centreline of the primary air inlet in at the point of entry of the primary air into the furnace. 20 continuous phase iterations per discrete phase iteration have been used initially, this was changed to 200 after 15000 iterations to speed convergence. Each injection comprised 10 particle streams, providing 10 discrete particle diameters, with a Rosin-Rammler particle size distribution. Particles were given an initial velocity of 2.59m/s in line with the calculated flow velocity of the transport air. The stochastic tracking model was set to 10 'tries' meaning that a total of 800 particles would be tracked on their course through the boiler. Gravity was switched off to prevent the risk of excessive particle capture in the ash pot at the base of the furnace. Particle density was set to 1130kg/m^3 and the vaporisation temperature was 300K. The two competing rates devolatilisation model was selected and the intrinsic model ($\alpha = 0.25$) was used to simulate char combustion.

The secondary and tertiary air temperatures were set to 673 K and a global heat flux of -200 W/m^2 was applied to the walls of the main furnace with a fixed wall temperature of 823 K applied to the wall of the deposition probe.

Convergence criteria were initially set to 10^{-3} for all residuals except energy and radiation which were set to 10^{-6}, however, the latter were changed to 10^{-4} after convergence proved difficult. An initial temperature of 1100 K was patched to the entire combustion domain, with a local area in the vicinity of the burner set to 2000 K to initiate combustion.

The mass flowrate of fuel in combustion trial 5 was increased such that the thermal output matched that of combustion trial 1 (511kW) rather than 500kW. A full list of the model settings for the initial two models can be seen in Appendix F.

7.7.3.2 Results of the Initial Test Models

Tables 7.8 and 7.9 show the key measurements from the associated combustion trials and the predicted results taken from the simulations. The predictions have been made for positions on the centreline of the boiler at the end of the combustion chamber (the point where the convergence starts) and the end of the transfer duct (the exit of the computational domain).

Table 7.8: Comparison of measured and predicted results for combustion trial 1 (simulation 1).

Simulation 1	Combustion Chamber		Transfer duct	
	Combustion Trial 1	Simulation 1	Combustion Trial 1	Simulation 1
Temperature / °C	1123	1577	788	1297
O_2 / $\%_{mol}$	n/a	0.54	4.18	1.59
CO / ppm	n/a	53100	193	0 - 3100
CO_2 / $\%_{mol}$	n/a	13.90	14.59	16.40
H_2O / $\%_{mol}$	n/a	7.68	n/a	6.55

Table 7.9: Comparison of measured and predicted results for combustion trial 5 (simulation 2).

Simulation 2	Combustion Chamber		Transfer duct	
	Combustion Trial 5	Simulation 2	Combustion Trial 5	Simulation 2
Temperature / °C	1026	1127	770	947
O_2 / %$_{vol}$	n/a	0.81	5.90	2.89
CO / ppm	n/a	24600	144	0 - 1900
CO_2 / %$_{vol}$	n/a	15.2	12.95	13.5
H_2O / %$_{vol}$	n/a	7.52	n/a	6.85

Figure 7.9 shows a typical temperature profile for the 500kW$_{th}$ furnace taken from data provided by ENEL. Also shown are the predicted temperature profiles for the combustion chamber and transfer duct for simulations 1 and 2. Due to the nature of the contour plots created by FLUENT, a temperature range is predicted at each point on the curve. It is therefore unlikely that the predicted profile follows the stepped form shown but rather a smooth curved profile within the bounds of the range.

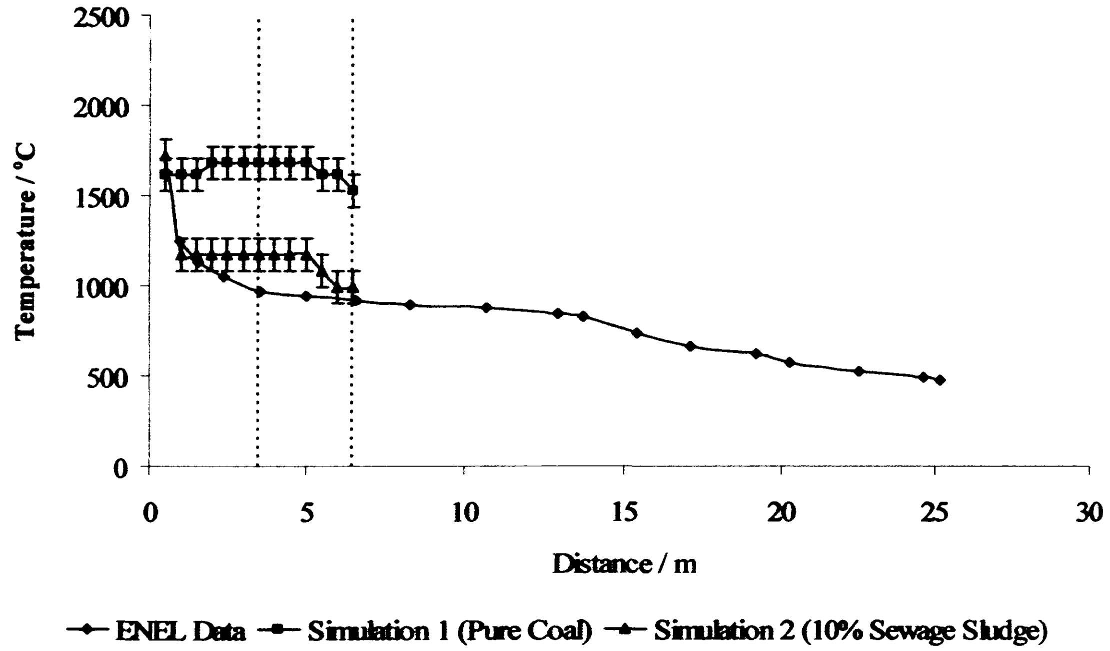

Figure 7.9: Measured and predicted temperature profiles for the ENEL 500kW$_{th}$ furnace (simulations 1 and 2).

Contour plots taken from FLUENT for static temperature, flue gas species and particle traces can be seen in Appendix F.

7.7.4 Simulations 3 and 4

Following simulations 1 and 2, several changes were made to the model. Simulations 3 and 4 were conducted using version 2 of the computational grid. Initially, modelling of the burner windboxes was carried out in order to better predict the swirl patterns in the secondary and tertiary air streams providing a more accurate model of the flame. This approach, however, proved unsuccessful and settings were applied to the secondary and tertiary inlets as in simulations 1 and 2. An improved model of the burner was also included in an attempt to improve the prediction of particle distribution and fuel mixing. A second deposition probe was modelled positioned 0.3m from the bottom of the combustion chamber and spanning the entire width.

Combustion trial 1 has been modelled again as in the initial models, however, combustion trial 3, a $95\%_{th}$ coal – $5\%_{th}$ sewage sludge blend with λ of 1.26 has been modelled in place of combustion trial 5.

7.7.4.1 Model Details for Simulations 3 and 4

The non-premixed combustion model combined with the Reynolds stress viscous model and the P1 radiation model were selected again for simulations 3 and 4. The discrete phase injections remained largely the same with the number of 'tries' in the stochastic tracking model being changed to 20 giving 1600 tracked particles. The locations of the injections changed slightly to accommodate the new burner geometry, however, the number (eight) remained the same. Initial particle velocity was changed to 1 m/s. Gravity remained switched off and the two competing rates devolatilisation model was selected again, along with the intrinsic model to simulate char combustion ($\alpha = 0.25$).

The boundary conditions were changed with a heat flux of -21.27 kW/m^2 applied to the combustion chamber walls to simulate heat removal by the cooling lances, a fixed wall temperature of 823 K was applied to the walls of both deposition probes. Secondary and tertiary air inlet boundary conditions remained the same.

Convergence criteria were again set to 10^{-3} for all residuals except energy and radiation, which were set to 10^{-6}. The same initialisation process was used to initiate combustion. However, in these simulations, the thermal input from the fuel was set to match that used in the combustion trials to try to improve comparisons between the model results and the simulations. A full list of the model settings for simulations 3 and 4 can be seen in Appendix F.

7.7.4.2 Particle Impaction Rates

The rate of particles impacting the deposition probe was calculated for simulations 3 and 4. This was achieved by using the report function during the discrete phase model iteration. This tracks each individual particle and sends a step by step report to a file detailing the mass, density, size and temperature of the particle as well as it's location in the furnace for each individual time-step. Given this information, the mass of each particle impacting the probe was noted. A second report details the mass flow rate of the 10 particle streams for each injection, where each particle stream corresponds to a discrete particle size, determined by the Rosin-Rammler size distribution. Taking the mass of each particle reported in the 1st time-step as the initial particle mass, the number of particles in each stream per second can be calculated using the mass flow rate of the stream. Tracking each of the 10 streams for each injection separately means that particles impacting the probe can be identified and the percentage of impacting particles from each stream can be calculated along with the mean mass of those particles when they impact. By multiplying this percentage by the mean mass of the impacting particle and the number of particles in the stream, it is possible to calculate the total mass of particles from each stream impacting the probes every second. Summing these values for all 10 streams allowed the calculation of the total mass of particles impacting the probes ($g/m^2/h$)

7.7.4.3 Results of Simulations 3 and 4

A summary of the results from simulations 3 and 4 can be found in tables 7.10 and 7.11 and figure 7.10. Contour plots for temperature, species, burnout and devolatilisation along with the particle tracking information used to calculate impaction rates can be found in Appendix F.

Table 7.10: Comparison of measured and predicted results for combustion trial 1 (simulation 3).

Simulation 3	Combustion Chamber		Transfer duct	
	Combustion Trial 1	Simulation 3	Combustion Trial 1	Simulation 3
Temperature / °C	1123	1437	788	1437
O_2 / $\%_{mol}$	n/a	2.63	4.18	4.73
CO / ppm	n/a	0 - 2980	193	0 - 2980
CO_2 / $\%_{mol}$	n/a	14.35	14.59	13.60
H_2O / $\%_{mol}$	n/a	7.02	n/a	6.36
Impaction Rate / $g/m^2/h$	19.13*	0.217	7.03*	0.695

*** These ENEL values are deposition rates not impaction rates as they do not include particles that have rebounded or have been shed from the deposition probe.**

Table 7.11: Comparison of measured and predicted results for combustion trial 3 (simulation 4).

Simulation 4	Combustion Chamber		Transfer duct	
	Combustion Trial 3	Simulation 4	Combustion Trial 3	Simulation 4
Temperature / °C	1090	1512	769	1292
O_2 / $\%_{mol}$	n/a	1.93	5.23	2.96
CO / ppm	n/a	8505	225	2320
CO_2 / $\%_{mol}$	n/a	14.65	12.75	14.65
H_2O / $\%_{mol}$	n/a	7.49	n/a	7.49
Impaction Rate / $g/m^2/h$	13.16*	5.252	17.58*	0.0473

*** These ENEL values are deposition rates not impaction rates as they do not include particles that have rebounded or have been shed from the deposition probe.**

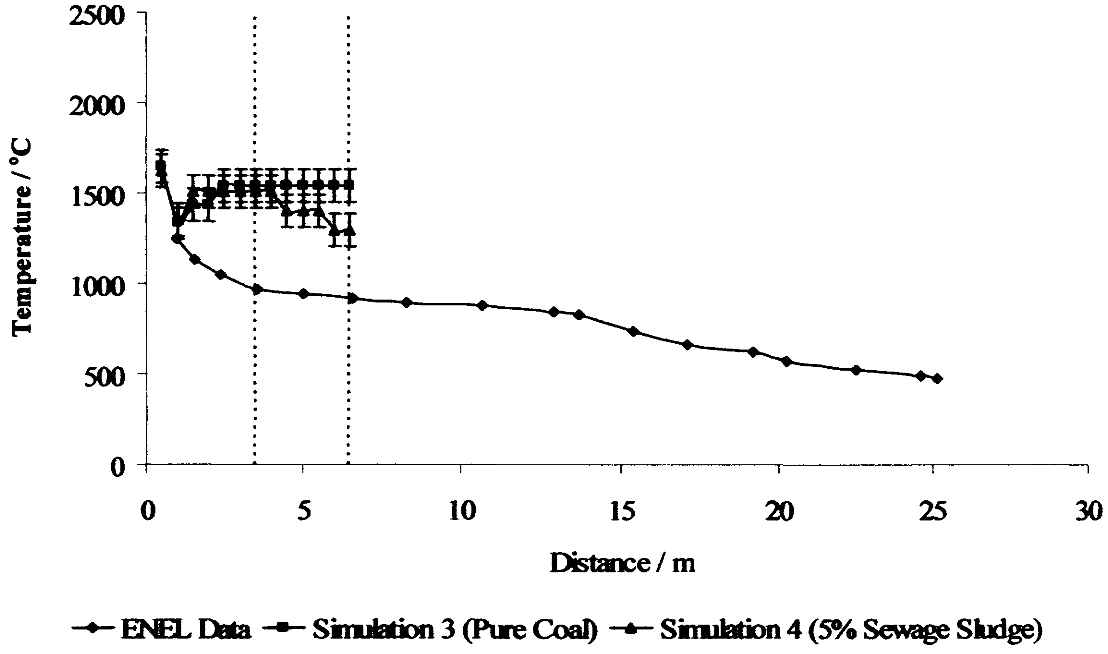

Figure 7.10: Measured and predicted temperature profiles for the ENEL 500kW$_{th}$ furnace (simulations 3 and 4).

7.7.5 Simulations 5 and 6

In order to improve the combustion predictions, simulations 5 and 6 have seen a departure from the non-premixed combustion model to allow the simulation of separate parent and substitute fuel streams. Version 3 of the computational grid has been used as it was hoped that an entirely hexahedral cell structure would aid accuracy and convergence. This version of the grid allows the cooling lances to be modelled separately, providing a better representation of the heat removed from the furnace, giving a more accurate prediction of the temperature regime. The difficulties faced in obtaining a sound hexahedral mesh structure in the burner region have forced the simplification of the burner geometry in order to keep the number of cells at a manageable level. To aid this, the deposition probe has been removed from the end of the combustion chamber, leaving the single probe in the transfer duct.

In simulations 5 and 6, combustion trial 3 has been modelled with a 2-stream species transport combustion model. The main difference between the simulations is the choice of particle combustion model; in simulation 5 the standard intrinsic combustion model ($\alpha = 0.25$) has been chosen, however, the particle surface reaction model has been utilised in simulation 6.

7.7.5.1 Model Details for Simulations 5 and 6

The solver, viscous model, energy model and radiation model settings have all remained the same as previous simulations. The species model has been changed to the species transport model with volumetric reactions and the finite rate/eddy diffusion turbulence – chemistry interaction model. For the discrete phase model, the number of continuous phase iterations per discrete phase iteration has been changed to 50 and the number of injections has changed from 8 coal injections to 4 coal injections and 4 sewage sludge injections equally spaced every other around the centreline of the primary air inlet. The fuel mass-flow rate and particle size distributions have been changed accordingly. Stochastic tracking settings have remained the same as those in simulations 3 and 4.

Heat flux at the furnace walls has changed such that heat removed by the cooling lances is better distributed see table 7.12.

Table 7.12: Wall heat fluxes for simulations 5 and 6

Axial Distance from Burner / m	Wall Heat flux W/m^2
0 – 0.28	-21327
0.28 – 0.84	-36589
0.84 – 2.52	-28565
2.52 – 2.80	-19578
2.80 – 3.5	-12586
Ash pot and transfer duct	-200

A full list of the settings for simulations 5 and 6 can be found in Appendix F.

7.7.5.2 Volumetric and Particle Surface Reactions.

The species transport model requires the user to define the combustion chemistry through a series of volumetric and particle surface chemical reactions rather than relying on the mixture fraction probability density function approach used in the non-premixed combustion model. The volumetric reactions define gas-phase interactions between the volatiles evolved from the coal particles and the oxygen in the combustion air, whilst the particle surface reactions define the solid-phase char combustion reactions on the particle surface.

The volumetric reactions used in simulations 5 and 6 are shown in table 7.13 and the particle surface reactions used in simulation six are shown in table 7.14.

Table 7.13: Volumetric reactions for simulations 5 and 6

	Reaction	Pre Exponential Factor [77]	Activation Energy [77] / J	A [77]	B [77]
1	vol-c+$aO_2 \rightarrow bCO+cH_2O+dN_2$	2.119E+11	0	4	0.5
2	vol-ss+$eO_2 \rightarrow fCO+gH_2O+hN_2$	2.119E+11	1.00E+08	4	0.5
5	$2CO+O_2 \rightarrow 2CO_2$	2.78E+15	1.84E+08	0.6	1.00E+12
6	$CO+H_2O \rightarrow CO_2+H_2$	2.75E+09	1.00E+08	0.6	1.00E+12
7	$2H_2+O_2 \rightarrow 2H_2O$	6.80E+15	1.70E+08	4	0.2

Where vol-c is FLUENT's coal volatile species for medium volatile coals, used here for the coal volatiles and vol-ss is FLUENT's coal volatile species for high volatile coal, used here for the sewage sludge volatiles. The composition of these species is set using the stoichiometric coefficients *a* to *h* (Ref: Appendix F). The pre-exponential factors and activation energies for these reactions as well as the values of A and B have been taken from work carried out by Kurniawan [77].

Table 7.14: Particle surface reactions for simulation 6

Reaction	Pre Exponential Factor [77]	Activation Energy [77] / J
2C<s>-c+$O_2 \rightarrow$ 2CO	0.00761	9.432E+07
2C<s>-ss+$O_2 \rightarrow$ 2CO	0.494	5.516E+07

Where C<s>-c and C<s>-ss are FLUENT's solid char species used here for coal and sewage sludge char respectively.

7.7.5.3 Results of Simulations 5 and 6

A summary of the results from simulations 5 and 6 is shown in table 7.15 and figure 7.11. Contour plots for temperature, species, burnout, devolatilisation and reaction rates can be found in Appendix F.

Table 7.15: Comparison of measured and predicted results for combustion trial 3 (simulations 5 and 6).

Simulation 5 & 6	Transfer Duct		
	Combustion Trial 3	Simulation 5	Simulation 6
Temperature / °C	769	1722	1722
O_2 / $\%_{mol}$	5.23	5.48	6.15
CO / ppm	225	0 - 1210	0 – 551
CO_2 / $\%_{mol}$	12.75	9.58	9.08
H_2O / $\%_{mol}$	n/a	13.15	12.25

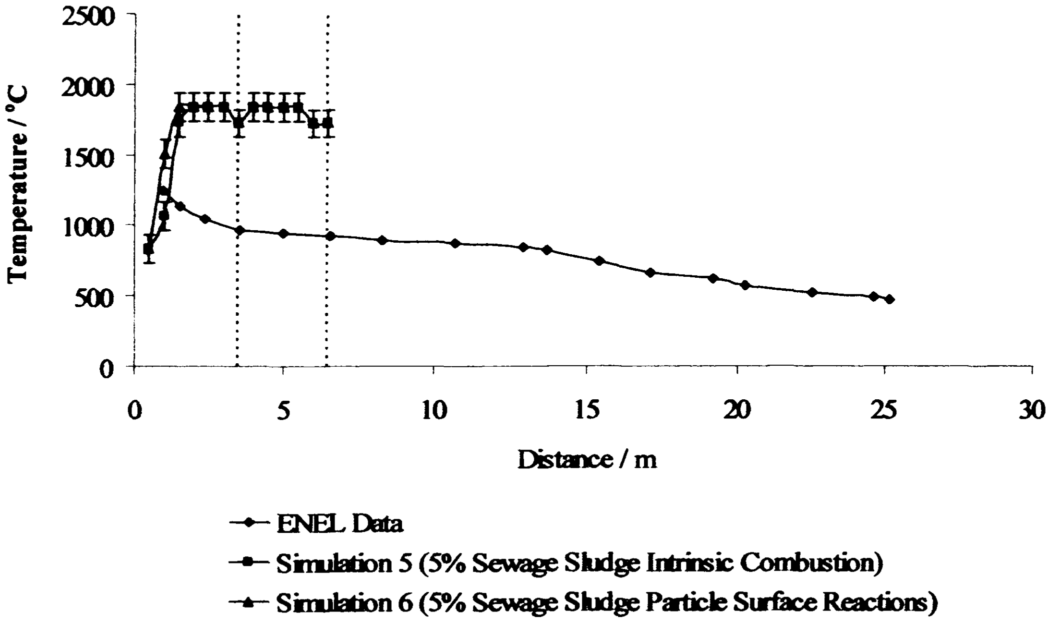

Figure 7.11: Measured and predicted temperature profiles for the ENEL 500kW$_{th}$ furnace (simulations 5 and 6).

Chapter 8 - Discussion

8.1 Introduction

This chapter features a detailed discussion of all of the work carried out within this research project. Initial discussions will focus on the computational fluid dynamics (CFD) work (Ref: Chapter 7). This is so that conclusions can be drawn prior to assessing the value of the CFD task when applied to the development of the prediction spreadsheet outlined in Chapter 6. The discussion will include a focus on the results achieved and how they compare with each other, the experimental data (ENEL combustion trials [98]) and combustion theory outlined in Chapter 4. Discussions will also focus on the problems encountered and their causes. Conclusions will be drawn on the merits of CFD simulation as a tool for the boiler operator.

The second part of the discussion will focus on the development of the Microsoft Excel-based prediction tool presented in Chapter 6. These discussions will include a focus on each of the models employed within the spreadsheet, their suitability and shortcomings as well as the reasons for their selection. Comparisons will be made between results obtained for different boilers for a range of fuels and how they compare with the theory (Ref: Chapter 2, Chapter 3 and Chapter 4). Comparisons will also be made between predictions made by the predictor and results from industry. This will include comparison between the predictor results for the 235MW$_e$ Langerlo plant run by Laborelec, the 500MW$_e$ Cottham plant run by EDF and experimental data from the 2-stage twin cyclone combustor developed at Cardiff University. Finally, results data taken from a review of related literature will be used to assess the accuracy of predictions.

An assessment of the predictor as a whole will be made, outlining its benefits, shortcomings and overall usefulness to the boiler operator. Areas for improvement and future work will also be identified.

8.2 Modelling of the ENEL 500kW$_{th}$ Furnace Using CFD

Six simulations have been presented in Chapter 7, however, these represent only a fraction of the total number of simulations carried out. Each of these six has been selected as the last in a series of refinements before a major change in the modelling process. Simulations 1 and 2 were the last in a series of initial simulations which closely followed the FLUENT non-premixed combustion tutorial. Simulations 3 and 4 were the last in a series of simulations using version 2 of the computational grid. Finally, simulations 5 and 6 were the last in a series of simulations resulting from a change from the non-premixed combustion model to the species transport model.

8.2.1 Simulations 1 and 2

Combustion trials 1 and 5, a pure coal, low excess air trial and a 10%$_{th}$ substitution of sewage sludge with low excess air, were modelled in simulations 1 and 2 respectively.

8.2.1.1 The Computational Grid

Simulations 1 and 2 were conducted using version 1 of the computational grid, which contained a mix of hexahedral, tetrahedral, wedge and pyramid cells. The hexahedral cells were used to mesh the bulk of the furnace where the geometry was relatively simple. The tetrahedral cells were used to mesh the complex parts of the furnace such as the burner, the deposition probe and the convergence. The wedge and pyramid cells were used, where necessary, to provide a transition between the tetrahedral and hexahedral cell topology. The more complex parts of the furnace geometry were characterised by small cells (typically 5mm), however, the combustion chamber was characterised by cells of typically 50mm. If the transition from small to large cells occurs over a short distance, errors can be introduced into the solution. Unfortunately the meshing scheme used in the generation of version 1 of the computational grid did not permit manual manipulation of the length of the transition zone and, as such, this transition was relatively short. It is recommended that changing from one cell topology to another within the domain is avoided as it is thought to introduce errors into the solution.

Despite efforts to the contrary, the mesh at the burner inlets was relatively coarse. Typically three or four cells spanned the inlet duct for primary, secondary and tertiary air. It is recommended that at least seven cells are used in order to provide an accurate representation of the flow field. This suggests that the mesh in these areas is too coarse

A measure of the mesh quality is the equi-angle skew, it is recommended that this is kept below 0.9. This was achieved, however, given the nature of the geometry, a significant number of cells had a skew greater than 0.5. High values of skew indicate a poor mesh and will reduce the accuracy of the predictions made as well as increasing the time to convergence.

8.2.1.2 The Results of Simulations 1 and 2

The results provided by ENEL were not comprehensive, so it is difficult to make a full comparison between the results of the combustion trials and the simulations. This is particularly true in the case of the temperature profile where a single temperature for the combustion chamber and a single temperature for the transfer duct have been provided for each trial. It is assumed that these are taken at the furnace exit and at the transfer duct exit respectively. Whilst figure 7.9 (page 208) shows a temperature profile for the ENEL 500kW$_{th}$ furnace, it is a 'typical' temperature profile and is only for reference. The same profile is used in figures 7.10 (page 212) and 7.11 (page 215) for simulations 3 to 6.

8.2.1.2a Temperature Profile

In both simulations 1 and 2, the CFD models over predict the temperatures measured during the combustion trials. In simulation 1, the predicted combustion chamber temperature is some 454°C higher than that measured during combustion trial 1, whilst the transfer duct temperature exceeds the measured value by some 509°C. In simulation 2, the predicted combustion chamber temperature is 101°C higher and that in the transfer duct 177°C higher than the measured value (Ref: table 7.8 (page 207) and table 7.9 (page 208)). Whilst at first, these over predictions seem alarming, it is understood that these initial models were very simple and that no effort was made to simulate the heat removed by the cooling lances in the main combustion chamber of the furnace. Even by assuming that the heat is removed uniformly over the combustion chamber walls, it is evident that the global heat flux of -200 W/m^2, applied in the simulations, is some two orders of magnitude lower than the estimated heat flux of approximately -23000 W/m^2 needed to simulate the cooling lances. As a result of this, the heat energy within the combustion gases is considerably higher in the simulations than that in the gases in the combustion trials. It is thought that this retention of heat energy could account for the disparity between predicted and measured temperatures.

During simulations 1 and 2, full convergence of the solution was not obtained for the energy and P1 radiation models. These differ from the other models in that they have a 10^{-6} convergence criterion compared to 10^{-3} for the other models. This means that the residuals for those models must reduce to one millionth of their original value instead of one thousandth. During the simulations the convergence criteria for the energy and P1 radiation models were changed to 10^{-4} so that convergence could be achieved. This means that the calculation did not reach the level of convergence recommended by FLUENT. This provides another possible explanation for the differences between predicted and measured results. This seems particularly relevant as these models are used to predict the heat transfer within the simulation.

8.2.1.2b Flue Gas Analysis

During the combustion trials, flue gas sampling was not conducted within the combustion chamber. Table 7.8 (page 207) and 7.9 (page 208) shows the predicted composition of the flue gases in the combustion chamber merely for reference. Concentrations of CO_2, CO, O_2 and NO_x however, were measured in the transfer duct; these have all been predicted in the simulations with the exception of NO_x. Tables 7.8 and 7.9 show that the predicted CO_2 concentration is higher than the measured value for both simulations, likewise O_2 concentrations are lower for both models. This can be explained by the higher temperatures in both the combustion chamber and the transfer duct for the simulations. Higher temperatures promote more vigorous combustion, as activation energy is reached more quickly, and hence, higher burnout is achieved meaning that less of the fuel carbon remains unburnt and, as a result, more CO_2 is produced, consuming more oxygen. It is evident that, as in the temperature profile, the disparity is less marked for simulation 2, and therefore, highlights the correlation between the temperature and the flue gas composition.

CO predictions are greatly over predicted in both simulations, this is due to the way FLUENT presents data as contour plots. Peak CO concentrations will be seen in the combustion chamber, as demonstrated by figures F1.2 and F1.10 in Appendix F, where the concentration can be several orders of magnitude higher than those in the transfer duct as oxidation of CO to CO_2 has not been completed. Relative to these concentrations, those in the transfer duct are almost zero, and the scale used by FLUENT to display the contours of CO concentration is not sensitive enough to display them. Therefore, the ability to differentiate between variations in concentration in the transfer duct is compromised and, as such, concentrations of 0 – 3100 ppm and 0 – 1900 ppm have been given for simulations 1 and 2 respectively. However, it is possible that the true value could be much closer to the 193 and 144 measured during the combustion trials.

8.2.1.3 Comparison of Simulations 1 and 2

Given the lack of similarity between the measured and predicted results, comparing the predicted results to one another to see if they are in line with the theory is perhaps a more valuable exercise.

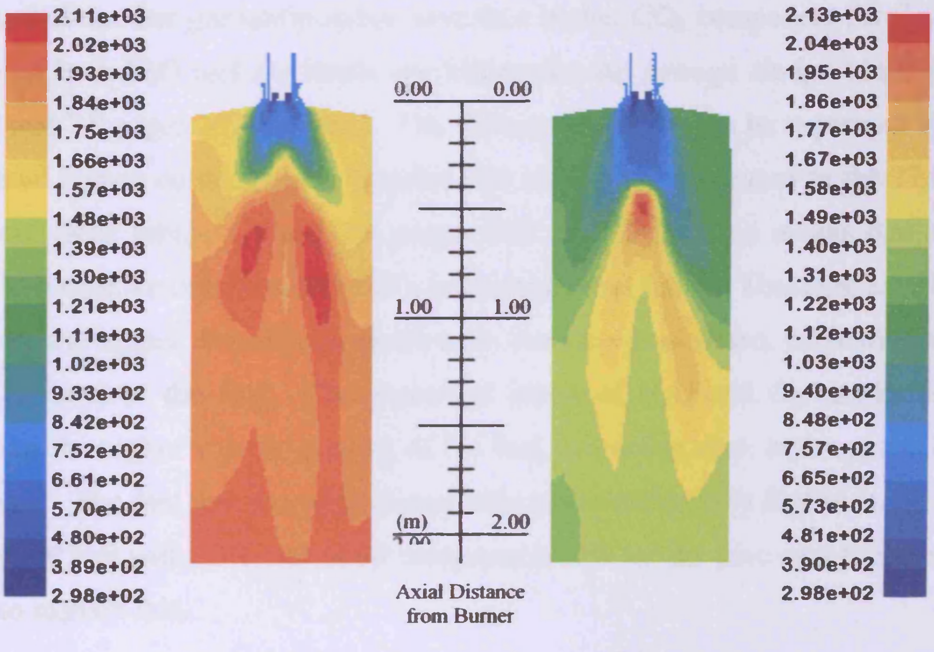

(a) **(b)**

Figure 8.1: Flame geometry for pure coal (a) and 90%$_{th}$ coal 10%$_{th}$ sewage sludge (b) (simulations 1 and 2)

Figure 8.1 shows how the flame geometries of simulation 1 and 2 compare. In both flames it is possible to see a delay before ignition; measured axially from the burner this equates to a distance of approximately 0.6m for pure coal and 0.8m for the sewage sludge blend. Despite this, the peak temperature occurs slightly earlier for the blended fuel. This can be explained by the higher volatile content of the sewage sludge blend at 41.7% compared to 39.0% for pure coal (Ref: tables 7.1 and 7.4 pages 185 and 186). The peak temperature is caused by the combustion of the volatile matter in the blended flame. The coal flame exhibits a peak temperature later in the combustion event; this is as a result of char combustion, which has a less energetic combustion regime.

Both flames have a similar shape, with a cooler central core and a hotter region surrounding it. This is probably dictated by the mixing of the fuel between the primary and secondary air streams. Both this phenomenon and the ignition delay can be explained by the simplified geometry of the burner, where the lack of a diffuser and simulation of swirl fail to provide adequate mixing of the fuel with the combustion air.

Comparison of the flue gas composition reveals a higher CO_2 component for the coal flame whilst both H_2O and O_2 levels are higher for the sewage sludge blend (Ref: tables 7.8 and 7.9 pages 207 and 208). The difference in CO_2 can be explained by the lower overall carbon content in the blended fuel at $73.3\%_{wt}$ compared to the $77.8\%_{wt}$ in pure coal (Ref: tables 7.1 and 7.4 pages 185 and 186). This means that more carbon is available for combustion to CO_2 in the pure coal flame. This may have been escalated by the higher overall temperatures in the pure coal flame, promoting more complete burnout of the fuel. The increased levels of H_2O and O_2 can be partly explained by the higher volatile content of the fuel, providing more hydrogen to form water vapour. The fact that the equivalence ratio was considerably higher in the case of the blended fuel with 23% excess air compared to 5% for the pure coal flame could also help to explain this.

8.2.1.4 Conclusion of Simulations 1 and 2

In conclusion, it was clear from these results that a more realistic attempt at modelling the combustion trials was necessary. The burner model needed to be improved to promote better mixing of the fuel and combustion air and the heat removed by the cooling lances should have been be modelled more accurately. However, the combustion model appeared to predict differences between the two flames in line with what was expected from the theory.

8.2.2 Simulations 3 and 4

The pure coal, low excess air trial is modelled again in simulation 3. Simulation 4 aims to predict the results of combustion trial 3, a 95%$_{th}$ coal – 5%$_{th}$ sewage sludge blend, fired with an equivalence ratio of 1.26.

8.2.2.1 The Computational Grid

The computational grid was modified for simulations 3 and 4 in an attempt to alleviate some of the problems witnessed in simulations 1 and 2. Firstly, the model of the burner was improved to give better cell density at the air inlets with the aim of promoting a more accurate velocity profile in this area. It was hoped that this, combined with the inclusion of a diffuser in the mouth of the primary air inlet, would promote better mixing of the fuel with the secondary and tertiary air streams. As well as deflecting the particles into the supplementary air streams, the diffuser should slow the particles down as they enter the combustion chamber. By providing better mixing, it was hoped that the fuel particles would reach their vaporisation temperature more quickly providing faster ignition and eliminating the ignition delay that was witnessed in simulations 1 and 2.

In order to achieve the very fine mesh needed to model the diffuser, a tetrahedral cell topology was selected for the entire combustion domain. The hexahedral mapping schemes used by gambit prohibit modelling areas of such complex geometry as they would have forced the projection of the cell pattern along the entire length of the combustion zone. In doing this, not only does the number of cells become prohibitively high, but it provides a region along the centreline of the combustion zone where a rapid transition from cells of nominal length 5mm to those with a nominal length of 50mm is seen. It was thought that this could induce errors into the solution. The combustion zone was divided into a number of regions during its construction, not only to enable better mesh control throughout the domain, but also to allow a more accurate representation of the cooling lances and the heat removed by them. In addition to this, a second deposition probe was added in the lower region of the combustion chamber at the request of the PowerFlam sponsors.

8.2.2.2 Changes to the Model Settings

The setup of simulations 3 and 4 remained largely unchanged from that of simulations 1 and 2. The major difference between these and the previous models was the heat flux applied to the boiler walls to simulate the cooling lances, instead of a global heat flux of -200W/mK applied uniformly to the boiler walls, the heat removed by each of the cooling lances was considered. This meant that heat fluxes of -21700W/mK were applied to the walls in the combustion chamber, which was deemed sufficient to simulate the heat removed by the cooling lances.

In another departure from simulations 1 and 2, a stepped approach to solution was taken. It was believed that simply 'turning on' all of the models from the start in simulations 1 and 2 may have caused some of the problems experienced. Without a converged solution for the velocity field, initial particle trajectories may not have been accurately predicted, this means that as they release heat energy into the continuous phase, they are doing so in the wrong place. Convection and pressure differentials caused by this heat release will affect the way in which the velocity field develops, meaning that the correct flow regime may never be achieved. To this end, the energy, radiation and discrete phase models were turned off and the solution for the non-combusting flow was achieved. Then, when the discrete phase model is switched on, the particles should be travelling in the right directions and releasing heat energy where they should be.

8.2.2.3 The Results of Simulations 3 and 4

As in simulations 1 and 2, convergence problems were experienced. These can be seen in the temperature profile as areas of extreme temperature gradient in the ash pot (Ref: figures F1.17 and F1.25 in Appendix F). This is caused as larger coal particles become entrapped in the ash pot as they escape the streamline into the transfer duct. The particle tracking model will only predict the trajectory of these particles for a defined number of time steps before it aborts the tracking of that particular particle to prevent an infinite DPM iteration. On doing this, all of the energy remaining in the particle is instantly released. This causes instabilities in the continuous phase, which produces the large temperature fluctuations seen.

8.2.2.3a Temperature Profile

When comparing the predicted results with those from the combustion trials, it can be seen that the problems encountered in simulations 1 and 2 have not been solved. Figure 8.2 shows how the ignition delay was still present in simulations 3 and 4.

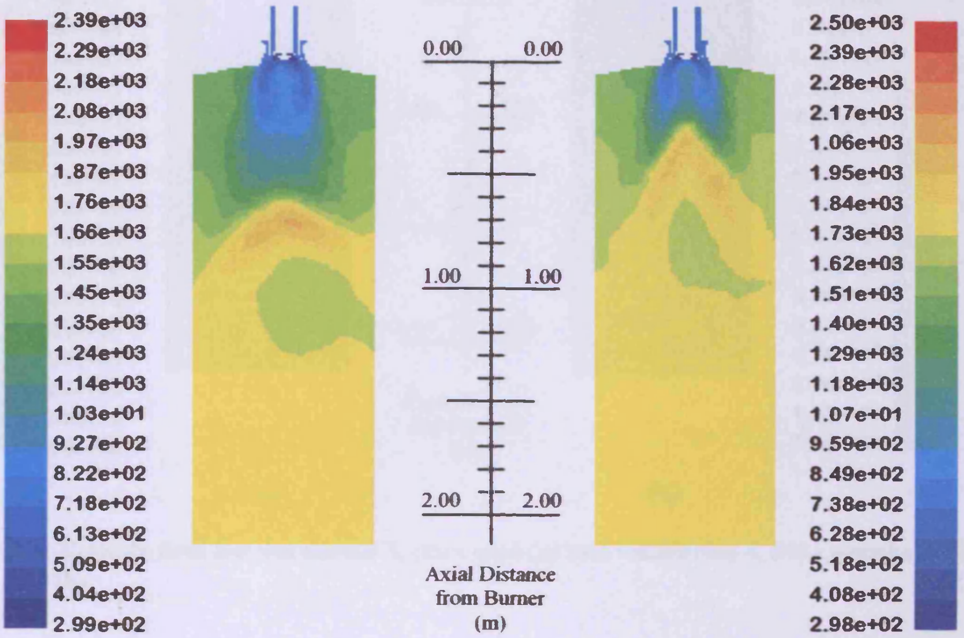

(a) (b)

Figure 8.2: Flame geometry for pure coal (a) and 95%$_{th}$ coal 5%$_{th}$ sewage sludge (b) (simulations 3 and 4)

The figure shows that for pure coal, ignition occurs some 1.2m from the burner, whereas for the 5% sewage sludge blend it is approximately 0.6m. This appears to be a reversal of the situation in simulations 1 and 2, where the pure coal flame saw the smaller delay. Figure 8.3 shows that the difference in ignition times cannot be attributed to the velocity profile as these are very similar for both cases, with a nominal velocity of 6 to 7m/s in the main mixing zone. This velocity profile shows an inner recirculation zone immediately in front of the burner approximately 0.4m in length, for both simulations, this is followed by a larger zone of higher velocity approximately 1m in length. This suggests that the ignition delay is more likely to be caused by the way the devolatilisation or fuel combustion is modelled. The use of the default arrhenius constants for the Kobayashi devolatilisation model for two inherently different fuels (coal and sewage sludge) could be one explanation for this.

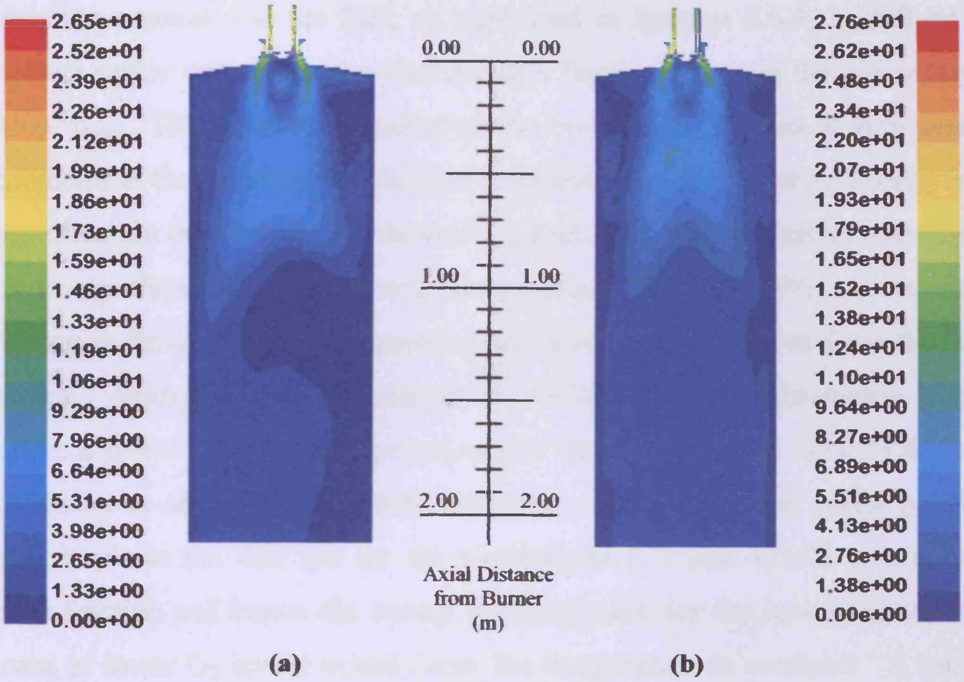

Figure 8.3: Velocity field for simulation 3, pure coal (a) and simulation 4, 5%$_{th}$ sewage sludge 95%$_{th}$ coal (b)

In addition to the ignition delay, as in the first simulations, the furnace temperatures are over predicted (Ref: tables 7.10 and 7.11 page 211). In simulation 3, the combustion chamber temperature is over predicted by some 314°C at 1437°C whilst the temperature in the transfer duct was over predicted by 649°C at 1437°C. In simulation 4, the combustion chamber temperature was 422°C higher than the measured temperature at 1512°C and the transfer duct temperature was 523°C higher at 1292°C. From these results it can be seen that in simulation 3 the flue gas temperature remained constant throughout the combustion chamber and transfer duct. This suggests that no heat energy is being removed from the combustion gases, however, alpha-numerical checking of the heat removed at the walls and at the outlet reveal that heat energy is in fact being removed through the walls in the correct quantities. This would suggest that an error is being introduced in the relationship between the heat energy (enthalpy) of the flue gases and their temperature.

This relationship is defined by look-up tables which are generated by the pre-PDF pre-processor and then accessed by the non-premixed combustion model within FLUENT. The working point in these look-up tables, and hence, the entire combustion reaction for the fuel, as explained in Section 6.6.1, is defined by two conserved scalar quantities: the fuel mixture fraction, f_{fuel} and the secondary partial fraction, p_{sec}. This simplified model of the combustion system is very sensitive to inaccuracies in the definition of the fuel and oxidser streams as they directly affect the mixture fraction of the fuel. As shown in figure B1.1, stoichiometric combustion will produce significantly higher flame temperatures than at 21% excess air. This difference in flame temperature grows as the heat energy removed from the flue gases increases. With an enthalpy change of -2500 kJ/kg, stoichiometric combustion produces a flame temperature approximately 400K hotter than with 21% excess air, this reduces to around 250K under adiabatic conditions. The under prediction of oxygen levels in the flue gas for the simulations 1, 2 and 4, will give an incorrect mixture fraction and hence the wrong working point for the lookup tables which, in the case of lower O_2 levels would cause the temperature to increase. A move away from the non-premixed combustion model in simulations 5 and 6 hopes to eliminate the potential for these errors.

8.2.2.3b Flue Gas Analysis

Comparing the flue gas composition of simulations 3 and 4 to those from the combustion trials shows an improvement in the prediction of CO_2 and O_2 for the pure coal flame (Ref: tables 7.10 and 7.11 page 211). CO_2 is down from $16.4\%_{mol}$ to $13.6\%_{mol}$ and O_2 up to $4.73\%_{mol}$ in simulation 3 from $1.59\%_{mol}$ in simulation 1. Prediction of the flue gas composition for the $5\%_{th}$ sewage sludge blend is similar to that of the $10\%_{th}$ blend in simulation 2. The O_2 levels are similar at $2.89\%_{mol}$ for simulation 2 and $2.96\%_{mol}$ for simulation 4. Both these values are consistently below the measured values of $5.90\%_{mol}$ and $5.23\%_{mol}$ for simulations 2 and 4 respectively. CO_2 prediction has worsened slightly in simulation 4, with an over prediction of $1.9\%_{mol}$ at $14.65\%_{mol}$ compared to only $0.55\%_{mol}$ in simulation 2 (Ref: tables 7.11 and 7.9 pages 211 and 208). The reason for this error is now unclear as it was initially thought that the errors in simulations 1 and 2 were introduced by the lack of heat removal at the furnace walls. Simulations 3 and 4 show similar errors in both temperature profile and flue gas composition despite having the correct heat removal rates at the furnace walls. It is possible that these errors stem from two sources; the computational grid and the combustion model.

Errors could be introduced by the computational grid due to the use of a tetrahedral cell structure in the complex regions of the boiler. As has previously been mentioned, tetrahedral cells have a lower tolerance for highly skewed cells, which will introduce calculation errors and increase convergence time. Using these cells in areas of high complexity will inherently increase the likelihood of them being highly skewed and, therefore, the likelihood of the associated errors being introduced. The use of these cells to model the burner region is of particular importance as the effect of these errors may be exaggerated in this highly turbulent region of flow.

The other possible source of error is the non-premixed combustion model, here, simplifying the combustion chemistry to two conserved scalars based upon the fuel mixture fraction may have caused errors in the prediction of species formed. This can have an effect on the mixture fraction of the fuel, which is used to find the working point in the pre-calculated look-up tables used to predict the flue gas temperature. If the calculated mixture fraction is too high, which is what is suggested by the under prediction of oxygen in the flue gas, then the flue gas temperature can be over predicted by as much as 400K.

8.2.2.3c Particle Impaction Rates

Particle impaction rates were measured during simulations 3 and 4, however, it is difficult to compare these to the deposition rate measured during the combustion trials as the sticking probability has not been assessed. In the simulations, it is assumed that every particle impacting the deposition probes is retained. In reality, this is not so, as explained in Chapter 2, many particles rebound on impact. Whether a particle sticks or not is dependant on several factors such as whether the particle is solid, sticky or molten, as well as its velocity, size and impact angle. It is also possible for impacting particles to dislodge existing deposits. These deposits can also grow sufficiently large that they fall of under their own weight (shedding). The predicted impaction rates from the simulations do not account for any of these factors.

8.2.2.4 Comparison of Simulations 1 to 4

Comparing these results to those from the combustion trials is not valid due to the reasons outlined above. One would expect the predicted impaction rates to be higher than the measured deposition rates as it is a measure of the number or impacting particles rather than sticking particles. However, the deposition rates measured are in the range 7 to 20 g/m^2/h (Ref: tables 7.10 and 7.11 page 211). This is 1 to 2 orders of magnitude higher than those predicted on both probes in simulation 3 and in the combustion chamber of simulation 4, which were in the range 0.047 to 0.695 g/m^2/h. The predicted impaction rate for the transfer duct in simulation 4 of 5.25 g/m^2/h is in the same order of magnitude as the measured results, however, it is still less than the lowest measured value. This is probably due to the way in which the deposition probes have been modelled. As in the modelling of the air inlets, a fine mesh is required in the vicinity of the probes to allow the accurate prediction of the velocity field in this area and hence, the accurate prediction of the particle paths dictated by this. It was expected that only the larger particles would hit the deposition probes as only they would have sufficient momentum to break the streamlines around the probe. Tables F1.1 to F1.6 show that the size played no part in dictating which particles impacted the probe during the simulations. This too suggests that the streamlines around the deposition probes were not fully developed.

8.2.3 Simulations 5 and 6

Owing to the problems encountered when using the non pre-mixed combustion model, simulations 5 and 6 see the adoption of the species transport model. This allows the simulation of two discrete phases and, therefore, individual coal and sewage sludge streams. In doing this, the effects of co-combustion of sewage sludge on the pulverised coal flame can be studied irrespective of the problems encountered in achieving the correct temperature distribution. Also to assess whether the combustion model is the cause of the problems seen, two different combustion models have been adopted; the intrinsic combustion model in simulation 5 and the multiple particle surface reactions model in simulation 6.

8.2.3.1 The Computational grid

As one of the reasons identified for the lack of agreement between predicted and measured results in simulations 1 to 4, the computational grid was developed further for simulations 5 and 6. The use of tetrahedral cells was thought to be the cause of some of the problems witnessed. Therefore, an entirely hexahedral cell structure has been used. To facilitate this, the burner geometry has been simplified and the deposition probe has been removed from the combustion chamber.

8.2.3.2 Changes to the Model Settings

The majority of the model settings have remained the same as for previous simulations, with the major change to the species model with the adoption of the species transport model. Initial models were created using a single equivalent blended fuel such as those used in simulations 2 and 4. However, one of the main advantages of the species transport model is that it allows the definition of multiple fuel streams. In simulations 5 and 6, the coal and sewage sludge streams have been modelled separately. This makes the model setup more complex as it requires the definition of different char and volatile species along with separate injections for each fuel (as seen in Appendix F)

8.2.3.3 Results of Simulations 5 and 6

When using the species transport approach, flame geometry differs greatly from those in previous simulations. Using the non-premixed combustion model, peak flame temperatures were in the region of 2000 to 2100K which corresponded to the adiabatic enthalpy slice within the look-up tables. Figures 8.1 (page 220) and 8.2 (page 224) show that the areas of peak temperature occur at the flame core where the volatiles are burning off following devolatilisation. In simulations 5 and 6, the area of peak temperature (circa 1900 to 2100K) extends throughout large areas of the furnace and into the transfer duct. This has resulted in an even greater over prediction of the furnace temperature profile than in the previous simulations, with transfer duct temperatures over predicted by almost 1000K (Ref: figures F1.32 and F1.47 and table 7.15 page 215). As in simulations 3 and 4, the heat removed by the cooling lances has been fully modelled so, as in those simulations, the error must have been introduced through the combustion model.

Critical to the correct functioning of the species transport model is the calculation of the reaction rates. These are in arrhenius form, where the activation energy determines how quickly the reaction starts, whilst the pre-exponential factor determines the speed of the reaction. These coefficients have been taken from work by Kurniawan [78] who successfully modelled coal combustion in a cement kiln. This, combined with figures F1.34 to F1.40 and figures F1.49 to F1.55 would suggest that the reaction rates are close to reality as the reactions all occur within the combustion zone. The problem seems to be that the heat energy within the furnace does not correlate with the reactions through which it is being released, or the areas where it is being removed. This would suggest errors in the heat transfer model (energy equation) and the radiation model. This leads again to the altered convergence criteria for these models and highlights the fact that these models must be fully converged before the correct temperature profile can be seen.

8.2.3.3a Temperature Profile

Figure 8.4 shows a significant ignition delay for both simulations 5 and 6. This is more marked than in previous combustion models. It is unlikely that this has been caused by the arrhenius rates in the devolatilisation model as they were taken from [101] and were measured experimentally for the two fuels in question. It is more likely that this was caused by the simplification of the burner. The diffuser, which was used to slow the particles upon entry to the boiler, whilst also promoting mixing with the secondary and tertiary air streams, has been removed as part of this process.

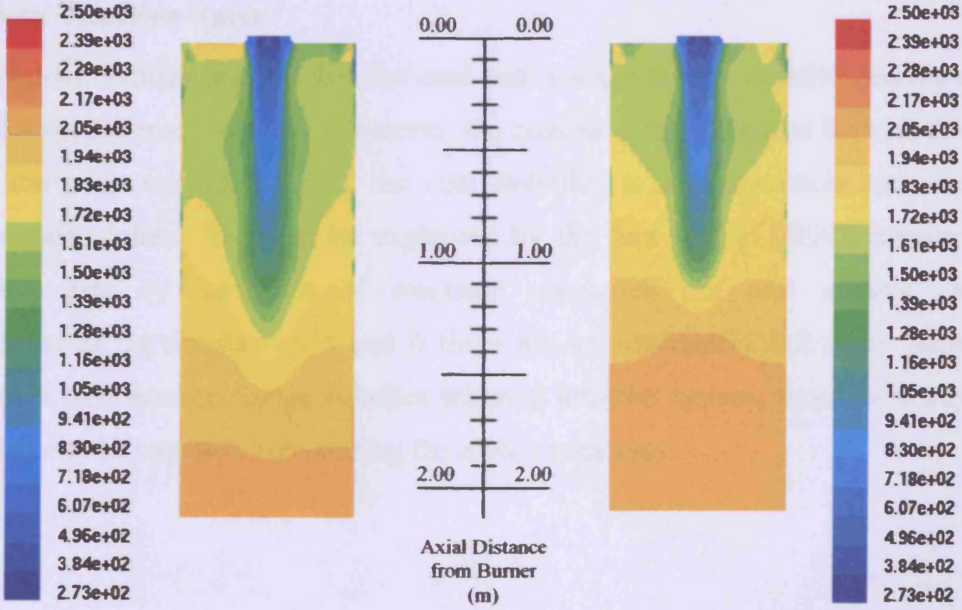

(a) (b)

Figure 8.4: Ignition delay in simulations 5 and 6

Figures F1.33 and F1.48 show a much higher peak velocity at 33m/s which extends further into the furnace than in previous simulations. This means that fuel particles will be travelling faster for longer and therefore, will have covered a much greater distance before the activation energy for the devolatilisation model is reached, resulting in a more significant ignition delay.

8.2.3.4 Comparison of Simulations 5 and 6

Again, given the poor prediction of the temperature profile, comparison of these results to the measured values is of limited value. By comparing the prediction results to one another, it is possible to tell if the combustion chemistry is behaving as it should. Figures 8.5 and 8.6 show the reaction rates for reactions 1, 2, 5, 6 and 7 for simulations 5 and 6. The figures show that reaction 2 is the first to reach peak reaction rate in both simulations, this is the combustion of the volatiles released from the sewage sludge. This is as expected and is caused by the lower activation energy for sewage sludge devolatilisation in the fast rate of the Kobayashi two competing rates devolatilisation model. The remaining reactions reach their peak around the same point, this is because the release of volatiles from the coal particles is beginning, whilst the further combustion of the volatile species released from the sewage sludge particles is beginning in reactions 5, 6 and 7.

8.2.3.4a Reaction Rates

The model settings suggest that the coal and sewage sludge volatile species should exhibit similar reaction rates. However, the contour plots in figures 8.5 and 8.6 show that the peak reaction rate of the coal volatiles is approximately one order of magnitude higher. This can be explained by the fact that FLUENT measures the reaction rate by the mass of reactants consumed per unit volume seconds (kgmol/m^{3}s); in simulations 5 and 6 there are approximately 6.2 times more coal volatiles than sewage sludge volatiles released into the system, thus, there are more available to be consumed, producing the higher peak rate.

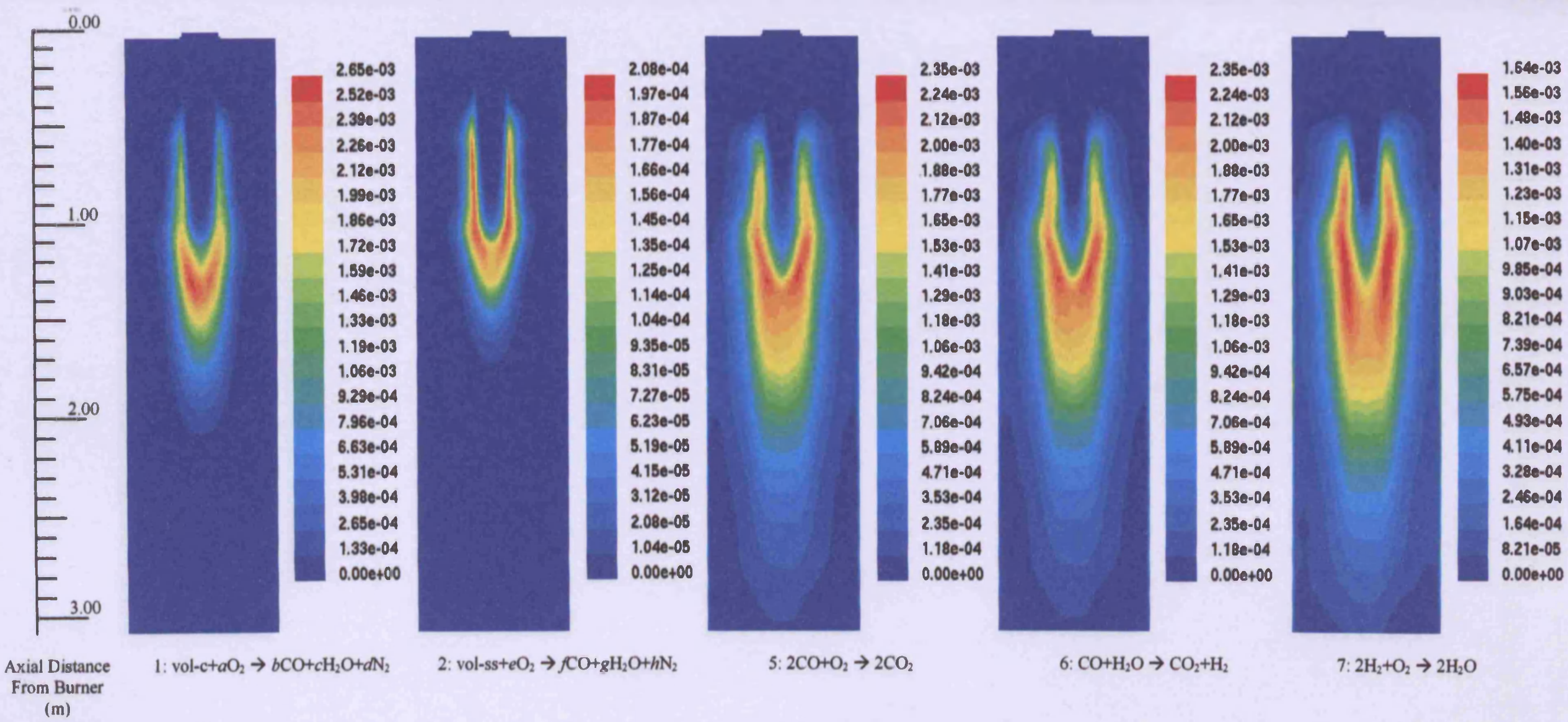

1: vol-c+aO$_2$ → bCO+cH$_2$O+dN$_2$

2: vol-ss+eO$_2$ → fCO+gH$_2$O+hN$_2$

5: 2CO+O$_2$ → 2CO$_2$

6: CO+H$_2$O → CO$_2$+H$_2$

7: 2H$_2$+O$_2$ → 2H$_2$O

Figure 8.5: Contours of reaction rate for reactions 1, 2, 5, 6 and 7 in simulation 5

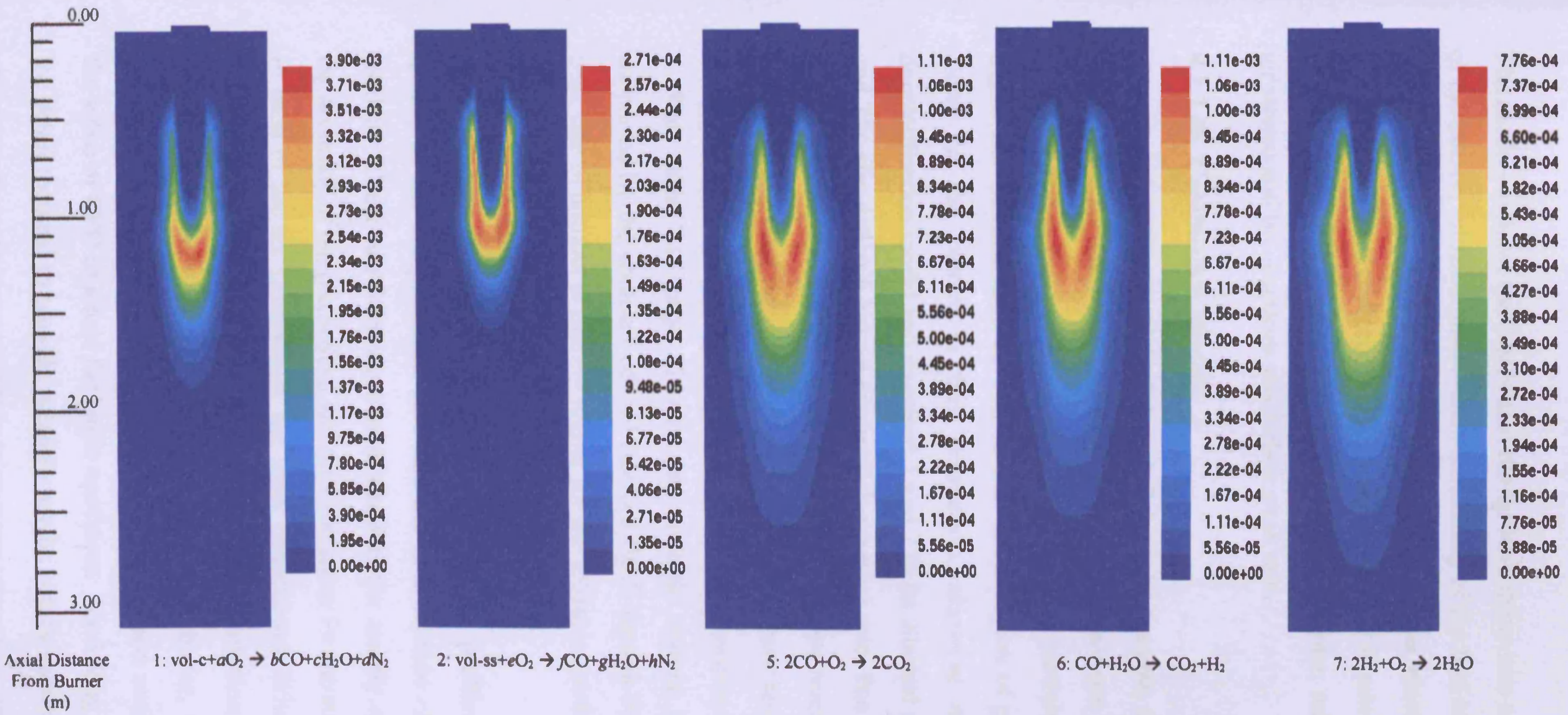

1: vol-c+$aO_2 \rightarrow bCO+cH_2O+dN_2$

2: vol-ss+$eO_2 \rightarrow fCO+gH_2O+hN_2$

5: $2CO+O_2 \rightarrow 2CO_2$

6: $CO+H_2O \rightarrow CO_2+H_2$

7: $2H_2+O_2 \rightarrow 2H_2O$

Figure 8.6: Contours of reaction rate for reactions 1, 2, 5, 6 and 7 in simulation 6

The models support the theory that the ignition delay was caused by the simplification of the burner, which compromised the mixing of the fuel and air streams. Each of the plots above demonstrates a central core where no reaction takes place. On the periphery of this, the reaction begins where the fuel is mixing with the secondary and tertiary air streams, finally, around 1m from the burner, mixing begins in the primary air stream and the reactions reach their peak rate.

8.2.3.4b Combustion Models

By comparing figures 8.4, 8.5 and 8.6, it is possible to identify the differences between the intrinsic and the multiple surface reactions combustion models. The devolatilisation of both the coal and sewage sludge particles occurred sooner and at a higher rate in simulation 6. This is due to the region of peak temperature beginning closer to the burner in this simulation, allowing activation energy for the devolatilisation model and reactions 1 and 2 to be attained more easily. Reactions 5, 6 and 7 in simulation 6 have a lower peak reaction rate, this is because, as well as their activation energies and pre-exponential factors, these reactions depend upon the rate of CO release from the char combustion model. These results would suggest that CO is produced more rapidly by the intrinsic char combustion model than reactions 3 and 4 (Ref: table 7.14 page 214) in the multiple surface reactions model. This is supported by the contours of fuel burnout (Ref: figures F1.35 and F1.30), where the peak rate of burnout is slightly higher for the intrinsic combustion model.

8.2.4 Conclusions

In all six simulations documented in this study, problems were attributed to the quality of the computational grid and the convergence of the energy and radiation models. These two factors are interlinked as the quality of the mesh directly affects the accuracy of the predictions and the time taken for the solution to converge if at all. In each of the six simulations, the strict convergence criterion of 10^{-6} for these two models was not met. This in turn, caused poor prediction of the temperature profile within the boiler. The modelling of a full scale boiler, where fine mesh densities would be needed around each of the burners and heat exchanger tubes detracts from the value of CFD as a tool for boiler operators. Modelling these areas of the boiler in the detail required to provide valuable results, whilst modelling the entire combustion zone would require a mesh with a vast number of cells. As the number of cells increases, so does the time taken to complete each iteration, so much so, that simulations could take days or even weeks to solve. This would make assessing the impact of fuel blending, where several simulations may be required to achieve an optimum level, a very lengthy process.

It should also be noted that in order to accurately model the fuel behaviour, several fuel parameters are required, outside the standard proximate and ultimate analysis and size distribution. These can only be derived through experimental analysis. For non-premixed combustion, these may only include devolatilisation rate constants used in the devolatilisation model. However, if the species transport model is to be used, ideal for fuel substitution simulations, then a great deal more are needed, including reaction rates controlling the assumed reaction chemistry for the two fuels, along with devolatilisation rate constants and standard state enthalpies for the volatile species. Gathering this type of data for a range of prospective substitute fuels could be a costly and time consuming task.

In addition to the above, there is the specialist knowledge and training required to use the CFD software and interpret the results produced. This study has shown that the results provided by CFD may be unreliable if one or more aspects of the simulation process is lacking in quality, and that many attempts may be needed to hone the model to the point where the results are reliable enough to derive significant meaning from them.

With the continued advancement in computer processing power, simulation times are continually falling such that with a well set up model, small combustion apparatus can be successfully modelled in hours. However, until the advancement is such that this is true for full scale boilers, then CFD remains a tool for the academic and not for the boiler operator.

8.3 The Development of a Universal Prediction Tool

One of the principal criteria for the boiler prediction tool was that it should be easy to use and transferable between workstations, requiring no specialist software. For this reason, the prediction tool has been developed in the form of a spreadsheet using Microsoft Excel. Microsoft Excel is a program owned by most PC users running the Windows operating system, and is a relatively in-expensive upgrade for those who do not. The spreadsheet has been developed using Microsoft Excel 2002, however none of the features used are unique to this version, and therefore, the spreadsheet should be fully backwards compatible. These factors should make the spreadsheet instantly accessible for most boiler operators. Using the spreadsheet is simply a data inputting task for the boiler operator, and although knowledge of combustion systems may make this task easier, no specialist training is required to use the tool.

8.3.1 Appraisal of the Models Used Within the Spreadsheet

The spreadsheet uses a series of empirical models to convert the fuel, boiler and process information entered by the boiler operator into a temperature profile and a prediction of the chemical species formed. These are in turn used to assess the likelihood of slagging, fouling and corrosion problems occurring.

8.3.1.1 Calculation of the Equivalent Fuel

The PrePDF model, which is used to define the temperature – enthalpy change relationship, can only cater for a single fuel input. Therefore, when fuel blends are used, the parent and substitute fuel streams must be combined into a single 'equivalent' fuel. This is done on the blend calculator page of the spreadsheet. This is an additive model, which uses the LCV of the parent and substitute fuels along with the thermal contribution of the substitute fuel, to define a new fuel based upon the combination of the two component fuels. This, in effect, defines a completely new fuel, where the defined chemical composition is assumed on a molecular level rather than the result of the mixing of two separate fuel streams.

The theory suggests that the behaviour of blended fuels is not additive [43]; in experiments with blends of different coals Rushdi et al [43] state "the performance of coal blends and their potential to form ash deposits cannot be predicted from the source coals" [43]. This statement arises from the finding that that the non-additive behaviour resulted from the interaction of ash particles of the different coals within the ash layer which are not seen when the coals are burned individually. However, because the spreadsheet assumes molecular mixing, the ash particles of the parent and substitute fuel streams essentially become a single ash particle of the 'equivalent fuel' and are therefore free to react with each other from the very outset of the calculation. Therefore, the physical mixing limitations seen in experimental fuel blending work of Rushdi, which cause non-additive behaviour, are negated by the assumed blending of the fuel at the molecular level within the spreadsheet. Thus the assumption of additive behaviour in the spreadsheet is justified.

8.3.1.2 The Flue Gas Analysis Model

The flue gas analysis model uses simple chemical reactions to compute a theoretical flue gas composition for use when calculating the excess air criterion and the mass of flue gas passing through the boiler. This flue gas composition is not carried over to the slagging and fouling or corrosion models. These use a flue gas composition defined by the minimisation of Gibb's free energy calculated by the FactSage thermochemical software package as part of the process of defining the empirical relationships within those models.

The model assumes a simple two-stage combustion process for carbon and sulphur, first to monoxides then, if sufficient oxygen remains, to dioxides. It assumes complete oxidation of hydrogen to form water vapour and that nitrogen in the fuel and combustion air along with the ash has no reaction with oxygen. The two-stage combustion technique has been used for carbon and sulphur to allow for the possibility of sub-stoichiometric combustion and the formation of CO and SO. The radical, HO, was considered too unstable to exist within the combustion environment and therefore, hydrogen was assumed to oxidise completely to H_2O. The prediction of NO_X has not been attempted, as this is highly dependant on temperature. The reaction of oxygen with ash has not been considered due to the complex interactions between ash species.

8.3.1.2a Comparison With FactSage Thermochemical Software

Table 8.1 shows how the results of the predictor flue gas analysis for a medium volatile bituminous coal with λ = 1.21 compare with those from the FactSage thermochemical software package.

Table 8.1: Comparison of flue gas compositions between FactSage and the flue gas analysis model within the spreadsheet

	Mass of Flue Gas Components / kg		
	FactSage		Spreadsheet
Temperature / K	2000	400	n/a
CO_2	2.448	2.465	2.465
CO	0.011	-	-
SO_3	-	-	-
SO_2	0.018	-	0.015
SO	-	-	-
N_2	7.789	8.479	8.479
NO_X	0.038	-	-
H_2O	0.501	0.501	0.506
OH	0.008	-	-
O_2	0.394	0.440	0.444
Others	0.706	-	-
Total	11.913	11.885	11.909

The table shows good agreement between the spreadsheet and the results predicted by FactSage, particularly at lower temperatures. It is important to note that the spreadsheet does not consider temperature when calculating the flue gas composition and whilst FacSage shows a slightly higher total mass of flue gas at elevated temperatures, this equates to a difference of only 0.23% which is negligible. The spreadsheet does over predict oxygen content at higher temperatures by 12.7%, however, this can be attributed to the fact that at higher temperatures, oxygen forms oxides with many of the ash species (seen as others in the table) leaving less oxygen in the flue gas. This phenomenon is not considered by the spreadsheet. The very low values of CO and OH suggest that the assumptions that hydrogen can be considered fully oxidised to H_2O and carbon fully oxidised to CO_2 for $\lambda > 1$ are justified.

Overall, considering the intended use of the flue gas composition produced by the spreadsheet (to calculate flue gas mass and to aid the user in attaining the correct equivalence ratio), this simplified model of the flue gas reactions is fit for purpose.

8.3.1.3 Thermodynamic Calculations for the Steam Cycle

This is a simple model where data from *Thermodynamic and Transport Properties of Fluids* by Rogers and Mayhew [92] have been digitised to eliminate the need for the user to carry out calculations to find the enthalpy change of the water / steam across each heat exchanger.

8.3.1.3a Comparison to the Steam Tables

Table 8.2 shows a comparison of the steam cycle calculations for the Langerlo boiler, made using the spreadsheet, to some made using the steam tables. The table shows that although the spreadsheet can predict the enthalpy values to within 1% of the steam tables, because the spreadsheet uses enthalpy change (Δh) rather than true enthalpy in the steady flow energy equation to calculate heat energy, these errors can grow by an order of magnitude to resemble those shown.

Table 8.2: Comparison of steam cycle calculations between the spreadsheet and the Steam Tables

	Steam Tables			Spreadsheet			
Heat Exchanger	Enthalpy Before / kJ/kg	Enthalpy After / kJ/kg	Heat Energy Gained / MJ	Enthalpy Before / kJ/kg	Enthalpy After / kJ/kg	Heat Energy Gained / MJ	+ / - Error / %
Water Walls	1402	2665	245.53	1402	2680	248.48	+ 1.20%
Superheater 2	2991	3088	18.88	2968	3079	21.57	+ 14.24%
Superheater 3	3088	3435	67.47	3079	3440	70.72	+ 4.82%
Reheater 2	3317	3516	38.65	3310	3518	40.56	+ 4.94%
Superheater 1	2665	2991	63.35	2680	2968	55.85	- 11.84%
Reheater 1	3102	3317	41.98	3093	3310	42.14	+ 0.38%
Economiser 2	1154	1402	48.19	1165	1402	46.28	- 3.96%
Economiser 1	1414	1154	27.34	1014	1164	29.22	+ 6.88%
Total			551.39			554.92	+ 0.64%

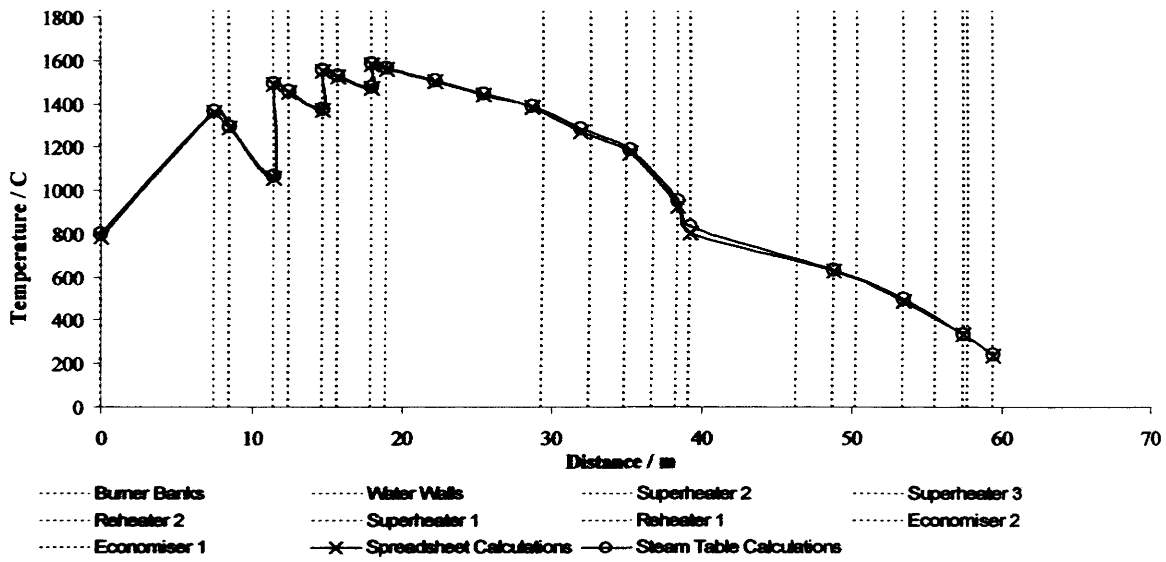

Figure 8.7: Effect of different steam cycle calculation methods on the temperature profile

Figure 8.7 shows that the effect of these errors on the temperature profile for the boiler is minimal, and therefore, the gains made in achieving a more user friendly tool outweigh the slight decrease in accuracy of the steam cycle calculation.

8.3.1.3b Sources of Error in the Steam Cycle Model

The source of the errors lies in the way the curves have been modelled; a single sixth order polynomial has been used to model the saturated liquid line and another for the saturated vapour line (Ref: equations 6.4 and 6.5 page 118). By producing curves, and hence, relationships that follow these lines more closely (Ref: figures 6.5 and 6.6 pages 116 and 117), the accuracy of the prediction could be improved. Dividing the lines into sections and producing a series of linear or quadratic relationships rather than a single high order polynomial would be a good way to achieve this. Further errors are introduced by the use of linear interpolation between the family of curves used to define superheated steam. The error could be further reduced by using a greater number of equations to define this region, this would provide closer pressure limits between which interpolation is required, thus improving accuracy. In addition non-linear interpolation could used, producing a temperature-pressure-enthalpy map similar to that used to define the melting temperature of the ternary alkali-iron system used in the corrosion model.

8.3.1.3c Heat Loss Simulation in the Steam Cycle Calculation

Once the heat energy gained by the steam has been calculated, the corresponding heat energy removed from the combustion gases is calculated. This is done by assuming a total global heat loss for the entire system. Whilst being a very simple and easy way of accounting for the losses within the system, it is not perhaps the best. This global heat loss is to account for the following losses incurred by the system:

- Heat transfer losses within the heat exchangers
- Steam side pipe losses (both pressure and heat)
- Gas side heat losses (through the boiler walls and ducting)

These losses would be better represented if they were defined separately, however, this does create additional information to be gathered by the boiler operator before using the spreadsheet. The high temperature corrosion model has shown that heat transfer losses (for clean tubes) can be modelled quite easily and the data required to do this is already required for the corrosion model to work, therefore, this would be a relatively simple model to include. However, as no attempt is made by the spreadsheet to quantify the build-up of deposits on the heat exchangers or evaluate the heat transfer coefficients of the deposits, then applying this model to a tube suffering form slagging and fouling would be very difficult.

8.3.1.4 The Temperature – Enthalpy Change Model

As has already been discussed, two methods have been used to model the relationship between the flue gas temperature and its enthalpy; an empirical modelling method and an artificial neural network (ANN) method. Both models use the same thermodynamic principles and use the same modelling assumptions and, as such, the ANN is an evolution of the empirical method; able to predict results for a wider range of fuels.

8.3.1.4a Use of the FLUENT PrePDF Non-premixed Combustion Model

Both models rely on data generated by the PrePDF pre-processor from the FLUENT CFD software package. This software essentially defines the combustion chemistry in terms of two conserved scalars; the fuel mixture fraction and the secondary partial fraction. It then uses these to produce a series of temperature plots for a number of fixed enthalpy values (slices). By calculating the value of the conserved scalars for the fuel in question, the flue gas temperature at each of the fixed enthalpy values is obtained and can be used to define a temperature – enthalpy relationship. The model uses the enthalpy change of the flue gas to calculate their temperature. It assumes an enthalpy change of zero (adiabatic) and the associated temperature (taken from the adiabatic enthalpy slice) for gases entering the boiler. As these gases pass through the boiler, heat energy is removed and their enthalpy changes. The temperature – enthalpy relationship is then used at pre-defined calculation points to convert these enthalpy changes into a temperature profile for the boiler.

8.3.1.4b Sources of Error

There are several concessions that come with using the PrePDF model. Firstly, as has already been mentioned, the software can only cope with a single fuel source and therefore, requires the combining of the parent and substitute fuels within a blend to form an 'equivalent fuel'. Whilst the non-additive effects of this combining of fuels are negated for matters concerning ash deposition, this is not so for the prediction of combustion behaviour, where the effect of combustion of inherently different fuel particles cannot be modelled. The literature [3, 5, 7, 8, 10, 12, 14] suggests that burning profile of biomass will be different to that of coal due to the higher volatile and ash contents, and that this behaviour will be evident even when mixed within the coal fuel stream. This differentiation between fuel types is lost when the fuels are combined to form the 'equivalent fuel'.

Secondly, were the software able to deal with two fuel streams, allowing the fuels to be considered separately, the subtleties in the differences between the combustion characteristics of biomass and coal would be negated by the very simple combustion chemistry model. Finally, fuel data must be entered into the PrePDF software on a dry, ash-free basis and therefore, the effects of moisture and ash on the flame temperature cannot be quantified.

8.3.1.4c The Empirical Model

For the empirical model, one of these temperature relationships was derived for a medium volatile bituminous coal and a range of blends of this fuel with a typical sewage sludge. The temperature – enthalpy profile was calculated for the parent fuel followed by the adiabatic flame temperature of a range of blends at $5\%_{th}$ intervals. A relationship between blend and adiabatic flame temperature was derived and then used to define the temperature – enthalpy relationship for fuel blends. The empirical model therefore, assumes that the difference in temperature between one blend and the next is constant across the entire enthalpy range. Table B1.2 and figure B1.1 in Appendix B suggests that this is not the case and that in fact, the difference in temperature between one blend and another grows as enthalpy decreases. Table 8.3 shows the error induced by this assumption for a blend of $10\%_{th}$ sewage sludge $90\%_{th}$ coal and Table 8.4 shows the worst possible error caused by this assumption at the very limit of the range of application of the model. As a result, when using the empirical correlations within this model, the spreadsheet is only valid for one coal and substitute fuel. It has been assumed that the relationships will hold a degree of validity for coals and sewage sludges of similar composition, however, the type of substitute fuel cannot be changed (for example to sawdust). It is conceivable that a matrix of relationships for a range of fuels could be derived and embedded within the spreadsheet, however, it is thought that the data required to achieve this would make it unfeasibly large.

Table 8.3: Error induced in the temperature – enthalpy relationship for $10\%_{th}$ sewage sludge blend

Enthalpy / kJ/kg	Temperature / K			+ / -Error in Predicted Temperature / K	Error as % of total temperature
	Pure Coal Predicted	10% Sewage Sludge Predicted	10% Sewage Sludge Actual		
0 (Adiabatic)	2183.02	2202.12	2202.12	0	0%
-2000	671.93	691.03	723.32	-32.39	-4.67%
-2400	299.92	319.02	358.29	-39.27	-12.30%

Table 8.4: Error induced in the temperature – enthalpy relationship for $40\%_{th}$ sewage sludge blend

Enthalpy / kJ/kg	Temperature / K			+ / -Error in Predicted Temperature / K	Error as % of total temperature
	Pure Coal Predicted	10% Sewage Sludge Predicted	10% Sewage Sludge Actual		
0 (Adiabatic)	2183.02	2281.38	2281.38	0	0%
-2000	671.93	770.29	872.84	-102.55	-13.32%
-2400	299.92	398.28	527.75	-129.47	-32.50%

Tables 8.3 and 8.4 show that within the reasonable operating range of the spreadsheet (0% - 10%$_{th}$ blends), the error introduced by this assumption is around 12.3% at worst. However, if using blends at the high end of the range, the error in predicted temperature can be as high as 32.5%. This does not include the inherent errors involved in using the relationship to model fuels different to those for which it was derived.

These results suggest that the empirical method is valid for blends in the lower end of the operational range, however, the accuracy of the temperature – enthalpy profile must be called into question when the blends approach the higher end of this range, even for the fuels for which it was derived. Therefore the ANN method was adopted because, along with being able to make predictions for a range of fuels, it eliminates these errors.

8.3.1.4d The ANN Model

In an attempt to address the problems caused by the limitations of the empirical model, the evolution to the ANN has been made. Here, over 300 temperature – enthalpy profiles have been used to train an ANN which can interpolate between data points to predict profiles for fuels with compositions falling within the limits of the training data set. This has allowed the use of the spreadsheet to predict sewage sludge, sawdust and refuse derived fuel (RDF) blends.

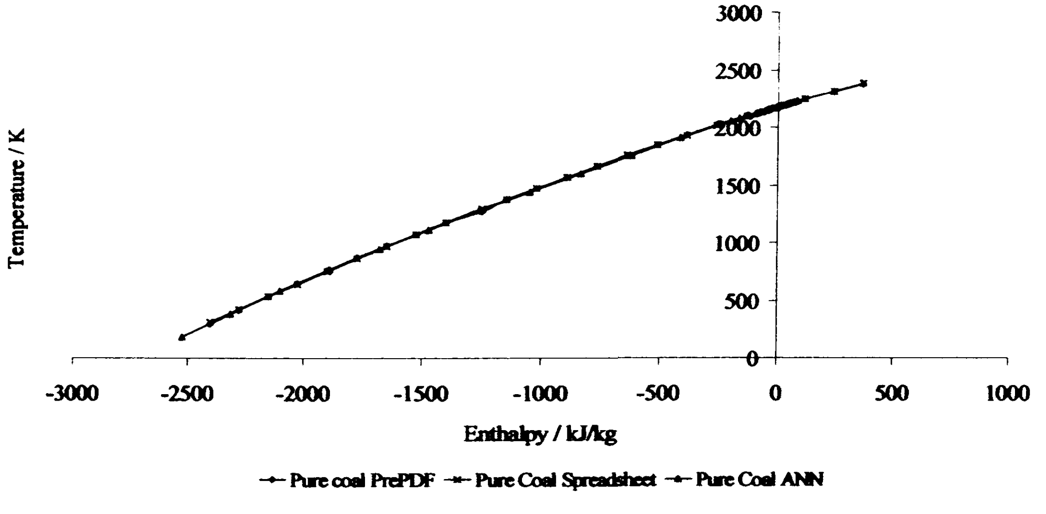

Figure 8.8: Comparison of PrePDF, empirical correlations and ANN temperature – enthalpy relationships for pure coal

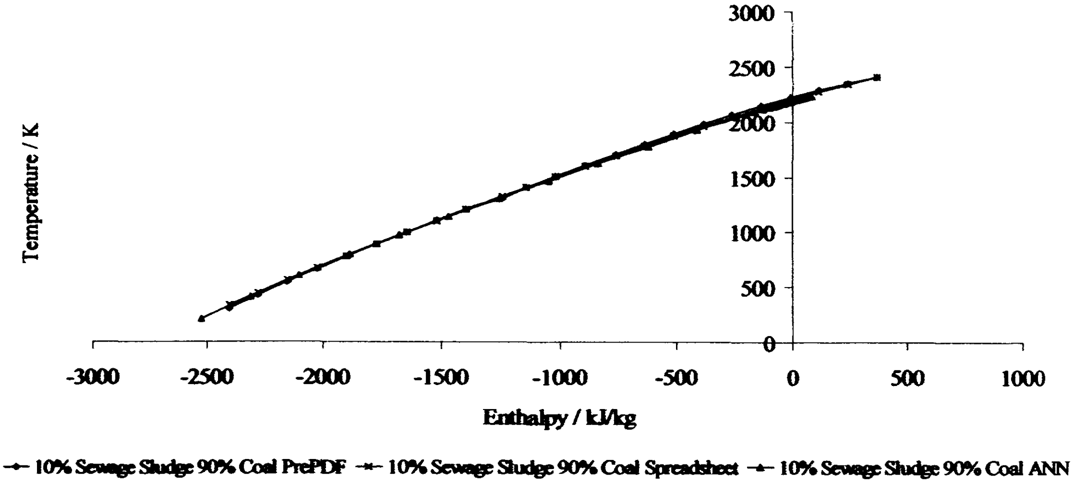

Figure 8.9: Comparison of PrePDF, Spreadsheet and ANN temperature – enthalpy relationships for 10%$_{th}$ sewage sludge 90%$_{th}$ coal

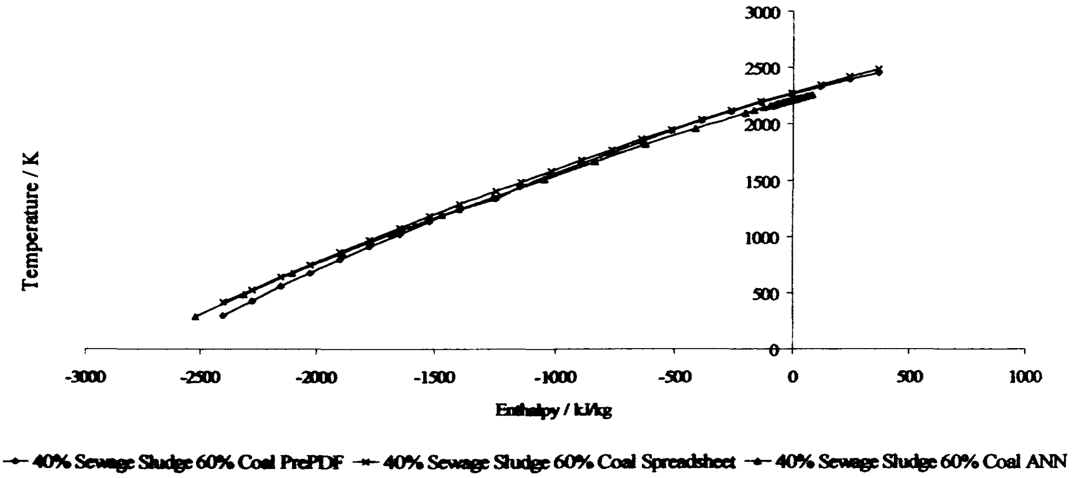

Figure 8.10: Comparison of PrePDF, Spreadsheet and ANN temperature – enthalpy relationships for 40%$_{th}$ sewage sludge 60%$_{th}$ coal

Another advantage of the ANN model is that a unique temperature enthalpy profile is defined for any blend specified. This level of detail was not possible in the empirical model. Figures 8.8 to 8.10 demonstrate the improvement in the prediction of the temperature – enthalpy relationship for the ANN over the empirical model.

8.3.1.5 The Formation of the Temperature Profile

The temperature profile is essentially formed by applying the temperature – enthalpy relationship to a one-dimensional model of the boiler. This means that no consideration is given to boiler cross-section and hence, gas velocity and flow patterns. This means that eddies and areas of re-circulation are not modelled, neither are the flow patterns and streamlines around the superheater tubes. This is not important however, as the physical mechanics of deposition are not being considered, merely the mass of 'harmful' species in the system which are capable of causing problems, and therefore, the calculation of gas velocities is not necessary. The flow regime inside the boiler is based on the assumption that the constant evolution of gases from the combustion of fuel at the burners maintains a constant flow of gas through the boiler.

8.3.1.5a Heat Transfer Assumptions

One of the most significant assumptions within this model is that of uniform heat transfer across each heat exchanger. This assumption is valid for the superheaters, reheaters and economisers, which can account for at most 15% of the total heat exchange individually. The distance over which they influence the flue gases is relatively short, in terms of the total length of the boiler centreline and therefore, they induce a relatively small temperature change on the flue gases. However, the water walls account for almost half of the heat removed from the boiler, and influence the flue gases for around 60% of their journey along the centreline. This means that they experience temperatures varying from circa 700°C at the bottom of the ash hopper to 1650°C in the combustion chamber and cooling to circa 1200°C in the penthouse. To assume uniform heat transfer along the length of the waterwalls under these varied temperature conditions is a departure from what happens in reality. However, one of the major criteria for the spreadsheet was that gas side measurements should not be required. Therefore, before the profile is calculated, there is no way of predicting what the temperature regime will be like inside the boiler and hence, the heat transfer profile for the waterwalls.

There are two possible solutions to this; the first is to take detailed steam side temperature measurements to provide a heat transfer profile. However, this sort of detailed information may not be readily available and may take time to acquire, if it is even possible. The second method is to try to introduce an iterative loop into the calculation whereby, at first, uniform heat transfer is assumed, and the temperature profile is calculated, then a new heat transfer profile is calculated based upon the temperature profile yielding new temperature profile. Although this iterative approach has not been used for this model in the current spreadsheet, other calculations have been iterated (for a fixed number of cycles) and it is thought that this sort of approach could be used here. However, care would need to be taken to ensure that the calculation remained stable.

8.3.1.5b Fuel Combustion Assumptions

The other key assumption in the temperature profile model is that of instantaneous combustion of fuel upon entry into the boiler. In essence, the model assumes a flow of combustion gases through the burners rather than fuel and air which then burns. This provides the instantaneous release of all heat energy from the fuel in the burner zone rather than a simulation of steady heat release over the burnout time of the particle (ca. 1.5s [39]). In reality, as discussed in Chapter 2, upon entry to the combustion zone, coal particles must undergo heating before they begin to combust, causing an initial delay (ca. 0.01s [36]) before the temperature is high enough for ignition. Following ignition, the combustion of volatiles takes place followed by char combustion. Given the short timescale for ignition and volatile combustion, the current instantaneous heat release model is a reasonable assumption, however, given the length of time for particulate burnout, a more realistic model of char combustion should be sought.

One of the key problems with introducing a fuel heat release model, which is more in line with the real combustion process, is that it would require the introduction of a time element to assess the fuel location within the boiler as it releases heat energy. This would require the calculation of mass flow-rates and simulation of the flow patterns in the combustion zone / burner region, requiring more detailed modelling of the boiler geometry, probably in two dimensions rather than the current one. The burning profile of the fuel would be required to dictate the rate of heat release from the fuel. This creates an additional piece of data required by the boiler operator before the spreadsheet can be used.

8.3.1.5c The Effects of Ash Loading

Ash loading is another important factor that is not included in the current model. In the combustion zone fuel ash is heated up to combustion temperatures. Unless they deposit on the heat exchangers, these particles cannot directly transfer the heat energy stored within them to the water or steam. These particles are instead cooled by the combustion gases as their temperature decreases following heat transfer in the heat exchangers. Therefore, these hot ash particles act as a heat store, which can only transfer energy once the flue gases have begun to cool down. This means that heat energy that would have been transferred to the water or steam in the combustion chamber is carried further down the boiler, increasing gas temperatures and hence, heat transfer in the superheaters, reheaters and economisers. Again, to implement this kind of model, velocity fields would be required to track the particles progress through the boiler, requiring 2D rather than 1D modelling.

8.3.1.5d The Need to Combine Steam Cycle and Temperature Profile Calculations

In its current form, the temperature profile is defined by the steam cycle. The user enters the steam cycle operating data along with the fuel data and boiler geometry, which is all used to define the temperature profile. This means that the heat being removed from the boiler is fixed whilst that entering is not. Therefore, the electrical output of the boiler remains the same regardless of how much or how little fuel is entered. Moreover, it is possible for the user to enter data that would lead to more energy being removed by the steam than can be supported by the fuel. If this happens, gas side temperatures can fall below the steam side temperatures in some heat exchangers, and in extreme cases can lead to negative temperatures. In this situation, heat transfer in the affected heat exchanger should be reversed and heat would be lost from the steam side, however, the spreadsheet is not capable of doing this. Instead it compares the gas temperature to the steam temperature in each heat exchanger, and should this situation arise, it will set the gas temperature equal to the steam temperature in that heat exchanger, warning the user of the problem.

This problem is exacerbated when using the empirical temperature – enthalpy model because, as discussed in Section 8.3.1.4c, the empirical method significantly under predicts the gas temperature at the lower end of the enthalpy range for blended fuels. The ANN method does not suffer from this problem as badly because of the better prediction of gas temperatures by the temperature – enthalpy relationship.

This problem stems from the use of the steam cycle to define the temperature profile. A better way of modelling this would be to interlink the steam cycle calculations to the temperature profile such that changes in the furnace temperature will have a knock on effect on the thermodynamics of the water or steam; influencing its temperature and pressure and hence, the electrical output of the boiler. This would require a far more complex heat transfer model which performs heat transfer calculations as part of the temperature profile creation process rather than relying on pre-defined heat transfer values to determine the gas temperature.

As has already been mentioned in Section 8.3.1.3, no attempt is made to consider the insulating effects of ash deposition on the heat transfer process, as this would need consideration of long-term deposit build-up and cleaning cycles over a weekly or monthly timescale. To reliably predict this sort of ash behaviour, iterative models or numerical methods would be required to predict velocity fields, particle trajectories, impaction rates and deposit composition. A model of this type would require considerable effort on the part of the user to create, and solve, and would therefore, compromise the remit for the development of this tool.

8.3.1.6 The Slagging and Fouling Model

The FactSage thermochemical software package has been used to create this model, and although separate fuel streams can be specified within FactSage, additive behaviour has been assumed for the parent and substitute fuel streams. FactSage considers the total mass of elements within the input stream and not what source they are from, therefore, entering the two fuels as separate streams would make no difference to the outcome. In addition, as was mentioned in Section 8.3.1.1, a problem exists where non-additive behaviour arises when attempting to make predictions of how a fuel blend will behave based upon the results of firing the component fuels individually. In this model, as is the case with all models in the spreadsheet, the fuels have been combined before any combustion simulations have been made or empirical correlations have been derived therefore, the assumption of additive behaviour is a valid approach to use.

8.3.1.6a Assessing the Potential for Slagging and Fouling

The molten and gaseous phases were selected as the criteria used to assess the potential for slagging and fouling. This is because it is believed that it is the condensation of species from the gaseous phase, and inertial impaction of slag droplets from the molten phase that form the initial sticky deposit layers which allow the solid particles to adhere. Without this layer, solid particles would rebound, and for this reason, are not used as criteria to assess the causes of slaging and fouling.

Another reason that solid phase species were not used for this was the variability in the mass of the solid species formed for example, at 1000K Na forms 8.55g of the solid species $NaAlSi_3O_8$ for pure coal, this has a molecular weight of 262 kg/mol equating to 0.75g of Na. However, at 900K, the same mass of sodium forms Na_2SO_4 which has a molecular weight of only 142 kg/mol giving a total mass of solid sodium species of only 2.315g despite containing the same mass of sodium. Given only the total mass of sodium species, one would think that there was a quarter of the sodium in the solid phase at 900K and therefore, a quarter of the risk of slagging and fouling problems. This sort of discrepancy does not occur to the same extent in the molten and gaseous phases because the species tend to form lower weight, shorter chain compounds.

The model considers the entire combustion system at different individual temperature states, rather than track the composition of the combustion products through the boiler. For this reason, removal of species from the system through deposition cannot be accounted for; essentially continuity of mass is maintained for each element throughout the entire system.

8.3.1.6b The Empirical Model

Initially, the slagging and fouling model used empirical correlations much like the temperature – enthalpy model discussed in Section 8.3.1.4. As with the other models, concerns over the applicability of the empirical model to other coals and substitute fuel types, has led to the development of an ANN to replace these empirical correlations.

The empirical correlations describe the relationship of solid, molten and gaseous sodium, potassium, phosphorous, iron, aluminium and silicon as a function of flue gas temperature and fuel blend. The empirical correlations, as for the temperature – enthalpy relationship, have been derived for a single medium volatile bituminous coal and a typical sewage sludge. As with the temperature – enthalpy model, it was hoped that they would hold a degree of validity for fuels of a similar composition. The correlations are derived from results produced by FactSage for blends of fuel up to $50\%_{th}$ sewage sludge across a temperature range of 400K to 2000K. Although specific species such as alkali sulphates are thought to cause slagging and fouling, these species were not singled out plotting. Rather, the total mass of species containing each of the 'harmful' elements in each phase was plotted. As a result, instead of the individual compounds identified within the literature, the total masses of 'harmful' species present in the gaseous and molten phases were used to assess the likelihood of problems occurring.

The correlations themselves start as plots of the total mass of each phase of species containing Na, K, P, Fe, Al and Si as a function of temperature. In their raw form many of these plots were very complex and in order to create correlations from them they were simplified. Although this simplification process induces errors into predicted mass, it was deemed justifiable due to the reduction in the number of correlations required to define the system. The majority of these simplifications were required in the solid phase plots because of the variability in mass from one temperature to the next as described above. Following simplification, temperature values or ranges were identified where mass remained constant; these bands were plotted showing the mass of species formed as a function of blend. Should a temperature fall outside a range or between discrete temperature values, then linear interpolation was used to find the corresponding mass value.

8.3.1.6c The ANN Model

The ANN is an expansion of the empirical correlation technique, which negates the need for interpolation between or simplification of mass – temperature - blend relationships. To train the ANN a data set was generated, in the same way as that used to define the correlations. Using this, the ANN is capable of predicting the mass and phase of species formed for a range of coals blended with sewage sludge, sawdust or RDF. The ANN needs to interpolate between data points in its training data set, however, it is thought that the 600 data points used to train it will have provided a sufficient density of data points within the range to enable it to do this competently and keeping any errors to a minimum.

8.2.1.6d Comparison of the Empirical Correlations and ANN to FactSage Predictions

Figures 8.11 to 8.14 show examples of the predicted mass of molten alkali metals (Na and K) for pure coal and a 10%$_{th}$ blend of sewage sludge made by the empirical correlations, the ANN and the FactSage software.

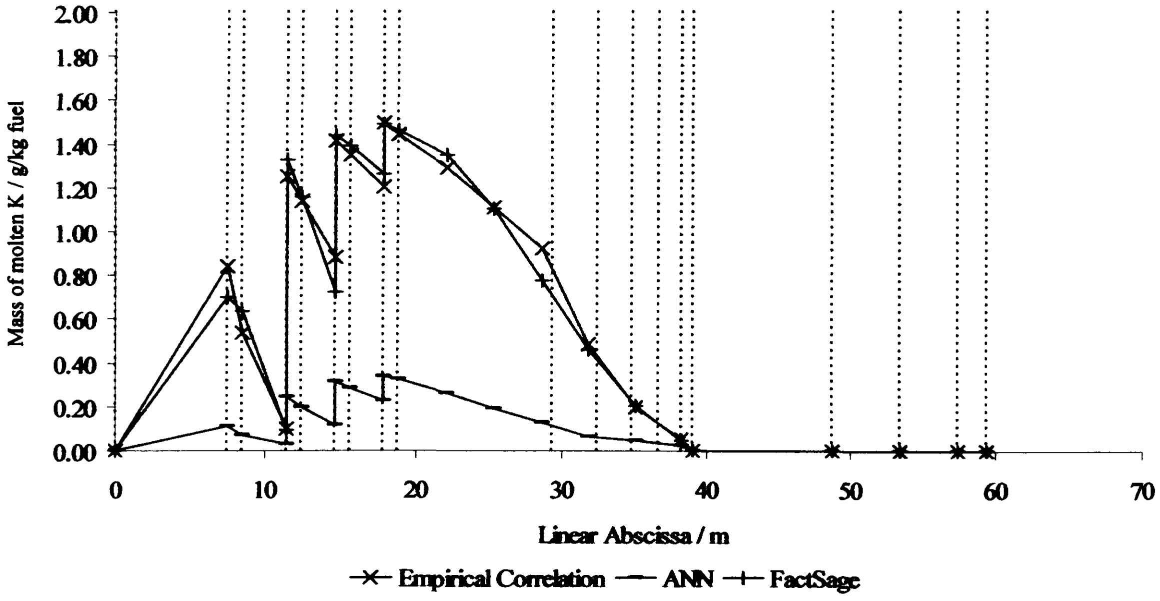

Figure 8.11: Comparison of the prediction of the formation of molten potassium for pure coal

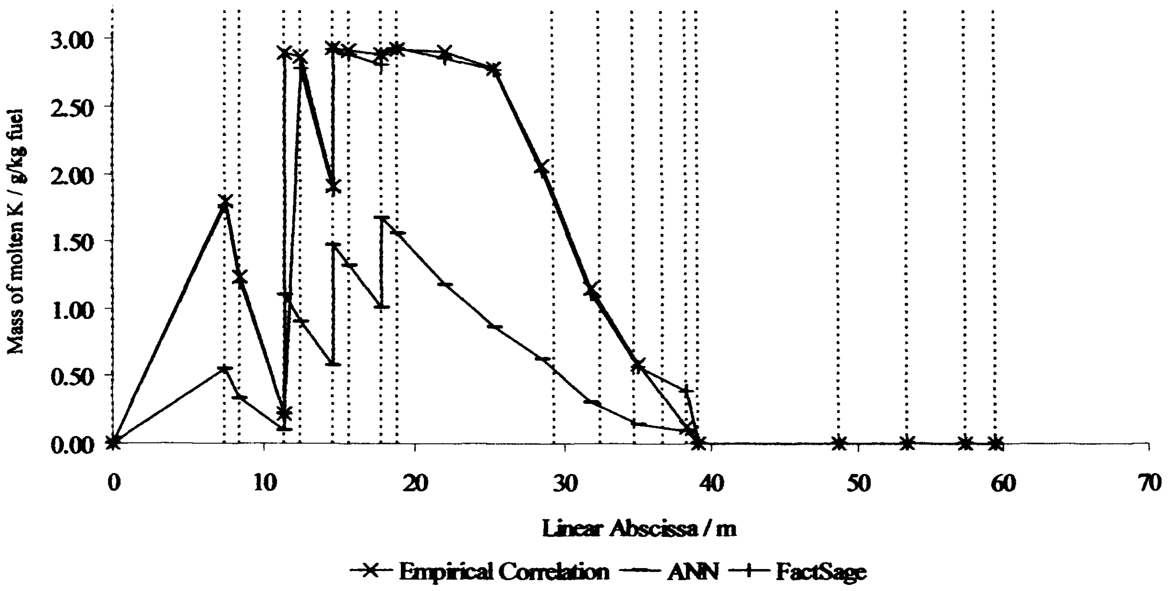

Figure 8.12: Comparison of the prediction of the formation of molten potassium for 10%$_{th}$ sewage sludge 90%$_{th}$ coal

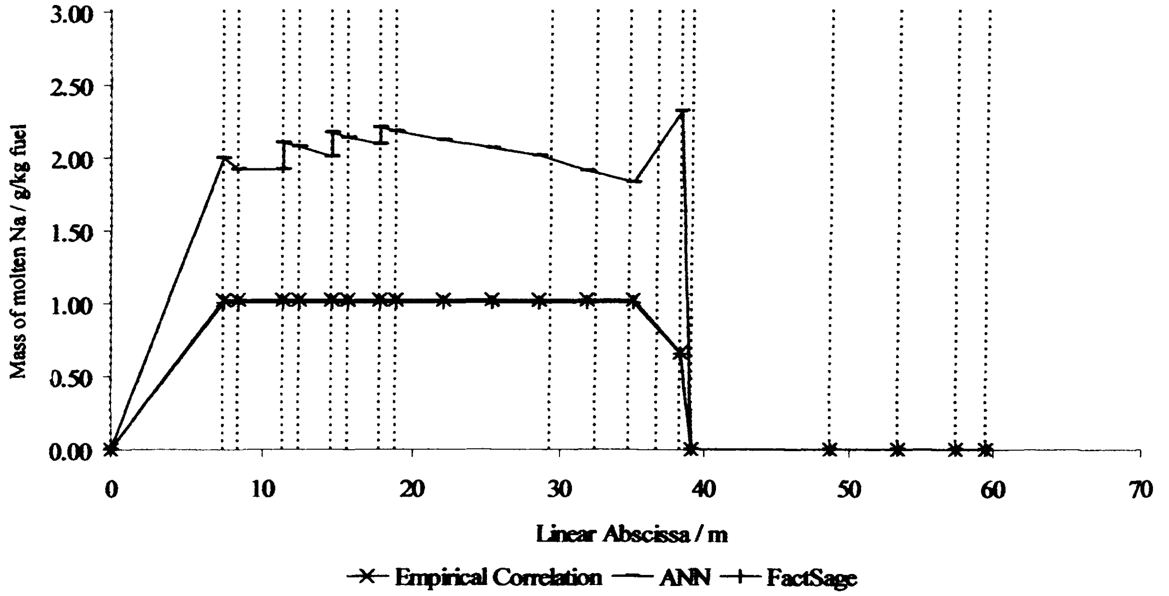

Figure 8.13: Comparison of the prediction of the formation of molten sodium for pure coal

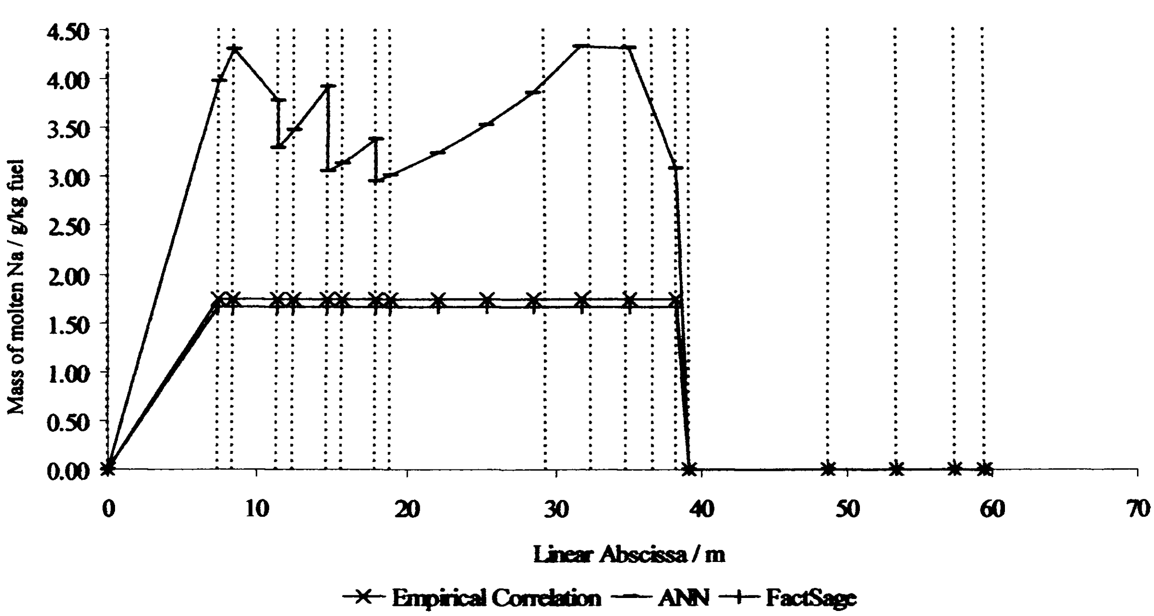

Figure 8.14: Comparison of the prediction of the formation of molten sodium for 10%$_{th}$ sewage sludge 90%$_{th}$ coal

The above figures show that the empirical correlations closely match the predictions taken directly from the Factsage software, as one would expect, since they are based on 112 data points taken specifically for the parent and substitute fuels being examined. The ANN displays a degree of error, however, some error is likely as the ANN is based upon a selection of fuels designed to give a broad scope of coals as the parent fuel whilst allowing blending with three types of substitute fuel. The data points used to train the ANN are more widely dispersed within the range and are not as tightly focussed around the fuel in question as those for the empirical correlations. As a result, the error in the ANN predicted value is greater. Whilst the magnitudes of the predictions made by the ANN are slightly awry, they do observe a similar shape to the FactSage results. The accuracy of the ANN could be improved by using more data points within the training data set.

8.3.1.6e Communicating the Result to the User

The purpose of the slagging and fouling model is to alert the user to the potential for problems based upon the fuel and boiler data he has entered. This is done through a series of warning flags, which communicate to the user whether a high, medium or low risk of slagging and fouling is present within each heat exchanger. The warnings are triggered when the levels of certain species in the molten or gaseous phases exceed pre-defined levels. Fouling warnings apply to all heat exchangers with the exception of the water walls and are based upon the level of the alkali metals sodium and potassium in the molten phase for the superheaters and reheaters, and the level of phosphorous in the gaseous phase in the economisers. Slagging warnings are applied to waterwalls, superheaters and reheaters and are based upon the mass of iron in the molten phase. The species used to define these warning flags are based upon deposition mechanisms described in the literature [43, 44, 47, 53, 54, 57] and outlined in Chapter 2.

The triggers are based upon information provided by Laborelec regarding sewage sludge co-firing tests within their boiler [95]. These triggers are considered valid for the empirical correlations because they are based upon blends of sewage sludge, however, they cannot be expected to work for the other substitute fuels covered by the ANN. Therefore, they are only considered valid for the earlier versions of the spreadsheet in which empirical correlations are used. When using the later versions of the spreadsheet containing the ANN, the user should ignore the warning flags, however, he can use the mass plots of the relevant species for comparative analysis to analyse the likely effects of different substitute fuels and blends. A more comprehensive system of warning flags needs to be developed for the ANN spreadsheet, drawing on a wider field of research covering co-combustion trials with other substitute fuels and coal types.

8.3.1.7 The High Temperature Corrosion Model

The corrosion model is based entirely on empirical correlations, the model has not been expanded to include an ANN however, this is due to time constraints rather than applicability of an ANN to the problem. These correlations have been derived for a typical medium volatile bituminous coal and a typical sewage sludge. This means that the model has limited applicability to other coal types and is not valid for alternative substitute fuels. However the development of an ANN would solve this.

8.3.1.7a Deposition Modelling

The corrosion model differs from the slagging and fouling model in that it assumes a deposition mechanism, and, whilst still focusing on alkali metals as the root of the problem, it considers alkali sulphates and alkali – iron trisulphates specifically, rather than the global alkali content. The model assumes a vapour deposition mechanism, where it identifies the solid and molten species condensed out when the flue gases cool from a range of flue gas temperatures to a range of heat exchanger tube surface temperatures.

When establishing the composition of the deposits, the model relies entirely on species condensed from the vapour phase as the sole form of deposition. It is likely that in reality, molten and solid particles would contribute to deposition also through inertial impaction, however, it is difficult to reliably quantify their contribution without an assessment of particle trajectories, composition and sticking probability. The deposition mechanisms suggested by the literature [43, 44, 47, 53, 54, 55] and outlined in Chapter 2 suggest that a sticky layer of deposit is required before larger solid particles will adhere. They suggest that the presence of this sticky layer is caused by condensation of species from the vapour phase onto the heat exchanger surfaces. Therefore, it is likely that it would be these species, which are in contact with the tube surface scale and therefore, form the corrosive species. For this reason, considering only vapour deposition for the high temperature corrosion model is valid, as it is most likely to be species deposited in this way that are in contact with the tube surface and able to attack it.

For vapour deposition, it is assumed that species are uniformly distributed within the vapour phase and therefore, the quantity deposited, is purely a function of their solidification temperature and not their local concentration within the vapour phase. The model makes no attempt to quantify the mass of deposits formed per kg of fuel input, it simply analyses what species would condense out if the combustion gases are cooled to tube surface temperatures, giving the deposit composition. This eliminates the need to assess gas velocity fields within the heat exchanger banks and simplifies the calculation. However, without the ability to quantify the mass of deposits collected on the tubes, the model is unable to account for the insulating effect these deposits have, and the subsequent increase in tube surface temperature. This means the spreadsheet cannot predict a situation where the surface temperature of a tube previously too cold to form a melt could climb high enough to allow a melt to form as deposits build up.

8.3.1.7b Prediction of the Sulphate Melt

The literature cites the formation of an alkali sulphate melt as the cause of high temperature corrosion [59, 63, 66], as outlined in Chapter 3 and Chapter 6. This melt increases the rate of diffusion of SO_3 to the metal surface, where it attacks the protective oxide layer between the tube and the deposits. This melt is formed by the the alkali sulphates Na_2SO_4 and K_2SO_4 combined with the iron trisuplhate $Fe_2(SO_4)_3$. The temperature at which this melt forms varies as the relative compositions of species which form it within the deposit changes. The model seeks to calculate the composition of the melt-forming species deposited on the heat exchanger tubes through vapour deposition, and hence, calculate the formation temperature of the melt. It will then compare this temperature with the surface temperature of the heat exchanger tube to see whether it is possible for the deposited species to exist above this melt formation temperature. If it is, then the spreadsheet will communicate this fact to the user via warning flags alerting him to the risk of increased corrosion rates.

The FactSage thermochemical software package was used to produce the data from which the correlations were derived. The predicted mass of deposits varied very little as the tube surface temperature changed, only when the tube surface temperature was reduced to 300°C was a difference detected as a slight reduction in the formation of alkali sulphates due to the formation of the species $K_3Na(SO_4)_2$. This phenomenon was observed for all blends. It is possible that this species could form part of the sulphate melt, however, as the melting temperature is determined by the composition of the ternary system Na_2SO_4 – K_2SO_4 – $Fe_2(SO_4)_3$, then this species must be neglected. This causes a 3.5% reduction in Na_2SO_4 and a 55% reduction in K_2SO_4 however, this is acceptable because given the predicted composition of deposits for all blends, an increase in $Fe_2(SO_4)_3$ would cause a decrease in melt formation temperature making the model more conservative. In addition, the minimum formation temperature of the melt is 550°C [59], some 250°C lower than the tube surface temperature at which this phenomenon occurs, therefore, it is not possible for a melt to form at all under these conditions.

8.3.1.7c The use of the Empirical Correlations

The spreadsheet uses the correlations of mass of Na_2SO_4, K_2SO_4 and $Fe_2(SO_4)_3$ formed as a function of flue gas temperature for discrete values of blend and tube surface temperature to predict the composition of deposits formed on each heat exchanger in the boiler. At each working point (heat exchanger), the spreadsheet calculates the mass of each species formed at the specified temperature for each blend in the range (0 – 25%$_{th}$ at 5%$_{th}$ intervals), it then uses Boolean logic to identify the correct limits and interpolates linearly to find the value for the exact blend. For example, for a blend of 7%$_{th}$ the spreadsheet would identify the mass produced at 5%$_{th}$ and 10%$_{th}$ as the correct limits and interpolate between them to find the mass at 7%$_{th}$. Figures 8.15 to 8.20 demonstrate that the use of linear interpolation between discrete blends is acceptable, given the linear nature of the mass – blend relationships shown for Na_2SO_4 and K_2SO_4 and the near linear relationship between blend and mass for $Fe_2(SO_4)_3$. This calculation is done for each tube surface temperature and, if necessary, a similar interpolation process is used to find the correct mass for the specified tube surface temperature. Linear interpolation must be assumed for this process too, as there are only two data points; tube surface temperatures in the range 650°C – 350°C, which share the same correlations and at 300°C, where the correlations change for the reasons mentioned above. Therefore, the only need for interpolation would be if the tube surface temperature was between 300°C and 350°C.

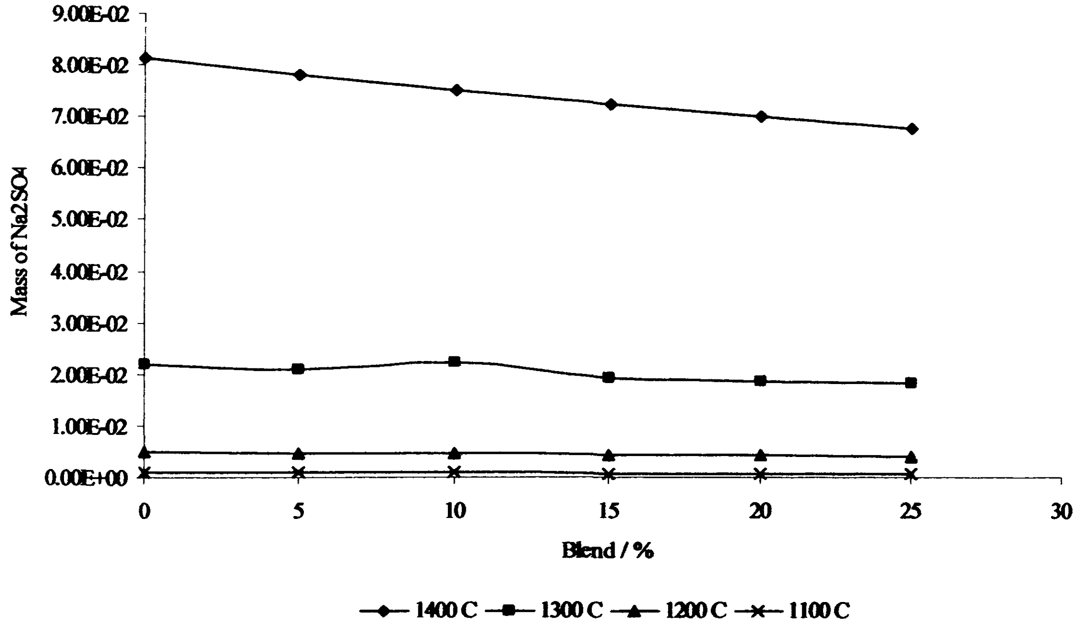

Figure 8.15: Mass of Na_2SO_4 as a function of blend for high gas temperatures

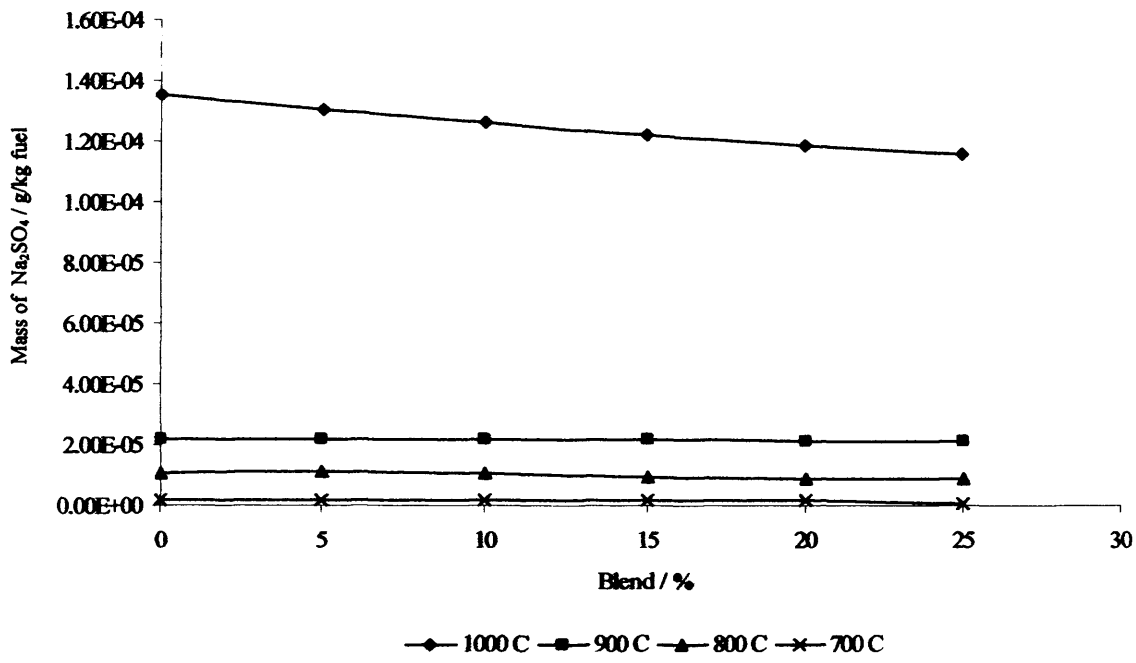

Figure 8.16: Mass of Na_2SO_4 as a function of blend for low gas temperatures

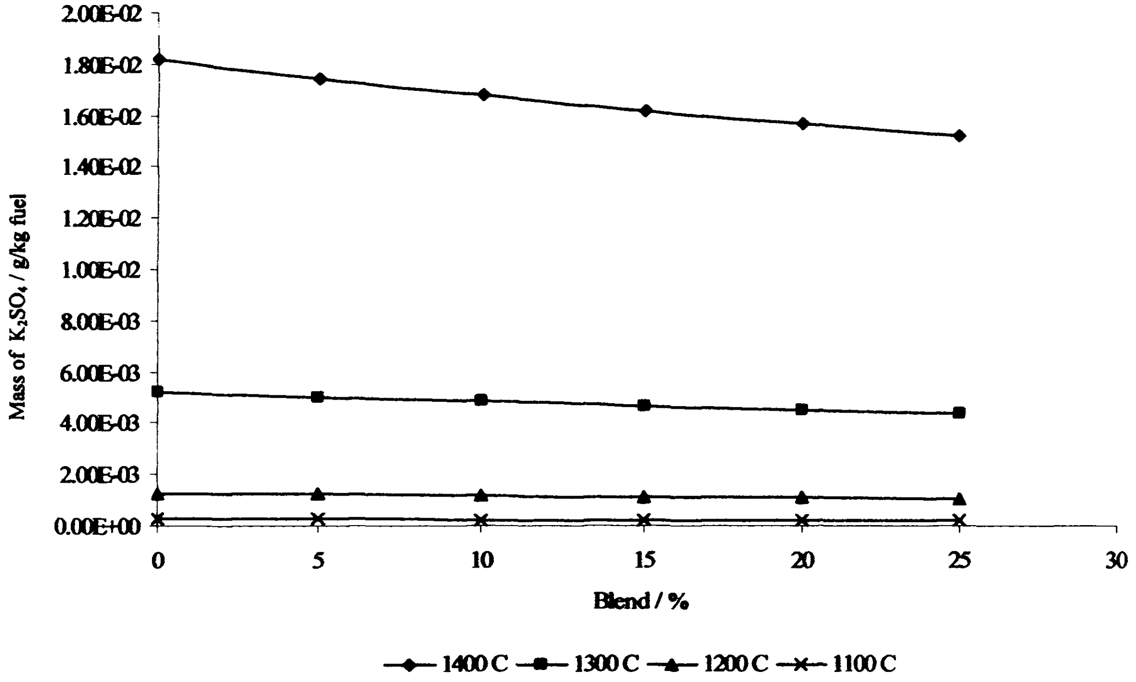

Figure 8.17: Mass of K_2SO_4 as a function of blend for high gas temperatures

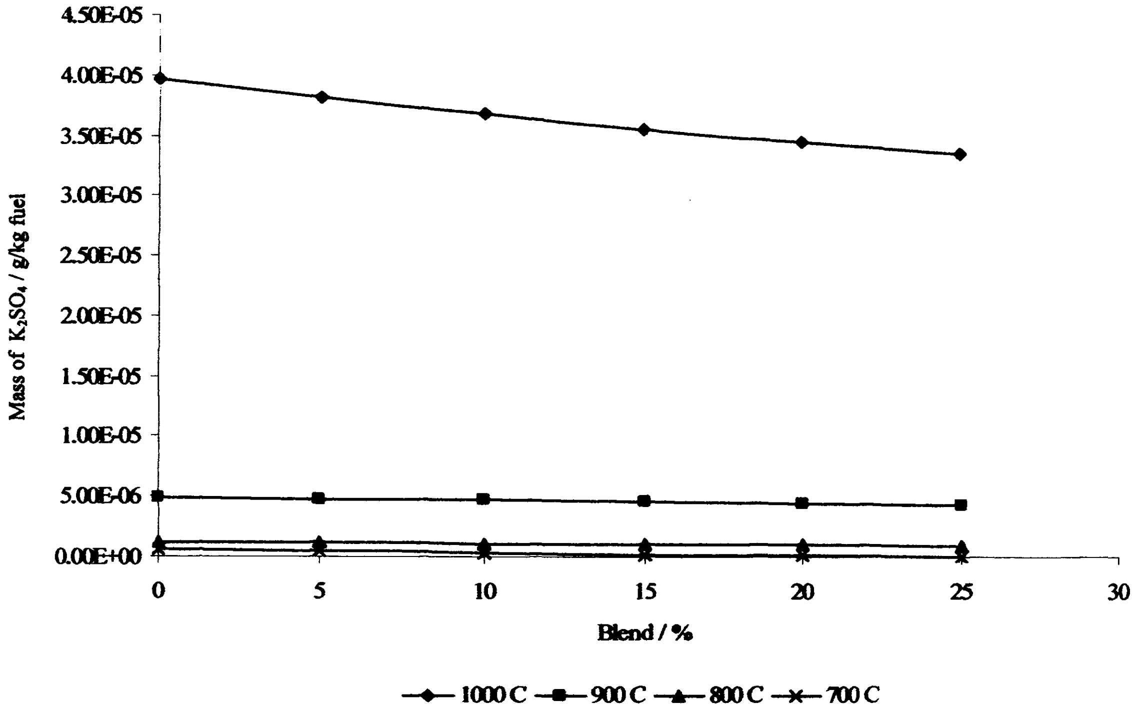

Figure 8.18: Mass of K_2SO_4 as a function of blend for low gas temperatures

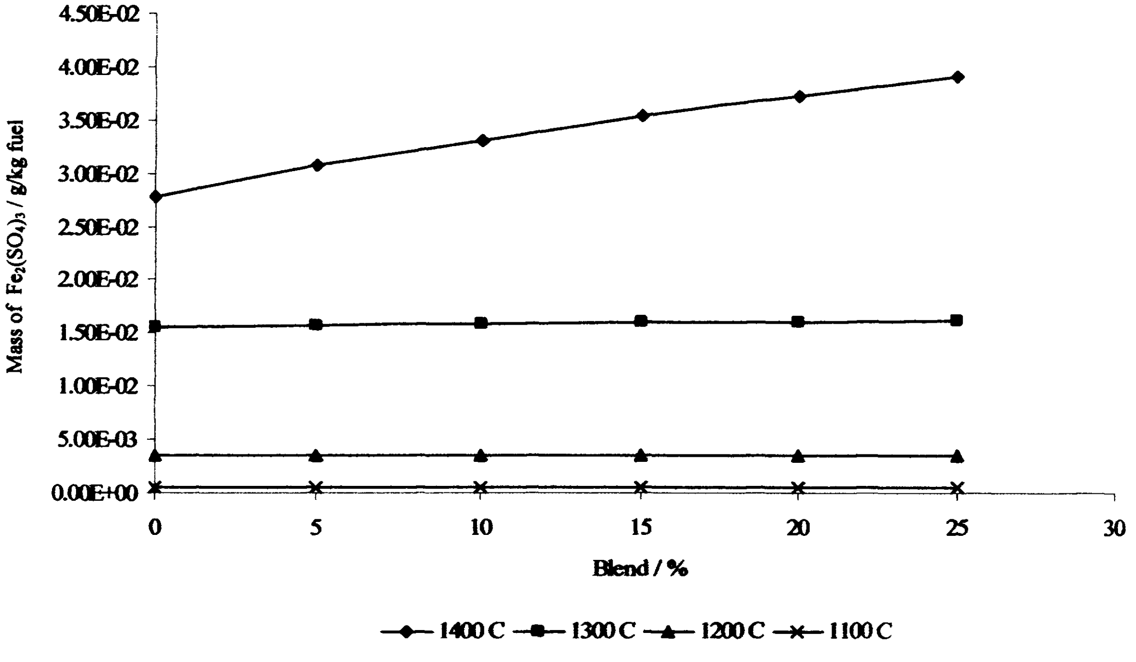

Figure 8.19: Mass of $Fe_2(SO_4)_3$ as a function of blend for high gas temperatures

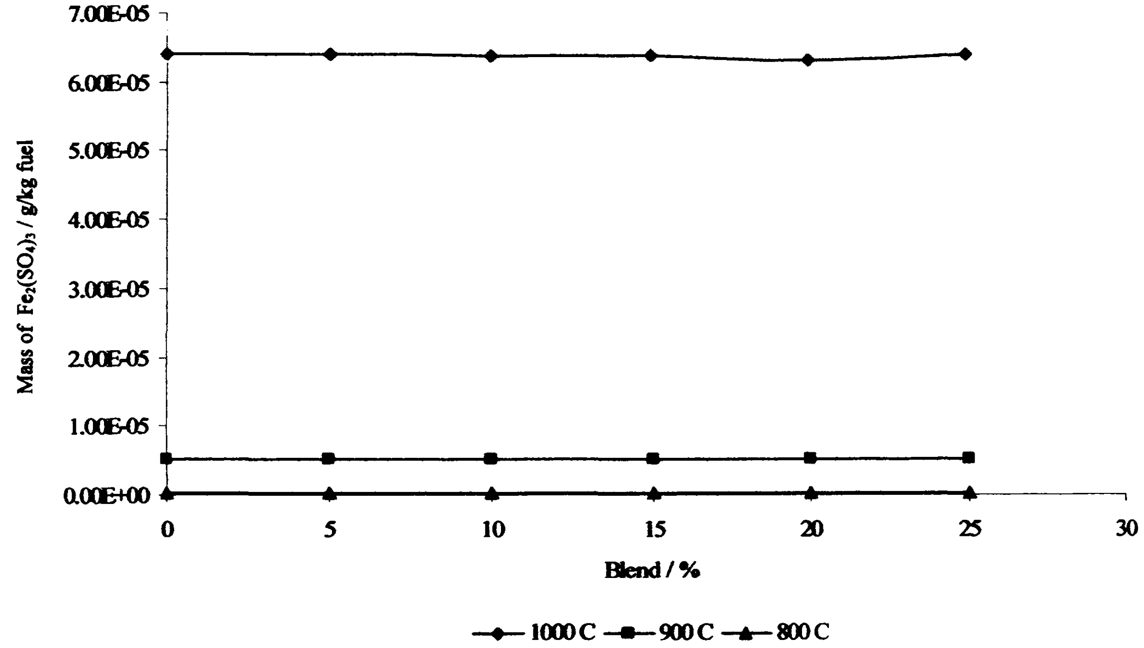

Figure 8.10: Mass of $Fe_2(SO_4)_3$ as a function of blend for low gas temperatures

8.3.1.7d Defining the Formation of the Sulphate Melt

In order to check the melt formation temperature, the spreadsheet uses an embedded 'melting temperature map' for the ternary system $Na_2SO_4 - K_2SO_4 - Fe_2(SO_4)_3$. This map is divided into three zones (A, B and C) according to different regions of the Na_2SO_4 - $Fe_2(SO_4)_3$ and K_2SO_4 - $Fe_2(SO_4)_3$ systems as shown in figure 8.21

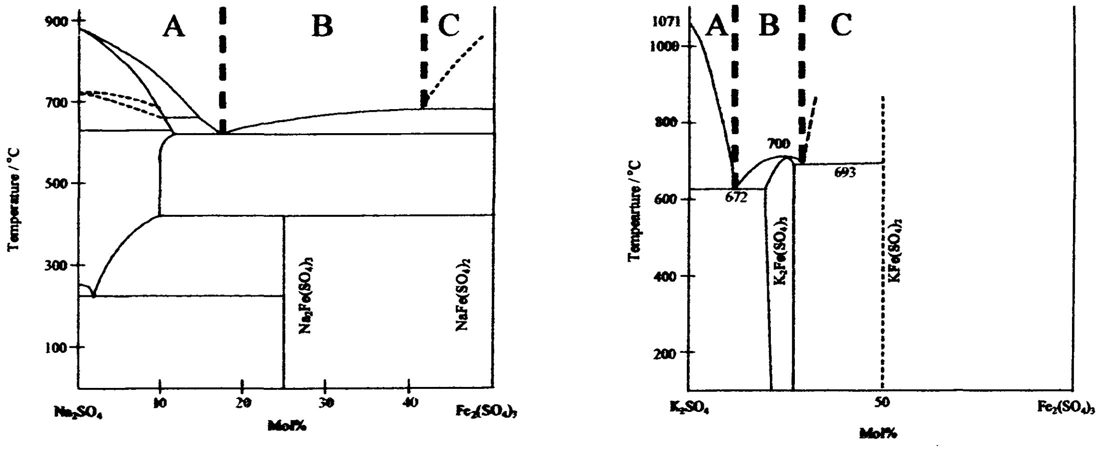

Figure 8.11: Zones A, B and C as defined by the liquidus curves of the $Na_2SO_4 - Fe_2(SO_4)_3$ and $K_2SO_4 - Fe_2(SO_4)_3$ systems

The left hand side of zone A is dominated by the Na_2SO_4 – K_2SO_4 liquidus (Ref: figure 6.26 page 151) whilst the right hand side of zone A is dominated by the $Na_3Fe(SO_4)_3$ – $K_3Fe(SO_4)_3$ liquidus (Ref: figure 6.29 page 152). Zones B and C are assumed to be dominated by the $Na_3Fe(SO_4)_3$ – $K_3Fe(SO_4)_3$ liquidus. A series of 11 curves for discrete

Na_2SO_4 – K_2SO_4 compositions from $100\%_{mol}$ Na_2SO_4 to $100\%_{mol}$ K_2SO_4 are interpolated along these liquidus curves between the two systems shown in figure 8.21 and describe the melting temperature of the system for concentrations of up to $50\%_{mol}$ $Fe_2(SO_4)_3$. This is simply an interpretation of the melting temperature of the system and as a result, it may be possible that there are further ‘undulations’ in the melting temperature of the system that have not been accounted for. A series of experiments to find the melting temperature of intermediate compositions would be required in order to accurately map the melting temperature of the entire system.

The melt formation temperature is calculated for working points corresponding to each heat exchanger within the boiler. The spreadsheet uses the Na_2SO_4 – K_2SO_4 composition predicted by the correlations to identify which of the 11 curves the working point falls on or between, then the $Fe_2(SO_4)_3$ component is used to identify where on those curves the working point is. For values between curves, linear interpolation is used to identify the melt formation temperature; this linear interpolation along non-linear curves is considered a small concession given the scope of the assumptions that have been made regarding the shape of the ‘melting temperature map’. Given the small amount of data available regarding this system, the assumptions made in order to provide this solution are deemed acceptable until its is surpassed by experimental data.

8.3.1.7e Assessing Tube Surface Temperatures

Finally, in order to predict the deposit composition and to make the final assessment as to whether a sulphate melt is formed, the spreadsheet must calculate the tube surface temperatures for each of the heat exchangers. A simple heat transfer model is used to do this based upon the enthalpy change of the steam as it passes through the heat exchanger. To perform this calculation the spreadsheet must take account of the thermal conductivity, k, of the steel used for the heat exchanger tubes. Unfortunately, k varies with steel temperature and since the surface temperature is not known, cannot be easily assessed. To cope with this, the spreadsheet initially assumes a high surface temperature of 1000°C, far in excess of the normal heat exchanger steel operating temperature to obtain an initial *k* value. Using this initial *k* value, a new surface temperature is calculated and hence, a new *k* value. This process is iterated for five steps to narrow down to the correct values. Whilst this process may not hone down to the correct value, it is considered to be better than assuming a constant value of *k* for the material regardless of the temperature.

In order to calculate *k* across arrange of temperatures, the variation of *k* as a function of temperature has been plotted for four different steels commonly used in heat exchanger applications. The equations of these relationships have been embedded in the spreadsheet for use in the calculation. The choice of steels to include was based upon recommendations in *Modern Powerstation Practice, Volume E: Chemistry and Metallurgy* by Akturk [27]. Akturk identified a carbon steel, two chromium molybdenum alloy steels and several austenitic and ferritic stainless steels. The values for the stainless steels were very similar and therefore, a mean *k* curve was calculated for stainless steel and used to represent all stainless steels. Although this would introduce slight errors into the calculation of the steel surface temperatures it was thought that these would be outweighed by those introduced by other, more profound, assumptions within the model.

8.3.1.8 Summary

In order to fulfil the remit for the development of the prediction tool several modelling assumptions and compromises have been made. Additive behaviour of fuel properties has been assumed for the combination of parent and substitute fuels when calculating blends. The only model that this really compromises is the calculation of the temperature – enthalpy profile because the individual behaviour of the parent and substitute fuels cannot be modelled. However, given the basic nature of the combustion model, this compromise is not of great concern. In addition, the assumption of additive behaviour of ash species is beneficial because the ash from each fuel stream becomes 'intimately mixed'. This means that when applying the slagging and fouling and high temperature corrosion models, reactions between ash particles from the different fuels can be considered. The one dimensional nature of the boiler model does not facilitate the prediction of flow fields within the boiler and, as such, particle trajectories and sticking probabilities cannot be calculated, meaning that deposit build-up cannot be predicted. Instead, the model considers the level of molten and gaseous species in the combustion products and, comparing them against pre-set thresholds, assesses the potential for slagging and fouling problems. A similar approach is used for the high temperature corrosion model whereby the composition of the predicted depositing species is used to assess whether a 'sulphate melt' will be formed, providing a medium for increased corrosion rates.

8.3.2 Comparison of the Predictions Made for Different Fuels and Boilers

Using the ANN version of the spreadsheet, it has been possible to make predictions for two different boilers with three different substitute fuels. Whilst industrial data with which to compare these predictions is scarce, it is possible to compare results between fuel types and boiler types to see whether they agree with what is expected from the literature. Two industrial boilers have been modelled using the spreadsheet; the 618MW$_{th}$ Langerlo boiler run by Laborelec and the 1316MW$_{th}$ Cottham boiler run by EDF. Table 8.5 shows some of the operational data for the boilers.

Table 8.5: Operational data for the Langerlo and Cottham boilers

Name	Langerlo	Cottham
Type	PF Wall fired	PF Wall fired
Thermal Input (MW)	618	1316
Electrical output (MW)	235	500
Plant Efficiency (%)	38.0	37.9
Steam Raised (kg/s)	700,000	1,540,000
Burner Configuration	4 rows of 4 burners	4 rows of 8 burners
Primary Air Share / Mass Flow-rate (% / kg/h)	13 / 139,000	14.4 / 264,000
Secondary Air Share /Mass Flow-rate (% / kg/h)	72 / 768,000	85 / 1,495,000
Over-fire Air Share / Mass-flow-rate (% / kg/h)	15 / 160,000	0 / 0
Excess Air (O_2 in Flue Gas) (%)	3.6	3.2

8.3.2.1 The Langerlo Boiler

The Langerlo boiler is a 618MW$_{th}$ wall fired pulverised coal-fired boiler run by the Belgian utility company Laborelec.

Table 8.6: Fuels used to assess spreadsheet performance

Fuel	Coal	Sewage Sludge	Sawdust	RDF
		Proximate Analysis		
Fixed Carbon (%)	52.64	4.50	9.40	13.70
Volatile Matter (%)	37.33	46.17	55.00	72.70
Ash Content (%)	5.74	37.61	0.70	8.90
Moisture Content (%)	4.29	11.72	34.90	4.70
Total (%)	100.00	100.00	100.00	100.00
LCV (MJ/kg)	28.617	10.241	10.935	16.558
		Ultimate Analysis		
Carbon (%)	69.93	24.05	32.07	41.76
Hydrogen (%)	4.94	3.55	3.90	6.49
Oxygen (%)	12.85	18.97	28.16	37.50
Nitrogen (%)	1.53	3.34	0.26	0.61
Sulphur (%)	0.72	0.76	0.01	0.04
Ash (%)	5.74	37.61	0.70	8.90
Moisture (%)	4.29	11.72	34.90	4.70
Total (%)	100.00	100.00	100.00	100.00
		Ash Composition		
Na_2O (%)	0.79	0.60	2.54	2.00
K_2O (%)	1.33	1.71	10.80	1.90
CaO (%)	3.28	7.58	44.10	22.90
Al_2O_3 (%)	20.62	12.17	4.52	23.70
MgO (%)	1.87	1.79	5.29	2.70
Fe_2O_3 (%)	8.33	14.23	1.76	2.30
SiO_2 (%)	58.60	56.02	26.13	39.80
SO_3 (%)	3.53	2.09	2.09	1.60
Mn_3O_4 (%)	0.16	0.22	-	-
TiO_2 (%)	1.03	0.68	0.44	2.10
P_2O_5 (%)	0.44	2.57	2.32	1.00
ZnO (%)	-	0.31	-	-
Li_2O (%)	0.02	0.03	-	-
Total (%)	100.00	100.00	100.00	100.00

All of the necessary boiler data required to set up the spreadsheet has been made available by Laborelec, including the results of a CFD simulation carried out on the boiler. Figures 8.22 and 8.23 show the results of a pure coal simulation and simulations with $10\%_{th}$ substitution of sewage sludge, sawdust and RDF respectively. Figure 8.22 also features the results of the CFD simulation for the boiler. The sawdust and RDF fuels used for these simulations are those used to generate the training data for the slagging and fouling ANN, whilst the coal and sewage sludge used are the Colombian coal and Belgian sewage sludge characterised in [100]. These fuels are shown in Table 8.6.

8.3.2.1a Temperature Profile Predictions for the Langerlo Boiler

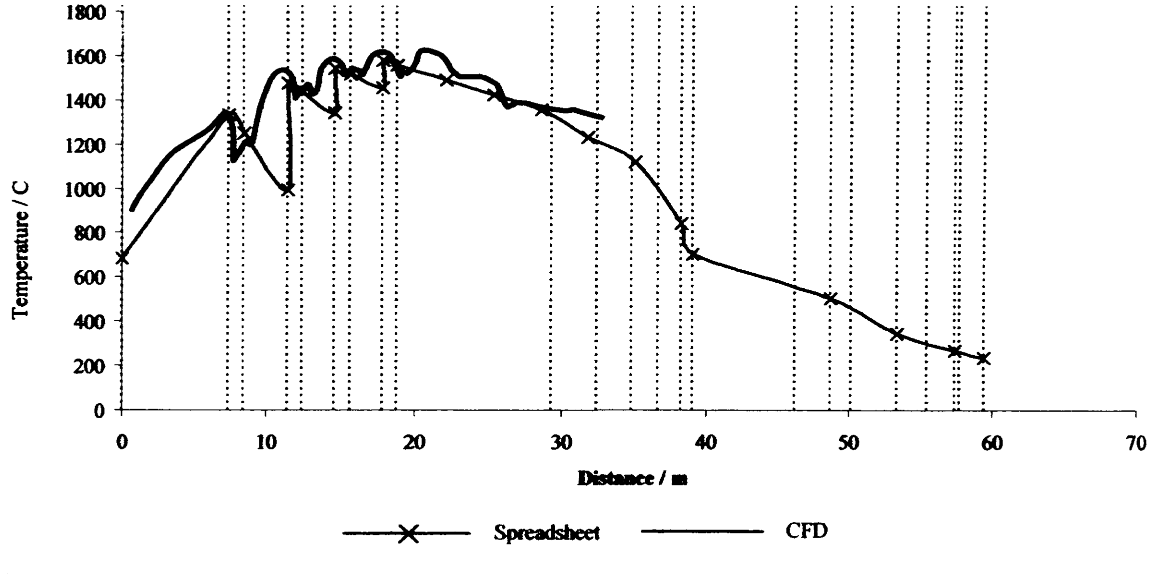

Figure 8.22: Comparison of the temperature profile prediction by spreadsheet to the CFD model for pure coal for the Langerlo boiler

Figure 8.22 shows that the temperature profile for a pure coal flame, as predicted by the spreadsheet, agrees quite well with that predicted by CFD. It is important to note that the coal used for the CFD simulation was not the same as that used in the spreadsheet, however, all other settings would have been the same or similar. The two profiles share a similar shape and the temperature peaks at the burner rows can clearly be seen on each. The temperature magnitude at each peak is under predicted by approximately 40°C by the spreadsheet. This equates to an error of between 2 and 5% which is reasonable given the differences between the models and the relative simplicity of the spreadsheet compared to a CFD simulation. The CFD profile identifies two additional peaks after the burner rows; these correspond to over-fire air, unfortunately, the spreadsheet is not able to model this and therefore, has missed them. The furnace exit gas temperature (FEGT) predicted by the spreadsheet is approximately 1250°C whilst that for the CFD model is approximately 1300°C. The literature recommends that FEGT is kept between 1100 and 1400°C, so these results are acceptable for both simulations [28].

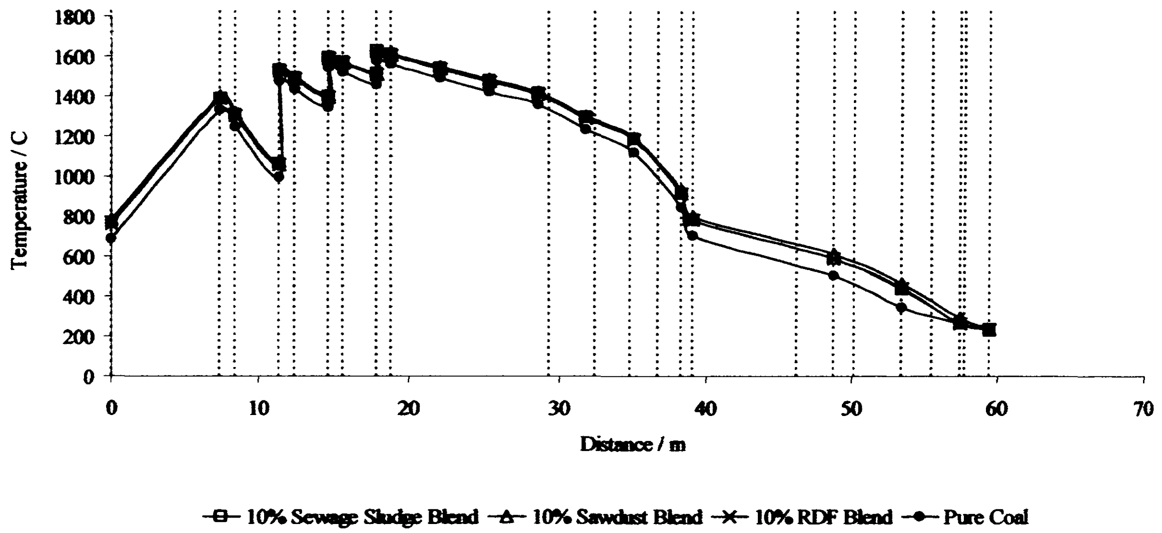

Figure 8.23: Temperature profile comparison for 10%$_{th}$ blends of sewage sludge sawdust and RDF for the Langerlo boiler

Figure 8.23 shows that for blends of 10%$_{th}$ sewage sludge, sawdust and RDF, the peak predicted temperature within the furnace, observed at the uppermost burner row is some 51°C, 52°C and 44°C higher than pure coal respectively. This is due to the fuel blends having higher adiabatic flame temperatures than pure coal; these were 36°C, 32°C and 28°C higher for sewage sludge, sawdust and RDF respectively. This is in accordance with what is expected from the literature [5, 7, 12, 13], which suggests that the rapid release and combustion of volatiles can increase the rate at which the fuels energy is released resulting in higher flame temperatures. This can lead to FEGT increasing by up to 100°C [12].

In addition to this, due to the higher LCV of the pure coal, the fuel mass flow-rate needed to fulfil the thermal input requirement of 618MW$_{th}$ was lower, resulting in a lower throughput of flue gases compared to the blended fuel. The fuel blends had mass flow-rates 1.32, 4.03 and 2.40 kg/s higher than pure coal for sewage sludge, sawdust and RDF respectively. This means that the enthalpy change induced by the heat exchangers as the gases pass through them is less severe in the case of the fuel blends than for the pure coal flame. This would also explain the higher temperatures observed in the convective section of the boiler for the blended fuels. Again, this is in line with what is expected from the literature with lower carbon contents and higher oxygen contents meaning that the blended fuel requires less combustion air to achieve burnout.

It should be noted that for the pure coal, sewage sludge and RDF predictions, the target temperatures were not met in the economisers (i.e. flue gas temperature fell below the water temperature within them). In the sawdust prediction, only economiser 1 failed to reach its target temperature. This can be explained by discrepancies between the fuels used to make the predictions and those being used when the steam cycle data was taken. Also this could be caused by a discrepancy between the assumed and actual efficiencies of the heat transfer process within the boiler. This problem highlights the need to combine the temperature profile calculation with the steam cycle calculations.

8.3.2.1b Species predictions for the Langerlo boiler

Figures 8.24 to 8.26 show the variation of predicted potassium sodium and iron in the molten phase for pure coal and 10%$_{th}$ blends of sewage sludge, sawdust and RDF. Table 8.7 summarises the mass of each of these elements introduced to the furnace per second. It should be noted that the values plotted in figures 8.24 to 8.26 show total mass of species containing molten sodium, potassium and iron per kg of fuel, and therefore, it is possible that these values can exceed those shown in table 8.7, which shows the elemental mass of these species introduced to the boiler per second.

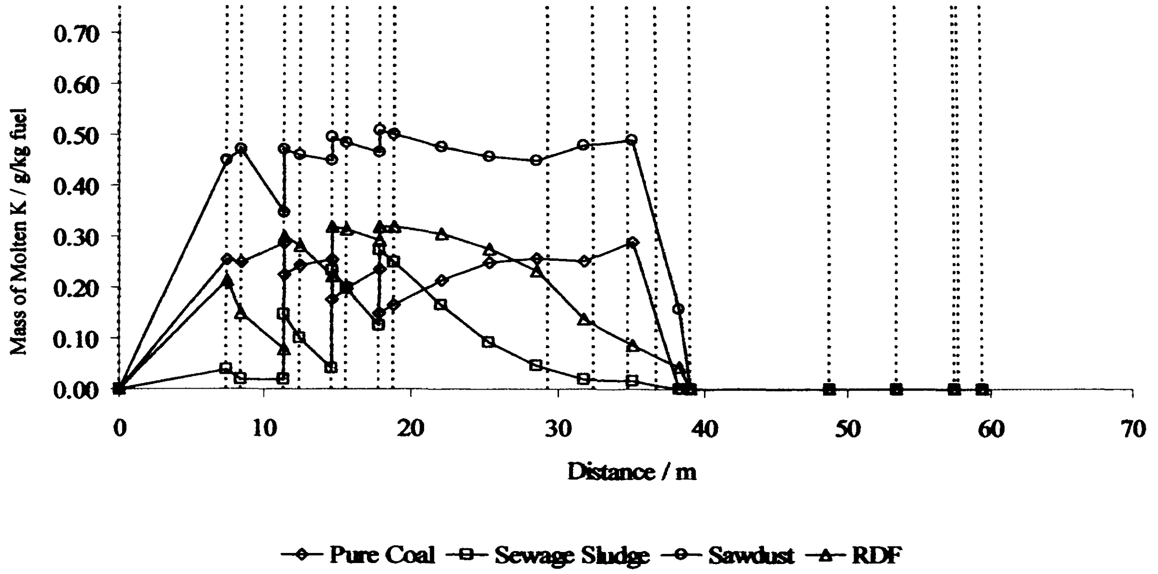

Figure 8.24: Comparison of predictions of molten K in the combustion products for pure coal and 10%$_{th}$ blends of sewage sludge, sawdust and RDF for the Langerlo boiler

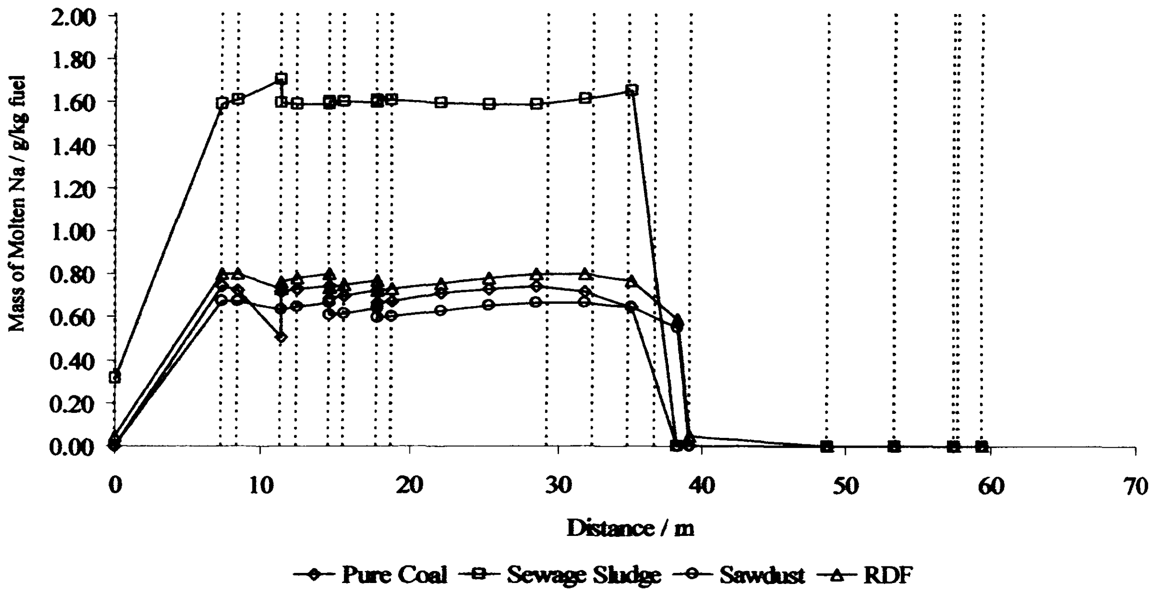

Figure 8.25: Comparison of predictions of molten Na in the combustion products for pure coal and 10%$_{th}$ blends of sewage sludge, sawdust and RDF for the Langerlo boiler

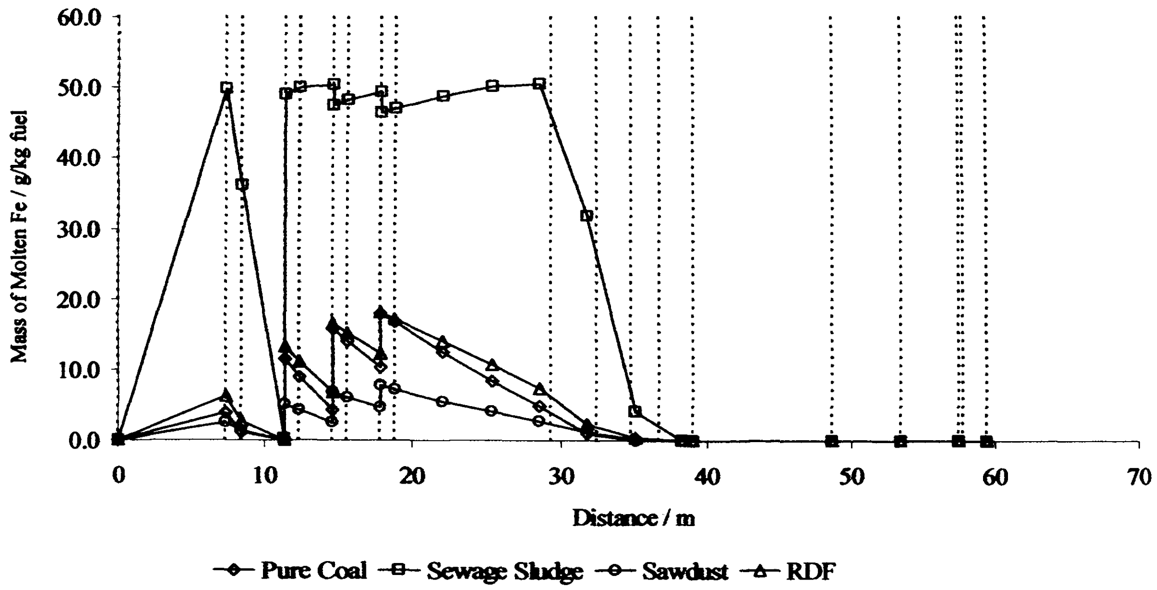

Figure 8.26: Comparison of predictions of molten Fe in the combustion products for pure coal and 10%$_{th}$ blends of sewage sludge, sawdust and RDF for the Langerlo boiler

Table 8.7: Rate of introduction of deposit forming elements into the Langerlo boiler

Fuel	Mass of Elemental Na / g/s	Mass of Elemental K / g/s	Mass of Elemental Fe / g/s
Pure Coal	7.20	13.57	71.68
10%$_{th}$ Sewage Sludge - 90%$_{th}$ Coal	18.12	39.89	230.60
10%$_{th}$ Sawdust - 90%$_{th}$ Coal	9.78	33.14	55.34
10%$_{th}$ RDF - 90%$_{th}$ Coal	10.25	17.10	74.61

The sawdust blend sees the highest predicted levels of K in the molten phase throughout the entire boiler, this is acceptable as it has the second highest rate of potassium introduction into the boiler behind sewage sludge. It is possible that this has occurred because of the unusually high levels of Ca in the sawdust ash (44%) reacting to form compounds with Si and Al which would otherwise react to form solid potassium alumino-silicates. This leaves more of the potassium free to form less stable compounds in the molten and vapour phases. The fact that the sewage sludge blend has the highest potassium input to the boiler yet the lowest levels of potassium in the molten phase suggests that there is a reaction taking place within the sewage sludge ash which is locking the potassium into the solid phase. This is possibly caused by the high levels of silicon and aluminium in the sewage sludge ash forming K-Al-Si compounds in the solid phase. This phenomenon was observed by Andersen [67] when co-firing straw.

Figure 8.25 demonstrates that the sewage sludge blend sees the highest predicted levels of Na in the molten phase, with the other blends and pure coal exhibiting levels of about 50% of this. This is in line with what was expected from table 8.7, since the sewage sludge blend introduces approximately double the elemental sodium into the boiler compared to the other fuels. All of the fuels exhibit an almost constant level of sodium in the molten phase throughout the boiler suggesting that it forms a relatively stable compound which is not affected by temperature.

As with sodium content, the mass of iron species found in the molten phase is proportional to the mass introduced by the fuel ash. Figure 8.26 shows that the mass of iron in the molten phase for sewage sludge is far in excess of that of the other fuels. This is in line with the data in table 8.7, which shows that the mass of iron introduced by the sewage sludge blend is more than three times that of pure coal and RDF and more than four times that of sawdust. The figure also shows that RDF and pure coal exhibit very similar levels of molten iron throughout the boiler. This was expected as they introduce almost exactly the same mass of iron into the boiler in their ash. The sawdust, with the lowest iron levels in the molten phase and the lowest rate of iron introduction to the boiler reinforces the proposed proportionality.

8.3.2.2 The Cottham Bolier

The Cottham boiler is a 1316MW$_{th}$ wall fired pulverised coal-fired boiler run by the French utility company EDF. All of the necessary data required to set up the spreadsheet has been made available by EDF, including the results of a sawdust co-firing combustion trial carried out at the plant in 2005. Figures 8.27 and 8.28 show the results of a pure coal simulation and simulations with 10%$_{th}$ substitution of sewage sludge, sawdust and RDF respectively. Figure 8.27 also features the design flue gas temperatures for the radiant superheaters and convective section. The fuels used in these simulations are the same as those used for the Langerlo simulations and are shown in Table 8.6.

8.3.2.2a Temperature Profile Predictions for the Cottham Boiler

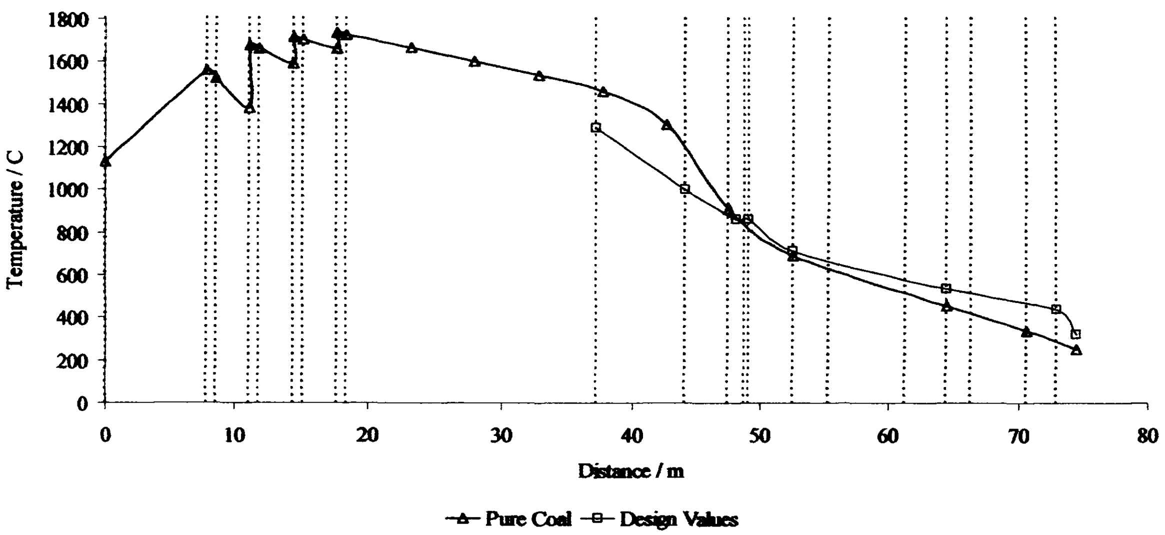

Figure 8.27: Comparison of the predicted temperature profile from the spreadsheet to boiler design values for the Cottham boiler

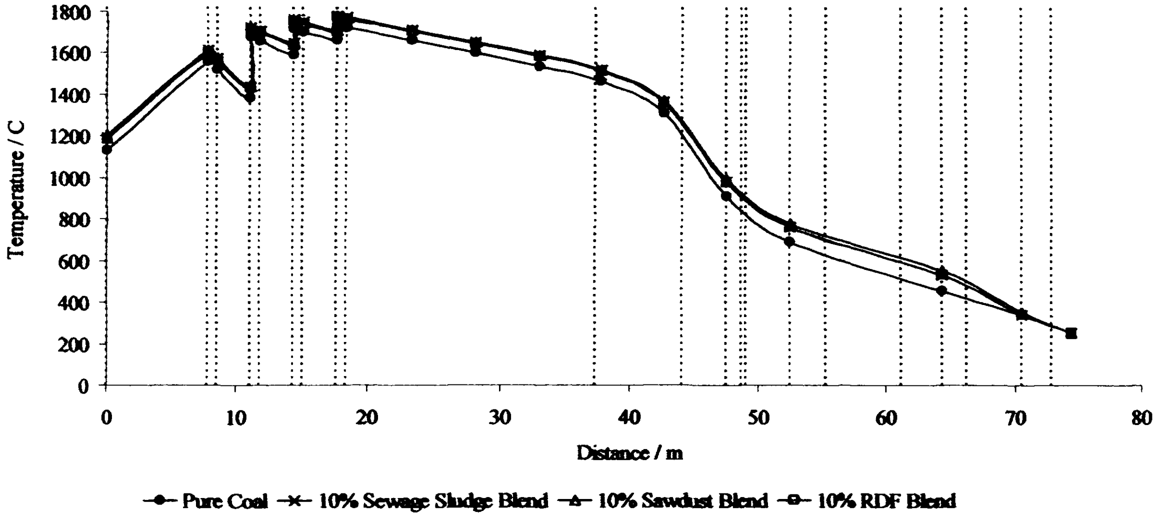

Figure 8.28: Temperature profile comparison for 10%$_{th}$ blends of sewage sludge sawdust and RDF for the Cottham boiler

Figure 8.27 shows a comparison between predictions made using the spreadsheet for pure coal and the recommended design operating temperatures for the boiler. The FEGT has been over predicted by almost 200°C by the spreadsheet, and at around 1450°C, exceeds the recommended FEGT from the literature by 50°C [28]. This over prediction can be attributed the way in which heat transfer is modelled in the waterwalls. The heat transfer model assumes uniform heat transfer along the entire length of the waterwalls, however, in reality this is not the case. A heat transfer profile such as that suggested by Bott [30] is more realistic; here, heat transfer is higher in the burner zone where flame temperatures are higher and steam temperatures are lower and lower in the upper region of the boiler where gas temperatures are lower and steam temperatures are higher. This means that, in reality, the proportion of the total heat energy removed by the waterwalls from the combustion gases by the time they reach the furnace exit is higher than that predicted by the spreadsheet, resulting a lower FEGT.

The profile also suggests that there is significant heat transfer between 35m and 50m, which is not evident in the design flue gas temperatures. This again can be attributed to the simplification of the heat transfer profile for the waterwalls, here, in the top of the boiler, the heat transfer by the waterwalls is over predicted. This, combined with heat transfer from the platen superheater produced the sharp down-turn it flue gas temperatures displayed by the spreadsheet between 40m and 50m.

Figure 8.28 shows that for blends of sewage sludge, sawdust and RDF, the peak temperature has risen above that of the pure coal simulation by 28°C, 25°C and 19°C respectively. This is due to the increase in volatile matter in the fuel that was noted in the simulations for the Langerlo plant. Peak temperatures are on average 136°C higher than those predicted during the Langerlo simulations. This can be attributed to two things; firstly due to the lower equivalence ratio used at Cottham ($\lambda = 1.18$ compared to 1.21 at Langerlo), the adiabatic flame temperature predicted by the temperature – enthalpy relationship has risen by an average of 25.1°C. In addition to this, the proportion of heat energy removed by the waterwalls is lower for the Cottham plant at 35% of the total thermal input compared to 40% at Langerlo. This means that the enthalpy change of the flue gases in the combustion chamber at Cottham is lower than at Langerlo, producing the higher peak temperatures.

8.3.2.2b Steel Surface Temperature Predictions for the Cottham Boiler

Table 8.8 shows the recommended maximum temperature limits for 100,000 hour of operation for the heat exchanger tubes in the Cottham boiler compared to the tube temperatures predicted by the spreadsheet during the pure coal simulation.

Table 8.8: Comparison of recommended heat exchanger surface temperatures to those predicted by the spreadsheet

Heat Exchanger	Maximum recommended working temperature for 100,000h service / °C	Tube surface temperature predicted by the spreadsheet / °C
Platen Superheater	646	506
Final Superheater	561	572
Final Reheater	625	569
Convective Reheater	572	522
Convective Superheater	431	415
Economiser	371	296

Whilst there is no provision in the spreadsheet for the user to enter and compare these values, they are worth noting because it shows that the spreadsheet is able to predict the tube surface temperatures to some degree of accuracy. A comparison of this type could be incorporated into the spreadsheet in the future. The high operating temperatures in the platen superheater and final reheater are afforded by the use of Esshete 1250 steel, a specialist steel offering excellent high temperature creep resistance. This steel has not been included in the corrosion model of the spreadsheet however, it is in common use in modern powerstations and should be included in future revisions of the model.

8.3.2.2c Species Predictions for the Cottham Boiler

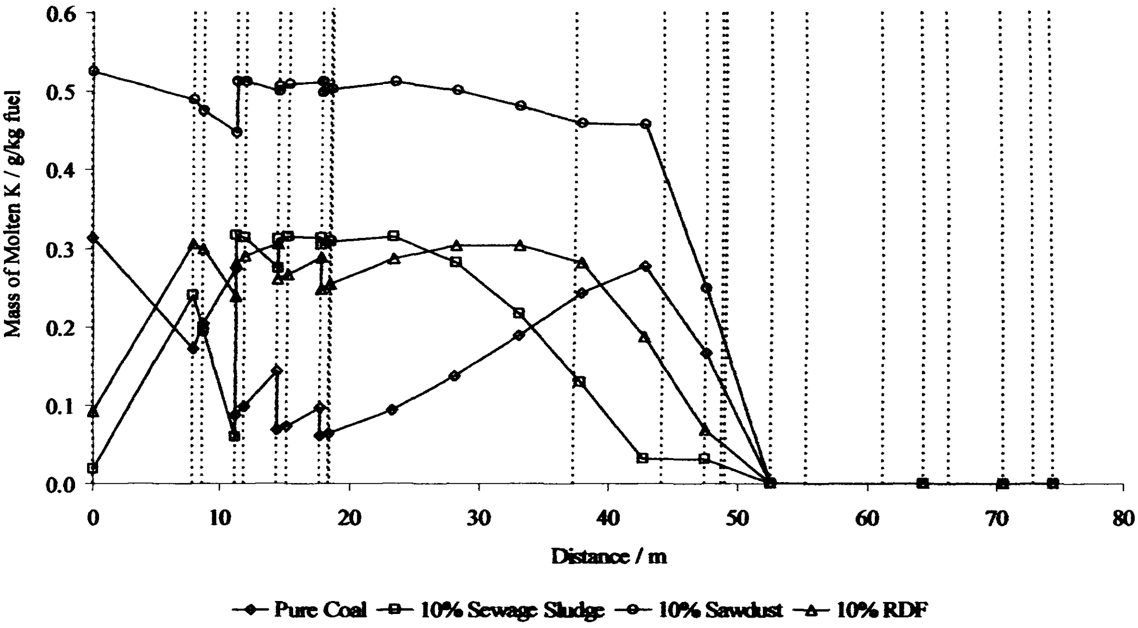

Figure 8.29: Comparison of Predictions of molten K in the combustion products for pure coal and 10%$_{th}$ blends of sewage sludge, sawdust and RDF for the Cottham boiler

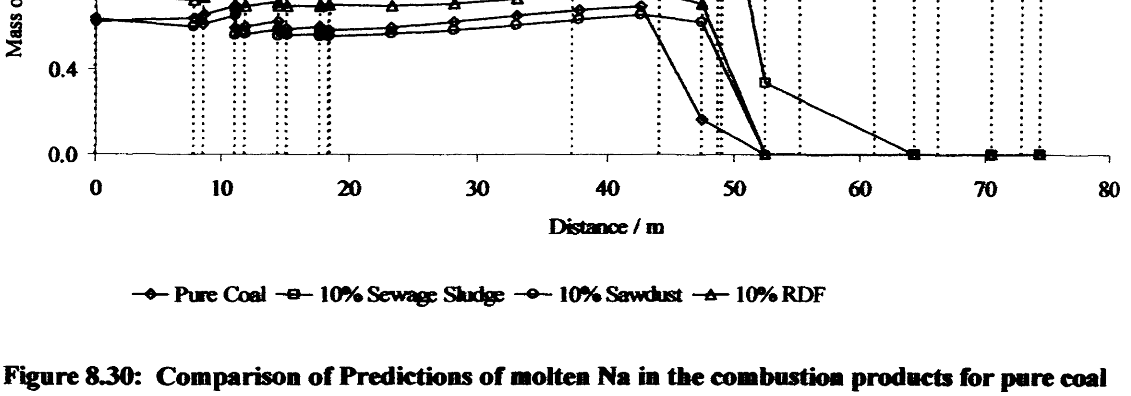

Figure 8.30: Comparison of Predictions of molten Na in the combustion products for pure coal and 10%$_{th}$ blends of sewage sludge, sawdust and RDF for the Cottham boiler

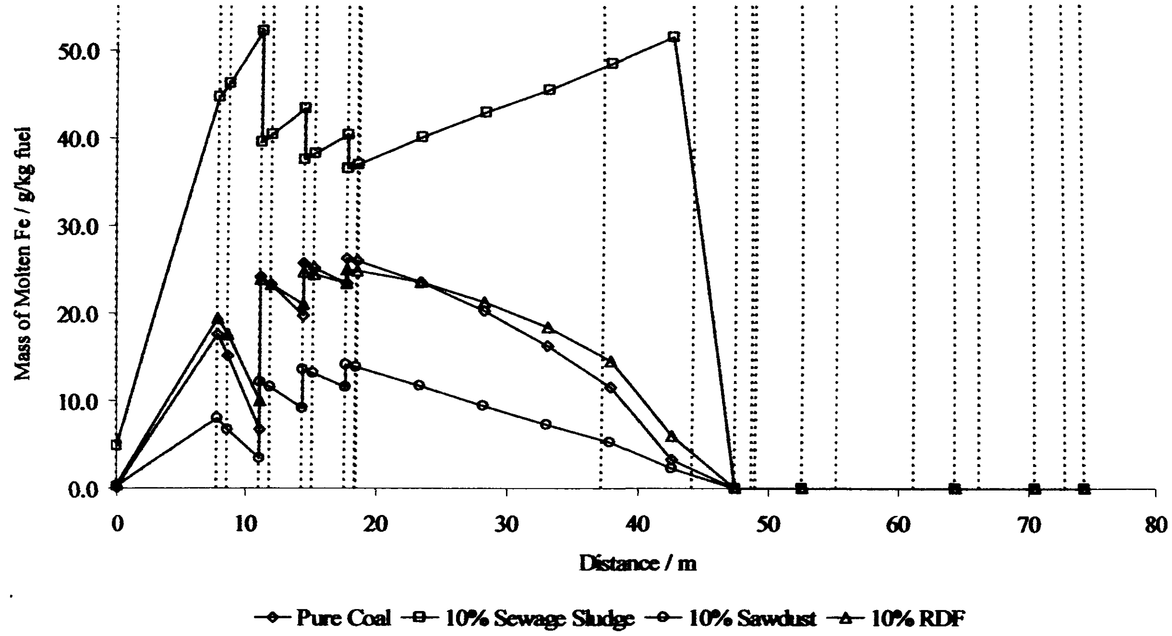

Figure 8.31: Comparison of Predictions of molten Fe in the combustion products for pure coal and 10%$_{th}$ blends of sewage sludge, sawdust and RDF for the Cottham boiler

Table 8.9: Rate of introduction of deposit forming elements into the Cottham boiler

Fuel	Mass of Elemental Na / g/s	Mass of Elemental K / g/s	Mass of Elemental Fe / g/s
Pure Coal	14.86	28.89	152.62
10%$_{th}$ Sewage Sludge - 90%$_{th}$ Coal	38.64	84.70	489.68
10%$_{th}$ Sawdust - 90%$_{th}$ Coal	20.77	70.37	117.52
10%$_{th}$ RDF - 90%$_{th}$ Coal	21.77	36.31	158.44

Figures 8.29 to 8.31 and table 8.9 show that the ash prediction for the Cottham boiler has yielded very similar results to those for the Langerlo boiler. Since the explanations for the Langerlo findings were all model or fuel related, they also stand for these findings. The slight differences in the shape of the prediction curves can be attributed to the higher temperatures in the furnace exit gas for the Cottham plant.

8.3.3 Comparisons between Prediction Results for Langerlo and Cottham

As has been mentioned above, the prediction of molten alkali and iron species for the Langerlo and Cottham boilers was largely similar. This is in line with what was expected given that the same fuels were used for the predictions and both boilers are of a similar type. The main difference between the predictions for the two boilers was the temperature profile, however, this has already been satisfactorily explained by short comings in the assumed heat transfer model for the waterwalls and the differing proportions of heat removed in the various heat exchangers between boilers.

Table 8.10 shows a comparison of the warning flags raised by the predictor when the $10\%_{th}$ sewage sludge is used. For reasons discussed earlier, the warning flags are not valid for substitute fuels other than sewage sludge.

Table 8.10: Comparison of warning flag predictions between the Langerlo and Cottham boilers

Heat Exchanger	Langerlo		Cottham	
	Sodium Level	Potassium Level	Sodium Level	Potassium Level
Superheater 2 / Platen Superheater	High	Low	High	Low
Superheater 3 / Final Superheater	High	Low	High	Low
Reheater 2 / Final Reheater	Low	Low	Medium	Low
Superheater 1 / Convective Superheater	Low	Low	Low	Low
Reheater 1 / Convective Reheater	Low	Low	Low	Low
	Phosphorous Level		Phosphorous Level	
Economser 1 / Economiser	Low		Low	
Economiser 2 / n/a	Low		n/a	
	Iron Level		Iron Level	
Superheater 3 / Final Superheater	High		High	
Reheater 2 / Final Reheater	Low		Low	
Superheater 1 / Convective Superheater	Low		Low	
Reheater 1 / Convective Reheater	Low		Low	

With the exception of the reheater 2 / final reheater predictions, the warning flags predict the same levels of sodium, potassium, phosphorous and iron throughout each boiler. The discrepancy between reheater 2 of the Langerlo boiler and final reheater of Cottham can be explained by a difference in temperature between them (Cottham is 63°C higher) leading to higher predicted levels of Na in Cottham (Ref: figures 8.25 and 8.23).

8.3.3.1 Summary of Comparisons

Overall the similarity between the results generated for the two boilers, which have similar configurations yet greatly different outputs, highlights the consistency of predictions made by the spreadsheet. This is reinforced by the warning flags shown in table 8.10. This similarity also demonstrates the versatility of the models, since the predictions were produced for both boilers with no alterations to the model setup within the spreadsheet, i.e. fuel and boiler details were the only changes made.

8.3.4 Comparison of Predictions to Results from Industry / Academia

Examples from industry / academia have been used to try to validate or reinforce the predictions made and models used within the spreadsheet. Unfortunately, information regarding full-scale industrial co-firing tests is scarce and, as a result, only general observations or comparisons can be made.

8.3.4.1 The Cardiff 2-Stage Combustor

When calculating the correlations and the ANN training data, the FACT SLAG-A model was used in FactSage to predict the composition of species in the molten (slag) phase. To try to validate this model choice, the FactSage software was used to simulate the slag formed in the Cardiff 2-stage twin-cyclone combustor. A 10%$_{th}$ blend of Belgian sewage sludge with Colombian coal, fired as part of research carried out for the PowerFlam project by Abd-Rahmann [94], was modelled. The two-stage combustor is designed to reproduce the slag types found in various parts of a full size boiler. Slag samples 1, 2 and 3 in figure 8.32 were taken from the primary chamber of the two stage reactor and are thought to represent the ash formed in the reducing conditions in the near burner region (known as burner 'eyebrows'). Sample 5 in figure 8.33 was taken from the floor of the second chamber of the combustor and is thought to be representative of slag found on the waterwalls of full scale boilers. Samples 8 and 9 in figure 8.34 were taken from the top of the second camber and the ash pot respectively. These are thought to represent deposits found in the convective superheaters and the economiser region of full-scale boilers. Figures 8.32 to 8.34 show the results of this validation exercise:

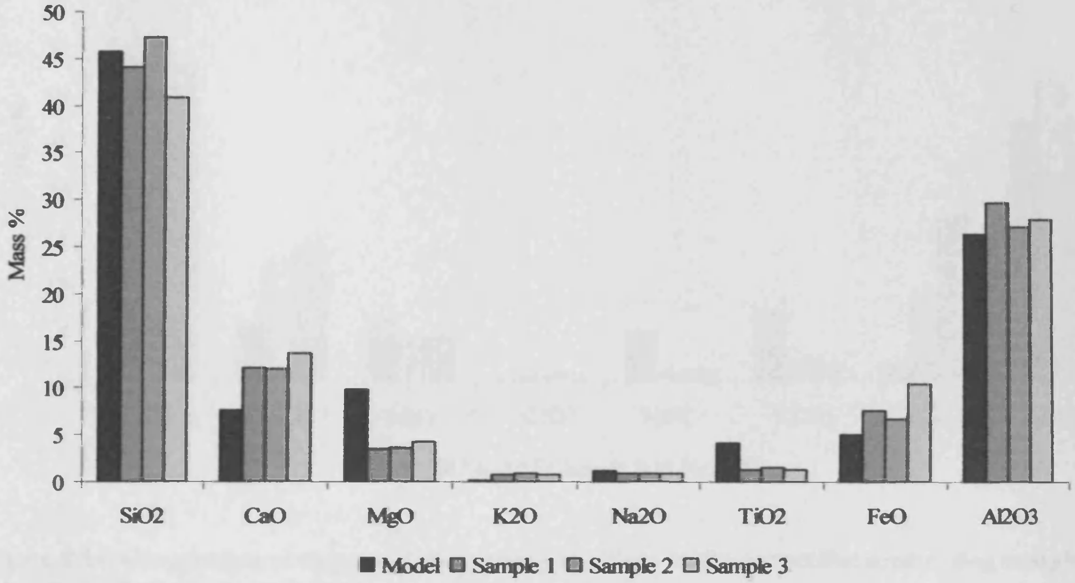

Figure 8.32: Comparison of slag predictions using FactSage to the near burner slag samples taken from the 2-stage combustor

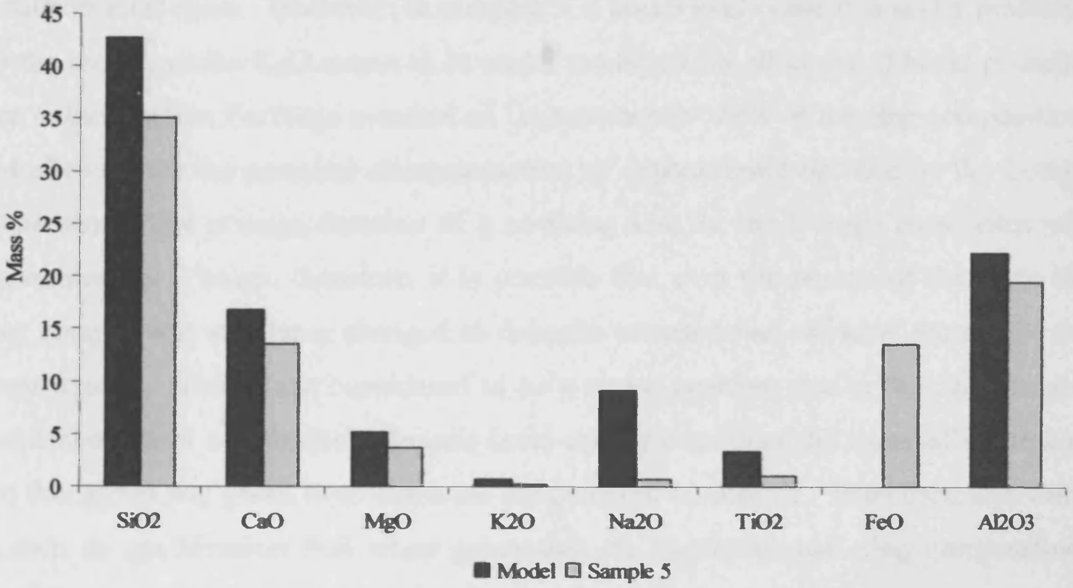

Figure 8.33: Comparison of slag predictions using FactSage to the waterwall slag samples taken from the 2-stage combustor

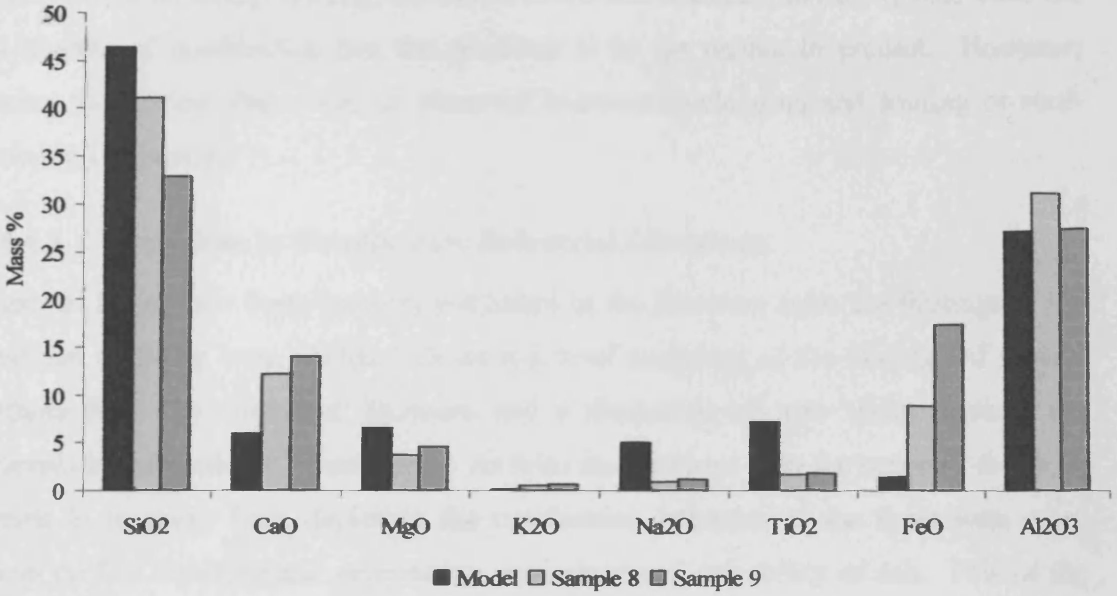

Figure 8.34: Comparison of slag predictions using FactSage to the convective section slag samples taken from the 2-stage combustor

The figures show reasonable agreement between the predictions and the experimental results in most cases. However, in samples 5, 8 and 9 FeO content is under predicted by the model, whilst K_2O seems to be under predicted for all cases. This is probably due to the fact that FactSage presents an 'instantaneous' view of the slag composition, not allowing for the potential changes caused by deposit build-up seen by the 2-stage combustor. The average duration of a co-firing test for the 2-stage combustor was approximately 2 hours, therefore, it is possible that over the course of this time the slag composition may have changed as deposits accumulated, skewing the results for some species. This is not considered to be a major problem due to the fact that the spreadsheet does not simulate deposit build-up but considers the mass of species in the flue gas at any given time that have the potential to deposit. Therefore, this work is seen as confirmation that when generating an 'instantaneous' slag composition, FactSage is predicting that the correct proportion of fuel ash elements are entering the molten phase.

8.3.4.2 Co-firing Tests in the Cottham Boiler

During 2005 EDF conducted a series of co-firing tests using the Cottham boiler featured in the spreadsheet predictions [101]. Tests were carried out using blends of 2.5%$_{th}$ and 5%$_{th}$ wood pellets (rather than sawdust). Unfortunately, the focus of the work was on handling, milling, emissions levels and marketability of fly ash; these are all aspects of combustion that the predictor is so far unable to predict. However, during the testing, there was no observed increase in slagging and fouling or soot-blowing frequency.

8.3.4.3 Comparison to Results from Industrial Literature

Many of the reports from industry published in the literature echo the findings of the Cottham co-firing tests. What follows is a brief summary of the findings of several authors from the published literature and a discussion of how these findings are relevant to the predictor spreadsheet. As with the Cottham tests the scope of the work seems to be away from depicting the combustion behavior of the fuels with more focus on fuel handling and preparation, emissions and saleability of ash. Few of the authors reported problems with biomass substitutions of up to $5\%_{th}$, however, some reported that alterations to furnace settings were necessary to achieve satisfactory running. Struckmann et al [102] report that when co-firing sewage sludge, initial blends of 2 – $3\%_{th}$ were causing severe fouling problems due to reduction reactions involving P_2O_5 in the near burner region. This frees up phosphorous, allowing it to enter the gas phase where it acts as a bonding agent promoting the adhesion of particles to heat transfer surfaces. By increasing the ratio of transport air during co-firing tests, this problem was eliminated and successful operation with $5\%_{th}$ sewage sludge was observed [102].

Gilberg [103] reports that a $3.5\%_{th}$ substitution of sewage sludge has been successfully observed in the 474MW lignite-fired Zolling power station. Difficulties experienced in the pulverisers forced the reduction of the initial $5\%_{th}$ blend to $3.5\%_{th}$ where satisfactory operation was observed. Wierick et al [104] have observed successful operation of the 500MW Boxberg lignite-fired powerstation whilst using a $5\%_{th}$ substitution of sewage sludge, reporting no deposition or corrosion problems, however, fuel feed problems were experienced. Buck and Triebel [105] have experienced similar problems in the 730MW Heilbronn power station, where a $4\%_{th}$ substitution of sewage sludge was used with no slagging, fouling or corrosion problems, however, severe problems were encountered in the fuel feeds, mainly caused by excessive water contents with in the sewage sludge.

The ability to sustain higher substitution ratios seems feasible when utilizing straw as a secondary fuel. Dietl and Schmidt [106] report that a 10%$_{th}$ substitution of straw has been successfully fired in the 516MW lignite-fired Schwandorf power station. An increase in the flue gas temperature was obsereved along with a higher propensity towards slagging on the waterwalls. However, due to the periodic nature (weekend shutdowns) of the boiler, thermal shock caused the self cleaning of the additional slag and therefore, no significant problems were reported. Problems were again reported in the fuel supply and pulverizing system, where grain sizes increased as a result of the straw addition, raising the unburned carbon in the ash from 4% to 8%, affecting its saleability. These findings are supported by the work of Andersen et al [68] who report on trials where up to 20%$_{th}$ straw has been fired in the 150MW$_e$ Midtkraft power station. They noted significant increases in the degree and tenacity of fouling deposits in the combustion chamber and platen superheaters. A thick layer of sintered deposit was observed where, under normal conditions, a thin layer with small nodes is seen. However, in the convective section of the boiler, there was no change in deposit structure.

These findings seem to support the supposition made when setting the warning flags in the spreadsheet that boilers can operate, relatively unaffected by slagging and fouling, at substitutions of up to 5%$_{th}$ biomass. In almost all of the full-scale tests the limiting factor in the level of biomass that could be successfully fired was found to be the fuel supply system of the mills/pulverizers. These findings perhaps highlight the focus for further development of the spreadsheet, allowing the user to identify potential fuel feed and pulverization problems associated with the biomass fuel of choice.

8.3.5 Summary

In order to fulfil the remit for the development of the prediction tool, modelling compromises have had to be made. In order to keep the tool simple, quick and easy to use, simplified combustion and chemistry models have been employed. In addition to this, the expectations of the kind of result the tool would produce have been revised; instead of predictions of the quantity and composition of the deposits formed, a more qualitative result has been produced; rather than try to simulate potential problems, the tool indicates to the user that the combustion settings or the chemistry of the combustion products pose a risk of problems occurring in certain areas of the boiler. Despite displaying better accuracy in some of their predictions, the empirical correlation methods used in the development of the tool can be seen as an intermediate step to assess how well the models would work prior to developing the more comprehensive ANN models. The ANN models demonstrate the feasibility of using this method to address the problem of predicting the complex combustion chemistry seen in a PF boiler. However, in order to be more useful, the ANNs either need to become very large to accommodate all of the potential coal and substitute fuel combinations or, more focused with the development of several ANNs each focusing on a single substitute fuel, much like the empirical correlations. By doing this, a more focused set of training data can be used providing a greater number of interpolation points per substitute fuel. This would help to improve the accuracy of the predictions made by the ANN.

The results of predictions for two different boilers, firing three different substitute fuels made using the model compare well to one another and with what was predicted by the literature. Consistency with the results achieved for the two different boilers, the theory suggested by the literature and the published results of industrial trials serve to underline the validity of the models used.

Chapter 9 - Conclusion

9.1 Introduction

The main focus of the research programme leading to the production of this thesis was to investigate the various modelling techniques used in industry and academia to assess the performance of combustion systems. The knowledge gained through this has been used to create a performance prediction tool capable of predicting the behaviour of blends of pulverised coal with biomass. A review of related literature was carried out and a number of potential modelling techniques were identified. An empirical prediction tool has been developed which processes fuel and boiler information using a number of derived correlations to predict temperature, deposition and high temperature corrosion problems. In parallel to this, computational fluid dynamics has been used to model a pilot scale furnace; this task has shed light on the problems faced when using this tool to simulate combustion systems. A number of conclusions can be made as a result of these tasks.

9.2 The Continued Use of Coal as a Fuel Source

- UK and European governments are committed, by the Kyoto Protocol, to reducing their CO_2 emissions to 8% below 1990 levels by the period 2008 – 2012. The UK government has taken on even more stringent targets, seeking to reduce CO_2 to 20% below 1990 levels by 2010.
- The power generation sector is one of the key areas in which these governments are seeking significant cuts.
- Coal has the highest CO_2 emission factor of all of the fossil fuels and therefore, the most significant CO_2 reductions have come about as a result of a reduction in the quantity of coal burnt.
- Recognising this, the UK government has sought to impose heavy taxes on the use of coal, driving up the price.
- This has forced power generators to seek alternative fuels as a way of keeping costs down.

- The fast depleting supplies of oil and gas have meant that rather than switch fuels, power generators must seek to reduce, or offset, the carbon emitted from coal firing.
- Co-firing of biomass fuels with coal is one way that many power generators are seeking to achieve this.

9.3 Pulverised Fuel Combustion and the Associated Problems

- The mechanisms of fuel ash deposition seen in pulverised fuel boilers are well understood. Coal and substitute fuels contain a number of in-combustible minerals, which, upon heating, can become molten or volatilise.
- Gaseous species volatilised to the vapour phase condense when they interact with cooler surfaces (heat exchanger tubes or ash particles). When this happens, they can form solid, molten or sticky deposits; it is these molten or sticky deposits which allow solid particles to adhere to heat transfer surfaces.
- Molten particles of fuel ash can impact heat transfer surfaces through inertial impaction and thermophoresis. In their molten state these particles are more likely to adhere to the surface.
- Over time, the thickness of deposits grows resulting in higher surface temperatures, this can lead to sintering of the deposits making them difficult to remove.
- Due to their high operation temperature, heat exchanger steels can be subject to high temperature corrosion. This is caused by the depletion of the protective oxide scale at the surface of the steel by corrosive species in the deposits.
- The alkali metals sodium and potassium along with chlorine found in the fuel ash have been identified as key to this process occurring.

9.4 Combustion of Biomass Fuels

- Most biomass fuels differ from coal in their chemical composition, moisture content, volatile content and ash content. These factors all affect the way a biomass fuel will behave during combustion, making prediction of coal and biomass co-combustion difficult.

- In order to minimise the effect of this uncertainty, power generators tend to use very low substitution ratios (ca. 5%$_{th}$).

9.5 Combustion Modelling Techniques

- Empirical indices, whilst offering a very quick and simple solution, provide a prediction of fuel behaviour rather than boiler performance. These methods also rely on very fundamental assumptions and, as a result, have limited accuracy, particularly for biomass co-firing.
- Similar to empirical indices, thermochemical analysis focuses on predicting fuel behaviour rather than boiler performance. However, due to its use of extensive databases and the minimisation of Gibb's Free Energy to produce results, the predictions made are more useful. However, the results from this sort of calculation will need some interpretation before combustion behaviour can be assessed.
- Many academics and industry bodies have developed bespoke combustion models to simulate boiler performance. These range from highly detailed models focusing on particular aspects of combustion to complex numerical methods predicting entire combustion regimes. Literature suggests that these types of models are often boiler specific and have limited transferability to other applications.

9.6 CFD Simulation of the ENEL 500kW Downfired Furnace

- Six combustion trials conducted by ENEL Produzione in its 500kW downfired, pilot-scale furnace have been modelled using the FLUENT CFD code with a limited degree of success.
- The prediction of an accurate temperature profile for the furnace proved difficult, resulting in poor flue gas prediction. After many evolutions of the modelling process this problem was believed to have been caused by the quality of the computational grid, which affected model convergence.
- Particle impaction rates on two deposition probes have been successfully calculated, however, these do not represent deposition rate as no attempt was made to model particle sticking probability.
- The species transport combustion model has been used to model the parent and substitute fuel streams separately. This can be useful for identifying the

effects of parent and substitute fuels on combustion behaviour. Due to the poor prediction of the temperature profile, this was not achieved.

- A high quality computational grid is necessary to achieve reliable results when using CFD modelling techniques.
- A great deal of training and experience is needed before a user can become competent enough to model full-scale boilers, requiring a high level of combustion knowledge to set up and solve models successfully.
- Computing power limits the size and quality of the computational grid that can be used. This makes generating grids for full scale boilers difficult given their overall size and the need for detailed meshing in the burners and heat exchangers.
- The timescales involved in generating a computational grid, setting up a model and running it to convergence make CFD unsuitable for the type of on-line investigative research needed by boiler operators.

9.7 The Development of a Universal Prediction Tool

- A Microsoft Excel based prediction tool has been produced capable of predicting the temperature profile, slagging, fouling and corrosion tendencies of coal and biomass blends in industrial boilers.
- The tool is not required to predict the type and quantity of deposits formed, but to provide an indication to the user whether the combination of fuels used will increase the risk of slagging, fouling and corrosion within the boiler.
- Empirical correlations were successfully derived using the FLUENT PrePDF CFD pre-processor detailing the relationship between the enthalpy of the combustion gases and their temperature. This was applied to a 1 dimensional model of the boiler to reveal the temperature profile.
- Further empirical correlations describing the mass of solid, molten and gaseous ash species formed have been derived using the FactSage thermochemical software package. These were successfully used to predict the likelihood of slagging and fouling for sewage sludge and coal blends based upon the mass of alkali metals and iron in the molten phase.
- An empirical high temperature corrosion model was successfully developed, capable of predicting the mass of Na_2SO_4, K_2SO_4 and $Fe_2(SO_4)_3$ produced by

blends of coal and sewage sludge. A 'melting temperature map' for this ternary system was used to predict the existence of a sulphate melt on heat exchanger tubes which would lead to increased corrosion rates.

- The empirical correlations developed in this way are of limited use when applied to other substitute fuels.
- The empirical correlations were successfully reproduced for a number of substitute fuels by an artificial neural network developed by C. K. Tan of the University of Glamorgan.
- The ANN model has been used to assess slagging, fouling and corrosion in the Langerlo and Cottham power station boilers, demonstrating its transferability
- The model has demonstrated consistent results when making predictions for these two boilers. Suggesting that operation with $5\%_{th}$ blends of biomass will produce few or no problems, whilst indicating that when firing $10\%_{th}$ biomass, significant slagging, fouling and corrosion related problems will start to occur. This has been backed-up by findings from related literature.

Chapter 10 - Recommendations for Future Work

10.1 Introduction

The research detailed within this thesis provides huge scope for further development and future work; the CFD models need to be refined in order to achieve accurate prediction of combustion conditions inside the ENEL 500kW furnace and the empirical prediction tool needs to be developed further to more accurately predict a wider range of coals and substitute fuels.

10.2 CFD Simulation of the ENEL 500kW Downfired Furnace

There are two areas for potential improvement of this model; improvement of the current models to better predict conditions within the furnace and the development of deposition model and fragmentation models to make the results given by the simulations more useful.

10.2.1 Improvements to the Current Model

The computational grid used in the current CFD model needs to be improved, thus providing better convergence and improving the accuracy of the predictions made. Keeping the hexahedral cell topology is important due to the benefits it provides (Ref: Section 7.3.5.1c) however, a more detailed model of the burner and deposition probe needs to be included. Particular attention should be paid to the mesh quality, ensuring that cell skewedness is not too high.

Once a good quality mesh has been developed and reasonable predictions of combustion conditions have been achieved, further investigation of the two-stream species transport approach should be carried out. This would provide an insight into the effects that the sewage sludge particles have on the combustion conditions within the boiler. Work needs to be done to establish the correct chemical kinetic rates used in this model to describe the combustion of the volatile species.

10.2.2 Development of New Models

In addition to this, development of the fragmentation model proposed by Kurniawan [77] for use with the PowerFlam fuels should be carried out to provide better prediction of particle behaviour within the furnace. Finally a sticking probability model should be developed that is able to predict whether a particle will adhere to the walls or deposition probes within the furnace. This would allow comparisons between predicted and measured deposition rates allowing further assessment of the merits of CFD as a tool for simulating pulverised fuel combustion.

10.3 The Development of a Universal Prediction Tool

There are two areas where future work should be focused for the empirical prediction tool; the improvement of the models already established, and the development of other models to predict other aspects of boiler/plant performance which may be affected by co-firing biomass fuels

10.3.1 Improvement of the Existing Models

The current models used in the spreadsheet have been developed to demonstrate the feasibility of this kind of modelling approach. Further development of these models should be carried out to improve the accuracy of their predictions.

Section 8.3.1.3a highlights the need to improve the accuracy of the model used to calculate the enthalpy change of the water or steam within the steam cycle. Errors of up to 15% were observed in the calculation of the heat energy gained in each heat exchanger.

The current range of fuels that the spreadsheet is valid for is limited to bituminous coal, sewage sludge, sawdust and RDF. This needs to be expanded to include anthracite and brown coals along with other types of substitute fuel. This could be done by either developing a single large ANN to cover every fuel, or by developing a series of specialist ANNs, each for a specific substitute fuel. In addition to this, the number of data points within each training data set for the ANNs needs to be increased in a bid to improve their accuracy.

An ANN needs to be developed for the high temperature corrosion model, allowing it to make predictions for substitute fuels other than sewage sludge. Other minor improvements could be made to the corrosion model; these include adding more types of steel to the tube surface temperature calculation, and the consideration of the effects of chlorine, which is considered to play a large role in high temperature corrosion. Other work associated with the corrosion model could include the validation of the melting temperature map by identifying the melting temperature of a range of compositions of the Na_2SO_4 - K_2SO_4 $Fe_2(SO_4)_3$ system experimentally.

Improvements to the heat transfer model are also necessary; the current model sees the temperature profile dictated by the settings entered by the user for the steam cycle. Modelling of the temperature profile in this way can lead to gas temperature falling below the steam temperature in some heat exchangers. A heat transfer model needs to be developed where the prediction of flue gas temperatures and steam cycle thermodynamics are calculated in tandem and are interdependent. This way, the model would better reflect reality, where steam temperatures are dictated by the flue gas temperature and not vice-versa.

Finally, consideration should also be given to the combustion model; the assumption of instantaneous heat release for the fuel upon entry to the boiler is not realistic. A model needs to be developed where the burning profile of the fuel is used to dictate the release of energy over a longer period. Consideration should also be given in this model to the effects of ash loading on downstream gas temperatures.

10.3.2 Further Development of the Spreadsheet to Cover Other Aspects of Combustion

A review of the literature has revealed that the limiting factor in biomass co-combustion in existing boilers seems to be the inadequacy of the fuel supply system. Many authors have reported problems in the mills/pulverisers and the fuel supply system, caused by the inclusion of the biomass fuel. These problems can include: exceeding the capacity of the mills, increases in grain size leading to higher unburned carbon in the ash, affecting its saleability and conveyor blockages.

The other chief concern of the boiler operator is the effect biomass co-combustion will have on emissions. Emissions to the atmosphere are very tightly regulated by the authorities, so, a model that would predict the effects of biomass co-combustion on emission levels would be a valuable tool for a boiler operator.

Inclusion of these models, which are able to predict the behaviour of fuel blends in these situations other than the combustion environment, would be of great benefit to the boiler operator. This would bring the spreadsheet closer to the proposed model shown in figure 6.1 on page 100, providing the boiler operator with a far more comprehensive boiler performance prediction tool.

[1] *The UK's third national communication under the United Nations framework convention on climate change.* Department for Environment, Food and Rural Affairs, United Kingdom: 2001.

[2] *Caring for climate: a guide to the climate change convention and the Kyoto protocol.* Climate change secretariat, United Nations Framework Convention on Climate Change, Bonn, Germany: 2003.

[3] Ninomiya, Y. Transformation of mineral and emission of particulate matters during co-combustion of coal with sewage sludge. *Fuel,* 2004; 83, 751-764.

[4] Jenkins, B. M. et al. Combustion properties of biomass. *Fuel Processing Technology,* 1998; 54, 71 – 46.

[5] Demibras, A. Combustion characteristics of different biomass fuels. *Progress in Energy and Combustion Science,* 2004; 30, 219 – 230.

[6] Bain. R. et al. Biomass fired power generation. *Fuel Processing Technology,* 1998; 54, 1 – 16.

[7] Sami, M. et al. Co-firing of coal and biomass fuel blends. *Progress in Energy and Combustion Science,* 2001; 27, 171 – 214.

[8] Ireland, S. N. et al. On the technical and economic issues involved in the co-firing of coal and waste in a conventional pf-fired power station, *Fuel,* 2004; 83, 905 – 915.

[9] Williams, A. et al. Combustion of pulverized coal and biomass. *Progress in Energy and Combustion Science,* 2001; 27, 587 – 610.

[10] Sondreal, E. A. et al. Review of advances in combustion technology and biomass cofiring. *Fuel Processing Technology,* 2001; 71, 7 – 38.

[11] Hein, K. R. G. and Bemtgen, J. M. EU clean coal technology – co-combustion of coal and biomass, *Fuel Processing Technology,* 1998; 54, 159 – 169.

[12] Gerhardt, Th. et al. Study of the combined combustion of municipal sewage sludge in coal dust furnaces. *VGB Kraftwerkstechnik,* 1996; 76, 372 – 382.

[13] Wolski, N. et al. Fine particle formation from co-combustion of sewage sludge and bituminous coal. *Fuel Processing Technology,* 2004; 85, 673 – 686.

[14] Otero, M. et al. Analysis of the co-combustion of sewage sludge and coal by TG-MS. *Biomass and Bioenergy,* 2002; 22, 319 – 329.

[15] Savolainen, K. Co-firing of biomass in coal-fired utility boilers. *Applied Energy,* 2003; 74, 369 – 381.

[16] BP Statistical review of world energy 2004. [WWW] URL:http://www.bp.co/statisticalreview2004.htm [Accessed 18th January 2005].

[17] Spliethoff, H. et al. Effect of co-combustion of sewage sludge and biomass on emissions and heavy metals behaviour, *Trans IChemE,* 2000; 78 part B, 33 – 39.

[18] Steenari, B. M. and Lindqvist, O. Fly ash characteristics in co-combustion of wood with coal, oil or peat. *Fuel,* 1999; 78, 479 – 488.

[19] Nadziakiewicz, J. and Koziol, M. Co-combustion of sludge with coal. *Applied Energy,* 2003; 75, 239 – 248.

[20] Heinzel, T. et al. Investigation of slagging in pulverized fuel co-combustion of biomass and coal at a pilot-scale test facility. *Fuel Processing Technology,* 1998; 54, 109 – 125.

[21] Frandsen, F. J. Utilizing biomass and waste for power production – a decade of contributing to the understanding, interpretation and analysis of deposits and corrosion products, *Fuel,* 2004; 83, 1 – 18.

[22] Wei, X. et al. Assessment of chlorine-alkali-mineral interactions during co-combustion of coal and straw, *Energy and Fuels,* 2002; 16, 1095 – 1108.

[23] Hansen, P. F. B. et al. Co-firing straw and coal in a 150MW$_e$ utility boiler: in situ measurements, *Fuel Processing Technology,* 1998; 54, 207 – 225.

[24] Srikanth, S. et al. Nature of fireside deposits in a bagasse and groundnut shell fired 20MW thermal boiler, *Biomass and Bioenergy,* 2004; 27, 375 – 384.

[25] Prinzing, D. E. Impacts of wood cofiring on coal pulverisation at the Shawville generating station, *Fuel Processing Technology,* 1998; 54, 143 – 157.

[26] Waldron, D. J. and Saimbi, S. Biomass co-firing in coal-fired power station boilers, *Energy World,* 2006; 14 – 15.

[27] Akturk, N. U. *Modern Powerstation Practice, Volume E: Chemistry and Metallurgy.* Third Edition, Pergamon Press, Oxford: British Electricity International, 1991.

[28] Couch, G. *Understanding slagging and fouling during PF combustion (IEACR/72).* London: IEA Coal Research, 1994.

[29] Harb, J. N. and Smith, E. J. Fireside corrosion in PC-fired boilers, *Progress in Energy and Combustion Science.* 1990; 16, 169 – 190.

[30] Bott, T. R. *Fouling and slagging in combustion plant.* Report number 92012. Birmingham: ESDU, Birmingham University

[31] Langerlo Boiler operational data pack, Lanorelec, 2002.

[32] Vitalis, B. P. *Constant and sliding pressure options for new supercritical plants.* [WWW] URL: http://www.babcockpower.com/pdf/rpi-14.pdf [Accessed 27th June 2006].

[33] Franke, J and Kral, R. *Supercritical boiler technology for future market conditions.* [WWW] URL: http://www.powergeneration.siemens.com/ download/ pool/Parsons_2003.pdf [Accessed 27th June 2006]

[34] Richardson, M et al. *Supercritical boiler technology matures.* [WWW] URL: http://www.hitachi.us/supportingdocs/forbus/powerindustrial/CG2004.pdf [Accessed 27th June 2006].

[35] Stultz, S. and Kitto, J. In: Akturk, N. U. *Modern Powerstation Practice, Volume E: Chemistry and Metallurgy.* Third Edition, Pergamon Press, Oxford: British Electricity International, 1991.

[36] Skorupska, N. M. *Coal specifications – impact on power station performance (IEACR/52).* London: IEA Coal Research, 1993.

[37] Chen, M. R. et al. In: Morrison, G. F. *Understanding pulverised coal combustion.* London: IEA Coal Research, 1986.

[38] Davini, P. et al. Investigation of the combustion of particles of coal, *Fuel*; 1996, 75, 1083 – 1088.

[39] Su, S. et al. Techniques to determine ignition, flame stability and burnout of blended coals in p.f. power station boilers, *Progress in Energy and Combustion Science*; 2001, 27, 75 – 98.

[40] Dacombe, P. et al. Combustion-induced fragmentation behaviour of isolated coal particles, *Fuel*; 1999, 78, 1847 – 1857.

[41] Liu, G. et al. Modelling the fragmentation of non-uniform porous char particles during pulverised coal combustion, *Fuel*; 2000, 79, 627 – 633.

[42] Gajewski, W and Kosowska, M. *The thermal fragmentation of polish coals during combustion process*, 12th International Conference on Coal Science. Cairns, Australia, 2003, 1–9.

[43] Rushdi, A. et al. An experimental study of the effect of coal blending on ash deposition, *Fuel*; 2003, 83, 495 – 506.

[44] Bryers, R. W. Fireside slagging, fouling and high temperature corrosion of heat-transfer surface due to impurities in steam-raising fuels. *Progress in Energy and Combustion Science.* 1996; 22, 29 – 120.

[45] Yamashita. T. et al. Modelling of ash formation behaviour during pulverized coal combustion. *IFRF Combustion Journal.* Article No. 200008, 2000.

[46] Sugawara, K. et al. *Release behaviour of alkali metals during coal pyrolysis,* 12th International Conference on Coal Science. Cairns, Australia, 2003, 1 – 5.

[47] Lee. B. E. et al. Computational study of fouling deposit due to surface coated particles in coal-fired power utility boilers, *Fuel.* 2002; 81, 2001 – 2008.

[48] Valero. A and Cortes. C. Ash fouling in coal-fired utility boilers. Monitoring and optimization of on-load cleaning, *Progress in Energy and Combustion Science.* 1996; 22, 189 – 200.

[49] Su. S. et al. Slagging propensities of blended coals, *Fuel.* 2001; 80, 1351 – 1360.

[50] Su. S. et al. Fouling propensities of blended coals in pulverized coal-fired power station boilers, *Fuel.* 2003; 82, 1653 – 1667.

[51] Mucahy et al. In: Akturk, N. U. *Modern Powerstation Practice, Volume E: Chemistry and Metallurgy.* Third Edition, Pergamon Press, Oxford: British Electricity International, 1991. [28]

[52] Honea et al. In: Couch, G. *Understanding slagging and fouling during PF combustion (IEACR/72).* London: IEA Coal Research, 1994.

[53] Bailey, C. W. et al. Ash deposits in a coal-fired power station related to experimentally measured ash character. *IFRF Combustion Journal.* Article No. 199903, 1999.

[54] Walsh, P. M. et al. Deposition of bituminous coal ash on an isolated heat exchanger tube: effects of coal properties on deposit growth, *Progress in Energy and Combustion Science.* 1990; 16, 327 – 346.

[55] Tomeczek, J. et al. Modelling of deposits formation on heating tubes in pulverised coal boilers, *Fuel.* 2004; 83, 213 – 231.

[56] Michel, J. R. and Wilcoxon, L. S. In: Dacombe, P. et al. Combustion-induced fragmentation behaviour of isolated coal particles, *Fuel*; 1999, 78, 1847 – 1857.

[57] Cutler, A. J. B. and Raask, E. External corrosion in coal-fired boilers: Assessment from laboratory data, *Corrosion Science.* 1981; 21, 789 – 800.

[58] Cain, C and Nelson, W. Corrosion of superheaters and reheaters of pulverized-coal-fired boilers, part 2, *American Society of Mechanical Engineers.* 1961; Paper 60-WA-180.

[59] Hendry, A and Lees, D. J. Corrosion of austenitic steels in molten sulphate deposits, *Corrosion Science.* 1980; 20, 383 – 404.

[60] meps steel prices. 2005. Carbon steel world price index. [WWW] <URL: http://www.meps.co.uk/world%20carbon%20price.htm> [Accessed 22nd September 2005]

[61] meps steel prices. 2005. Stainless steel world price index. [WWW] <URL: http://www.meps.co.uk/stainless%20prices.htm> [Accessed 22nd September 2005]

[62] Akturk, N. U. *Modern Powerstation Practice, Volume B: Boilers and Ancillary plant.* Third Edition, Pergamon Press, Oxford: British Electricity International, 1991.

[63] Srivastava, S. C. and Godiwalla, K. M. Review: fuel ash corrosion of boiler and superheater tubes, *Journal of Materials Science.* 1997; 32, 835 – 849.

[64] Otsuka, N. Effects of fuel impurities on the fireside corrosion of boiler tubes in advanced power generating systems – a thermodynamic calculation of deposit chemistry, *Corrosion Science.* 2002; 44, 265 – 283.

[65] Corey et al. In Tomeczek, J. et al. Modelling of deposits formation on heating tubes in pulverised coal boilers, *Fuel.* 2004; 83, 213 – 231

[66] Cain, C and Nelson, W. Corrosion of superheaters and reheaters of pulverized-coal-fired boilers, part 2, *American Society of Mechanical Engineers.* 1961; Paper 60-WA-180.

[67] Carpenter, A. M and Skorupska, N. M. *Coal combustion – analysis and testing.* London: IEA Coal Research, 1993.

[68] Andersen, K. H et al. Deposit formation in a 150MW$_e$ utility PF-boiler during co combustion of coal and straw. *Energy and Fuels.* 2000; 14, 765-780.

[69] Skrifvars, B-J. et al. Ash behaviour in a pulverised wood fired boiler – a case study. *Fuel.* 2004; 83, 1371-1379.

[70] Gera, D et al. Computational fluid dynamics modelling for biomass cofiring design in pulverised coal boilers. *FLUENT Inc.* Morgantown, West Virginia.

[71] Sheng, C et al. A computational fluid dynamics based study of the combustion characteristics of coal blends in a pulverised-coal furnace. *Fuel.* 2004; 85, 1543-1552.

[72] Vanormelingen, J et al. *CFD-study of a 230 MW$_e$ coal fired boiler to predict the influence of secondary fuels on slagging, fouling, CO, corrosion and NO$_X$ formation,* 13th IFRF Members Conference, Noordwijkerhout, 2003; 1 – 11.

[73] Backreedy, R. I. et al

[74] Kurose, R. et al. Effects of moisture in coal on pulverised coal combustion characteristics. *Fuel.* 2001; 80, 1457 – 1465.

[75] Kurose, R et al. Numerical analysis of pulverised coal combustion characteristics using advanced low-NO$_x$ burner. *Fuel.* 2004; 83, 693 – 703.

[76] Kær, S. K. Numerical modelling of a straw fired grate boiler. *Fuel.* 2004; 83, 1183 – 1190.

[77] Kurniawan, K. *The modelling of coal combustion in an inverted cyclone apparatus.* PhD Thesis, Cardiff University, 2002.

[78] Scribano, G. *Numerical simulation of a two stage combustor, period July – December 2002.* Report number 2946. Cardiff: Cardiff University, 2002.

[79] Carrieri, R *Numerical simulation of a 500kW downfired furnace, period November 2002 – April 2003.* Report number 3018. Cardiff: Cardiff University, 2003.

[80] Svensson, C. *Modelling particle fragmentation in a CFD code, period January – June 2003.* Report nnmber 3011. Cardiff: Cardiff University, 2003.

[81] Harb, J. N. and Wang, H. Modelling of ash deposition in large-scale combustion facilities burning pulverised coal. *Progress in Energy and Combustion Science.* 1997; 23, 267 – 282.

[82] Fan, J. R. et al, Simulation of deposit growth in a pulverised coal-fired boiler. *Fuel.* 2001; 80, 645 – 654.

[83] Lee, F. C. and Lockwood, F.C. Modelling ash deposition in pulverised coal-fired applications. *Progress in Energy and Combustion Science.* 1999; 25, 117 – 132.

[84] Pyykönen, J. and Jokiniemi, J. Modelling alkal chloride superheater deposition and its implications. *Fuel Processing Technology.* 2003; 80, 225 – 262.

[85] Kouprianov, V. I. Modelling of thermal characteristics for a furnace of a 500MW boiler fired with high-ash coal. *Energy.* 2001; 26, 839 – 853.

[86] Erickson, T. A. et al. Modelling of fouling and slagging in coal-fired utility boilers. *Fuel processing technology.* 1995; 44, 155 – 171.

[87] Bale, C. W. et al. FactSage thermochemical software and databases. *Calphad.* 2002; 26, 189 – 228.

[88] Jak, E. Prediction of coal ash fusion temperatures with the F*A*C*T thermodynamic computer package. *Fuel.* 2002; 81, 1655 – 1668.

[89] Jak, E. et al. *The prediction and representation of phase equilibria and physiochemical properties in complex coal ash slag systems.* 12th International Conference on Coal Science. Cairns, Australia, 2003, 1 – 13.

[90] Thompson, D. and Argent, B. B. The mobilisation of sodium and potassium during coal combustion and gasification. *Fuel,* 1999; 78, 1679 – 1689.

[91] Turn, S. et al. *Fouling characteristics of processed biomass: Comparison of chemical equilibrium predictions with full scale test results.* 12th European conference and technology exhibition on biomass for energy and climate protection. Amsterdam, The Netherlands, 2002, 1 – 8.

[92] Rogers, G. F. C and Mayhew, Y. R. *Thermodynamic and Transport Properties of Fluids.* 5th Edition. Blackwell Publishing, 1995.

[93] *FLUENT 6 Users guide volume 3,* Lebanon, USA, 2001

[94] Abd Rahman. A. *Studies of Co-Firing Coal with Biomass on a Two Stage Simulator for Utility Boilers.* PhD Thesis, Cardiff University, 2006.

[95] Vanormelingen. J. Private Communications With, January 2004.

[96] Rogers. G and Mayhew. Y. *Engineering Thermodynamics: Work and Heat Transfer 4th Edition.* Longman, Harlow, England; 1992.

[97] Hassoun. M. H. *Fundamentals of Artificial Neural Networks.* MIT Press, Cambridge, Massechusetts; 1995

[98] Graziadio, M and Costansi, F. *ENEL* $500kW_{th}$ *Furnace Tests.* IFRF, Velsen – Noord, June 2003.

[99] *PowerFlam 1-2 proposal,* IJmuiden, Netherlands, June 2001.

[100] Leiser. S. *Characterisation of Powerflam1 fuels using the IFRF Isothermal plug flow reactor.* IFRF Doc. No. F107/y/5, IJmuiden, June 2003.

[101] Neveu-Dubosc. A. *Effect of co-firing of substitute fuel blends on individual pulverised coal boilers.* IFRF Doc. No. NNE5-2001-00907, Chatou Cedex, May 2005.

[102] Struckmann. P, et al. Co-combustion of secondary fuels – prevention or reduction of operating problems. *VGB Powertech.* 2004; 84, 72 – 76.

[103] Gilberg. G. Co-combustion of special fuels in the Zolling power station of E.ON Kraftwerke GmbH. *VGB Powertech.* 2002; 82, 78 – 83.

[104] Wierick. H. G, et al. Experience with the co-combustion of sewage sludge in the Boxberg lignite-fired power plant of VEAG. *VGB Powertech.* 2001; 81, 43 – 46.

[105] Buck. P and Tiebel. W. Operating experience with sewage sludge co-combustion in the coal fired power plant in Helibronn. *VGB Powertech.* 2000; 80, 56 – 58.

[106] Dietl. R and Schmidt. W. Technical large-scale test of biomass co-combustion in a lignite-fired power plant. *VGB Powertech.* 1999; 79, 60 – 64.